



**QUEEN'S
UNIVERSITY
BELFAST**

DOCTOR OF PHILOSOPHY

An Exploration of Quantum Critical Phenomena in One-Dimensional Lattice Systems: Geometric Frustration & Quantum Fluctuations

Cartwright, Christine

Award date:
2019

Awarding institution:
Queen's University Belfast

[Link to publication](#)

Terms of use

All those accessing thesis content in Queen's University Belfast Research Portal are subject to the following terms and conditions of use

- Copyright is subject to the Copyright, Designs and Patent Act 1988, or as modified by any successor legislation
- Copyright and moral rights for thesis content are retained by the author and/or other copyright owners
- A copy of a thesis may be downloaded for personal non-commercial research/study without the need for permission or charge
- Distribution or reproduction of thesis content in any format is not permitted without the permission of the copyright holder
- When citing this work, full bibliographic details should be supplied, including the author, title, awarding institution and date of thesis

Take down policy

A thesis can be removed from the Research Portal if there has been a breach of copyright, or a similarly robust reason. If you believe this document breaches copyright, or there is sufficient cause to take down, please contact us, citing details. Email: openaccess@qub.ac.uk

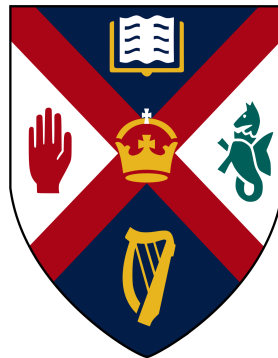
Supplementary materials

Where possible, we endeavour to provide supplementary materials to theses. This may include video, audio and other types of files. We endeavour to capture all content and upload as part of the Pure record for each thesis. Note, it may not be possible in all instances to convert analogue formats to usable digital formats for some supplementary materials. We exercise best efforts on our behalf and, in such instances, encourage the individual to consult the physical thesis for further information.

An Exploration of Quantum Critical Phenomena in One-Dimensional Lattice Systems:

Geometric Frustration & Quantum Fluctuations

School of Mathematics and Physics
QUEEN'S UNIVERSITY BELFAST



Author:
Christine Cartwright
(*Msci Maths*)

Supervisor:
Dr. Gabriele De Chiara

This thesis is submitted for the degree of:
Doctor of Philosophy

June 2019

I believe in Christianity as I believe that the sun has risen: not only because I see it, but because by it I see everything else. CS. Lewis

I would like to dedicate this thesis to my loving parents and sister.

ACKNOWLEDGEMENTS

There is a massive amount of work that goes into a thesis but more importantly there are hordes of people who support and pull up the individual student. This thesis would not have been possible without the patience, dedication, support and explanations of my supervisor, Gabriele De Chiara, and our collaborators, in particular, Matteo Rizzi. I would like to thank both of these people for the amount of time that they invested in guiding me along to a point of understanding and for always being so encouraging and supportive. Gabriele, to you I owe additional thanks. Thank you so much for providing me with the opportunity to do a PhD and for all of the time and effort that you have put in to help me, to firstly conduct the work and then all of the detailed corrections to improve this thesis.

I would also like to thank Alessandro Ferraro and Mauro Paternostro, both of whom are fantastic role models in the field and who have always had time to make me feel welcome and to explain the many things that I don't understand.

Working through and creating a PhD can often seem like walking through quicksand with no way out and in fact the end getting further away. So I need to give a massive thanks to all of those who have offered me the emotional support and encouragement that has finally led to this work appearing as a finished thesis. My greatest thanks and love to my wonderful family, in particular my sister Allison, whose main advice throughout the whole process has been 'I told you not to do a PhD', whilst she was completing one herself. I would also like to give a humongous thanks to my friends who have reassured me that I am not indeed as stupid as I sometimes feel and who have provided catch-ups, movie nights and general banter which has improved my productivity when needed. Robyn thanks for also doing a PhD so that you could empathise as well as distract me. Also, thank you to all of my Christian friends and fellow Sunday school leaders, who have reminded me that God and His plans are what really matters.

Additionally, the place that you work, and how much you enjoy being there, has a huge impact on how well you are able to perform. The atmosphere and support within CTAMOP and the school as a whole has been amazing. Right from when I started the PhD, I was made to feel welcome by the lecturers, post-docs,

students and support staff. I really couldn't have gotten here without all of your support! I am very blessed to have made some extraordinary new friends here and I will cherish the time spent with you. I'm not going to list all of you here for fear of forgetting someone, but know that each and every one of you has impacted my time here as a PhD student and I would like to thank you all for your support and inspiration. Particular thanks goes to Helena, Kathryn, Kenny, Hannah, Ricardo, Adam, Marta and Giorgio who have put up with my endless questions and kept me sane through chats and laughter. I would also like to give a special mention to our system administrator, Ian Stewart, who not only has always been on hand to deal with any issues that arise but also who is the perfect person to go to when you fancy a long chat and an update on the latest (mostly apple) gadgets.

Finally, I would like to add in a catch-all for all of the people who are not mentioned here. I know that this is in no way a comprehensive list, so to all of the people with whom I've had discussions at schools, visits or in Belfast and to all of the people who have been available for chats and support thank you very much.

ABSTRACT

This thesis focuses on identifying different types of critical phenomena within one-dimensional quantum lattice spin systems. People are exposed to classical critical phenomena everyday in the form of phase transitions, such as from water to ice. Surrounding quantum phase transitions, there is a number of exciting phenomena still to be explored, enhancing our knowledge of the quantum effects.

We will examine the features of quantum phase transitions within spin chains, where our focus will be on the use of entanglement measures, and we will explore an extension of the standard Bose-Hubbard model on a one-dimensional lattice with a non-trivial elementary cell.

Our first main focus will be on the use of entanglement scaling as an indicator of when a phase transition has occurred, more specifically for first-order quantum phase transitions in the vicinity of second-order quantum phase transitions. In this context, we show the dramatic importance of finite-size effects when a first-order quantum phase transition occurs in the nearby region of multi-critical point containing also a second-order quantum phase transition. Through the use of finite-size scaling we highlight that a bipartite measure of entanglement can correctly identify a given first-order quantum phase transition.

Motivated by the plethora of diverse features that geometric frustration may lead to, we will also examine the Bose-Hubbard model on a geometrically frustrated lattice. The lattice we will examine is a one-dimensional chain of rhombi and causes the particles to form pairs in the presence of repulsive interactions. We perform a detailed numerical analysis of the different phases emerging from the model, including the block entropy and entanglement spectrum. Additionally, we perform an analysis of the model under dynamics with a single, a pair of particles and for unit filling.

LIST OF PUBLICATIONS

Yuste, A., Cartwright, C., De Chiara, G., and Sanpera, A. (2018). Entanglement scaling at first order quantum phase transitions. *New Journal of Physics*, 20(4):043006.

Cartwright, C., De Chiara, G., and Rizzi, M. (2018). Rhombi-chain Bose-Hubbard model: Geometric frustration and interactions. *Phys. Rev. B*, 98:184508.

Cartwright, C. (2018) The Bose-Hubbard model on a flat-band lattice: A community of bosons. T. Calarco, R. Fazio and P. Mataloni *Proceedings of the International School of Physics “Enrico Fermi” Course 198 “Quantum Simulators”* (pp. 17-20). IOS, Amsterdam; SIF Bologna.

TABLE OF CONTENTS

List of Publications	vi
List of Figures	x
List of Tables	xxiii
List of Acronyms	xxiv
1 Introduction	1
2 Quantum Critical Phenomena and Ultracold Atoms	6
2.1 Definitions of Quantum Phase Transitions	6
2.2 Features in Critical Models	10
2.2.1 Ising model	10
2.2.2 Bose-Hubbard Model	13
2.2.3 Scaling Laws	19
2.3 Entanglement Measures of Many-body Systems	20
2.3.1 Measures of Entanglement	23
2.3.2 Entanglement Scaling around Quantum Phase Transitions	24
2.4 Frustration within lattices	25
2.4.1 Features of frustrated lattices	27
2.4.2 Examples of frustrated lattices	28
2.5 Experiments with Ultracold Atoms	30
2.5.1 Optical Lattices	30
2.5.2 Experimental Realisations of Frustrated Lattices	31
2.6 Conclusions	34
3 Computational Methods for Ground State Simulations	35
3.1 Density Matrix Renormalisation Group	36
3.1.1 Infinite system DMRG	37
3.1.2 Finite system DMRG	40
3.2 Truncation of the Hilbert Space	42

3.3	Matrix Product States (MPS)	43
3.3.1	Singular Value Decomposition (SVD)	44
3.3.2	Schmidt Decomposition	46
3.3.3	Methodology of MPS	47
3.3.4	DMRG in the MPS ansatz	54
3.3.5	Symmetries and Conserved quantities within MPS	59
3.4	Comparison of Methods	60
3.4.1	Non-MPS DMRG implementation	60
3.4.2	MPS DMRG implementations	61
3.5	Conclusions	65
4	Computational Methods for Simulations of Time Dynamics	66
4.1	Suzuki-Trotter Decomposition	67
4.2	Time-dependent Density Matrix Renormalisation Group	68
4.3	Time Evolving Block Decimation (TEBD)	70
4.3.1	MPS in Vidal's Notation	70
4.3.2	TEBD method	72
4.4	Time-Dependent Variational Principle (TDVP)	73
4.5	Krylov Based Time Evolution	75
4.6	A Case-study of Time Evolution	77
4.7	Conclusion	79
5	Entanglement Scaling of First Order Quantum Phase Transitions	80
5.1	Key theorems for Entanglement at a Phase Transition	81
5.1.1	Kohn-Sham Theorem and its Expansion	81
5.1.2	Scaling Theorem for First-Order Transitions	83
5.2	Scaling applied to Bipartite Entanglement Measures	85
5.2.1	Spin-1/2 Ising chain with longitudinal field	85
5.2.2	Spin-1 XXZ chain with uniaxial single-ion anisotropy	88
5.3	Analysis of Entanglement Features through Density Matrices	96
5.4	Conclusions	98
6	The Frustrated Rhombi (Diamond) Model	99
6.1	Formulation of the Rhombi Model	99
6.2	Previous studies of the model	101
6.3	Single-Particle Representation of the Model	103
6.3.1	The Energy Eigenspectrum	103
6.3.2	The Aharonov-Bohm Cage Formulation	103
6.4	Identifying the Phases	107
6.4.1	The Mott-Insulator Lobe	108

6.4.2	Gapless Phases	111
6.5	The Complete Phase Diagram	116
6.6	Experimental Realisation of the Model	119
6.6.1	Appropriate Experimental Implementations	119
6.6.2	Alternative Formulations of the Rhombi Model	120
6.7	Entropy and Entanglement Measures	121
6.7.1	Entanglement Entropy	122
6.7.2	Entanglement Spectrum	124
6.8	Conclusions	127
7	Time Dynamics of the Frustrated Rhombi Model	128
7.1	Recent Studies of Non-Equilibrium Geometric Models	129
7.2	The Rabi Model	130
7.3	Dynamics of the Single Particle	132
7.3.1	Single Particle with Perfect Frustration	133
7.3.2	Single Particle with Imperfect Flux	138
7.4	Dynamics of a Pair of Particles	141
7.4.1	The Effect of Interaction on Escaping the Cage	143
7.5	Dynamics of a System with Unit Filling	144
7.5.1	Finding the Optimal MPS Implementation	145
7.5.2	Propagation from Half of the Chain	146
7.6	Conclusions and Further Analyses	149
8	Conclusion	150
	References	155
	Appndx A Cage basis for the rhombi model at full-frustration	171

LIST OF FIGURES

2.1	A sketch of the characteristic features surrounding a first-order quantum phase transition (1OQPT) which occurs at $h = h_c$. (a): Sketch of the energy crossing that occurs at the first-order quantum phase transition (1OQPT). (b): An example of the discontinuity in the state using the magnetisation M	8
2.2	A sketch of the magnetisation M_x around the second-order quantum phase transition (2OQPT) at $B_z/J_x = 1$ within the spin-1/2 Ising model. The critical point is circled and labelled.	11
2.3	The appearance of the magnetisation and the energy at the first-order quantum phase transition (1OQPT) in a finite system, where we have assumed $J_x = 1$. (a): The magnetisation along x for the Ising model's ground state around the first-order quantum phase transition (1OQPT). A discontinuity appears at $B_x = 0$ in the thermodynamic limit (orange) but this is not always evident in finite systems (blue dashed). (b): A sketch of the ground state energy, E_0 , and the first excited energy, E_1 , plotted around the critical point $B_x = 0$. The critical point is signalled by a vertical dashed grey line.	12
2.4	Sketch of the phase transition in the Bose-Hubbard (BH) model, showing the characteristic Mott lobes at density $\langle n_j \rangle = 1$ and density $\langle n_j \rangle = 2$ in yellow and the superfluid (SF) phase outside of these. The dashed lines are where the constant integer density extends out of the lobes. The Berezinskii-Kosterlitz-Thouless (BKT) transitions are marked by the purple crosses.	15
2.5	The energy eigenspectrum $E(k)$ (Bloch band) of the single particle in a lattice against the quasimomentum k	17

2.6	Illustration of the particles considered using measures of entanglement. The zig-zagged lines represent that there is some entanglement measure being considered. (a) : the entanglement between one bipartition of a lattice (\mathcal{A}) and the other (\mathcal{B}). (b) : the entanglement between two particles A and B . (c) : the entanglement between two particles, which are at the centre of the lattice in a bipartition of parts \mathcal{A} and \mathcal{B} (shown by the blue boxes).	23
2.7	The geometrical frustration arising as a result of the Ising model with anti-ferromagnetic ordering. Once the bottom two are set, the top site in the triangle wants to orient the spin in conflicting directions as shown by both arrows and the question mark.	26
2.8	(a) : Example of a geometric lattice by showing the layout of the Creutz-ladder. The tunnelling parameters are varied at the different types of legs, which are labelled in different colours to correspond to their coefficient. (b) : The two flat-bands at $\pm 2t$ that arise in the single particle energy spectrum $E(k)$ of the Creutz Ladder in quasimomentum space k	29
2.9	Illustration of the setup of a two-dimensional (2-D) optical lattice. Propagating laser light (red arrows) forms an artificial crystal structure, which traps the atoms (circles) except for small tunnellings to nearby sites.	31
2.10	Illustration of a digital micromirror device (DMD). Within a given digital micromirror device (DMD) chip there is an array of individually tuneable micromirrors which are shown in the grid.	33
2.11	Diagram of a standard setup for a quantum gas microscope. A microscopic device is used which has a vacuum window and a mirror above it. The optical lattice is formed above the mirror, where the atoms are set up in a focal plane so that an image of the plane can be obtained.	34
3.1	Illustration of the blocks \mathcal{A} and \mathcal{B} and free sites $\mathcal{S}_\mathcal{A}$ and $\mathcal{S}_\mathcal{B}$ in the density matrix renormalisation group (DMRG) method.	36
3.2	Illustration of the growing procedure of expanding blocks in the infinite system density matrix renormalisation group (DMRG) method.	37
3.3	Illustration of the sweep procedure of increasing blocks and moving free sites in the finite density matrix renormalisation group (DMRG) method. Initially the free sites are in the centre of the chain. Block \mathcal{A} is expanded until \mathcal{B} is of minimal size (first quarter sweep), then block \mathcal{B} is expanded until block \mathcal{A} is of minimal size (second and third quarter sweep). Lastly, block \mathcal{A} is expanded until it is of size $\frac{L-2}{2}$, completing a full sweep.	41

- 3.4 **(a)**: Illustration of the relevant manifold that can be kept within the full Hilbert space \mathbb{H} . **(b)**: The bipartition of the lattice in order to measure the von Neumann entropy. The sites on the border of the bipartition are shown in red. 43
- 3.5 Demonstration of how the singular value decomposition (SVD) method forms the new decomposition of the matrix \mathbf{M} in terms of the matrix \mathbf{S} of singular values and the matrices \mathbf{U} and \mathbf{V}^\dagger of the left and right singular vectors, respectively. **(a)** shows the case when $N_A > N_B$, **(b)** illustrates when $N_A < N_B$ and **(c)** illustrates the general properties of \mathbf{U} and \mathbf{V} . Any white squares have zero elements and any black squares are strictly one, i.e. the white and black matrices are the identity matrix \mathbb{I} 44
- 3.6 Illustration of how to represent matrix product states (MPS) operators. The \mathbf{A} matrices are left normalised, shown by the triangle pointing to the right and the \mathbf{B} matrices are right normalised, with a triangle pointing to the left. The vertical legs represent the physical state labels and the horizontal lines are the internal indices of the matrix. 48
- 3.7 An example of how to reshape the vector $\Psi_{(\sigma_1, \sigma_2, \sigma_3), 1}$ for qubits ($d = 2$) to $\Psi_{\sigma_1, (\sigma_2, \sigma_3)}$. The triangles in different positions match up with the reshaped matrix to highlight where each element came from. 49
- 3.8 Illustration of **(a)** the left and **(b)** the right, normalisation via singular value decomposition (SVD) to create a left (right) canonical matrix product states (MPS) system. The physical indices are labelled in black and the matrix (internal) indices are labelled in green. The direction of the triangle inside the site indicates whether it is left (pointing right) or right (pointing left) normalised. 51
- 3.9 Illustration of the left normalisation followed by right normalisation via singular value decomposition (SVD) to create a mixed canonical matrix product states (MPS) system. The physical indices are labelled in black and the matrix (internal) indices are labelled in green. The direction of the triangle inside the site indicates whether it is left (pointing right) or right (pointing left) normalised. The diamond represents the the matrix of singular values between two sites. 53
- 3.10 An example of how the expectation is measured of an arbitrary operator in matrix product operator (MPO) form O for a lattice of length $L = 8$. No assumptions are made about the normalisation of these sites. 55

- 3.11 Illustrations of how the matrix product operator (MPO) formulation can be thought of as a weighted walk. The start and the termination nodes are in orange to highlight them. **(a)**: An example of the operator $-B_z\sigma^z$ acting on site three. **(b)**: The representation of O_z (in Eq. (3.38)). **(c)**: The matrix product operator (MPO) representation for the whole Hamiltonian in Eq. (3.38). 56
- 3.12 Illustration of the procedure applied within the two-site minimisation procedure for a given pair of sites $j = 4, 5$, where we assume that we are sweeping to the right. The Hamiltonian \mathcal{H} is applied as a tensor of operators, W_j for $j = 1, \dots, L$ (coloured in pink or yellow). In order to highlight the two sites being considered their operators are in yellow and their states in light blue. The triangles show the normalisation as they point to the right for left-normalised (A) matrices and to the left for right-normalised (B) matrices. The effective Hamiltonian, \mathcal{H}_{eff} , is given by the (effective) operators in purple. 58
- 3.13 Comparison of how different implementations of density matrix renormalisation group (DMRG) perform against the truncation χ when finding the ground state for a chain of length $L = 10$. The methods being compared are Powder with Power (PwP), which does not explicitly use matrix product states (MPS) and then open source matrix product states (OSMPS), IndMPS- “Independent matrix product states (MPS)” and tensor network theory (TNT) Library, which all use matrix product states (MPS). A comparison is shown of **(a)** the energy difference of the approximate energy \tilde{E}_G minus the exact E_G and **(b)** the time taken for the different methods. **(c)** shows the ℓ^2 norm of the error of the on-site density $\Delta n_i = ||\langle \tilde{n}_i \rangle - \langle n_i \rangle||$ and finally **(d)** illustrates the measure of error provided by the methods Powder with Power (PwP) and open source matrix product states (OSMPS) with the actual error in the energy in the inset. 63
- 4.1 Illustration of the adaptation of the finite density matrix renormalisation group (DMRG) method to implement the time-dependent density matrix renormalisation group (tDMRG) method, where the operator $\mathcal{U}_{(\ell, \ell+1)} = e^{-i\tilde{\mathcal{H}}^{(\ell, \ell+1)}\delta t}$ is applied to the free sites (green circles). The sweeps are carried out in the same manner as the finite procedure, with the blocks (blue rectangles) being expanded and contracted. 69

- 4.2 An illustration of Vidal's form of the matrix product states (MPS) with two free sites. The diamonds are the singular values (Λ), whereas the circles represent the Γ s. **(a)** shows the original mixed matrix product states (MPS) setup, whereas in **(b)** the tensor $\Theta_{a_{\ell-1}, a_{\ell+1}}^{\sigma_{\ell} \sigma_{\ell+1}}$ (defined in Eq. (4.12)) has been formed from the free sites. 71
- 4.3 The spreading of the on-site density $\langle n_j \rangle$ with time t , when all of the particles are initially started at the central site $j = 4$ and $J = U = 1$ 77
- 4.4 The ℓ^2 norm of the error $\Delta n_i(t) = ||\langle \tilde{n}_i(t) \rangle - \langle n_i(t) \rangle||$ for different times t and $\chi = 200$ against the size of the time steps δt . The results are shown using both the Krylov (circles) and the time dependent variational principle (TDVP) method (stars). 78
- 5.1 Illustration of **(a)** the analytic magnetisation M_x and **(b)** the energy gap Δ , which measurements taken around the first-order quantum phase transition (1OQPT), with various parameters, should collapse to. 84
- 5.2 Phase diagram for the spin-1/2 Ising chain with a longitudinal field. The dashed line (- -) depicts the first-order quantum phase transition (1OQPT) while the dotted line (...) the second-order quantum phase transition (2OQPT). 85
- 5.3 Concurrence of the longitudinal Ising model with length $L = 40$, Eq. (5.6), as a function of B_x near the first-order quantum phase transition (1OQPT), for different values of the transverse magnetic field B_z . We observe a spike at the first-order quantum phase transition (1OQPT) critical point, $B_x = 0$, for $B_z < 1$ 86
- 5.4 Concurrence of the longitudinal Ising model, Eq. (5.6), as a function of κ_1 , defined in Eq. (5.7), near the first-order quantum phase transition (1OQPT) for different values of the transverse magnetic field B_z . **(a)**: Concurrence normalised by its maximum, $\tilde{\mathcal{C}}$, as a function of the scaling variable κ_1 ; there is no data collapse. **(b)**: Derivative of the concurrence normalised by its minimum, $\widetilde{\partial_{B_x} \mathcal{C}}$, plotted as a function of κ_1 showing a universal behaviour for the same set of values in **(a)**. The results are obtained with density matrix renormalisation group (DMRG) and bond dimension $\chi = 80$ for which they are converged. 88

- 5.5 **(a):** Phase diagram for the spin-1 model in Eq. (5.10) with $D > 0$. The dashed lines depict first-order quantum phase transitions (1OQPTs) and the arrows the points where we cross them. The black dotted line depicts the second-order quantum phase transition (2OQPT) between Haldane and Néel phases. The red circles signal the tri-critical points present in the phase diagram. The ovals show the areas where we add an external field to induce a first-order quantum phase transition (1OQPT) between the two-fold degenerate ground states in the ferromagnetic and Néel phases, which are shown fully in **(b)** and **(c)** respectively. 89
- 5.6 Measures around the first-order quantum phase transition (1OQPT) between the Néel and the Anti-Néel phases. **(a)** and **(b):** The staggered magnetisation M_z^{st} and the negativity \mathcal{N} as a function of B_z^{st} for different J_z and $L = 8$, $D = 0$. This is calculated using ED. 90
- 5.7 **(a)** and **(b):** The renormalised magnetisation M_z^{st}/m_0^{st} and energy gap $\Delta(\kappa_2)/\Delta_L$ plotted against the scaling variable κ_2 , Eq. (5.12). M_z^{st} fulfils the universal scaling, Eq. (5.5) and $\Delta(\kappa_2)/\Delta_L$ follows Eq. (5.4). The dashed lines are those Campostrini *et al.* analytically obtained. **(c):** The renormalised negativity $\tilde{\mathcal{N}} = \mathcal{N}/\mathcal{N}(B_z^{st} = 0)$ plotted against κ_2 (no collapse occurs). **(d):** The renormalised derivative of the negativity $\widetilde{\partial_{B_z^{st}} \mathcal{N}}(\kappa_2)$ (derivative normalised by its maximum) where a good data collapse is observed. density matrix renormalisation group (DMRG) was used to obtain these results. . 91
- 5.8 Negativity \mathcal{N} as a function of J_z for $D = 3.5$ and $L = 8$. We observe a discontinuity in the first-order quantum phase transition (1OQPT) from ferromagnetic to large- D phases (shown by the green arrow) and a smooth slope for the first-order quantum phase transition (1OQPT) between the large- D and Néel phases (shown by the orange arrow). The results are obtained with ED. 93
- 5.9 Phase transition between ferromagnetic and large- D for $D = 2$ and $L = 8$. **(a)** The energy crossing between the two-fold degenerate ferromagnetic ground state at $J_z < J_{zc}$ (circles and crosses) and the large- D ground state at $J_z > J_{zc}$ (squares), where the critical energy is $E_c \approx -0.2660$ and $J_{zc} \approx -2.5897$. **(b):** We observe a jump in the negativity (dotted line) for J_{zc} even when using a step $\delta = 10^{-13}$. The results are obtained with ED. 94

- 5.10 The staggered magnetisation and the negativity around the large- D /Néel transition, where $J_z = 3.8$. The staggered magnetisation M_z^{st} is shown in **(a)** against the parameter D and in **(b)** against the scaling variable κ_3 , Eq. (5.14). The negativity is shown against D in **(c)** and against κ_3 in **(d)**. We observe a smooth slope of both the negativity and the staggered magnetisation where the first-order quantum phase transition (1OQPT) is expected. Both measurements, as a function of κ_3 , show a tendency to converge towards a universal function. The results are obtained with density matrix renormalisation group (DMRG) and bond dimension $\chi = 150$ for which they are converged. 95
- 5.11 Matrix component behaviour for the reduced density matrix $\rho^{ij}(A, B) = \langle A | \rho^{ij} | B \rangle$ of the two central spins (i, j) for a chain of length $L = 12$ along the first-order quantum phase transition (1OQPT) for Ising model in the longitudinal field (Eq. (5.6)). For simplicity of notation we remove the indices (i, j) , see text. **(a)**: Example of a spike at the critical point in $\rho(1, 1)$ for different values of B_z . **(b)**: Example of a discontinuity in $\rho(1, 2)$ at the critical point. **(c)**: Scaling behaviour of $\partial B_x \widetilde{\rho(1, 2)}$ as a function of κ_1 . **(d)**: Scaling behaviour of renormalised $\widetilde{\rho(1, 2)}$ as a function of the scaling parameter κ_1 ; d) Results obtained with ED. 97
- 6.1 one-dimensional (1-D) lattice of rhombi with M cells and L sites. Each cell contains three sites labelled A, B, C . Solid (dashed) line connections indicate a tunnelling amplitude $-J$ ($-Je^{i\phi}$). **(a)** is the representation of the model in real space showing the number of sites whereas **(b)** is a schematic diagram to illustrate the cells more clearly. 100
- 6.2 The single particle energy band $E(k)$ as a function of the lattice momentum k . The fully-frustrated $\phi = \pi$ bands are the solid lines, whereas the non-frustrated $\phi = 0$ are shown by dashed lines. An intermediate frustration (at $\phi = \frac{\pi}{6}$) is shown by the dotted lines. 104
- 6.3 An illustration of a restricted single particle tunnelling for the fully-frustrated system. The sites outside the box are those that leave the Aharonov-Bohm (AB) cage and therefore cannot be accessed. It is shown in **(a)** and **(b)** how there is zero probability amplitude of the single particle exiting the cage on the left or the right, respectively. 105

- 6.4 Illustration of the type of cage terms that control the movement and the interaction of the pairs of particles. \tilde{U} is the on-cell interaction of pairs, \tilde{J} is the hopping of pairs between cells and \tilde{V} can be interpreted as nearest-neighbour interaction or correlated swapping of 2 particles across neighbouring sites. 106
- 6.5 Ground state phase diagram at unit filling $N = L$ and full frustration $\phi = \pi$ in the $\mu/U - J/U$ plane. Circles and squares represent the numerical data for μ_+ and μ_- , respectively. The region $\mu_- < \mu < \mu_+$ is the Mott-insulator lobe. The two lines are cubic splines approximations. Their crossing occurs at the Berezinskii-Kosterlitz-Thouless (BKT) point $J_c \approx (0.78 \pm 0.03)U$ indicated by the shaded region. 109
- 6.6 Sample density sites for **(a)**: $J = 0.1$ (Mott insulator (MI)) and **(b)**: $J = 0.5U$ (Luttinger liquid (LL)) in the unfrustrated ($\phi = 0$) case and for **(c)**: $J = 0.5$ (Mott insulator (MI)) and **(d)**: $J = 0.9$ (pair Luttinger liquid (PLL)) in the frustrated ($\phi = \pi$) case for $L=226$. The sample densities are shown for the A (blue), B (red) and C (cyan) sites in vertical order from top to bottom. The area of each cell on the grid is one, to correspond to uniform filling. The area of the coloured squares are the on-site density at the labelled sites. 110
- 6.7 Illustration of the spread of the on-site density $\langle n_\alpha \rangle$ averaged over the lattice of 226 sites for $\chi = 300$ as the tunnelling and frustration is varied. Here the non-frustrated ($\phi = 0$) is shown by the red circles (\circ), the intermediate frustration ($\phi = 0.9\pi$) is shown by the green dotted pentagrams (\star) and the fully frustrated ($\phi = \pi$) are the blue dashed diamonds (\diamond). The density of the B sites is shown by filled markers and sites A and C (which have equal on-site density) are shown by the empty markers. Again the approximate critical points are highlighted by the shaded regions at $J_c^{[\phi=0]} = 0.14$ (red), $J_c^{[\phi=0.9\pi]} = 0.33$ (green) and $J_c^{[\phi=\pi]} = 0.78$ (blue). The inset is a zoomed in version close to the $\phi = 0$ Mott insulator (MI)-Luttinger liquid (LL) transition. 111

- 6.8 The spatial correlation functions $\eta_\varepsilon^{[\gamma]}$ (where $\gamma = s, p$ and $\varepsilon = 1, 2, 3$) against the intersite distance for an intermediate frustrated case $\phi = 0.5\pi$, $J = 0.9U$, $L = 226$ and $\chi = 300$. The decay is shown of the eigenvalues of the **(a)** single correlations $\langle b_i^\dagger b_{i+r} \rangle$ and **(b)** pair correlations $\langle b_i^{\dagger 2} b_{i+r}^2 \rangle$. Values below a threshold of 10^{-7} , which are below our numerical error, have been excluded. In the diagrams, η_1 (dark blue \bigcirc) is the largest eigenvalue, η_2 (red $*$) is the second largest and η_3 (green \square) is the smallest eigenvalue. 113
- 6.9 The spatial correlation functions against the intersite distance for the fully frustrated case ($\phi = \pi$) with $L = 226$ and $\chi = 300$. Values below a threshold of 10^{-10} , which constitutes numerical error, have been excluded. η_1 (dark blue \bigcirc) is the largest eigenvalue, η_2 (red $*$) is the second largest and η_3 (green \square) is the smallest eigenvalue. The decay of the eigenvalues of the pair correlations $\langle b_i^{\dagger 2} b_{i+r}^2 \rangle$ for **(a)** $J = 0.4U$ in semi-logarithmic scale and for **(b)** $J = 0.9U$ in a double logarithmic scale. The inset is the decay of the eigenvalues of the correlation matrices for the corresponding single correlations $\langle b_i^\dagger b_{i+r} \rangle$ at $J = 0.4$ (Mott insulator (MI) phase) and $J = 0.9U$ (pair Luttinger liquid (PLL) phase). 114
- 6.10 **(a-b):** Parameter $\kappa[p]$ ($\kappa[s]$) obtained from fitting the pair (single)-correlation function for $\phi = \pi$ ($\phi = 0$) with a power law (see Eq.(6.17)) as a function of J/U for $L=226$. The shaded region indicates the Mott-pair Luttinger liquid (PLL) (Mott-Luttinger liquid (LL)) transition region of uncertainty obtained in Sec. 6.5. The inset in **(a)** shows the pair correlations for the B sites $\langle b_i^{\dagger 2} b_{i+r}^2 \rangle$ from $i \approx L/4$ for $J/U = 0.9$ and the corresponding $\eta_1^{[p]*}$ values, which are the maximum eigenvalues retaining their sign. 115
- 6.11 Eigenvalues $\zeta_\varepsilon^{[p]}$ of the structure factor matrix for the pair correlations for $J = 0.9U$, $\chi = 300$ for **(a)** $L = 226$ and as a function of the crystal momentum k and **(b)** the peak at $k = \pi$ for different system lengths L 116

- 6.12 The phase-diagram with different phase shifts ϕ against the tunnelling coefficient J/U . The Luttinger liquid (LL), pair Luttinger liquid (PLL) and the Mott insulator (MI) regions are labelled. The critical points delimiting the Mott insulator (MI) region are obtained from the energy gap as in Sec. 6.4.1. The critical points separating the Luttinger liquid (LL) and pair Luttinger liquid (PLL) phases are obtained by looking at the decay of the single and pair correlation functions. The error bars have been omitted when they are smaller than the marker size. **(a)** is the full variation of ϕ using a filling=1, whilst **(b)** and **(c)** are regions close to full frustration for filling=1 and filling=2 respectively. The \star in **(a)** denotes $\tilde{G}(\pi)$, where Vidal and Douçot predicted the Luttinger liquid (LL)-pair Luttinger liquid (PLL) transition to be at $\phi = \pi$. The dashed line represents their Mott insulator (MI)-Luttinger liquid (LL) transition prediction, $G^*(\phi)$ in Eq. (6.22), which is only valid for small ϕ values. 117
- 6.13 The phase diagram for an infinite estimated length of the Hamiltonian Eq. (6.23) for amplitude modulation of $\cos(\phi)$ against parameters J/U . The Mott insulator (MI), Luttinger liquid (LL) and pair Luttinger liquid (PLL) regions are as labelled. The Mott insulator (MI)-Luttinger liquid (LL) and the Mott insulator (MI)-pair Luttinger liquid (PLL) transitions are again obtained from the compressibility of the energy gap (see Sec. 6.4.1). The Luttinger liquid (LL) and pair Luttinger liquid (PLL) phases are characterised by the decay of the correlation functions as illustrated in Sec. 6.4.2). 121
- 6.14 The single particle energy band $E(k)$ as a function of the lattice momentum k . The fully-frustrated $\phi = \pi$ bands are the solid lines, whereas the intermediate frustrated $\phi = 0.9\pi$ are shown for method (i) which is the original model using the magnetic field and for method (ii) which is using the $\cos(\phi)$ amplitude modulation. . . . 122
- 6.15 **(a)**: An illustration of the different cuts that can be made on the model. The cuts after A, B and C are distinguished using the symbols $*$, $+$, \star respectively. **(b)**: Block entanglement entropy of the whole system (Eq. (6.26)) for $L = 76$. **(c)-(d)**: Block entanglement entropy for $J = 0.9U$ and $L = 226$ as a function of the chord length $\ln(d(m|M)) = \ln\left(\left[\frac{M}{\pi} \sin\left(\frac{m\pi}{M}\right)\right]\right)$ and compared to the conformal field theory (CFT) prediction, Eq. (6.27) for **(c)** the non-frustrated case ($\phi = 0$) and **(d)** the fully frustrated case ($\phi = \pi$). 123

- 6.16 **(a)**: The entanglement spectrum as a function of the dispersion from uniform filling δN of the number of bosons for the cut after C . $\phi = 0$ denotes the unfrustrated case (\circ), $\phi = 0.9\pi$ the intermediate frustration (\square) and $\phi = \pi$ denotes the fully frustrated case (\star), simulated at $J = 0.9U$. In **(a)** a solid line is used to join the degenerate eigenvalues in all cases. **(b)**: Approximate parabolas for $\phi = 0$, $\phi = 0.9\pi$ and $\phi = \pi$ (left to right) based on the length $L = 226$. In the third panel different colours denote the possible curve fitting to even and odd δN . **(c)**: The unfrustrated ES for a cut after C at $L = 226$ with the thermodynamic limit approximation shown by the parabolas. The legend shows the degeneracy of each parabola. 125
- 7.1 Illustration of the two-level atom that can be described by a Rabi model, where the two possible states are $|e\rangle$, $|g\rangle$ and ω is the transition frequency, which measures the separation between the energies. 130
- 7.2 The representation of the one-dimensional lattice of rhombi in real space showing the number of sites. The (green) rectangle encloses a given cell to show that each cell contains three sites labelled A, B, C . Solid (dashed) line connections indicate a tunnelling amplitude $-J$ ($-Je^{i\phi}$). The square highlights the sites that are contained in a full Aharonov-Bohm (AB) cage, when $\phi = \pi$ 132
- 7.3 One-dimensional lattice of rhombi, where each cell contains three sites labelled A, B, C . Solid (dashed) line connections indicate a tunnelling amplitude $-J$ ($-Je^{i\phi}$). This is the representation of the model in real space showing the number of sites. The squares highlight the sites that are contained in a full Aharonov-Bohm (AB) cage, when $\phi = \pi$. The overlap between two different cages is shown occurring at the A and C sites. Each square has parallel lines in a given direction to represent which sites are obtained within a cage and which intersect two cages. 134
- 7.4 The movement of the single particle throughout the system over time t described by the on-site density $\langle n^{[\ell]}(t) \rangle$. A single particle is loaded at site **(a)**: $\ell = 9$ (a central A site) and at **(b)**: $\ell = 11$ (a central C site). The insets above each figure show the initial site the particle is in by the filled circle and the corresponding cage borders to this site by the lines. We have also included a small diagram of the connections of each site inside the top of each figure, where B sites are squares, C sites are diamonds and A sites are circles. 135

- 7.5 The Rabi oscillation from Eq. (7.15) and Eq. (7.16) of the single particle within its cage and the on-site density $\langle n_{j,\alpha}(t) \rangle$ from exact diagonalisation (ED). **(a):** The oscillation on the j_B site that the particle was originally placed in (which in this case is $\ell = 10$ and $j = 4$). **(b):** The oscillation on the j_A and j_C sites (which are equal to the oscillation on $(j - 1)_C$ and $(j + 1)_A$) in the corresponding cage (i.e. for any of $\ell = 8, 9, 11, 12$). 136
- 7.6 The on-site density $\langle n^{[\ell]}(t) \rangle$ of a single particle where the initial setup is $n_{4,B}^{[10]}(t) = 1$ for a chain of length $L = 19$ and where $\phi = \pi$. The inset shows this initial condition, where the grey lines mark the borders of the corresponding Aharonov-Bohm (AB) cage. We have also included a small diagram of the connections of each site inside the top of the figure, where B sites are squares, C sites are diamonds and A sites are circles. 137
- 7.7 The oscillation of the single particle density at the central B site, $\langle n_{j,B}(t) \rangle$, where $j = 4$ (which corresponds to $\ell = 10$) when it can escape its cage due to imperfect frustration $\phi = 0.9\pi$. The dashed line joins the maximal values at the top of the peaks to emphasise the effect of the damping more clearly. 138
- 7.8 The density on the next B site $\langle n_{j+1,B}(t) \rangle$, which is at $\ell = 13$ here, given that this is for a single particle initially loaded at $\ell = 10$ for $\delta\phi = 0.1\pi$. The on-site density is obtained both using exact diagonalisation (ED) and a perturbation theory fitting (see Eq. (7.24)). 140
- 7.9 The on-site density of a pair of particles which are initially started at the central $\ell = 10$ site within an $L = 19$ chain, where $\phi = \pi$. A snapshot is shown of the on-site density $\langle n^{[\ell]}(t) \rangle$ for $t = 0, 1, 2, 3, 4, 5$. The inset shows the initial setup with the dashed lines where the cage borders would appear. 141
- 7.10 The on-site density $\langle n_{j,B}(t) \rangle$ for $j = 4$ which is at $\ell = 10$ with $U = 1$ for a pair of particles which are loaded at the same center site. The dashed line is a guide for the eye to observe the type of damping. 142
- 7.11 The evolution of the particles when the parameter U is changed. The amount that has escaped the cage $\langle n_{out} \rangle$ is shown for different U values against time t . The inset is a plot of the range from $U \in [1, 30]$ in steps of 0.5 in order to illustrate that there is a clear boundary of the U parameters which will be optimal at a given time t 144

- 7.12 The dependence of $\langle n_{out} \rangle$ on U . **(a):** An example is given for $t = 0.7$ against different interaction strengths U . **(b):** The dependence of $\langle n_{out} \rangle$ on U is considered for a range of t , where at each time step the value $\langle n_{out} \rangle$ is normalised by its maximum, giving $\widetilde{\langle n_{out} \rangle}$, so that it is more clear which U dominates excluding the effect that as more time has occurred more particles will have escaped. . . . 145
- 7.13 Comparison between the Krylov and the time dependent variational principle (TDVP) method for an example case $T = 1$, $U = 1.2$, $\chi = 200$ and $L = 10$ as the time-step size δt is varied. **(a):** The evolution energy for the two methods as the step-size is changed. **(b):** The CPU time required to perform the method and obtain the measures of observables for each method. 146
- 7.14 The evolution $\langle n^{[\ell]} \rangle$ of the bosons for different times t , $\phi = \pi$, $L = 22$ and $U = 1$ obtained using time dependent variational principle (TDVP) with time steps $\delta t = 2 \times 10^{-4}$. The initial state is double occupation in the first half of the chain as shown in the inset. The border of the occupied cages is shown by the grey dashed line. These results have converged to a suitable tolerance. The connections between sites is shown at the top of the figure, where squares correspond to the B sites, diamonds to the C sites and circles to the A sites. 147
- 7.15 A comparison of the damped interference that occurs at $\langle n_{4,B}(t) \rangle$ which corresponds to $\ell = 10$ and the Rabi frequency that corresponds to a pair of particles with no interaction, i.e. $U = 0$ 148

LIST OF TABLES

3.1	Summary of the methodology used within each of the implementations of density matrix renormalisation group (DMRG) within our comparison.	62
-----	--	----

LIST OF ACRONYMS

1OQPT	first-order quantum phase transition	4
1-D	one-dimensional	2
2-D	two-dimensional	10
2OQPT	second-order quantum phase transition	3
3-D	three-dimensional	
nOQPT	n^{th} order quantum phase transition	8
AB	Aharonov-Bohm	27
ARPACK	Arnoldi <i>package</i>	61
BEC	Bose-Einstein condensate	3
BH	Bose-Hubbard	2
BLAS	basic linear algebra subprograms	61
BKT	Berezinskii-Kosterlitz-Thouless	9
CFME	commutator-free Magnus expansion	75
CFT	conformal field theory	123
DMD	digital micromirror device	31
DMRG	density matrix renormalisation group	4
FSS	finite size scaling	25
ED	exact diagonalisation	64
JJA	Josephson junction array	3
KT	Kosterlitz-Thouless	9
LAPACK	linear algebra <i>package</i>	61
LL	Luttinger liquid	15
LRO	long-range order	9
MERA	multiscale entanglement renormalization ansatz	36
MI	Mott insulator	15
MPO	matrix product operator	54
MPS	matrix product states	4

OBC	open boundary conditions.....	11
OSMPS	open source matrix product states.....	61
PBC	periodic boundary conditions.....	16
PEPS	projected entangled pair states.....	36
PLL	pair Luttinger liquid.....	99
PPT	Positive Partial Transpose.....	22
PwP	Powder with Power.....	60
QPT	quantum phase transition.....	2
QLRO	quasi long-range order.....	10
SF	superfluid.....	15
SVD	singular value decomposition.....	43
tDMRG	time-dependent density matrix renormalisation group.....	68
TDVP	time dependent variational principle.....	73
TEBD	time evolution block decimation.....	70
TNT	tensor network theory.....	61

HAPTER

INTRODUCTION

*“Every new beginning comes from
some other beginning’s end”
Seneca*

Ever since there has been consciousness, there has been thought and as long as there has been thought, there have been questions. Science as a whole revolves around questions of how does something work or why does something work.

Initially, human curiosity started with what could be seen with the naked eye, but as more knowledge has been counted as fact, our inquisitiveness has grown leading us to explore the macroscopic world, namely pointing our gazes and energy towards outer space, and on the opposite scale, the world in a microscopic scale. It is within the microscopic world (in particular on the atomic scale) that the effects of quantum mechanics and quantum information are the most attainable and evident.

The analysis of quantum properties has provided the tools to advance our understanding within the natural world, cementing our knowledge of a wide range of phenomena such as superfluids and superconductors which defy friction. Despite these advancements and others that have occurred since the early 20th century, when quantum properties were first discovered, there are still a number of questions surrounding quantum phenomena left unresolved today. Within this thesis we will not attempt to tackle the magnitude of issues still remaining but will instead focus on some advancements within the area called ‘quantum critical phenomena’. Classical critical phenomena are something people are exposed to every single day, whether aware of them or not, in the form of thermal phase transitions such as water to steam and water to ice. Although these transformations are perhaps taken for granted, the initial analysis of the causes and the

identification of different types of thermal phase transitions, provided by a number of industrious physicists, including Gibbs, Maxwell, Landau and Ehrenfest, was quite substantial [1–4]. Landau provided an analysis of classical thermal phase transitions, which has been extended to quantum phase transitions (QPTs), in terms of symmetry breaking. He also identified the existence of an order parameter, which is a measure that characterises the intrinsic order of the system within a phase and fulfils the symmetry of the system. Typically an order parameter will be zero in one phase and non-zero in the other. Ehrenfest provided a classification of the different orders of transitions based on the non-analytical behaviour of a system’s free energy and a measure of the state at the point where the phase transition occurs, referred to as the critical point. The quantum phase transitions, which are what we examine, occur at fixed zero temperature [5]. These transitions are driven by quantum fluctuations instead of the thermal fluctuations in the classical case. Another fundamental discovery, which enables the identification of the second-order and higher QPTs is the existence of a universal scaling procedure for QPTs of a given type. This means that regardless of the system size, scaling of different measures close to the QPT leads to a collapse in the thermodynamic limit which is dictated by specified coefficients, referred to as the critical exponents [6].

Within this thesis, the focus will be on the theoretical study of one-dimensional (1-D) quantum lattice systems. These play a crucial role in identifying properties of many-body systems. Critical phenomena will be examined within spin systems with different approaches and motivations. We will explore the features surrounding phase transitions in the spin-1/2 Ising model and the spin-1 XXZ model on a chain and an extension of the standard Bose-Hubbard (BH) model on a 1-D lattice with a non-trivial elementary cell, providing a plethora of different features.

To examine these, we will need to explore the quantumness of a given state. Entanglement is an invaluable resource for quantum information tasks, e.g. quantum communication protocols, when working with quantum correlated systems. Measures of entanglement are precisely those that are able to identify the unique property that particles have non-local correlations between them regardless of their separation [7]. This feature occurs usually due to some previous interaction between the particles and means that these particles cannot be described independently of each other. Entanglement assists in finding novel ways to analyse the quantum information content of a many-body state, which is where our focus is. It is also believed to be one of the resources most linked to the speed-up of quantum computations [8].

Entanglement measures can be employed to estimate the amount of entanglement between two particles or between two sub-systems within a bipartition of a larger system [7]. There are also extensions for measuring multipartite entanglement

shared by many particles but these are much more difficult to obtain and will not be covered within this thesis [9–11].

We will show the utility of entanglement in classifying the occurrence of a [QPT](#) and in distinguishing two different phases. The behaviour of entanglement was first investigated close to a [QPT](#) by analysing a bipartite entanglement measure of two spins in simple spin models like the spin-1/2 Ising chain, which exhibits a second-order quantum phase transition ([2OQPT](#)) [12, 13]. Entanglement measures show non-analytic features surrounding a critical point, which can be used to identify the occurrence of a [QPT](#). Namely, a number of entanglement measures have been shown to experience scaling around the [QPT](#), in a similar manner to physical observables of the state.

In the last few decades, the study of quantum lattice systems has increased in depth and popularity, largely due to improved experimental techniques and increased computational power within computers. Additionally, there is more availability of platforms that can be used to tailor synthetic quantum matter due to recent technological developments within quantum simulations [14]. Amongst the ideal platforms are quantum-dot lattices for electrons [15], Josephson junction arrays ([JJAs](#)) for Cooper pairs [16], photonic lattices [17–21] and optical lattices for cold atoms [22–24], which will be our focus. Ultracold atoms are the ideal platform for quantum simulations of difficult quantum many-body systems as they are reliable with a high level of coherence and are very controllable. The interest in experiments with ultracold atoms was accelerated when the Bose-Einstein condensate ([BEC](#)) [25–27] was first realised in 1995, followed by the creation of a quantum degenerate Fermi gas in 1999 [28]. Optical lattices using ultracold atoms are now standardly used to realise models of quantum many-body systems [22]. Another reason for the popularity of ultracold atoms, is that they are applicable to a broad range of situations, meaning they are used in studies within statistical physics, quantum chemistry and high-energy physics [29]. More details of the use of ultracold atoms are given in Ch. 2.

The advancements of classical computers, including the processing power and storage has advanced in mammoth proportions within the last 20 or so years. A newspaper from 1995¹ boasts of most computers having 8 MB memory, a hard-drive of up to 1000 MB and a processor of 33 MHz. It is not difficult to realise that there has been a massive advancement on this in the last two decades. To provide a more concrete comparison, the recommended specification for students wishing to purchase a laptop in 2017-2018 was that it had a minimum of

¹The Gazette, Montreal, October 30, 1995.

a two core processor of 2.0 GHz, a RAM of 8 GB and a hard-drive of 500 GB². This increased availability of computational resources and power has led to the increased ability to numerically simulate several detailed and complex situations within quantum systems. In addition to this, these advancements have spurred on a number of works in optimising theoretical algorithms. We will examine a few such algorithms in Ch. 3 and 4. It should, however, be noted that whilst the technology has advanced at an incredible rate, it will very soon reach its classical limit, which has led to the search for a quantum alternative. Data storage is one such example of this, with online storage and cloud servers becoming common. Moore’s law [30] states that the number of transistors that may be placed on a single integrated-chip doubles every two years but it has been suggested by Intel in 2016 that silicon transistor can only keep shrinking for another five years [31, 32].

In Ch. 2 we provide a detailed description of the groundwork required to obtain a brief understanding of QPTs, entanglement measures and geometrically frustrated lattices. We also motivate some possible experimental realisations using ultracold atoms.

Within Ch. 3 and 4 we motivate some advanced simulation methods, largely within the class of matrix product states (MPS), to model quantum lattice systems. This class includes the renowned density matrix renormalisation group (DMRG) method, which provides a very efficient way to analyse the ground-state properties of a lattice system. This method, and others in the MPS class, perform so well due to the area-law bounding the amount of entanglement within the system, which reduces the amount of error arising from approximations. In Ch. 4 some examples of different simulation methods of the time-dependent Schrödinger equation are given, most of which rely on the MPS ansatz again. Simulations of time evolution are more difficult as the initial state can drastically change as it evolves, meaning that care needs to be taken that any approximations do not rely too strongly on those made for the initial state. The techniques of avoiding this difficulty and each method’s advantages and disadvantages are examined briefly.

As previously stated, entanglement is an exceedingly useful resource in examining QPTs. In Ch. 5, we focus on entanglement scaling around a first-order quantum phase transition (1OQPT). There are no well-defined critical exponents, resulting from a collapse surrounding the 1OQPTs, as there are in the case of 2OQPTs [33]. The singular behaviour in 1OQPTs occurs as an abrupt discontinuity of some local observables while for 2OQPTs the order parameters change

²Recommended by New Mexico State University, Computer Specifications 2017-2018, https://nmpltw.nmsu.edu/wp-content/uploads/sites/29/2017/07/Computer_Specs-2017-2018.pdf

continuously with a power law. Despite this clear distinction, when examining a system of fixed length, it can be hard to distinguish between a 1OQPT and a 2OQPT due to finite-size effects. Bipartite entanglement, measured by the von Neumann entropy of the reduced density matrix of a block, follows a scaling based on conformal symmetry in the region of QPTs [34, 35]. Motivated by other works' advancements in entanglement, we analyse the scaling properties of pairwise entanglement measures for Hamiltonians with only nearest-neighbour interactions near multi-critical points. We demonstrate a scaling method, first prescribed by Camprostrini *et al.* [36], which when applied to a bipartite entanglement measure, identifies the correct order of the QPT. This is particularly relevant for 1OQPTs crossed in the vicinity of 2OQPTs.

We then expand our study of critical phenomena by focusing on a geometrically frustrated model in Ch. 6 and 7. Having a geometrically frustrated model enables the observation of a number of interesting effects. The frustration substantially changes the way that the particles would behave in its absence and often results in more complex phenomena. Some common features of frustration are the occurrence of energy flat-bands, particle localisation and enforced pairing of particles. The energy flat-band essentially means that the system has a highly degenerate energy manifold, which can mimic a number of physical phenomena [37, 38]. We will observe that the localisation occurs as a direct result of the frustration and that, to overcome the frustration effects and move freely, the particles form pairs when the tunnelling dominates over the interaction. The geometry studied is a quasi-1-D chain of rhombi, which is described by the BH Hamiltonian, where the frustration is created within the geometry by adding a magnetic flux to each rhombus.

Lastly, in Ch. 8 we state our conclusions and provide some insights into further work that can be performed to enhance what has been studied within this thesis.

HAPTER

QUANTUM CRITICAL PHENOMENA AND ULTRACOLD ATOMS

*“Well, well, well ... how curious ...
how very curious ...”
J.K. Rowling, Harry Potter and the
Philosopher’s Stone*

Critical phenomena have been studied widely in both classical and quantum systems as it is an area rich in detail demanding exploration. There are still a number of interesting properties and phases to be found due to increased technological capabilities and scientific knowledge, which makes this a very appealing area of study. In order to be able to study quantum critical phenomena on [1-D](#) quantum lattices, it is important to have some knowledge of the different types of quantum phase transitions that lead to criticality, as well as possible experimental setups in which this theory can be verified. We will focus on models that can be simulated using ultracold atoms in order to explore many-body problems. Experiments with ultracold atoms are well established as a useful tool for quantum simulations, but this is an area that is constantly evolving as further advancements occur [22, 23].

2.1 Definitions of Quantum Phase Transitions

A phase transition occurs whenever matter goes through a substantial change to a different form. Classical phase transitions are driven by thermal fluctuations and have been well understood for a long time. A well known example is water changing its state with the parameter temperature to form steam. For a transition to occur there is a parameter, called the control parameter, which, when varied,

causes a distinct difference depending on which side of the transition (i.e. which phase) it is in. The transition will take place at specified temperature(s) in the classical case. If the transition occurs for more than one control parameter, e.g. temperature and pressure, then this range of values forms a transition line. Typically, we have a critical point, which is a single value of the control parameter where the transition takes place.

The works within this thesis will focus largely on critical phenomena as we examine the regions and effects of quantum phase transitions (QPTs). A QPT is a phase transition which occurs between different states of quantum matter at zero temperature driven by quantum fluctuations [5, 39]. QPTs are associated with the non-analytical behaviour in the expectation value of some observable (such as the correlation function) which can be either local or non-local.

The majority (but not all) QPTs can be classified into different orders of transition based on how the transition from one state to another occurs. This classification is an extension of the Ehrenfest classification of thermal phase transitions [2, 3], which considers the continuity of the free energy of a system and its derivatives with respect to the control parameter at the critical point. Assuming that we have obtained the ground state $|\psi_G\rangle$ and its energy E_G of a given model, then the transition occurs as we vary some control parameter h , which controls some aspect of the model. In general, the value of the control parameter at the critical point will be denoted by h_c .

A 1OQPT is defined as follows:

Definition 2.1.1 (First-Order Quantum Phase Transition-1OQPT): A 1OQPT occurs when for a specified $h = h_c$:

$$\frac{\partial E_G}{\partial h} \text{ is discontinuous and} \tag{2.1}$$

$$|\psi_G\rangle \text{ is discontinuous.}$$

A 1OQPT typically occurs when an energy crossing occurs between the two minimum energies. As the transition is crossed, what was the first excited energy becomes the ground energy and what was the ground becomes the first excited as shown in Fig. 2.1a. This type of transition has a discontinuity apparent in the state itself; an example is given for a measure of the state, the magnetisation, in Fig. 2.1b [5]. Magnetisation is a very useful measure in spin systems as the intrinsic magnetism is the underlying cause of many key phenomena in solid state physics [39]. In order to obtain the magnetisation along a given axis, say x , we

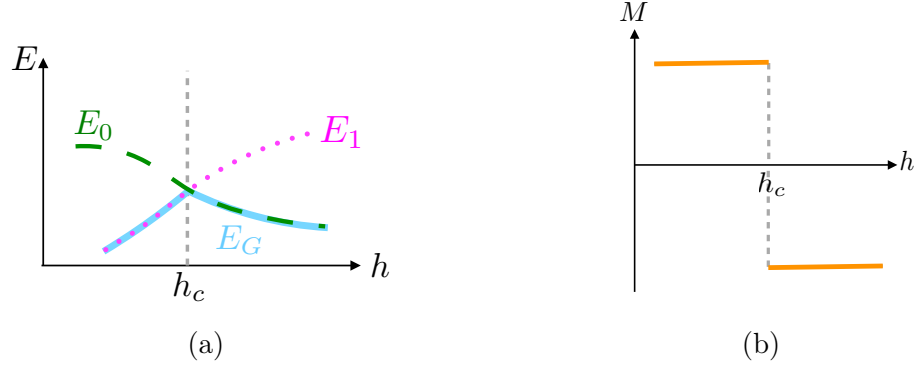


Fig. 2.1 A sketch of the characteristic features surrounding a **1OQPT** which occurs at $h = h_c$. **(a):** Sketch of the energy crossing that occurs at the **1OQPT**. **(b):** An example of the discontinuity in the state using the magnetisation M .

need to calculate:

$$M_x = \sum_i \langle s_i^x \rangle, \quad (2.2)$$

where s^x is the operator used to describe the spin of particle i in the x direction and the sum is over all particles in the system.

The definition of the **1OQPT** can simply be extended for higher orders, so that we have a general definition for an n^{th} order quantum phase transition (**nOQPT**) defined as:

Definition 2.1.2 (n^{th} -Order Quantum Phase Transition-nOQPT**):** An **nOQPT** exists when for some $h = h_c$:

$$\begin{aligned} \frac{\partial^n E_G}{\partial h^n} \text{ is discontinuous or diverging and} \\ \frac{\partial^{n-1} |\psi_G\rangle}{\partial h^{n-1}} \text{ is discontinuous.} \end{aligned} \quad (2.3)$$

For $n > 1$ these classes of phase transitions are typically referred to as continuous **QPTs**. These fall under Landau's paradigm, which describes continuous **QPTs** by symmetry breaking of the system [4]. This paradigm is based on the reasoning that a phase within the system has some intrinsic symmetry. At the critical point this symmetry is destroyed, hence the name symmetry breaking, and either a new symmetry or some order can take effect instead. First-order transitions can occur by symmetry breaking as well, but this is not guaranteed, nor is it their defining feature.

The intrinsic symmetry of a system can be an indicator of the phase and the change that occurs at the transition. When Landau first commented on this, he was considering the different internal symmetries between a crystal (solid) and a

liquid. The difference in their symmetries means that by examining the symmetry property, one can state categorically which phase they are in. The symmetry will either exist or not exist but cannot experience some gradual change across the transition. For continuous classical phase transitions the change in the symmetry may result from a change in ordering of the crystal or due to the displacement in the atoms. Typically for these, the state of the body changes discontinuously [4]. Symmetries arise within a quantum system when the Hamiltonian commutes with an operator that generates the transformation under which the symmetry is realised. In **QPTs**, the reason quantum fluctuations cause the change from one phase to another is due to non-commuting terms within the Hamiltonian [40]. Some examples of the symmetries and order parameters will be provided as we proceed to clarify this.

There is a measure, called the order parameter, which characterises the intrinsic order of the system across a **QPT** and fulfils this symmetry. Typically, an order parameter will be zero in one phase and non-zero in the other. Another feature associated with the order parameter is that correlations have the property of long-range order (**LRO**) in one phase and not in the other. **LRO** occurs when there is a predictable arrangement for all of the atoms. An archetypical example of this is within the ferromagnetic phase, which has all spins pointing in the same direction. This has **LRO**, since if you know the direction of the first spin, you are certain of the direction of all the other spins within this phase. A system has **LRO** of the correlations if a given correlation function $\langle c_i^\dagger c_{i+r} \rangle = D$ for $\forall i, r$, where D is a constant and c_i is the order parameter of the system Hamiltonian. Continuous **QPTs** are signalled by singularities in the derivatives of the (free) energy [5], in analogy to their classical counterparts. In such cases, phase transitions are classified by the minimum order of the derivative of the ground state energy which is not continuous. **1OQPTs** are more common naturally but **2OQPTs** have received a lot of attention theoretically due to the fact that they link with a number of other fields, including high-energy physics, string theory and quantum computation.

Berezinskii-Kosterlitz-Thouless (**BKT**) is the final type of phase transition that we examine, which does not fall under Ehrenfest's classifications. A **BKT** (or sometimes called Kosterlitz-Thouless (**KT**)) is a **QPT** which does not (yet) have a formal definition. This makes a phase transition of this type much more difficult to classify than its continuous counterparts and as such it is normally identified by its features. It is sometimes referred to as an infinite order phase transition as neither its energy nor state (nor their derivatives) show a discontinuity or divergence [41, 42]. This phase transition does not follow Landau's paradigm as it does not involve any spontaneous symmetry breaking. It was shown that this

type of phase transition occurs as a result of some topological order, which in a two-dimensional (2-D) system comes from circulating vortices [43]. Historically, a feature that has been used to identify the BKT transition is a property called the superfluid density. This will show a sudden jump at the transition point, where the size of the jump is related to a specific exponent, which governs this decay [44].

Other features that can be examined to observe the BKT phase transition are the order of correlations within the system and the scaling of the energy gap across the transition [45]. The correlations of the order parameter follow a power law decay at (or very close to) the critical point.

One of the most famous examples of a BKT is within the 1-D BH model at zero temperature and integer fixed filling, which we will describe below (Sec. 2.2.2). To identify the BKT phase transition within this model, we will focus on the correlations of the order parameter. On one side of the transition the correlation of the phase will display LRO (or quasi long-range order (QLRO) in lower dimensions). Simply put, QLRO manifests itself in the algebraic decay of two-point correlations. This property will be absent on the other side of the transition, where the correlations of the order parameter will decay exponentially [46].

2.2 Features in Critical Models

Modelling the key features of a complicated system so that it becomes more accessible in a simplified form has been crucial to developing an understanding of its underlying quantum features. There are a number of simple models that capture the basics of more advanced many-body systems. We will introduce two such models in order to be able to examine the different types of phase transitions and the features that arise from them.

2.2.1 Ising model

The Ising model was initially set up in 1925 by Lenz and Ising [47] to describe magnetic systems in the classical regime, where it relied on the classical spin operators $S_j = \pm 1$. We will, however, focus on the quantum Ising model, which is its quantum extension. The Ising model is defined for a lattice of spins where, in the spin-1/2 case, each site will have either a spin up $|\uparrow\rangle$ or a spin down $|\downarrow\rangle$. It is a very important model as a benchmark as it is integrable in its simplest form. The Ising model can be expressed using the operators σ^x , σ^y and σ^z , described by the Pauli matrices (in the eigenbasis of the σ^z):

$$\sigma^x = \begin{pmatrix} 0 & 1 \\ 1 & 0 \end{pmatrix}, \quad \sigma^y = \begin{pmatrix} 0 & -i \\ i & 0 \end{pmatrix}, \quad \sigma^z = \begin{pmatrix} 1 & 0 \\ 0 & -1 \end{pmatrix}. \quad (2.4)$$

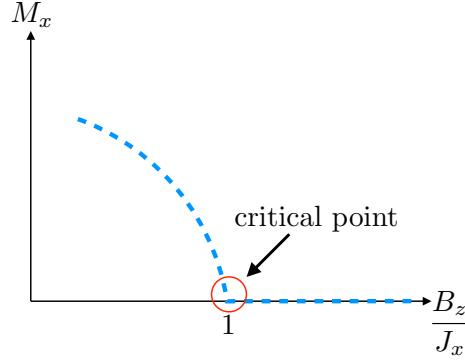


Fig. 2.2 A sketch of the magnetisation M_x around the 2OQPT at $B_z/J_x = 1$ within the spin-1/2 Ising model. The critical point is circled and labelled.

The Hamiltonian of the 1-D Ising model with a transverse field and open boundary conditions (OBC) is given by:

$$\mathcal{H}_{Ising} = -J_x \sum_{j=1}^{L-1} \sigma_j^x \sigma_{j+1}^x - B_z \sum_{j=1}^L \sigma_j^z, \quad (2.5)$$

where we assume that there are L sites in the lattice, and that the positive parameters J_x and B_z can be tuned.

An example of a 2OQPT can be shown using the Ising model with a transverse field as shown in Eq. (2.5). This transition occurs at the critical point $\left(\frac{B_z}{J_x}\right)_c = 1$, or if we set $J_x = 1$ this occurs for $B_{zc} = 1$. This transition point arises from Kramers–Wannier duality theorem in statistical physics, which originally was to relate the free energy of one Ising model to another at differing temperatures [48, 49]. For $B_z < 1$ the system’s ground state is in the ferromagnetic phase, which has a finite fraction of all spins pointing in the same direction. In the absence of any magnetic field, i.e. $B_z = 0$, and in the thermodynamic limit, all spins point up or down with degenerate energy. For a finite chain, this degeneracy is lifted (but only with an exponentially small gap) because there is a finite rate of tunnelling between the two states which is exponentially small in the system size. On the other side, $B_z > 1$ (where $J_x = 1$), the system is in the paramagnetic phase. The paramagnetic phase is influenced by the magnetic field B_z , meaning a state within the phase is adiabatically connected to the representative state where all of the spins align to the magnetic field B_z . The order parameter for this transition is the total magnetisation along x , M_x , which is zero on one side (in the paramagnetic phase) and non-zero on the other (within the ferromagnetic phases) as shown in Fig. 2.2. It is clear that at the transition point there is a sharp change from one to the other. In agreement with its definition, the 2OQPT

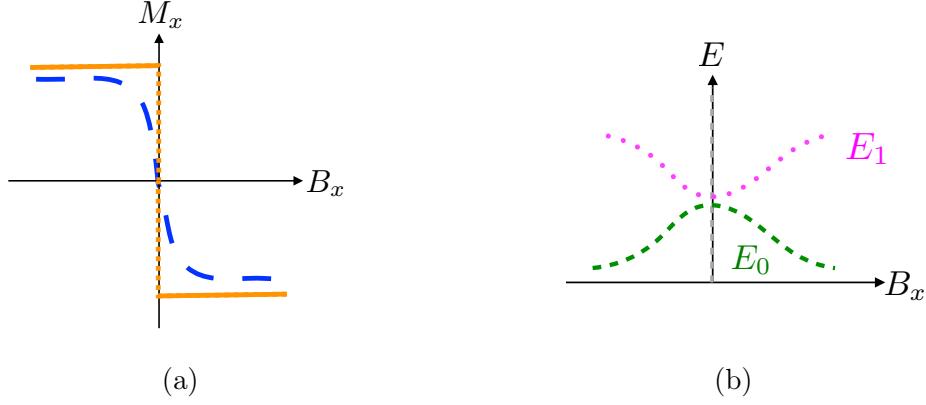


Fig. 2.3 The appearance of the magnetisation and the energy at the **1OQPT** in a finite system, where we have assumed $J_x = 1$. **(a)**: The magnetisation along x for the Ising model's ground state around the **1OQPT**. A discontinuity appears at $B_x = 0$ in the thermodynamic limit (orange) but this is not always evident in finite systems (blue dashed). **(b)**: A sketch of the ground state energy, E_0 , and the first excited energy, E_1 , plotted around the critical point $B_x = 0$. The critical point is signalled by a vertical dashed grey line.

will then have diverging or discontinuous derivative of the magnetisation, which is a property of the state.

The phenomenon of spontaneous symmetry breaking is fundamental to **2OQPT** within the Ising model. Within this model there is a completely symmetric scenario arising from parity symmetry (governed under the class of \mathbb{Z}_2 symmetry). This is because the Hamiltonian is invariant under the transformation $\sigma_j^x \rightarrow -\sigma_j^x$. When we decrease B_z and enter into the ferromagnetic phase, a spontaneous symmetry breaking occurs at $B_{zc} = 1$ because the ferromagnetic material becomes magnetised in one of the two possible directions.

A **1OQPT** can also be observed if we consider the Ising model for a spin-1/2 system with an additional longitudinal field [5]:

$$\mathcal{H}_{Ising} = -J_x \sum_{j=1}^{L-1} \sigma_j^x \sigma_{j+1}^x - B_x \sum_{j=1}^L \sigma_j^x - B_z \sum_{j=1}^L \sigma_j^z, \quad (2.6)$$

where we again assume that there are L sites in the lattice, and that the parameters J_x , B_x and B_z can be tuned.

A **1OQPT** can be seen by varying the ratio of the control parameters B_x/J_x . The critical point occurs at $B_x/J_x = 0$, when B_z is within the range $0 \leq B_z/J_x < 1$. For $B_z < J_x$, the two phases that we obtain are either ferromagnetic \uparrow with the ground state adiabatically connected to that of all spins pointing upwards $|\uparrow \dots \uparrow\rangle$ when $B_x < 0$ and the ferromagnetic \downarrow which is adiabatically connected to the state with the spins $|\downarrow \dots \downarrow\rangle$ for $B_x > 0$. If $B_x/J_x = 0$ (and $B_z = 0$)

then we have a degenerate ground state energy for the two states, but when we consider a non-zero B_x , we are biasing which of the two states to choose and destroying the \mathbb{Z}_2 symmetry of $\sigma_j^x \rightarrow -\sigma_j^x$ within the Hamiltonian, even within the thermodynamic limit. In other words, adding the magnetic field along x promotes one ferromagnetic ordering over the other. This QPT can be assessed by examining the order parameter, the magnetisation along the x axis, M_x , of the ground state. As seen in Fig. 2.3a, we observe an effect of the same spirit as the one shown in Fig. 2.1b, where a discontinuity occurs at $B_x/J_x = 0$ signalling a 1OQPT. With finite systems, however, the discontinuity might not be as evident, for example, close to the transition the magnetisation can be continuous as shown by the blue dashed line in Fig. 2.3a and the energy crossing no longer occurs as motivated in Fig 2.3b.

2.2.2 Bose-Hubbard Model

The Hubbard model was first introduced within a selection of works that Hubbard carried out regarding electrons in the 1960s [50–52]. The BH model is a simplified model enabling the analysis of the tunnelling and interactions between bosons (integer spins), which is a variation of the original (Fermi-)Hubbard model which explores fermions (semi-integer spins).

The model is expressed in terms of creation (b^\dagger) and annihilation (b) operators, which enable us to add and remove bosons from lattice sites. The annihilation and creation operators act on states within the Hilbert space and satisfy the commutation relation:

$$[b, b^\dagger] = \mathbb{I}. \quad (2.7)$$

$n = b^\dagger b$ is a Hermitian operator called the number operator. If we let $|n\rangle$ be an eigenstate of $n = b^\dagger b$, then:

$$b^\dagger b |n\rangle = n |n\rangle, \quad (2.8)$$

which means that n keeps track of the number of bosons within the system. The annihilation and creation operators enforce the removal or addition of one boson:

$$b |n\rangle = \sqrt{n} |n-1\rangle \quad (2.9)$$

and

$$b^\dagger |n\rangle = \sqrt{n+1} |n+1\rangle. \quad (2.10)$$

As we will apply the operators to sites within a lattice, we will express the states in second quantisation as Fock states to make the occupation on each site clear. The Fock state representation of the system, $|n_1 n_2 \dots n_L\rangle$, means that

there are n_j particles at sites $j = 1, \dots, L$. Then the annihilation and creation operator applied to site k will result in the following:

$$b_k |n_1 \dots n_k \dots n_L\rangle = \sqrt{n_k} |n_1 \dots (n_k - 1) \dots n_L\rangle, \quad (2.11)$$

and

$$b_k^\dagger |n_1 \dots n_k \dots n_L\rangle = \sqrt{n_k + 1} |n_1 \dots (n_k + 1) \dots n_L\rangle, \quad (2.12)$$

with the bosonic commutation relations:

$$\begin{aligned} [b_j, b_k] &= 0 \\ [b_j, b_k^\dagger] &= \delta_{jk}. \end{aligned} \quad (2.13)$$

The boson operators can also be expressed in matrix form within the Fock basis as the infinite matrices:

$$b^\dagger = \begin{pmatrix} 0 & 0 & \dots & 0 & 0 & \dots \\ 1 & 0 & \dots & 0 & 0 & \dots \\ 0 & \sqrt{2} & \dots & 0 & 0 & \dots \\ \vdots & \vdots & \ddots & \vdots & \vdots & \dots \\ 0 & 0 & \dots & \sqrt{N} & 0 & \dots \\ 0 & 0 & \dots & 0 & \ddots & \ddots \end{pmatrix} \text{ and } b = \begin{pmatrix} 0 & 1 & 0 & \dots & 0 & \dots \\ 0 & 0 & \sqrt{2} & \dots & 0 & \dots \\ 0 & 0 & 0 & \ddots & \vdots & \dots \\ 0 & 0 & 0 & \ddots & \sqrt{N} & \dots \\ 0 & 0 & 0 & \dots & 0 & \ddots \\ 0 & 0 & 0 & \dots & 0 & \ddots \end{pmatrix}. \quad (2.14)$$

The number matrix is then such that:

$$n = b^\dagger b = \begin{pmatrix} 0 & 0 & 0 & \dots & 0 & \dots \\ 0 & 1 & 0 & \dots & 0 & \dots \\ 0 & 0 & 2 & \dots & 0 & \dots \\ \vdots & \vdots & \vdots & \ddots & \vdots & \dots \\ 0 & 0 & 0 & \dots & N & \dots \\ 0 & 0 & 0 & \dots & \dots & \ddots \end{pmatrix}. \quad (2.15)$$

In computational practice, these infinite matrices are customarily reduced to retain a fixed number of bosons instead, which means that the commutation relations are only approximately true.

By applying $b_j^\dagger b_k$ on different sites ($j \neq k$) we can create tunnelling from one site to another within a given system. The Hamiltonian of the [BH](#) model is then as follows:

$$\mathcal{H}_{BH} = -J \sum_{j=1}^{L-1} (b_j^\dagger b_{j+1} + b_j b_{j+1}^\dagger) + \frac{U}{2} \sum_{j=1}^L n_j (n_j - 1) - \mu \sum_{j=1}^L n_j. \quad (2.16)$$

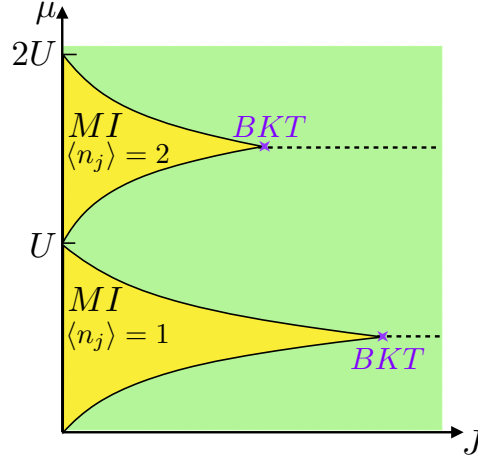


Fig. 2.4 Sketch of the phase transition in the BH model, showing the characteristic Mott lobes at density $\langle n_j \rangle = 1$ and density $\langle n_j \rangle = 2$ in yellow and the superfluid (SF) phase outside of these. The dashed lines are where the constant integer density extends out of the lobes. The BKT transitions are marked by the purple crosses.

The first summation deals with the tunnelling between sites j and $j + 1$, the second is the on-site interaction at a given site j and the last is the chemical potential. We then have the parameters J , U and μ which we can use to control the system. These are the tunnelling, the interaction and the chemical potential parameter, respectively. This Hamiltonian obeys a $U(1)$ symmetry because the model is invariant under the transformation $b_j \rightarrow e^{i\phi} b_j$, with $\phi \in \mathbb{R}$.

The Phase Diagram

For a general 1-D BH model there are two main phases. If there are small interactions or large tunnelling (i.e. the ratio J/U is large) then the bosons become completely delocalised and enter into what is called the Luttinger liquid (LL) (essentially superfluid (SF)) phase. If the density is commensurate with the lattice and the interaction is strong compared to the tunnelling (i.e. J/U is small) then the bosons become localised and are in the Mott insulator (MI) phase. The MI is a gapped phase whereas the LL is a gapless phase. If the chemical potential is varied within the lattice then the regions containing the MI phase are marked by ‘Mott lobes’, which are based on the density within the lattice. A sketch of its appearance is shown in Fig. 2.4. In each lobe, the density is fixed and there is a line that extends out of the tip of the lobe which also has the same constant density. The BKT transition occurs at the tip of the lobe, where the density is still commensurate as marked in the diagram.

In 1-D systems containing interactions, the Fermi-liquid theory underlying SF breaks down and instead the analogous LL is the phase obtained [53]. The

order parameter to distinguish between the **MI** and the **LL** phase is the operator b . To detect **QLRO** we, therefore, examine the correlation function $\langle b_i^\dagger b_j \rangle$, which exhibits exponential decay in the **MI** phase and power law decay in the **LL** phase. As a side note, in our dealings with this model, we will typically retain a fixed number of particles N meaning that we focus only on a line of the full phase diagram shown (Fig. 2.4), corresponding to a fixed U and μ .

To obtain more details on the model itself we can examine the single particle energy spectrum, otherwise known as the Bloch bands, which we will describe below. This feature is particularly relevant when dealing with frustrated systems (Sec. 2.4).

Bloch Bands

If we consider the dynamics of a single particle in a **1-D** lattice and assume that we have periodic boundary conditions (**PBC**) for simplicity then the applicable Hamiltonian reduces to:

$$\mathcal{H}_{BH}^{sing} = -J \sum_{j=1}^L \left(b_j^\dagger b_{j+1} + b_j b_{j+1}^\dagger \right) , \quad (2.17)$$

where $b_{L+1} \equiv b_1$. Excluding the boundaries, this is precisely the **BH** Hamiltonian obtained above (Eq. (2.16)) with $\mu = 0$ and $U = 0$ set. The eigenvalues of the single-particle Hamiltonian within quasi-momentum space, provide the energy bands, which are referred to as the Bloch bands. Here, $E(k)^m$ represents the m^{th} energy band as a function of the quasi-momentum k where $m = 0, 1, 2, \dots$, with 0 corresponding to the lowest Bloch band, which has the minimum energy.

We will briefly describe how to obtain these eigenvalues for the single particle system. Assuming that we have a lattice of L sites and only a single particle, we can restrict the Fock basis described above to the states $|j\rangle$, where $j = 1, \dots, L$ such that:

$$|j\rangle = |0 \dots \underbrace{1}_{j^{th}} \dots 0\rangle . \quad (2.18)$$

Here $|j\rangle$ implies that there is a single particle at the site j and 0 at all of the other $L - 1$ sites. Rewriting the Hamiltonian in this basis we obtain the following form as:

$$\mathcal{H}_{BH}^{sing} = -J \sum_{j=1}^L (|j\rangle \langle j+1| + |j+1\rangle \langle j|) , \quad (2.19)$$

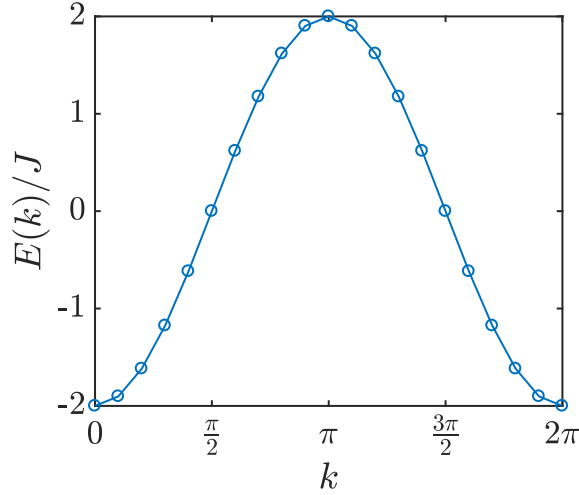


Fig. 2.5 The energy eigenspectrum $E(k)$ (Bloch band) of the single particle in a lattice against the quasimomentum k .

because $\langle j | \mathcal{H}_{BH} | k \rangle = -J(\delta_{j,k+1} + \delta_{j+1,k})$. Here $|L+1\rangle \equiv |1\rangle$ due to [PBC](#). This can equivalently be written in matrix form:

$$\mathcal{H}_{BH}^{sing} = -J \begin{matrix} & |1\rangle & |2\rangle & |3\rangle & \dots & |L\rangle \\ \begin{matrix} \langle 1| \\ \langle 2| \\ \langle 3| \\ \langle 4| \\ \vdots \\ \langle L| \end{matrix} & \begin{pmatrix} 0 & 1 & 0 & 0 & \dots & 1 \\ 1 & 0 & 1 & 0 & \dots & 0 \\ 0 & 1 & 0 & 1 & \dots & 0 \\ & & 1 & & \ddots & \\ 0 & 0 & \dots & \ddots & & 1 \\ 1 & 0 & 0 & \dots & 1 & 0 \end{pmatrix} \end{matrix}. \quad (2.20)$$

This can be rewritten in a new basis using the discrete Fourier transform, which is a linear superposition of the local basis $\{|j\rangle\}$:

$$|\tilde{k}\rangle = \frac{1}{\sqrt{L}} \sum_{j=1}^L e^{-ikj} |j\rangle, \quad (2.21)$$

where $k = \frac{2\pi m}{L}$ for $m = 0, \dots, L-1$. It can be seen that these obey the orthonormal relations $\langle \tilde{k} | \tilde{k}' \rangle = \delta_{k,k'}$. Using this basis, the Hamiltonian in Eq. (2.16) can be rewritten in its diagonal form:

$$\mathcal{H}_{BH}^{sing} = -2J \sum_k \cos(k) |\tilde{k}\rangle \langle \tilde{k}|. \quad (2.22)$$

The eigenvalues, $E_k = -2J \cos(k)$, are precisely what forms the first Bloch band as shown in Fig. 2.5. For more complex systems, more than one Bloch band can

occur from the BH model, which will be shown in Ch. 6 and by an example in Sec. 2.4. The ground state of the system occurs when $k = 0$ or more precisely when $k = 2x$, where $x = 0, 1, \dots$, and has the form:

$$|\tilde{k}_0\rangle = \frac{1}{\sqrt{L}} \left(\sum_{j=1}^L b_j^\dagger \right) |vac\rangle , \quad (2.23)$$

where $|vac\rangle$ is the vacuum state of zeros on all sites.

If instead we consider $N = L$ bosons in the system, with $U = 0$ still set, then the state has the following form:

$$|\tilde{k}_0\rangle = \frac{1}{\sqrt{L}} \left(\sum_{j=1}^L b_j^\dagger \right)^N |vac\rangle . \quad (2.24)$$

This corresponds to having an energy $E = -2JN$ and occurs by placing all of the particles in the $k = 0$ state with minimum energy $E_0 = -2J$. This is the state that corresponds to a BEC, which occurs when a system of bosons is cooled to a temperature close to absolute zero.

Another important case to consider is the other limiting case, which is when $J = 0$ (and $\mu = 0$ for convenience). In this case the Hamiltonian reduces to:

$$\mathcal{H}_{BH}^{int} = \frac{U}{2} \sum_{j=1}^L n_j(n_j - 1) , \quad (2.25)$$

which is diagonal in the Fock basis, meaning that every Fock state is an eigenstate of the Hamiltonian:

$$\mathcal{H}_{BH}^{int} |n_1 n_2 \dots n_L\rangle = \frac{U}{2} \sum_{j=1}^L n_j(n_j - 1) |n_1 n_2 \dots n_L\rangle . \quad (2.26)$$

This means that the energy distribution depends on the distribution of the atoms on the sites:

$$E(\{n_j\}) = \frac{U}{2} \sum_{j=1}^L n_j(n_j - 1) . \quad (2.27)$$

As a result, the ground state (which corresponds to the minimum energy) is a configuration where the atoms are maximally spread among all sites, as we pay energy for putting any particles in the same site.

2.2.3 Scaling Laws

An important feature of QPTs is that scaling is often required in order to identify a transition in the thermodynamic limit. We have motivated this by our example of the magnetisation (see Sec. 2.2.1), which does not show a discontinuity in a finite-size system at a 1QQPT. Continuous phase transitions are described by a certain set of parameters called critical exponents, arising from Landau's theory, that describe how some properties of the system behave close to a critical point. Models sharing the same critical phenomena can be grouped together, using their critical exponents, into the same universality class. This means that with a well-defined set of scaling rules (coming from the critical exponents) the same features will be recovered in the thermodynamic limit [6]. Until recently [36, 54], no semblance of this had existed for 1QQPT systems which will be the focus of one of our chapters (see Ch. 5). To provide an example we will state some of the critical exponents in the quantum Ising model in 1-D (Eq. (2.6)) [5, 40, 55]. The critical exponents are valid close to a 2OQPT in a model of Ising-type. At the quantum critical point in the thermodynamic limit, the energy gap Δ , which is the difference between the ground energy and the first excited energy vanishes. To make this more concrete, as the control parameter $h \rightarrow h_c$ and moves away from $h = 0$, the gap $\Delta \rightarrow 0$. There is a scaling procedure to account for this, which contains the critical exponents z and ν , which are respectively the critical exponents for the correlation time and the correlation length:

$$\Delta \propto |h - h_c|^{\nu z} . \quad (2.28)$$

The first example of a critical exponent that we focus on is the correlation length exponent ν . 2OQPTs typically have a characteristic length scale (often called the correlation length), ξ , which can be the length scale determining the exponential decay of two-point correlations of the order parameter $\langle O(x)O(x+r) \rangle$ between two points separated by a distance r in the ground state, or the length scale over which some characteristic crossover occurs to the correlations at longer distances:

$$\xi \approx \Gamma |h - h_c|^{-\nu} , \quad (2.29)$$

as $h \rightarrow h_c$, where Γ is a non-universal inverse length scale [5]. Another feature is that some observables have a power law behaviour near the critical point, which means that a scaling law can be provided for the order parameter, which is M_x for the Ising model. In general M_x has the scaling law and property:

$$M_x = \begin{cases} D(h_c - h)^\beta & \text{for } h < h_c \\ 0 & \text{for } h \geq h_c , \end{cases} \quad (2.30)$$

where D is a constant and β is the associated critical exponent as $h \rightarrow h_c$. The critical exponent β , is therefore, defined by the way the order parameter (which is M_x for the Ising model described) approaches zero i.e. as it reaches the critical point entering the paramagnetic phase. For the Ising model with the longitudinal and transverse fields, the values of the critical exponents discussed are: $\nu = 1$, $z = 1$ and $\beta = \frac{1}{8}$ [40]. These hold for models of this Ising-type and allow a scaling procedure to obtain the same thermodynamic features, regardless of the differences in the finite models.

For the BH model, at the BKT transition between the MI and the SF, scaling laws can be different than the general framework explained above. The relevant behaviour of the 1-D BH model can be explained by the theory of Luttinger liquids, characterised by the so-called Luttinger liquid parameter K which varies in the SF phase and reaches the value $1/2$ at the critical point [56]. In the gapless SF/LL phase the correlations of the order parameter [57] can be described by:

$$\langle b_i^\dagger b_j \rangle \approx |j - i|^{-K/2} . \quad (2.31)$$

Another difference surrounding this BKT transition is that the gap scales exponentially instead of with a power law. The scaling of the gap has the following form:

$$\Delta \propto \exp \left(\frac{-W}{\sqrt{|h - h_c|}} \right) , \quad (2.32)$$

for $|h - h_c| \ll 1$, where W is some independent parameter [58].

2.3 Entanglement Measures of Many-body Systems

Entanglement is an extremely useful resource which has properties unique to quantum many-body systems. It is crucial in identifying the non-local nature of quantum states [7] as quantum entanglement can witness, for pure states, the existence of non-local correlations between separated particles, where these separated states cannot be described independently of each other, regardless of their spatial separation. Entanglement assists in finding novel ways to analyse quantum information, which is where our focus is. It is also believed to be one of the resources most linked to the speed-up of quantum computations [8]. In the previous sections we have commented on how correlations can indicate when a phase transition has taken place. As we are dealing with quantum systems we have quantum correlations as well as classical ones. Entanglement can measure the amount of quantumness within these correlations and is therefore of great

importance in analysing QPTs.

We will now provide a more formal definition of what entanglement is but we need to define a few concepts first. Given a set of possible pure states $|\psi_i\rangle$, the density operator can be defined as:

$$\rho = \sum_i p_i |\psi_i\rangle \langle \psi_i| , \quad (2.33)$$

where p_i are the probabilities of a given state i occurring. If $p_i = 0 \ \forall i \neq j$, meaning $p_j = 1$ with j fixed, then the density matrix is called “pure”. Conversely if $p_i > 0$ for more than two i 's then the density operator ρ and the corresponding state are called “mixed”.

Entanglement is most easily defined by examining its converse. If entanglement does not exist then for a pure state we have a product state:

Definition 2.3.1 (Product State): Assume that our state is defined within the Hilbert space, which consists of a tensor product of Hilbert spaces $\mathbb{H} = \mathbb{H}_A \otimes \mathbb{H}_B$. A product (separable) state is one that can be written as the tensor product of a state in the Hilbert space \mathbb{H}_A and a state in \mathbb{H}_B . This has the form:

$$|\psi\rangle = |p_A\rangle |q_B\rangle . \quad (2.34)$$

Any state which cannot be written in this form is considered to be entangled. For mixed states, there is a similar definition, where the state is referred to as separable if it is not entangled:

Definition 2.3.2 (Separable State): A mixed state is considered separable if the density matrix can be written as:

$$\rho = \sum_i p_i \rho_i^A \otimes \rho_i^B , \quad (2.35)$$

where the non-negative coefficients p_i fulfil $\sum_i p_i = 1$ and ρ^A (ρ^B) belongs to \mathbb{H}_A (\mathbb{H}_B), respectively.

Using these definitions it can be difficult to classify whether it is possible to find a separable or product state form of a mixed (pure) state. For pure states we can identify if a state is separable or not using a method called the Schmidt decomposition, which bipartitions the state.

Theorem 2.3.3 (Schmidt Decomposition): For any pure unit vector $|\psi\rangle \in \mathbb{H}_A \otimes \mathbb{H}_B$, there exists an integer $1 \leq r \leq \min(N_A \otimes N_B)$, where N_A (N_B) is

the dimension of \mathbb{H}_A (\mathbb{H}_B), such that

$$|\psi\rangle = \sum_{i=1}^r \gamma_i |p_{A_i}\rangle |q_{B_i}\rangle, \quad (2.36)$$

where $\{|p_{A_i}\rangle\}_{i=1}^r$ is an orthonormal set of vectors of \mathbb{H}_A and $\{|q_{B_i}\rangle\}_{i=1}^r$ is an orthonormal set of vectors of \mathbb{H}_B . Here $\{\gamma_i\}_{i=1}^r$ are strictly positive real scalars called the Schmidt coefficients of $|\psi\rangle$. These are the non-zero square roots of the eigenvalues of $\text{Tr}_A(|\psi\rangle\langle\psi|)$, where Tr_A is the partial trace with respect to the system A.

The Schmidt integer r is called the Schmidt rank. This is used to identify if a pure state is separable or entangled. If $r = 1$ then the state is separable, whereas if $r > 1$ then the state is entangled.

It is not as easy to identify whether a mixed state is separable or entangled because there is no well-defined test like the Schmidt decomposition. As a result of this difficulty, instead of having a general method to test separability, we rely on the use of one-sided tests that are able to prove the separability or the entanglement of states. These tests are referred to as separability criteria. One such test for entanglement can be carried out using the partial transpose of a density matrix:

Definition 2.3.4 (Partial Transpose of a density matrix): If the density matrix is $\rho_{AB} \in \mathbb{H}_A \otimes \mathbb{H}_B$. Then the most general density matrix can be written as:

$$\rho_{AB} = \sum_{i,j,k,l} p_{k,l}^{i,j} |ik\rangle_{AB} \langle jl| = \sum_{i,j,k,l} p_{k,l}^{i,j} |i\rangle_A \langle j| \otimes |k\rangle_B \langle l|. \quad (2.37)$$

The partial transpose of A is then defined as:

$$\rho_{AB}^{T_A} = \sum_{i,j,k,l} (p_{k,l}^{i,j} |i\rangle_A \langle j|)^T \otimes |k\rangle_B \langle l| = \sum_{i,j,k,l} p_{k,l}^{i,j} |j\rangle_A \langle i| \otimes |k\rangle_B \langle l|. \quad (2.38)$$

A common test to identify the entanglement is called the Positive Partial Transpose (PPT) criterion, which uses the partial transpose of the density matrix to identify whether a given state is entangled:

Definition 2.3.5 (Peres-Horodecki (Positive Partial Transposed) Criterion [59, 60]): The partial transpose of the density matrix $\rho_{AB}^{T_A}$ of a separable state has non-negative eigenvalues i.e. a separable state must necessarily have $\rho_{AB}^{T_A} \geq 0$.

There has been a study which has shown that if this test is used in small dimensions ($N_A N_B \leq 6$), then ρ is separable if and only if all of the eigenvalues of $\rho_{AB}^{T_A}$ are positive. In the general case, however, we are only able to identify

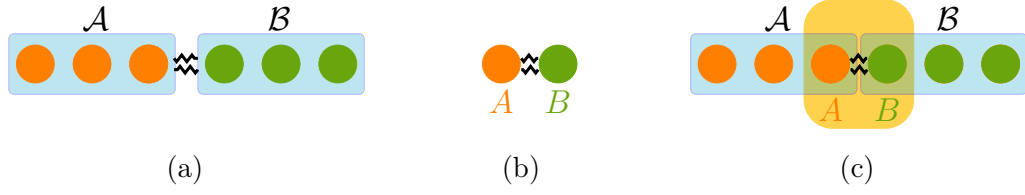


Fig. 2.6 Illustration of the particles considered using measures of entanglement. The zig-zagged lines represent that there is some entanglement measure being considered. **(a)**: the entanglement between one bipartition of a lattice (\mathcal{A}) and the other (\mathcal{B}). **(b)**: the entanglement between two particles A and B . **(c)**: the entanglement between two particles, which are at the centre of the lattice in a bipartition of parts \mathcal{A} and \mathcal{B} (shown by the blue boxes).

that the state is not separable (i.e. that it is entangled), when it has at least one negative eigenvalue. If the eigenvalues are zero, we are unable to draw any conclusions about the state.

Now that we have seen how to identify entanglement, we will define some measures of the amount of entanglement and then we will explain how entanglement behaves across QPTs.

2.3.1 Measures of Entanglement

A key entanglement measure is the von Neumann entanglement entropy, which is for pure states:

Definition 2.3.6 (Von Neumann Entropy): Given a bipartite system of pure states split into block \mathcal{A} and block \mathcal{B} , the von Neumann entropy is defined as:

$$\mathcal{S}_{\mathcal{A}|\mathcal{B}} = -\text{Tr}(\rho_{\mathcal{A}} \log_2 \rho_{\mathcal{A}}) , \quad (2.39)$$

where $\rho_{\mathcal{A}}$ is the reduced density matrix of block \mathcal{A} , $\rho_{\mathcal{A}} = \text{Tr}_{\mathcal{B}} \rho$.

This measures the entanglement of a composite system [8] and essentially measures the uncertainty of the density operators. If we have a lattice system and we bipartition it into two parts, say part \mathcal{A} and part \mathcal{B} , this allows us to measure the entanglement between the two subsystems as shown in Fig. 2.6a. Assuming that block \mathcal{A} has ℓ particles and block \mathcal{B} has $L - \ell$, this will be measuring the entanglement between the first ℓ and the last $L - \ell$ sites.

We will now consider the entanglement measures between two particles, called A and B , as illustrated in Fig. 2.6b. As we will be dealing with lattice systems of longer lengths, this calculation is done by calculating the entanglement of the reduced density matrix of two spins as illustrated in Fig. 2.6c. For pure states, all measures of bipartite entanglement are in one-to-one correspondence and are all a

function of the eigenvalues of the reduced density matrix arising from the chosen partition. For mixed states, this is not the case anymore and the entanglement measure has to be calculated as the convex roof of the corresponding pure state measure. The concurrence \mathcal{C} can be used for mixed states ρ of two spin-1/2 particles or qubits [61], which is in a one-to-one relation to the cost of forming entanglement and is defined as:

Definition 2.3.7 (Concurrence): Assume that we have two spin-1/2 particles, where $\sigma_y \otimes \sigma_y$ is defined in their Hilbert space. Given the density matrix of two spin-1/2 particles or qubits, ρ and its complex conjugate ρ^* , the concurrence is defined as:

$$\mathcal{C}(\rho) = \max(0, \lambda_1 - \lambda_2 - \lambda_3 - \lambda_4), \quad (2.40)$$

where λ_i are the eigenvalues, in decreasing order, of the matrix $R = \sqrt{\sqrt{\rho}\tilde{\rho}\sqrt{\rho}}$ with $\tilde{\rho} = (\sigma_y \otimes \sigma_y)\rho^*(\sigma_y \otimes \sigma_y)$.

The concurrence is a monogamous measure, meaning that the entanglement of a pair of qubits cannot exceed the sum of pairs of qubits including the original pair [62, 63]. The concurrence is also strictly zero if the states are non-entangled.

Another useful measure is negativity which is derived from the Positive-Partial Transposed criterion (Def. 2.3.5) and is defined as:

Definition 2.3.8 (Negativity): Suppose that we have a bipartite mixed state ρ and its partial transpose is denoted ρ^{TA} . Then the negativity is defined as follows:

$$\mathcal{N}(\rho) = \frac{||\rho^{TA}||_1 - 1}{2}, \quad (2.41)$$

where $||\dots||_1$ is the sum of the absolute value of all singular values (which are the square root of the eigenvalues) and $\mathbb{1}$ is the unit matrix.

The negativity provides a lower bound of entanglement and is strictly zero for non-entangled states [64, 65]. A caveat with this though is that $\mathcal{N}(\rho) = 0$ does not necessarily mean that no entanglement exists.

2.3.2 Entanglement Scaling around Quantum Phase Transitions

The behaviour of entanglement was first investigated close to a QPT by analysing the bipartite entanglement in simple spin models, like the spin-1/2 Ising chain, which contain a 2OQPT [12, 13]. It was found that the entanglement scales

around the critical point, but in a different manner to the correlations for example, which diverge at the critical point whilst the entanglement remains short-ranged. A bipartite measure of entanglement between two spins (the concurrence) was used to confirm this feature. It was also shown that a finite size scaling (FSS) can be performed on finite-size systems resulting in a collapse of a bipartite measure and allowing the correct extraction of the critical exponents. For example, in the spin-1/2 Ising model, Osterloh *et al.* [12] were able to extract the critical exponent of the correlation length $\nu = 1$ using the derivative of the concurrence. After these works, the field has gained in popularity with a large amount of work being devoted to deepening the connections between quantum information and QPTs. We will provide a few examples of some of the developments that have been made to highlight the interest in entanglement. The microscopic properties of entanglement have been examined in spin systems to prove that a scaling exists and that it depends on conformal symmetry [34, 35]. Concurrence has been used as a measure of the entanglement, showing the expected properties in both 1OQPTs [66, 67] and 2OQPTs [68] in spin-1/2 systems. It has been shown that for certain models, such as the XXZ model, the concurrence is maximal at the critical point [69]. It was discovered that 1OQPTs can cause macroscopic changes in pairwise entanglement within spin systems [70]. Another measure of entanglement, the geometric entanglement (which measures how well an entangled state can be approximated by some unentangled state) has also been proposed by Orus and Wei to enable the detection of elusive QPTs, and has the expected non-analyticities at the critical point [71].

Although the focus within this thesis will be on the scaling of bipartite entanglement measures, there has been substantial work on multi-partite entanglement, with some works including the examining of tri-partite entanglement in the XXZ model [9] and in the XY model [10] with the expected effects, i.e. symmetry breaking, long-range ordering and effective scaling procedures. There has also been a generalisation of entanglement based on its relation to a subspace of observables as a tool to extend multipartite analysis [11].

2.4 Frustration within lattices

Examining frustrated lattices can lead to even more interesting critical phenomena to examine. A number of earlier studies of frustration were in classical antiferromagnetic systems, where there are competing interaction terms that contribute to the energy, which cannot be simultaneously minimised [5, 72]. In general frustration involves inhibiting in some way how a component of the system would typically behave (in the absence of the other components or effects). The models we have examined so far are standard versions, describing 1-D lattice systems

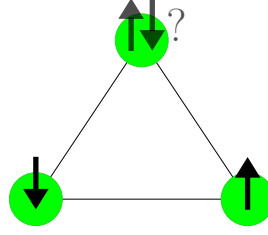


Fig. 2.7 The geometrical frustration arising as a result of the Ising model with anti-ferromagnetic ordering. Once the bottom two are set, the top site in the triangle wants to orient the spin in conflicting directions as shown by both arrows and the question mark.

with uniform coupling and only nearest-neighbour interactions. These and others can be diversely adapted in order to make them more interesting and to enable the exploration of a wider area of physical phenomena. An adaptation that has gained a lot of recent interest is to consider a quantum model on a lattice which contains geometric frustration within it. Simply put, this means that the geometry and tunnelling parameters are chosen so that the particles cannot move freely through the system due to some constraints/restrictions which occur typically as a result of gauge potentials. We will motivate the advantages of using geometrically frustrated systems below after providing a brief example of geometric frustration in a classical scenario.

One of the earliest examinations of a geometrically frustrated lattice was carried out with an anti-ferromagnetic Ising model on a 2-D triangular lattice in the classical case [73]. Simply put geometrical frustration arises when there are conflicting forces between particles, i.e. where they would favour typically simple but different structures, which results in a more complex system. In the case of the Ising model with anti-ferromagnetism, the spins prefer to be ordered in opposing directions when beside each other. Place these in a lattice, with a non-trivial geometry such as a triangular lattice and this is no longer possible. For example, in Fig. 2.7 we show the setup for a single triangle within the lattice, where there is some uncertainty which direction the third spin should point given that it has opposing desires as a result of the spins on either side. Considering that the lattice is 2-D, consisting of joined triangles in both directions, this increases the complexity. It is apparent that the original simple anti-ferromagnetic ordering cannot exist in the same way that it would without this geometrical effect. In this manner, frustration can lead to much more complex structures. Typically, in the bosonic models we will examine, the frustration is implemented through some adaptation to how the particles tunnel from site to site. We will explain this more as we motivate why geometric frustrated lattices are useful to examine.

2.4.1 Features of frustrated lattices

Frustrated systems are of great interest due to their diverse features, which open up a rich amount of detail for us to focus on. In particular our focus will be on geometrically frustrated systems. The three primary features that make these models interesting are that they lead to (i) energy flat-bands, (ii) localisation and (iii) can lead to pairing of particles which will be defined below.

(i) Energy Flat-bands

A desirable feature of models with geometric frustration is that they lead to flat-bands, which is defined as degeneracy within the low-energy manifold, as this is a feature which is apparent in a number of physical contexts, meaning that we can mimic these to examine the intriguing phenomena surrounding flat-bands more. To provide an example of a case with a degenerate low-energy manifold, aside from within frustrated spin systems [37, 38], we will briefly examine how this occurs in disordered media with random impurities [74]. It is well-established that disordered media can lead to localisation of states due to the Anderson localisation effect. Suppose that an electron is propagating through a disordered medium from a point A to a point B, then the probability of the electron reaching B will consist of the sum of the amplitudes of all possible paths. This probability consists of a classical, incoherent contribution, plus many cross-product, interference terms. If the interference terms are discounted then the electron diffuses, however considering them, it can be seen that the electron falls under localisation.

Anderson localisation [75] can be defined formally as the phenomenon in which static disorder within a single particle Hamiltonian of an infinite system, causes the localisation of all eigenstates in space. Within an infinite system, an apparent feature of near degenerate energy levels can arise, as it is possible to have bound states with infinitely close energy due to their correspondence with localised eigenstates that are infinitely far apart and hardly overlap [23].

(ii) Localisation Effects

As motivated above, degeneracies can occur in systems which have constraints of a geometric nature. The features causing geometrical frustration and the degeneracy, also often have the consequence of causing localisation. The geometrical frustration can be created as a result of the dimensionality of the system and the lattice structure chosen. It can also be as a result of gauge potentials (e.g. the vector potential of a magnetic field). Often geometrically frustrated lattices are caused by the interplay of these two features. There are a number of ways of achieving localisation, such as through the use of disorder as motivated above. Here we will focus on localisation occurring due to the interplay of the dimensionality and the gauge potential chosen, which leads to the case of Aharonov-Bohm (AB)

cages [76, 77].

AB cages [77] occur when the set of sites that are visited by a wavepacket are bounded due to destructive interference of **AB** type, i.e. there is a localisation effect. The **AB** type of interference was first introduced by Aharonov and Bohm in 1959 [78], who focused on how the vector potential could influence an electron. An example of an **AB** cage will be provided below in Sec. 2.4.2.

(iii) Pairing Effects

Another feature that will be focused on within this thesis and that can arise from frustrated lattices is a pairing effect within the particles. For bosons loaded into a system with certain fractional filling, the interaction dominates over the kinetic terms and can lead to incompressible ground states of the form of the Wigner crystal ground states. A Wigner crystal is a crystalline phase of particles, first predicted in 1934 for electrons [79]. This phase occurs when a gas of electrons, in an appropriate environment, crystallises to form a lattice when the electron density is less than a critical value. Here, these are determined by the possibility of occupying non-overlapping localised eigenstates and can also lead to the appearance of supersolid phases [80, 81]. When an additional particle is added to the critical density number forming the Wigner crystals [82], this leads to two of the particles forming a pair.

In the opposite limit of large occupation number, known as the quantum rotor limit, one can examine the quantum rotor model which is particularly relevant for **JJAs** within superconducting devices [16]. Within the quantum rotor limit, Douçot and Vidal highlighted the possibility of obtaining a coherent transport of particle pairs with the corresponding absence of single-particle transport [83–85]. This will be expanded on in Sec. 6.2. There are also a number of other studies that invoke three-body hardcore constraints to obtain pair superfluids in cold atomic systems, which we omit [86–91].

Lastly, another reason that the interest in frustrated systems has peaked is that the experimental aspects to tailor synthetic quantum matter have been enhanced, meaning there is now the possibility of experimental replication of the theory. This is explained in detail in Sec. 2.5 after giving an example of a quantum geometrically frustrated lattice, which contains all of the features just mentioned.

2.4.2 Examples of frustrated lattices

A number of lattices have been examined with different geometries in order to gain further insights and understanding of quantum phenomena. Some examples of geometries that have been studied in **1-D** (or quasi-**1-D**) are the sawtooth lattice [92], the zigzag lattice [93] and the ladder lattice [94]. Here we will focus on the

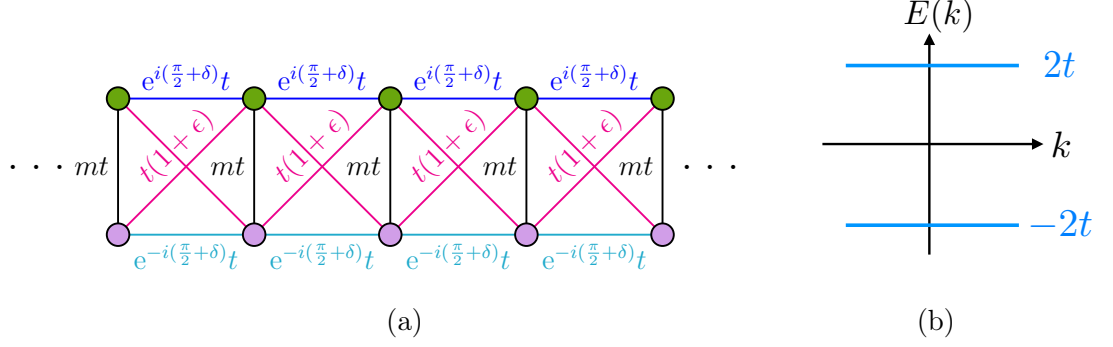


Fig. 2.8 **(a)**: Example of a geometric lattice by showing the layout of the Creutz-ladder. The tunnelling parameters are varied at the different types of legs, which are labelled in different colours to correspond to their coefficient. **(b)**: The two flat-bands at $\pm 2t$ that arise in the single particle energy spectrum $E(k)$ of the Creutz Ladder in quasimomentum space k .

Creutz (cross-linked) ladder as an example, which has been studied by Takayoshi *et al.* and Tovmasyan *et al.* [95, 96] for a system of fractionally filled bosons. This is merely to illustrate how geometric frustration can be formed; we will provide a detailed study of a geometrically frustrated lattice later in Ch. 6 when we investigate the so called Rhombi-model in a quasi-1-D scenario.

The Creutz ladder is set up as shown in Fig. 2.8a. It can be seen that in the bulk of the chain, there are two individual site types, which have the same tunnelling parameters acting on them. As this is a bosonic system, its Hamiltonian is merely an adaptation of the BH Hamiltonian (Eq. (2.16)) with different tunnelling parameters to correspond to the geometry and labelling chosen. If this geometry was considered in the classical case with anti-ferromagnetic ordering of the Ising model as before, then it is clear, that once again, some spins which are nearest neighbours must point in the same direction, resulting in frustration.

The tunnellings are $t(1 + \epsilon)$ on the diagonal connections between the two rungs, mt on the vertical legs and $e^{\pm i(\frac{\pi}{2} + \delta)t}$ on the top and bottom rungs, where $\epsilon, m, \delta \geq 0$. The manner of the tunnelling between the top (bottom) rungs means that an AB phase of $\pm(\frac{\pi}{2} + \delta)$, respectively is set up. This corresponds to a flux of $\pi + 2\delta$ through each square plaquette, which means that a particle will acquire a phase $\approx \pi$ when going around a square plaquette. The existence of this AB phase is what introduces the frustration to the model, with the possibility of bosons becoming trapped (localised) to a certain plaquette, i.e. each plaquette becomes an AB cage. The frustration causes flat-bands as previously motivated, meaning the particles have an effective infinite mass. Within this model there are two Bloch bands due to the geometry. These are flat-bands when $\epsilon = m = \delta = 0$ as sketched in Fig. 2.8b.

2.5 Experiments with Ultracold Atoms

There is an enhanced availability of platforms for tailoring so-called *synthetic quantum matter* [14] due to recent technological developments. Some ideal platforms are quantum-dot lattices for electrons [15], [JJAs](#) for Cooper pairs [16], photonic lattices [17–21] and optical lattices for cold atoms [22–24]. Within this thesis, we will focus on the use of optical lattices for modelling ultracold atoms.

Ultracold atoms are the ideal platform for quantum simulations of difficult quantum many-body system problems as they are reliable, with a high level of coherence, and are very controllable. Initially, ultracold atoms were predominantly used to examine overlapping coherent matter waves. The interest in ultracold atoms was accelerated when an atomic [BEC](#) [25–27] was realised in 1995, followed by the creation of a quantum degenerate Fermi gas in 1999 [28]. The first realisation of the atomic [BEC](#) obtained a wider interest when the Nobel Prize in Physics was awarded to Cornell, Ketterle and Wieman in 2001 [97]. These key achievements led to cold atoms being regularly used to form quantum simulations analogous to quantum many-body systems [22]. There is also a diverse range of applications using ultracold atoms other than within condensed matter systems, as they can be used for statistical physics, quantum chemistry and high-energy physics [29].

2.5.1 Optical Lattices

The many-body quantum systems we will focus on are those that are based on a quantum lattice system. The study of strongly correlated many-body physics in ultracold gases began with the realisation of the [SF-MI](#) transition in a bosonic system [45]. This was done by examining a [BEC](#) with repulsive interactions, fixed in a [3-D](#) optical lattice potential. Increasing the depth in this potential, led to the observation of the transition, which was identified by examining the phase coherence, energy gap and the position of the atoms.

Optical lattices are amongst the most well-established platforms to synthesise quantum matter [22–24]. In general an optical lattice is formed for an experiment by interfering laser beams, forming a periodic light potential. The laser light is used to trap the particles in place. A standing (or stationary) wave is created when two waves of light of equal wavelength are propagated towards each other. Within a stationary wave the peaks and troughs do not move spatially, meaning that if the laser is turned on adiabatically, it is possible to trap particles within the troughs of this optical lattice. One pair of counter-propagating lasers creates a single sinusoidal standing wave, which will restrict the movement of the particle in its direction. Additional pairs of lasers need to be added to restrict the particle’s movement along other axis directions [98]. In [2-D](#), two pairs of counter-propagating waves are required, meaning that the kinetic energy of the particles is frozen,

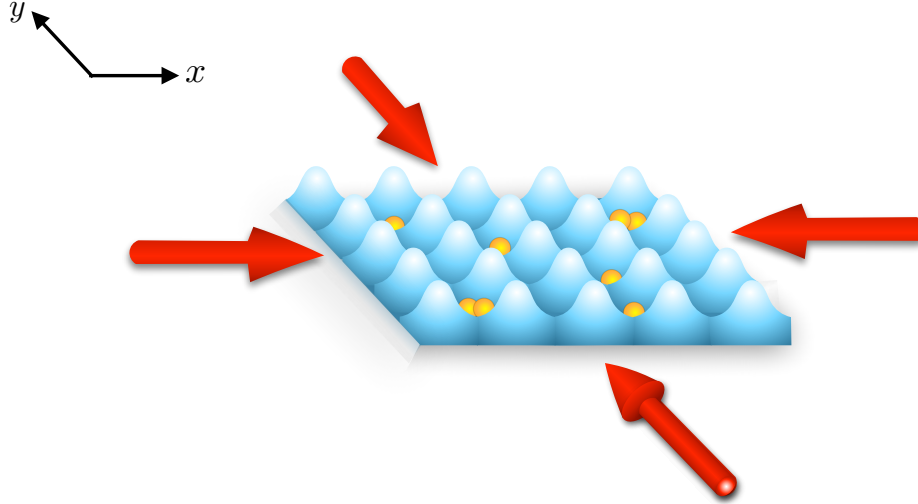


Fig. 2.9 Illustration of the setup of a 2-D optical lattice. Propagating laser light (red arrows) forms an artificial crystal structure, which traps the atoms (circles) except for small tunnellings to nearby sites.

except for the small tunnelling amplitude to neighbouring sites [22].

An advantage of optical lattices is that they are very controllable, meaning that their geometry and dimensionality can be modified. It is also possible to add features, such as disorder or an artificial magnetism throughout the system [29]. An example of an optical lattice for creating a 2-D optical lattice is shown in Fig. 2.9, where there are two pairs of counter-propagating waves forming the lattice. The height of the lattice can be used to control the strength of atom-atom interactions or they can be varied by making use of Feshbach resonances. An experimental realisation of the Bose-Hubbard model was proposed and performed using an optical lattice with ultracold bosons [45, 99].

2.5.2 Experimental Realisations of Frustrated Lattices

As previously motivated, frustrated lattices have a number of uses, which has made them appealing models to investigate. Due to experimental advancements there are now a number of setups which are equipped to create a geometrically frustrated model. We will briefly describe three different experimental platforms that can be used to create geometric frustration within cold atomic systems. These are adapted optical lattices, digital micromirror devices (DMDs) and single-atom microscopes. Within these methods we require some way to form interactions/couplings that differ depending on the site (i.e. geometric couplings) and/or some way of imposing a magnetic flux which will circulate around a given plaquette. As an example, in the Creutz ladder we require different tunnelling parameters depending on where the hopping is taking place from and to. The AB phase has been imposed using the tunnelling parameters as specified above in the top and bottom rungs but

depending on the parameters chosen this creates the complication of imaginary couplings, so often a magnetic flux is applied to the plaquette directly to create this effect. We will discuss this and other methods in the three implementations below.

(i) Optical Lattices with unique tunnelling

Firstly optical lattices can be used with some adaptations. Within these, it is now routine to produce synthetic gauge fields via laser-assisted tunnelling [100, 101] and/or via shaking of the lattice structure [102–105]. When an optical lattice is subject to a sufficiently large constant force, then the ground energy levels of the lattice are shifted out of resonance and tunnelling is suppressed. Then by shaking the lattice, the levels are coupled by low-frequency photons and tunnelling can resume. This enables the localisation effects from the \mathbf{AB} flux to be added. Another possibility is to load the lattices with fermionic, bosonic or a mixture of particles and then tune the interactions between them via Fano-Feshbach resonances.

Lastly, a geometric frustration can be set up using real-space geometries by having lasers intersecting at ± 45 degrees with the lattice dimension plus additional superlattices transverse to it to isolate single plaquettes [106, 107].

(ii) Digital Micromirror Devices-DMD

DMDs can be used to set up a geometrically frustrated lattice in real space as they can be used to obtain direct imaging of an amplitude pattern. In general, a DMD is a type of spatial light modulator, which imposes a spatial variation of the modulation on an incident beam of light. Manipulating the intensity profile of a laser beam through a DMD enables an arbitrary optical potential to be projected on ultra-cold atoms. With this, a broad variety of 1-D and 2-D arrangements of optical trapping potentials can be created.

A DMD can consist of up to one million micromirrors which can be individually tuned allowing a huge level of control. In Fig. 2.10 an illustration of what a typical DMD looks like is shown. A DMD can be considered as a dynamically configurable amplitude mask, which makes it appropriate for direct imaging applications. Each mirror is positioned above an electrical memory cell. If the projection is turned off, the mirror rests in parallel to the cell. When projection is on, each mirror can be angled to a fixed degree representing on and another representing off. The light from the off position is discharged in another direction (often to a beam-dumper). A portion of the light in the on position is reflected so that it displays an image in greyscale on the DMD screen, which has a one-to-one correspondence with the micromirrors of the device [108, 109]. Using DMD the geometrical positioning of the sites should be obtainable and then a synthetic magnetic flux can be added to each plaquette to cause the frustration, through the use of methods such as

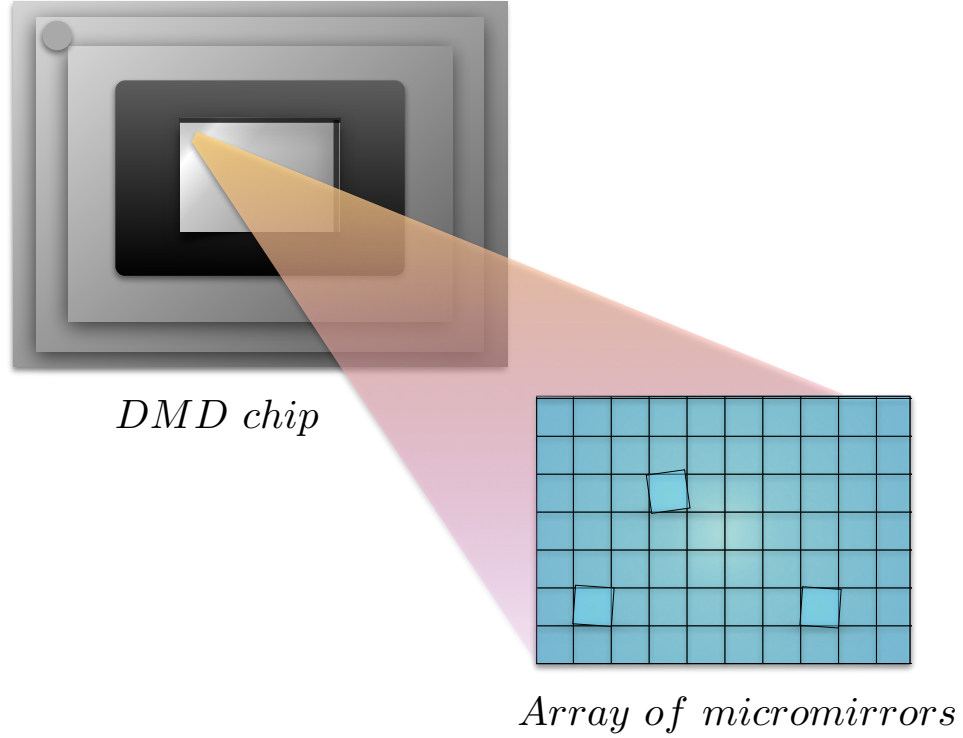


Fig. 2.10 Illustration of a [DMD](#). Within a given [DMD](#) chip there is an array of individually tuneable micromirrors which are shown in the grid.

laser-assisted tunnelling, mentioned above.

(iii) Single Atom (Quantum Gas) microscope

Single atom (or quantum gas) microscopes are exceptionally useful as they enable control at a single-atom level, greatly increasing the experimental models that are obtainable [29, 110, 111]. Using the single atom microscope, a ‘snapshot’ of the many-body system can be taken, which makes a wide range of measures more directly available such as magnetism and topological order. There is also the advantage that the ultracold atoms can be very well removed from the environment, making isolated quantum systems possible. The basic design of this is that there is some microscopic component, which contains the objective lens. This is typically formed using a [DMD](#) to create a light potential which is then projected through an objective lens. On top of this, a vacuum window is prepared. The optical lattice is created using propagating laser beams above the vacuum window. The subtlety here is that the atoms are prepared in a focal plane, which is adjusted so that fluorescence will capture the desired ‘snapshot’. The detection of the single atom, or precisely the local parity of the onsite atom number, is based on a laser cooling technique within the trap [29]. For this to work a sufficient number of fluorescent photons are scattered during the laser cooling using a high-resolution imaging objective so that atoms on neighbouring sites can be distinguished from

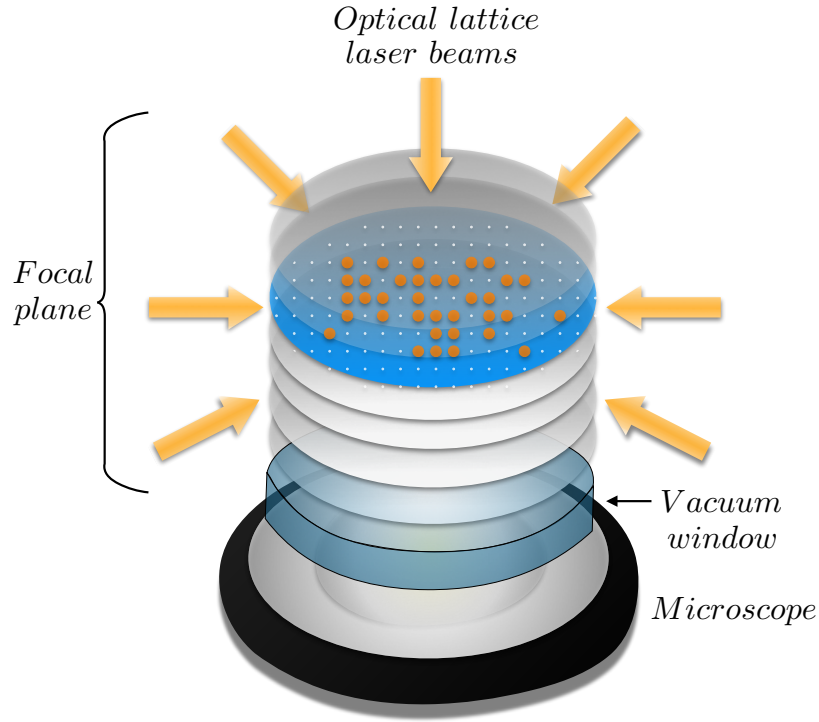


Fig. 2.11 Diagram of a standard setup for a quantum gas microscope. A microscopic device is used which has a vacuum window and a mirror above it. The optical lattice is formed above the mirror, where the atoms are set up in a focal plane so that an image of the plane can be obtained.

each other. This is quite an achievement as typical lattice spacing is $5\mu\text{m}$. The laser cooling is also necessary because it prevents atoms from hopping to nearby sites whilst the imaging is taking place.

2.6 Conclusions

We have summarised the information required in order to understand and identify quantum critical phenomena. In addition to this, we have motivated the use of entanglement as a diagnostic tool around QPTs. Frustrated systems are an invaluable tool to explore fascinating aspects of critical phenomena and physical systems. A number of experimental realisations have been briefly mentioned to give the reader an idea of how quantum simulations are performed within an experiment. As the focus of this thesis will be on theoretical methods, we also need to cover how these quantum models are simulated computationally to identify features, which will be discussed in our next chapter.

HAPTER

COMPUTATIONAL METHODS FOR GROUND STATE SIMULATIONS

“We can only see a short distance ahead but we can see plenty there that needs to be done.”

Alan Turing

Strongly correlated quantum systems in low-dimensional lattices have been explored in great depth within recent works [56, 112, 113]. These models are challenging both to simulate numerically and to implement experimentally, which has prompted a substantial amount of work in how to form simplified approximations of these models in both scenarios. There are a number of interesting models that still need to be explored, in particular lattices that have some geometric frustration including ones within higher dimensions. The advancements in technology with optical lattices [22–24] and developments such as single-atom (quantum-gas) microscopes [29] and DMDs [109] are making more complicated lattice structures a lot more attainable than they were even 10 years ago. With this increase in experimental capability, there also needs to be a corresponding improvement of the theoretical methods so that these more complex lattices can be investigated in as efficient and accurate a manner as possible. This chapter is going to provide an overview of some of the theoretical techniques that can be used to simulate a correlated many-body system to obtain the ground state properties and provides some insight into the efficiency of these methods.

There are a number of numerical methods available to find the ground state properties of a system when an analytical procedure is not possible. The most

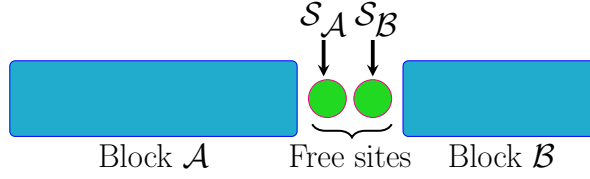


Fig. 3.1 Illustration of the blocks \mathcal{A} and \mathcal{B} and free sites \mathcal{S}_A and \mathcal{S}_B in the DMRG method.

notable types of methods are the stochastic Quantum Monte Carlo methods [114–117], the recent machine learning algorithms, using artificial neural networks to obtain the Hamiltonian properties [118, 119] and compression methods such as matrix product states (MPS) and other standard tensor network algorithms, which rely on finding an efficient representation of the wave function. Amongst the compression ansatzes are MPS [120, 121], projected entangled pair states (PEPS) and multiscale entanglement renormalization ansatz (MERA) [122–124]. Within this thesis we focus on 1-D lattice systems, so we restrict ourselves to the DMRG algorithm, and its representation as an MPS, as our ground-state method. In order to give an introduction to DMRG, we will discuss its origins and how it has been improved upon by expressing it in an MPS ansatz.

3.1 Density Matrix Renormalisation Group

DMRG is a well-established method that was first introduced in 1992 by Steven White [121, 125] as a tool to find the ground energy and state of a given system specified by some Hamiltonian \mathcal{H} . It is an iterative, variational procedure which is an adaptation of the real space renormalisation group algorithm, described by Kenneth Wilson [126], by making use of the reduced density matrix of one of the two partitions of the system. The typical DMRG algorithm is designed to work on a 1-D lattice with OBC but PBC are also possible. In general, we will assume that the lattice has L sites in total and that a local Hilbert space dimension of size d is retained. The main premise behind the DMRG algorithm is the use of two blocks, labelled \mathcal{A} and \mathcal{B} , with free sites between them. In general, a block will refer to a subset of a collection of adjacent sites within the lattice. The free sites, labelled \mathcal{S}_A and \mathcal{S}_B are two sites which are not part of the subset of either block. Block \mathcal{A} is a subset of $1, \dots, \ell$ sites, the free site \mathcal{S}_A is site $\ell + 1$, \mathcal{S}_B is site $\ell + 2$ and block \mathcal{B} is a subset containing the sites $\ell + 3, \dots, L$. A diagram of this arrangement is shown in Fig. 3.1. The size of these blocks will change within the algorithm, i.e. they will refer to subsets of a different number of sites. To distinguish the block-size we will provide additional labels, such that

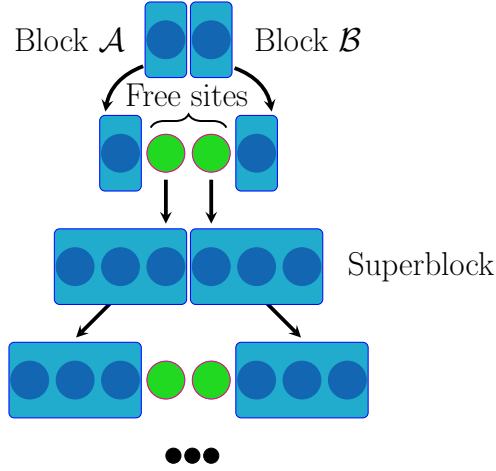


Fig. 3.2 Illustration of the growing procedure of expanding blocks in the infinite system [DMRG](#) method.

$\mathcal{A}(\ell, \chi)$ implies \mathcal{A} is a block of size ℓ (i.e. containing ℓ sites). There is a second label included called χ (can be D or m in other literature), which is called the bond-dimension or block-dimension. This dictates the size of a subspace of the total Hilbert space of the block that is retained to keep computations manageable. This will be explained in more detail after we have considered the two types of [DMRG](#) algorithms for ground-state calculations, called the infinite system and the finite system [DMRG](#) [120].

3.1.1 Infinite system DMRG

In the infinite system [DMRG](#) case, the spatial size of the system is iteratively increased to obtain an approximation for an infinite system or for a system of a prescribed length L . The algorithm is initially started with 2 sites, where one essentially forms a block labelled \mathcal{A} and the other forms a block labelled \mathcal{B} [120, 121, 125, 127]. It should be noted that some implementations start with four sites (two in each block), or more instead, which makes no fundamental difference to how the algorithm proceeds. The procedure to implement the infinite system [DMRG](#) method is described in Alg. 3.1.1. It will be assumed that a generic block $\mathcal{A}(\ell, \chi)$ can be effectively represented by the orthonormal basis $|a_{\mathcal{A}}\rangle$ (and block $\mathcal{B}(\ell, \chi)$ by $|a_{\mathcal{B}}\rangle$) in the following.

Algorithm 3.1.1 (Infinite system DMRG):

Initialisation

Step 0: Start with a chain of 2 sites which form block $\mathcal{A}(1, \chi)$ and $\mathcal{B}(1, \chi)$.

For $\ell = 1, \dots$:

Step 1: Insert 2 additional free sites \mathcal{S}_A and \mathcal{S}_B between the two blocks.

Step 2: Form the enlarged block representation, which is the representation of each free site joined to its adjacent block. To do this, form the enlarged Hamiltonians:

$$\begin{aligned}\mathcal{H}_{E_A} &= \mathcal{H}_A + \mathcal{H}_{\mathcal{S}_A} + \mathcal{H}_{A\mathcal{S}_A} , \\ \mathcal{H}_{E_B} &= \mathcal{H}_{\mathcal{S}_B} + \mathcal{H}_B + \mathcal{H}_{\mathcal{S}_B B} ,\end{aligned}\tag{3.1}$$

which are the sum of the Hamiltonian of the local block (\mathcal{H}_A or \mathcal{H}_B), the Hamiltonian of the corresponding free site ($\mathcal{H}_{\mathcal{S}_A}$ or $\mathcal{H}_{\mathcal{S}_B}$) and the Hamiltonian of the interaction between the block and its adjacent free site ($\mathcal{H}_{A\mathcal{S}_A}$ or $\mathcal{H}_{\mathcal{S}_B B}$).¹

Step 3: Form the representation of the superblock, which is the global representation of the two enlarged blocks:

$$\mathcal{H}_{sup} = \mathcal{H}_{E_A} + \mathcal{H}_{E_B} + \mathcal{H}_{\mathcal{S}_A \mathcal{S}_B} .\tag{3.2}$$

Any state within the superblock $\mathcal{A}\mathcal{S}_A\mathcal{S}_B\mathcal{B}$ can be written in the form:

$$|\psi\rangle = \sum_{a_A \sigma_A a_B \sigma_B} \Psi_{a_A \sigma_A \sigma_B a_B} |a_A\rangle |\sigma_A\rangle |\sigma_B\rangle |a_B\rangle ,\tag{3.3}$$

where $\{|\sigma_A\rangle\}$ and $\{|\sigma_B\rangle\}$ are d -dimensional bases for the free sites in \mathcal{A} (\mathcal{S}_A) and \mathcal{B} (\mathcal{S}_B) and $\Psi_{a_A \sigma_A \sigma_B a_B}$ stores the corresponding coefficient.

Step 4: Find the state $|\psi_G\rangle$ which minimises the energy of the superblock $\mathcal{A}\mathcal{S}_A\mathcal{S}_B\mathcal{B}$, by minimising:

$$E = \frac{\langle \psi | \mathcal{H}_{sup} | \psi \rangle}{\langle \psi | \psi \rangle} .\tag{3.4}$$

Step 5: Calculate the reduced density matrices ρ_A and ρ_B and retain the top χ eigenstates corresponding to the largest eigenvalues to form a new truncated basis.

Step 6: Renormalise the blocks and free sites, so that we obtain $\mathcal{A}(\ell + 1, \chi)$ and $\mathcal{B}(\ell + 1, \chi)$ for the next iteration.

Step 7: Repeat steps 1-6 until the prescribed length, or some convergence criterion, is met.

¹If we have a system with a global reflection symmetry this can be simplified greatly as the enlarged block of \mathcal{B} is just a reflection of the enlarged block of \mathcal{A} .

Final Step

Step 8: Calculate any measurements required using the ground state $|\psi_G\rangle$. The expectation of a given observable O is given by:

$$\langle O \rangle = \langle \psi_G | O | \psi_G \rangle . \quad (3.5)$$

Now, a few remarks on the algorithm that we have just seen are in order. There are a number of numerical methods that can be employed to perform the diagonalisation in Step 4 of Alg. 3.1.1 efficiently, such as Lanczos, Arnoldi or Jacobi-Davidson methods [128, 129]. Typically the method will be chosen to avail of the fact that the matrix is sparse for short-ranged Hamiltonians. Each time that a block is expanded by adding a free site, its basis increases in size by $d\chi$ where d is the physical dimension of a single site. To avoid an exponential growth in the block state space we truncate this block size back down to χ states (in Step 5), which essentially means we only retain a region of the Hilbert space that is relevant. This is done using the partial trace of the density matrix. From the ground state $|\psi_G\rangle$, we can obtain the full density matrix using the following equation:

$$\rho = |\psi_G\rangle\langle\psi_G|. \quad (3.6)$$

To reduce the expansion of the basis we truncate the space by using the reduced density matrices to represent the states of \mathcal{AS}_A and $\mathcal{S}_B\mathcal{B}$:

$$\begin{aligned} \rho_{\mathcal{AS}_A} &= \text{Tr}_{\mathcal{S}_B\mathcal{B}} |\psi_G\rangle\langle\psi_G|, \\ \rho_{\mathcal{S}_B\mathcal{B}} &= \text{Tr}_{\mathcal{AS}_A} |\psi_G\rangle\langle\psi_G|. \end{aligned} \quad (3.7)$$

Then $\rho_{\mathcal{AS}_A}$ and $\rho_{\mathcal{S}_B\mathcal{B}}$ are diagonalised separately and only the largest χ eigenvalues and the corresponding eigenvectors are retained to form a representation in a reduced basis for each. It should be noted that this truncation only takes place once the system has grown to a size such that a given block of length $d^\ell > \chi$.

Suppose that we stop the procedure for some specified length (i.e. superblock of length) L . The approximation that we have obtained can either be used as an approximation to a system with exactly L sites or to obtain an approximation of the infinite length system. It is an approximation of fixed length with limited accuracy as the first truncations were unlikely to be good estimates of a larger system size, whereas if we want an infinite approximation we will ignore the boundary effects and focus on the central sites, gaining a reasonable level of accuracy for translationally invariant systems if L has been extrapolated sufficiently.

3.1.2 Finite system DMRG

Before performing the finite system DMRG, it is standard procedure to form an approximation using the infinite system DMRG, stopping when the system reaches the desired length L . In the finite DMRG case, one block is expanded at the expense of the other in order to keep the total system size constant. Other than this it is essentially the same procedure as above. As there is a specified system size this will begin with a lattice of L sites, where block \mathcal{A} and block \mathcal{B} are formed of $(L - 2)/2$ sites each (assuming for simplicity that L is even) and there are two free sites $\mathcal{S}_\mathcal{A}$ and $\mathcal{S}_\mathcal{B}$ between them. An illustration of this procedure is shown in Fig. 3.3. Then in order to increase block \mathcal{A} to an enlarged block by absorbing a site, block \mathcal{B} loses a site which becomes the new free site $\mathcal{S}_\mathcal{B}$. Another difference with the infinite system DMRG is that the truncation procedure will only be applied to the block which is being enlarged. The full procedure is explained in Alg. 3.1.2.

Algorithm 3.1.2 (Finite DMRG):

Initialisation

Step 0: Perform infinite system DMRG up until the desired length L .

First Quarter Sweep-Expand Block \mathcal{A}

Step 1: Start with a lattice split into $\mathcal{A}\left(\frac{L-2}{2}, \chi\right) \mathcal{S}_\mathcal{A} \mathcal{S}_\mathcal{B} \mathcal{B}\left(\frac{L-2}{2}, \chi\right)$.

Repeat for $j = 1, \dots, \frac{L}{2} - 2$

Step 2: Expand block $\mathcal{A}(\frac{L}{2} - 2 + j, \chi)$ by one site to form $\mathcal{A}(\frac{L}{2} - 1 + j, \chi)$ and reduce block $\mathcal{B}(\frac{L}{2} - j)$ by one site to form $\mathcal{B}(\frac{L}{2} - 1 - j)$. The expanded block \mathcal{A} is formed by combining the free site $\mathcal{S}_\mathcal{A}$ with the old block \mathcal{A} to form an enlarged block whose reduced density matrix $\rho_{\mathcal{A}\mathcal{S}_\mathcal{A}}$ is then diagonalised and only the largest χ eigenvalues and eigenvectors are retained. For block \mathcal{B} its reduced state $\mathcal{B}(\frac{L}{2} - 1 - j, \chi)$ can be loaded from memory to save additional calculations.

Step 3: Save the block $\mathcal{A}(\frac{L}{2} - 1 + j, \chi)$ in memory.

Second Quarter Sweep-Expand Block \mathcal{B}

Step 4: Start with a lattice split into $\mathcal{A}(L - 3, \chi) \mathcal{S}_\mathcal{A} \mathcal{S}_\mathcal{B} \mathcal{B}(1, \chi)$

Repeat for steps $j = 1, \dots, \frac{L}{2} - 2$

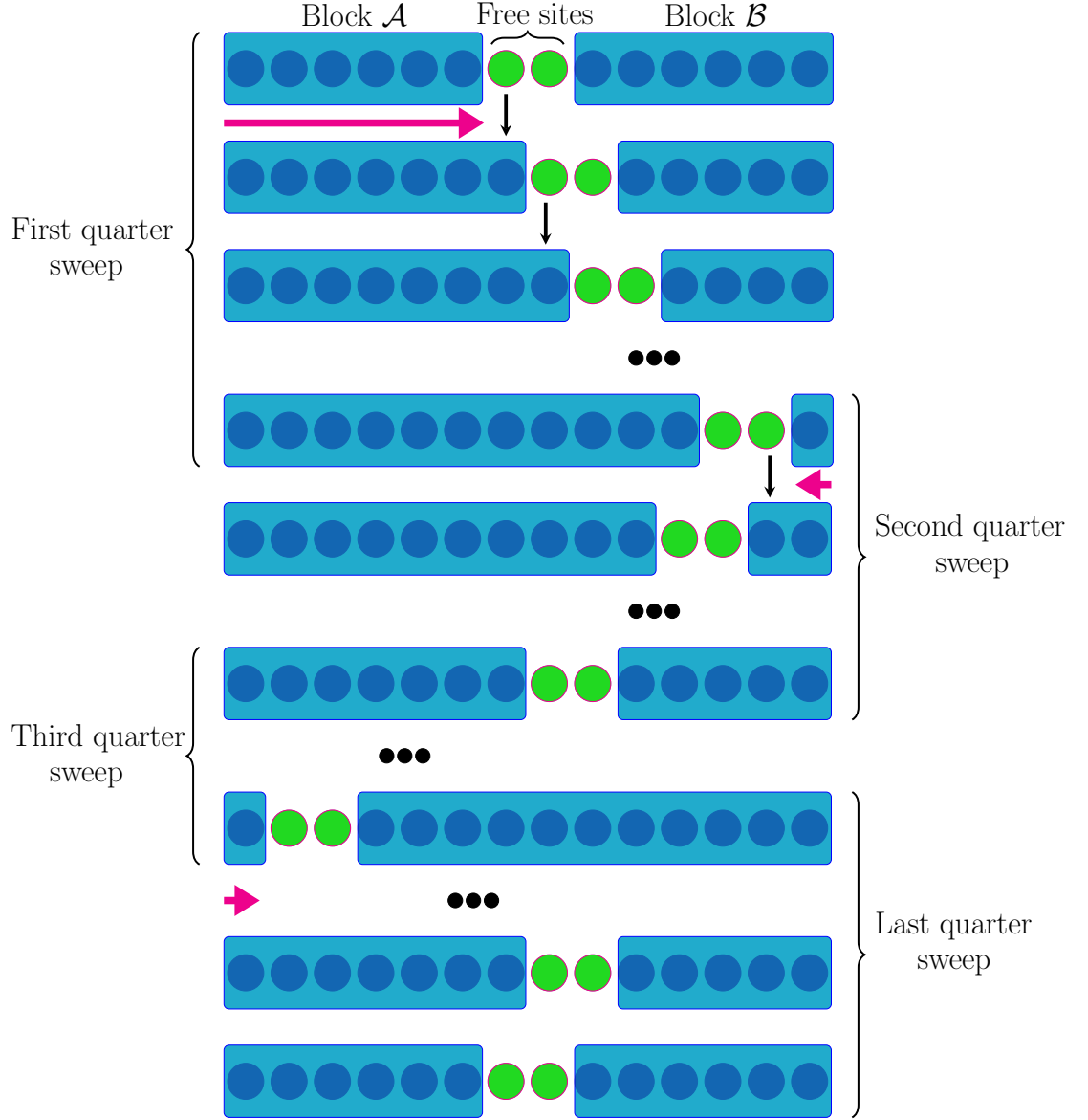


Fig. 3.3 Illustration of the sweep procedure of increasing blocks and moving free sites in the finite DMRG method. Initially the free sites are in the centre of the chain. Block \mathcal{A} is expanded until \mathcal{B} is of minimal size (first quarter sweep), then block \mathcal{B} is expanded until block \mathcal{A} is of minimal size (second and third quarter sweep). Lastly, block \mathcal{A} is expanded until it is of size $\frac{L-2}{2}$, completing a full sweep.

Step 5: Expand block $\mathcal{B}(j, \chi)$ to become $\mathcal{B}(1 + j, \chi)$ by forming the enlarged block and diagonalising its reduced density matrix $\rho_{\mathcal{S}_B \mathcal{B}}$ and only retaining χ eigenstates to form the basis. Shrink block $\mathcal{A}(L - 2 - j, \chi)$ to become $\mathcal{A}(L - 3 - j, \chi)$ by loading the saved block from memory.

Step 6: Save the block $\mathcal{B}(1 + j, \chi)$ in memory.

Second Half-Sweep

Step 8: Now perform steps 1-6 but with \mathcal{A} and \mathcal{B} reversed, i.e. start by expanding \mathcal{B} into the first half of the system and then expand \mathcal{A} once $N_A = 1$.

Convergence Check

Step 9: Check for convergence of the energy or any other observable to a required tolerance. If convergence has been reached end algorithm, otherwise return to step 1.

3.2 Truncation of the Hilbert Space

Truncating the Hilbert space, so that a reduced and more computationally reasonably sized subspace is kept, is a key part of the [DMRG](#) algorithms we have just examined and the other algorithms which occur in the [MPS](#) ansatz, which we will explain in the next section. In our description of the [DMRG](#) method, we have mentioned a truncation value χ which dictates the number of eigenvalues retained in our new basis. We will provide some motivation and explanation of why this procedure still retains a reasonable accuracy.

Firstly, if no truncation is applied, calculations are very costly as the full formulation of a state with physical dimension d scales exponentially with system size d^L . To avoid this problem an efficient representation of a small manifold of the total Hilbert space, commonly referred to as ‘the relevant corner of the Hilbert space’ can be kept as shown in [Fig. 3.4a](#).

An argument why a system written in the new efficient manifold basis is a sufficient estimate is due to the scaling of bipartite entanglement with the length of the system. A [1-D](#) gapped system with only nearest-neighbour coupling is subject to the area law [\[35, 130–133\]](#). An area law also holds for systems in higher

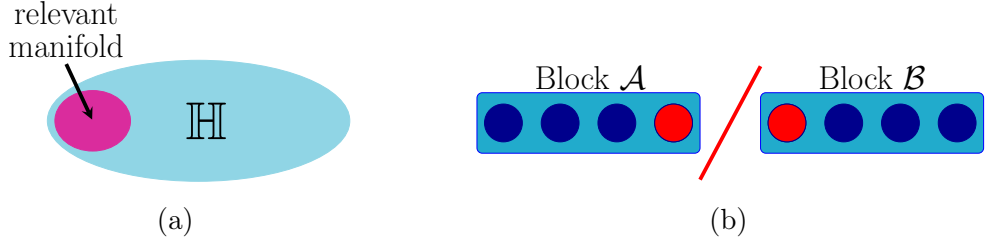


Fig. 3.4 **(a)**: Illustration of the relevant manifold that can be kept within the full Hilbert space \mathbb{H} . **(b)**: The bipartition of the lattice in order to measure the von Neumann entropy. The sites on the border of the bipartition are shown in red.

dimensions, which are represented in a similar ansatz [134, 135]. The area law states that the bipartite entanglement within the system scales with the boundary upon which the bipartition occurs. In a 1-D model, there are only two sites on the boundary as shown in red in Fig. 3.4b. This means that the von Neumann entropy (defined in Def. 2.3.6) scales as $\mathcal{S}_{\mathcal{A}|\mathcal{B}} \propto L^0$. There are then, system-dependent corrections, which are typically logarithmic for critical systems, that can be applied to this. In DMRG specifically, it can be seen that retaining this relevant manifold optimises three primary contributors, the expectation values, the state (wave function) itself and the entanglement, as described in Schollwöck’s 2005 review [136].

3.3 Matrix Product States (MPS)

Matrix product states (MPS) are based on tensor theory and are used as a more efficient way to represent the state of the sites within a chain and to make the system more computationally manageable by discarding some of its complexity. There is no single origin of MPS, as the formulation was already well established within a number of works but without a consistent name, until in 1995 Ostlund and Rommer [137] identified that the growth steps in the infinite system DMRG could be formulated in a matrix form that matches MPS. This was then expanded on in 1998 by Dukelsky *et al.* who showed that quantum states in the finite system DMRG could also be expressed in the MPS ansatz form [138]. It will be explained below that DMRG is made more simple by using this formulation [120].

In order to rewrite a given state in its MPS form we need to reformulate and normalise its expression for each site. To do this a procedure which results in a bipartition of a certain form is required; the most common ones that can be used are the QR decomposition, the Schmidt decomposition or the singular value decomposition (SVD) [120, 139]. It should be noted that the QR decomposition requires the least computational effort (though not substantially so as both SVD

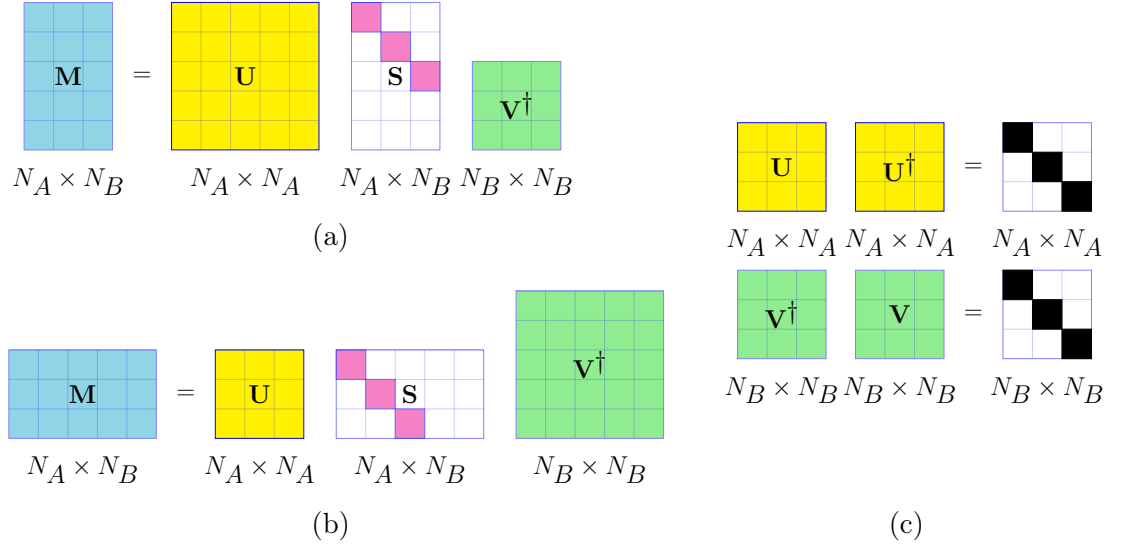


Fig. 3.5 Demonstration of how the [SVD](#) method forms the new decomposition of the matrix \mathbf{M} in terms of the matrix \mathbf{S} of singular values and the matrices \mathbf{U} and \mathbf{V}^\dagger of the left and right singular vectors, respectively. (a) shows the case when $N_A > N_B$, (b) illustrates when $N_A < N_B$ and (c) illustrates the general properties of \mathbf{U} and \mathbf{V} . Any white squares have zero elements and any black squares are strictly one, i.e. the white and black matrices are the identity matrix \mathbb{I} .

and QR are of $O(n^3)$ for a square ($n \times n$) matrix) but it is only relevant if we do not require the eigenvalues of the system, so in order to keep this general we will omit it here.

3.3.1 Singular Value Decomposition (SVD)

[SVD](#) is a linear algebra procedure to decompose a matrix into its singular values and left and right eigenvectors (called singular vectors). This will be used in the [MPS](#) notation to efficiently renormalise the state $|\psi\rangle$. If we assume we have a matrix \mathbf{M} (which can be square or non-square) of dimension ($N_A \times N_B$). Without loss of generality, we can choose $N_A \geq N_B$, which is the scenario shown in Fig. 3.5a. Then the aim of the [SVD](#) is to determine a factorisation of \mathbf{M} such that:

$$\mathbf{M} = \mathbf{U} \mathbf{S} \mathbf{V}^\dagger, \quad (3.8)$$

where \mathbf{U} is the matrix containing the left singular vectors, \mathbf{S} is a diagonal matrix containing the singular values and \mathbf{V}^\dagger is a matrix containing the right singular vectors. To be precise \mathbf{S} will be an $N_A \times N_B$ rectangular diagonal matrix, which only has non-zero entries for $(S)_{ii} \equiv s_i \geq 0$ for $i = 1, \dots, N_B$ and \mathbf{U} and \mathbf{V} are square unitary matrices of dimension N_A and N_B respectively. We now require \mathbf{S} , \mathbf{U} and \mathbf{V} to form the decomposition in Eq. (3.8).

Finding **S**

Find the real non-negative eigenvalues, s_i^2 , of the Hermitian $(N_B \times N_B)$ square matrix $\mathbf{M}^\dagger \mathbf{M}$. Then order them from largest to smallest, with s_k^2 as the smallest non-zero eigenvalue and s_1^2 as the largest:

$$s_1^2 \geq s_2^2 \geq \dots \geq s_k^2 > s_{k+1}^2 = \dots = s_{N_B}^2 = 0 . \quad (3.9)$$

The positive square roots of these eigenvalues form **S** and are called the **singular values of M** .

$$\mathbf{S} = \begin{pmatrix} s_1 & 0 & \dots & 0 \\ 0 & s_2 & \ddots & \vdots \\ \vdots & \ddots & \ddots & 0 \\ 0 & \dots & 0 & s_{N_B} \\ 0 & .. & .. & 0 \\ \vdots & \ddots & \ddots & \vdots \\ 0 & .. & .. & 0 \end{pmatrix} \quad \text{where } s_i = 0 \text{ for } k < i \leq N_A.$$

Constructing **V**

The square $N_B \times N_B$ matrix $\mathbf{M}^\dagger \mathbf{M}$ is Hermitian, which means that there exists [139] the factorisation:

$$\mathbf{M}^\dagger \mathbf{M} = \mathbf{V} \mathbf{D} \mathbf{V}^\dagger , \quad (3.10)$$

where **D** is a diagonal matrix of dimension $N_B \times N_B$, with entries of the eigenvalues of $\mathbf{M}^\dagger \mathbf{M}$. These eigenvalues correspond to the square of the first N_B diagonal elements of the matrix **S**. The columns of \mathbf{V}^\dagger are the orthonormal (normalised orthogonal) eigenvectors corresponding to the eigenvalues of **D**. This means that $\mathbf{V}^\dagger \mathbf{V} = \mathbb{I}$ (see Fig. 3.5c).

Constructing **U**

U can either be calculated from **V** by finding its first N_B columns using:

$$\mathbf{u}_i = \frac{1}{s_i} \mathbf{M} \mathbf{v}_i \text{ for } i = 1, 2, \dots, N_B , \quad (3.11)$$

where v_i is the i^{th} row of **V**. This requires forming the remaining columns by ensuring they make a linearly independent set. Alternatively, we can make use of the fact that $\mathbf{M} \mathbf{M}^\dagger$ is by construction Hermitian, meaning that we can formulate:

$$\mathbf{M} \mathbf{M}^\dagger = \mathbf{U} \mathbf{D}^\dagger \mathbf{U}^\dagger \equiv \mathbf{U} \mathbf{D} \mathbf{U}^\dagger . \quad (3.12)$$

The rows of \mathbf{U} are the orthonormal (normalised orthogonal) eigenvectors corresponding to the eigenvalues of \mathbf{D} . This means that $\mathbf{U}\mathbf{U}^\dagger = \mathbb{I}$ (see Fig. 3.5c).

If we had chosen $N_B > N_A$ instead, then a similar procedure is followed where the k^{th} column in \mathbf{S} for $k > N_A$ will contain only zero elements (see Fig. 3.5b). In the general case, i.e. making no assumptions about the sizes of N_A and N_B , the dimensions of the matrix \mathbf{S} can be reduced from the dimensions $N_A \times N_B$. This is done by considering the fact that its entries are zero for any k^{th} row/column such that $k > \min(N_A, N_B)$, meaning that \mathbf{S} can instead be reduced to a diagonal matrix of dimension $\min(N_A, N_B)$. This means the dimension of \mathbf{U} becomes $(N_A, \min(N_A, N_B))$ and the dimension of \mathbf{V}^\dagger is $(\min(N_A, N_B), N_B)$. In this formulation if $N_A \geq N_B$ then \mathbf{U} is unitary but if $N_B \geq N_A$ (see Fig. 3.5b) then \mathbf{V} is instead unitary [120, 139].

3.3.2 Schmidt Decomposition

Previously, we have defined the Schmidt decomposition as a means to identify whether a pure state is entangled or not (see Sec. 2.3). Here we will redefine it with different notation that better matches our lattice notation, in order to illustrate how the SVD method can be used to form the Schmidt decomposition. The Schmidt decomposition provides a compact representation of a bipartition of a state [8, 120]. For this we assume that we have a system with a given pure state $|\psi\rangle$, which belongs to the Hilbert space \mathbb{H} that can be split into a bipartition $\mathbb{H} = \mathbb{H}_A \otimes \mathbb{H}_B$ of two subspaces \mathbb{H}_A and \mathbb{H}_B respectively. The subspaces \mathbb{H}_A and \mathbb{H}_B can each be described by a set of states forming an orthonormal basis. We will assume that N_A states are required to represent \mathbb{H}_A , called $|j_A\rangle$ ($j = 1, \dots, N_A$) and that a set of N_B states form the space \mathbb{H}_B , $|k_B\rangle$ ($k = 1, \dots, N_B$). Any pure state $|\psi\rangle$ can be expressed as a linear combination of these orthonormal bases:

$$|\psi\rangle = \sum_{j=1}^{N_A} \sum_{k=1}^{N_B} \Psi_{j,k} |j_A\rangle |k_B\rangle, \quad (3.13)$$

where Ψ is a matrix which stores the required coefficients for each state. We can reformulate the reduced density matrices of the systems A and B in terms of the basis of each subspace: $\rho_A = \text{Tr}_B |\psi\rangle\langle\psi|$ and $\rho_B = \text{Tr}_A |\psi\rangle\langle\psi|$. The reduced density matrices can be rewritten in terms of the matrix Ψ as $\rho_A = \Psi\Psi^\dagger$ and $\rho_B = \Psi^\dagger\Psi$. Then if we perform an SVD on the matrix Ψ in Eq. (3.13) we obtain:

$$|\psi\rangle = \sum_{j=1}^{N_A} \sum_{k=1}^{N_B} \sum_{\alpha=1}^{\min(N_A, N_B)} U_{j,\alpha} S_{\alpha,\alpha} V_{\alpha,k}^\dagger |j_A\rangle |k_B\rangle, \quad (3.14)$$

which after rearranging gives us:

$$|\psi\rangle = \sum_{\alpha=1}^{\min(N_A, N_B)} \left(\sum_{j=1}^{N_A} U_{j,\alpha} |j_A\rangle \right) S_{\alpha,\alpha} \left(\sum_{k=1}^{N_B} V_{\alpha,k}^\dagger |k_B\rangle \right). \quad (3.15)$$

We will define $|\alpha_A\rangle = \sum_{j=1}^{N_A} U_{j,\alpha} |j_A\rangle$ and $|\alpha_B\rangle = \sum_{k=1}^{N_B} V_{\alpha,k}^\dagger |k_B\rangle$. The orthonormality properties of \mathbf{U} and \mathbf{V}^\dagger means the sets $|\alpha_A\rangle$ and $|\alpha_B\rangle$ are orthonormal and can be extended to be orthonormal bases of A and B . In addition to this we will only retain non-zero singular values meaning that we will keep $r \leq \min(N_A, N_B)$ if we assume that $s_r > s_{r+1} = s_{r+2} \dots = 0$. Using these assumptions we obtain the Schmidt decomposition:

$$|\psi\rangle = \sum_{\alpha=1}^r s_\alpha |\alpha_A\rangle |\alpha_B\rangle. \quad (3.16)$$

The Schmidt decomposition provides a convenient way to calculate the reduced density matrices, as by carrying out the partial trace we can obtain: $\rho_A = \sum_\alpha s_\alpha^2 |\alpha_A\rangle \langle \alpha_A|$ and $\rho_B = \sum_\alpha s_\alpha^2 |\alpha_B\rangle \langle \alpha_B|$. The square of the singular values are very useful measures, where their full spectrum is referred to as the entanglement spectrum, defined as $\lambda_i = s_i^2$ [140].

The Schmidt decomposition also provides a simpler way to calculate the von Neumann entropy [120]. The von Neumann entropy typically requires the calculation of the reduced density matrix, however, when [SVD](#) is used, this additional calculation can be avoided. The von Neumann entropy can instead be expressed as:

$$\mathcal{S}_{A|B} = -\text{Tr}(\rho_A \log_2(\rho_A)) \equiv -\sum_{\alpha=1}^r \lambda_\alpha \log_2 \lambda_\alpha. \quad (3.17)$$

3.3.3 Methodology of MPS

Rewriting a given state $|\psi\rangle$ in the [MPS](#) ansatz means it needs to be efficiently expressed in a more succinct state class. Consider a lattice of L sites with local state spaces denoted by $|\sigma_j\rangle$ ($j = 1 \dots L$) of dimension d . Then a pure state of the entire lattice can be expressed by the following:

$$|\psi\rangle = \sum_{\sigma_1, \dots, \sigma_L} c_{\sigma_1, \dots, \sigma_L} |\sigma_1 \dots \sigma_L\rangle. \quad (3.18)$$

This expression of the state $|\psi\rangle$ describes the whole lattice together but it is more convenient to have a form which lends itself to a local interpretation of the state. This can be done by using [SVD](#), where there are three different approaches as

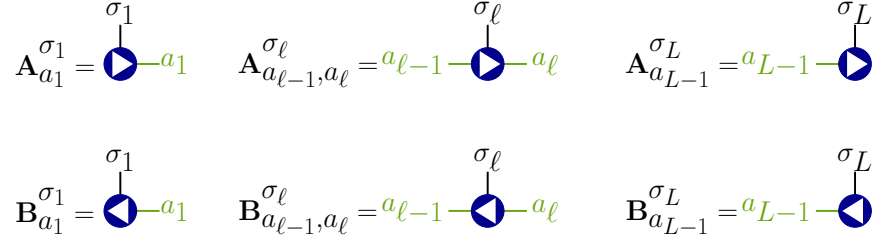


Fig. 3.6 Illustration of how to represent MPS operators. The \mathbf{A} matrices are left normalised, shown by the triangle pointing to the right and the \mathbf{B} matrices are right normalised, with a triangle pointing to the left. The vertical legs represent the physical state labels and the horizontal lines are the internal indices of the matrix.

outlined below [120].

(i) Left-normalised (Left Canonical) Quantum State

The left normalised site matrices will be called \mathbf{A} with the appropriate indices. The indices will depend on if it is at a boundary site or within the chain. In principle, the left-normalised representation for a local site $j \in [1, L]$ will be denoted by $\mathbf{A}_{a_{j-1}, a_j}^{\sigma_j} = \mathbf{A}_{(a_{j-1}\sigma_j), a_j}$ which is a matrix of dimension $a_{j-1}\sigma_j \times a_j$. At the boundaries there are then the dummy matrix indices a_0 and a_L which have dimension one and can be omitted. An illustration of how these \mathbf{A} matrices are represented diagrammatically as a circle in MPS form is given in Fig. 3.6. The vertical legs give the physical indices σ_j and the horizontal legs are the internal indices of the system denoted a_j . A closed line between tensors means that the corresponding index is summed over. To highlight that each one is left-normalised, the circle representing \mathbf{A} contains a triangle pointing to the right. Now that we know how a site matrix is represented in an MPS, let us describe the method to extract the matrices from the full state.

We will start with a state $|\psi\rangle$ in the format shown in Eq. (3.18). The coefficients $c_{\sigma_1, \dots, \sigma_L}$ can be considered to be a matrix $\Psi_{\sigma_1, \sigma_2, \dots, \sigma_L}$, where initially this, in principle, can be rewritten using a dummy index as $\Psi_{(\sigma_1, \sigma_2, \dots, \sigma_L), 1}$, which is a vector of length d^L . As we are carrying out a left normalisation we will start by splitting the physical indices of the first local state σ_1 from the others. This can be done by reshaping the matrix Ψ to have $d \times d^{L-1}$ dimensions: $\Psi_{\sigma_1, (\sigma_2, \dots, \sigma_L)}$. An example of this is shown for qubits (i.e. $d = 2$), where $L = 3$ in Fig. 3.7. We then perform an SVD on $\Psi_{\sigma_1 \dots \sigma_L}$ and define $A_{a_1}^{\sigma_1} = U_{\sigma_1, a_1}$ and $c_{a_1, (\sigma_2 \dots \sigma_L)} = S_{a_1, a_1} V_{a_1, (\sigma_2, \dots, \sigma_L)}^\dagger$ as

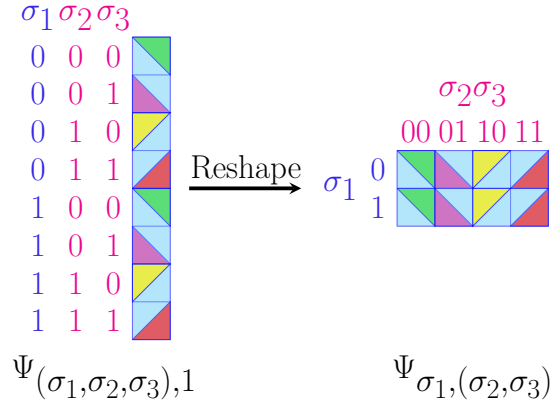


Fig. 3.7 An example of how to reshape the vector $\Psi_{(\sigma_1, \sigma_2, \sigma_3), 1}$ for qubits ($d = 2$) to $\Psi_{\sigma_1, (\sigma_2, \sigma_3)}$. The triangles in different positions match up with the reshaped matrix to highlight where each element came from.

shown:

$$\begin{aligned}
 c_{\sigma_1 \dots \sigma_L} &\equiv \Psi_{(\sigma_1 \dots \sigma_L), 1} \\
 &\stackrel{\text{reshape}}{=} \Psi_{\sigma_1, (\sigma_2, \dots, \sigma_L)} \\
 &\stackrel{\text{SVD}}{=} \sum_{a_1} U_{\sigma_1, a_1} S_{a_1, a_1} V_{a_1, (\sigma_2, \dots, \sigma_L)}^\dagger \\
 &\equiv \sum_{a_1} U_{\sigma_1, a_1} c_{a_1, (\sigma_2 \dots \sigma_L)} \\
 &\equiv \sum_{a_1} A_{a_1}^{\sigma_1} c_{a_1, (\sigma_2 \dots \sigma_L)} .
 \end{aligned} \tag{3.19}$$

This procedure is then continued by reshaping $c_{a_1, (\sigma_2 \dots \sigma_L)}$ to become $c_{a_1 \sigma_2, (\sigma_3 \dots \sigma_L)}$ and then performing an SVD on this as shown in Alg. 3.3.1 and in Fig. 3.8a.

Algorithm 3.3.1 (Finding left-normalised matrices A):

Initialisation:

Step 0: Reshape $c_{\sigma_1 \dots \sigma_L} = \Psi_{(\sigma_1 \dots \sigma_L), 1}$ to be $\Psi_{\sigma_1, (\sigma_2 \dots \sigma_L)}$. Perform SVD on this to obtain:

$$\begin{aligned}
 \Psi_{\sigma_1, (\sigma_2 \dots \sigma_L)} &\stackrel{\text{SVD}}{=} \sum_{a_1} U_{\sigma_1, a_1} S_{a_1, a_1} V_{a_1, (\sigma_2, \dots, \sigma_L)}^\dagger \\
 &\equiv \sum_{a_1} A_{1, a_1}^{\sigma_1} c_{a_1, (\sigma_2, \dots, \sigma_L)} .
 \end{aligned} \tag{3.20}$$

For each $\ell = 2, \dots, L - 1$ repeat steps 1-5:

Step 1: At each step we will have a matrix of the coefficients of the local states ℓ, \dots, L : $c_{a_{\ell-1}, (\sigma_\ell \dots \sigma_L)} = \Psi_{a_{\ell-1}, (\sigma_\ell \dots \sigma_L)}$.

Step 2: Reshape Ψ so that we have: $\Psi_{a_{\ell-1}\sigma_\ell,(\sigma_{\ell+1}\dots\sigma_L)}$.

Step 3: Perform SVD on $\Psi_{a_{\ell-1}\sigma_\ell,(\sigma_{\ell+1}\dots\sigma_L)}$ to get

$$\Psi_{a_{\ell-1}\sigma_\ell,(\sigma_{\ell+1}\dots\sigma_L)} \stackrel{SVD}{=} \sum_{a_\ell} U_{a_{\ell-1}\sigma_\ell,a_\ell} S_{a_\ell,a_\ell} V_{a_\ell,(\sigma_{\ell+1},\dots,\sigma_L)}^\dagger . \quad (3.21)$$

Step 4: Define $A_{a_{\ell-1},a_\ell}^{\sigma_\ell} = U_{a_{\ell-1}\sigma_\ell,a_\ell}$ and $c_{a_\ell,(\sigma_{\ell+1}\dots\sigma_L)} = S_{a_\ell,a_\ell} V_{a_\ell,(\sigma_{\ell+1},\dots,\sigma_L)}^\dagger$ so that we have:

$$\Psi_{a_{\ell-1}\sigma_\ell,(\sigma_{\ell+1}\dots\sigma_L)} = \sum_{a_\ell} A_{a_{\ell-1},a_\ell}^{\sigma_\ell} c_{a_\ell,(\sigma_{\ell+1}\dots\sigma_L)} . \quad (3.22)$$

Step 5: Place $\Psi_{a_{\ell-1}\sigma_\ell,(\sigma_{\ell+1}\dots\sigma_L)}$ back into the equation with all of the coefficients:

$$c_{\sigma_1,\dots,\sigma_L} = \sum_{a_1,\dots,a_\ell} A_{a_1}^{\sigma_1} \dots A_{a_{\ell-1},a_\ell}^{\sigma_\ell} c_{a_\ell,(\sigma_{\ell+1}\dots\sigma_L)} . \quad (3.23)$$

Final step:

Step 6: For $\ell = L$: c_{a_{L-1},σ_L} is reshaped to $c_{a_{L-1}\sigma_L,1}$ which is a column vector and becomes $A_{a_{L-1}}^{\sigma_L}$.

If Alg. 3.3.1 is performed, we obtain the left-canonical MPS consisting of the left normalised \mathbf{A} matrices. Eq. (3.18) now becomes:

$$|\psi\rangle = \sum_{a_1,\dots,a_\ell} \sum_{\sigma_1,\dots,\sigma_L} A_{1,a_1}^{\sigma_1} A_{a_1,a_2}^{\sigma_2} \dots A_{a_{L-1},1}^{\sigma_L} |\sigma_1 \dots \sigma_L\rangle, \quad (3.24)$$

which multiplying out the matrices can be more succinctly written as:

$$|\psi\rangle = \sum_{\sigma_1,\dots,\sigma_L} A^{\sigma_1} A^{\sigma_2} \dots A^{\sigma_L} |\sigma_1 \dots \sigma_L\rangle. \quad (3.25)$$

We also obtain a useful property for the left-normalised matrices due to the $U^\dagger U = \mathbb{I}$ property :

$$\sum_{\sigma_\ell} A^{\sigma_\ell \dagger} A^{\sigma_\ell} = \mathbb{I}. \quad (3.26)$$

(ii) Right-normalised (Right Canonical) Quantum State

The right normalisation is carried out in the same way that we found the left canonical state except here we start from the right and instead of splitting \mathbf{U} and

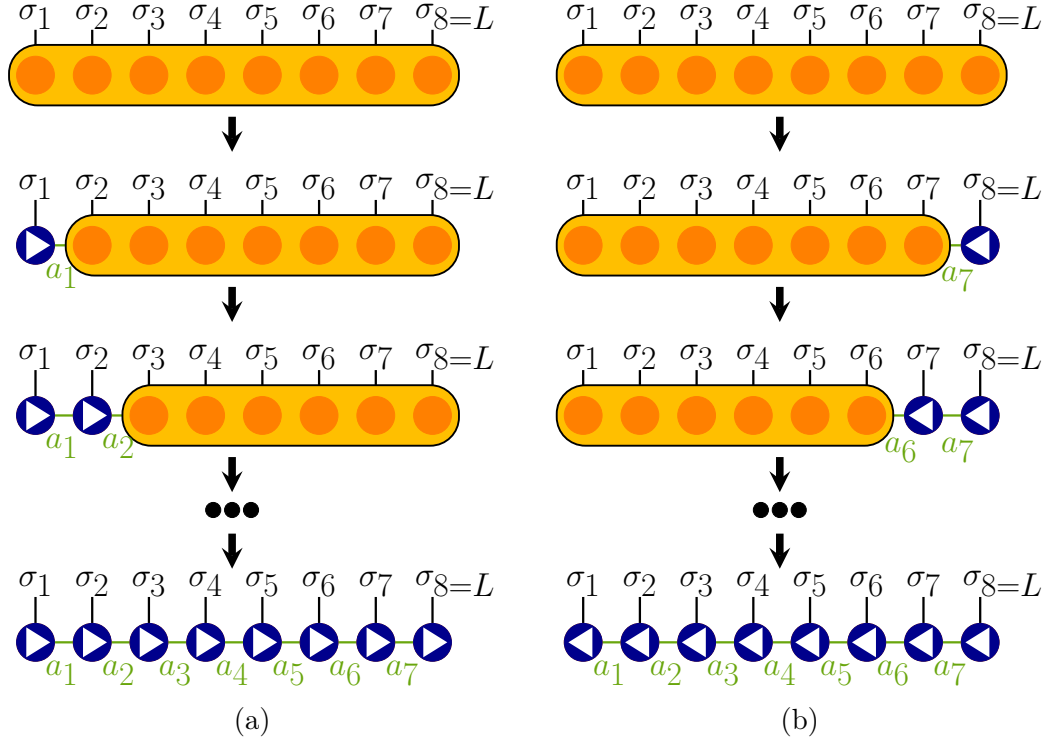


Fig. 3.8 Illustration of (a) the left and (b) the right, normalisation via SVD to create a left (right) canonical MPS system. The physical indices are labelled in black and the matrix (internal) indices are labelled in green. The direction of the triangle inside the site indicates whether it is left (pointing right) or right (pointing left) normalised.

$\mathbf{S}\mathbf{V}^\dagger$, we will obtain the right normalised vectors \mathbf{B} directly from \mathbf{V}^\dagger and then we will reshape $\mathbf{U}\mathbf{S}$. The \mathbf{B} matrices are denoted in the same way as the left matrices but as they are right-normalised they have a triangle pointing left inside each one (see Fig. 3.6). We once again start with the initial representation of a state shown in Eq. (3.18). The procedure is carried out very similarly as shown in Alg. 3.3.2 and in Fig. 3.8b.

Algorithm 3.3.2 (Finding right-normalised matrices B):

Initialisation:

Step 0: Reshape $c_{\sigma_1 \dots \sigma_L} = \Psi_{(\sigma_1 \dots \sigma_L), 1}$ to be $\Psi_{(\sigma_1 \dots \sigma_{L-1}), \sigma_L}$. Perform SVD on this to obtain:

$$\begin{aligned} \Psi_{(\sigma_1 \dots \sigma_{L-1}), \sigma_L} &\stackrel{SVD}{=} \sum_{a_{L-1}} U_{(\sigma_1 \dots \sigma_{L-1}), a_{L-1}} S_{a_{L-1}, a_{L-1}} V_{a_{L-1}, \sigma_L}^\dagger \\ &\equiv \sum_{a_{L-1}} c_{(\sigma_1, \dots, \sigma_{L-1}), a_{L-1}} B_{a_{L-1}, 1}^{\sigma_L} . \end{aligned} \quad (3.27)$$

For each $\ell = L - 1, L - 2, \dots, 2$ repeat steps 1-5:

Step 1: At each step we will have a matrix of the coefficients of the local states $1, \dots, \ell$: $c_{(\sigma_1 \dots \sigma_\ell), a_\ell} = \Psi_{(\sigma_1 \dots \sigma_\ell), a_\ell}$.

Step 2: Reshape Ψ so that we have: $\Psi_{(\sigma_1 \dots \sigma_{\ell-1}), a_\ell \sigma_\ell}$.

Step 3: Perform **SVD** on $\Psi_{(\sigma_1 \dots \sigma_{\ell-1}), a_\ell \sigma_\ell}$ to get:

$$\Psi_{(\sigma_1 \dots \sigma_{\ell-1}), a_\ell \sigma_\ell} \stackrel{\text{SVD}}{=} \sum_{a_{\ell-1}} U_{(\sigma_1 \dots \sigma_{\ell-1}), a_{\ell-1}} S_{a_{\ell-1}, a_\ell} V_{a_{\ell-1}, a_\ell \sigma_\ell}^\dagger. \quad (3.28)$$

Step 4: Define $B_{a_{\ell-1}, a_\ell}^{\sigma_\ell} = V_{a_{\ell-1}, a_\ell \sigma_\ell}^\dagger$ and $c_{(\sigma_1 \dots \sigma_{\ell-1}), a_{\ell-1}} = U_{(\sigma_1 \dots \sigma_{\ell-1}), a_{\ell-1}} S_{a_{\ell-1}, a_\ell}$ so that we have:

$$\Psi_{(\sigma_1 \dots \sigma_{\ell-1}), a_\ell \sigma_\ell} = \sum_{a_{\ell-1}} c_{(\sigma_1 \dots \sigma_{\ell-1}), a_{\ell-1}} B_{a_{\ell-1}, a_\ell}^{\sigma_\ell}. \quad (3.29)$$

Step 5: Place $\Psi_{(\sigma_1 \dots \sigma_{\ell-1}), a_\ell \sigma_\ell}$ back into the equation with all of the coefficients:

$$c_{\sigma_1 \dots \sigma_L} = \sum_{a_{\ell-1}, \dots, a_{L-1}} c_{(\sigma_1 \dots \sigma_{\ell-1}), a_{\ell-1}} B_{a_{\ell-1}, a_\ell}^{\sigma_\ell} \dots B_{a_{L-1}, 1}^{\sigma_L}. \quad (3.30)$$

Final step:

Step 6: For $\ell = 1$: c_{σ_1, a_1} is reshaped to $c_{1, a_1 \sigma_1}$ which is a row vector and forms $B_{a_1}^{\sigma_1}$.

Once all sites have been normalised by carrying out the procedure in Alg. 3.3.2, Eq. (3.18) becomes:

$$|\psi\rangle = \sum_{a_1, \dots, a_{L-1}} \sum_{\sigma_1, \dots, \sigma_L} B_{1, a_1}^{\sigma_1} B_{a_1, a_2}^{\sigma_2} \dots B_{a_{L-1}, 1}^{\sigma_L} |\sigma_1 \dots \sigma_L\rangle, \quad (3.31)$$

which multiplying out the matrices can be more succinctly written as:

$$|\psi\rangle = \sum_{\sigma_1, \dots, \sigma_L} B^{\sigma_1} B^{\sigma_2} \dots B^{\sigma_L} |\sigma_1 \dots \sigma_L\rangle. \quad (3.32)$$

As a result of the **SVD** matrices the **B** normalised matrices will have the property:

$$\sum_{\sigma_\ell} B^{\sigma_\ell} B^{\sigma_\ell \dagger} = \mathbb{I}. \quad (3.33)$$

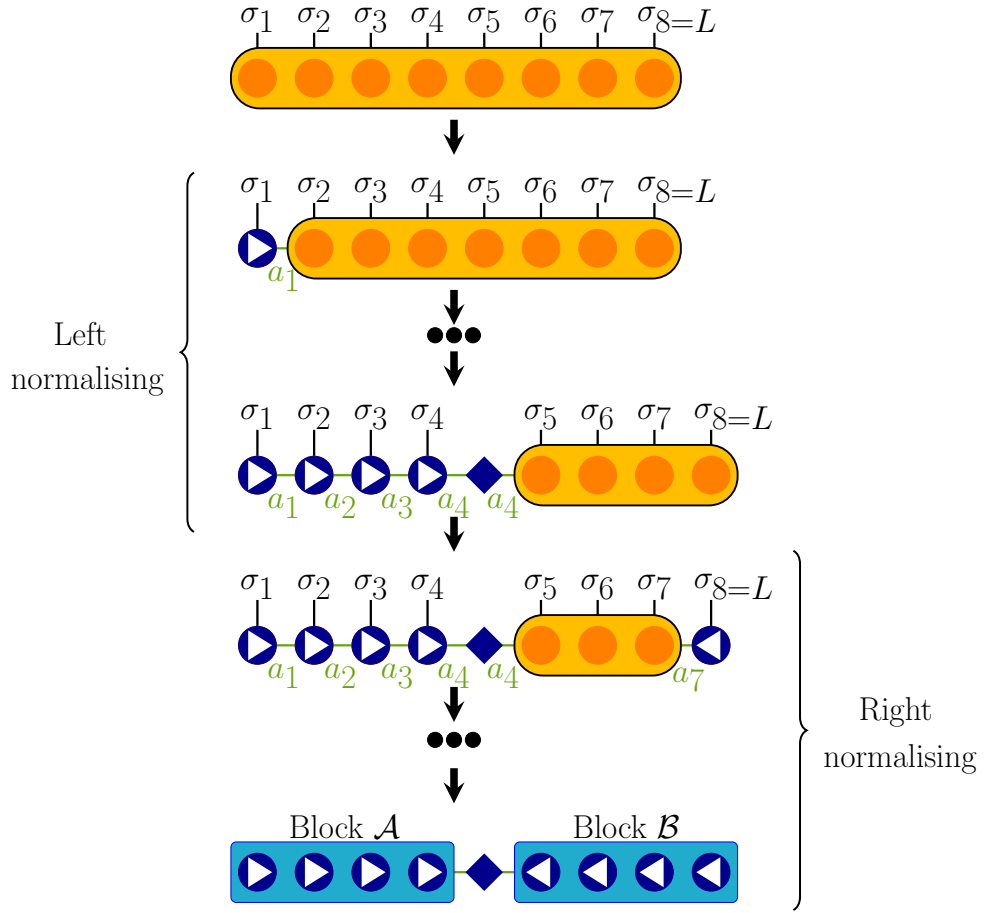


Fig. 3.9 Illustration of the left normalisation followed by right normalisation via [SVD](#) to create a mixed canonical [MPS](#) system. The physical indices are labelled in black and the matrix (internal) indices are labelled in green. The direction of the triangle inside the site indicates whether it is left (pointing right) or right (pointing left) normalised. The diamond represents the the matrix of singular values between two sites.

(iii) Mixed Canonical Quantum State

Alternatively, we can have a mixed canonical state with some of its local states left-normalised and some of them right-normalised. Assume that we left normalise the states up to site ℓ using the procedure outlined in [Alg. 3.3.1](#) and [Fig. 3.8a](#). This means that the coefficients of our state can be written in the following form:

$$\begin{aligned}
 c_{\sigma_1 \dots \sigma_L} &= \sum_{a_1, \dots, a_\ell} A_{1,a_1}^{\sigma_1} A_{a_1,a_2}^{\sigma_2} \dots A_{a_{\ell-1},a_\ell}^{\sigma_\ell} S_{a_\ell,a_\ell} V_{a_\ell,(\sigma_{\ell+1}, \dots, \sigma_L)}^\dagger \\
 &= \sum_{a_\ell} (A^{\sigma_1} A^{\sigma_2} \dots A^{\sigma_{\ell-1}} A^{\sigma_\ell})_{a_\ell} S_{a_\ell,a_\ell} V_{a_\ell,(\sigma_{\ell+1}, \dots, \sigma_L)}^\dagger .
 \end{aligned} \tag{3.34}$$

We leave the singular values untouched and only adjust V^\dagger :

$$V_{a_\ell, (\sigma_{\ell+1}, \dots, \sigma_L)}^\dagger = \Psi_{a_\ell, (\sigma_{\ell+1}, \dots, \sigma_L)} \stackrel{\text{reshape}}{=} \Psi_{(a_\ell, (\sigma_{\ell+1}, \dots, \sigma_{L-1}), \sigma_L)} . \quad (3.35)$$

Now perform the right-normalisation starting from $\Psi_{a_\ell, (\sigma_{\ell+1}, \dots, \sigma_{L-1}, \sigma_L)}$ as described in Alg. 3.3.2 and Fig. 3.8b up until $\sigma_{\ell+2}$. At the last step we will have $U_{a_\ell \sigma_{\ell+1}, a_{\ell+1}} S_{a_{\ell+1}, a_{\ell+1}}$ which we reshape to form $B_{a_\ell, a_{\ell+1}}^{\sigma_{\ell+1}}$. This means that:

$$\begin{aligned} V_{a_\ell, (\sigma_{\ell+1}, \dots, \sigma_L)}^\dagger &= \sum_{a_{\ell+1} \dots a_{L-1}} B_{a_\ell, a_{\ell+1}}^{\sigma_{\ell+1}} B_{a_{\ell+1}, a_{\ell+2}}^{\sigma_{\ell+2}} \dots B_{a_{L-1}, 1}^{\sigma_L} \\ &= (B^{\sigma_{\ell+1}} B^{\sigma_{\ell+2}} \dots B^{\sigma_L})_{a_\ell} . \end{aligned} \quad (3.36)$$

Now if we substitute our new equation for $V_{a_\ell, (\sigma_{\ell+1}, \dots, \sigma_L)}^\dagger$ back into Eq. (3.34), we obtain:

$$\begin{aligned} c_{\sigma_1 \dots \sigma_L} &= \sum_{a_\ell} (A^{\sigma_1} A^{\sigma_2} \dots A^{\sigma_{\ell-1}} A^{\sigma_\ell})_{a_\ell} S_{a_\ell, a_\ell} (B^{\sigma_{\ell+1}} B^{\sigma_{\ell+2}} \dots B^{\sigma_L})_{a_\ell} \\ &= A^{\sigma_1} A^{\sigma_2} \dots A^{\sigma_\ell} S_{a_\ell, a_\ell} B^{\sigma_{\ell+1}} B^{\sigma_{\ell+2}} \dots B^{\sigma_L} . \end{aligned} \quad (3.37)$$

This retains the singular value between site ℓ and $\ell + 1$, which is shown by a diamond in Fig. 3.9. It should also be noted that this is the exact same form of the Schmidt decomposition in Eq. (3.15).

3.3.4 DMRG in the MPS ansatz

Up to this point we have focused on expressing a state in the MPS ansatz, but to perform DMRG using MPS we also need to discover how the minimisation is carried out and how to represent operators.

First, we will focus on how an operator is represented in the MPS ansatz. To do this we are going to look at matrix product operators (MPOs) with specific focus on how to express the Hamiltonian \mathcal{H} in its MPO form, \mathcal{H}^{MPO} . There are a number of different methods [141–144] used in order to express the Hamiltonian in such a way, but basically what we require is a collection of matrices that can apply the operations throughout the system. To put this more mathematically, an MPO is applied to the whole lattice as a product of tensors W_j , in the form $O = W_1 W_2 \dots W_{L-1} W_L$. This means a general expectation measure of the MPO O can be represented by placing each tensor W_j between an MPS and its Hermitian conjugate, so that the physical legs connect them as shown in Fig. 3.10. For an OBC uniform lattice the same operator can be repeated for all sites except the boundary ones. This means $W = W_j$ for $j = 1, 2, 3, \dots, L - 1$ and then we

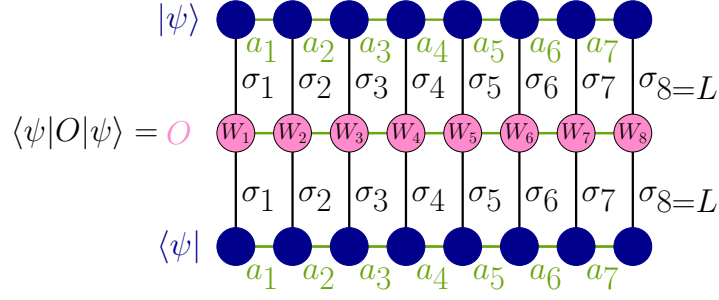


Fig. 3.10 An example of how the expectation is measured of an arbitrary operator in **MPO** form O for a lattice of length $L = 8$. No assumptions are made about the normalisation of these sites.

have the left and right boundary operators $Le = W_0$, $Ri = W_L$ [141], so that $\mathcal{H}^{MPO} = LeW \dots WRi$.

Let us consider a simple example of a $L = 5$ system which is described by the Ising model with a transverse field. The Hamiltonian for this is:

$$\begin{aligned} \mathcal{H} &= -J_x \sum_{j=1}^{L-1} \sigma_j^x \sigma_{j+1}^x - B_z \sum_j^L \sigma_j^z \\ &\equiv O_{xx} + O_z . \end{aligned} \quad (3.38)$$

First we will focus on how to represent the transverse field $O_z = -B_z \sum_j^L \sigma_j^z$, which can instead be expressed as the sum of a tensor of the operation on each site as shown:

$$\begin{aligned} O_z &= -B_z (\sigma^z \otimes \mathbb{I} \otimes \mathbb{I} \otimes \mathbb{I} \otimes \mathbb{I} + \mathbb{I} \otimes \sigma^z \otimes \mathbb{I} \otimes \mathbb{I} \otimes \mathbb{I} + \\ &\quad \dots + \mathbb{I} \otimes \mathbb{I} \otimes \mathbb{I} \otimes \mathbb{I} \otimes \sigma^z) . \end{aligned} \quad (3.39)$$

The **MPO** consists of these chains of tensors. The easiest way to form an **MPO** is to consider the possible pathways that an operator could take, for example, if we consider the on-site operator at site $j = 3$, then this will be represented by $\mathbb{I} \otimes \mathbb{I} \otimes (-B_z \sigma^z) \otimes \mathbb{I} \otimes \mathbb{I}$. If we have a uniform lattice, a simple way to construct the operator in **MPO** form is to think of its actions as a weighted graph [144–146] with a specified starting and end node. The edges of the graph will be labelled by their weight which is the coefficient times the operator. An example of this is shown for the $-B_z \sigma^z$ acting on the third site in Fig. 3.11a. The nodes are labelled by the site they correspond to, with the start node (in orange) at the dummy site $j = 0$ and the end node (in orange) at the site L (where $L = 5$ in this example). The edges of the graph are labelled by the operator that is being applied to the node it is directed towards. Of course this is only representing a single site, upon which the operator can be applied, whereas we want our **MPO** to have more

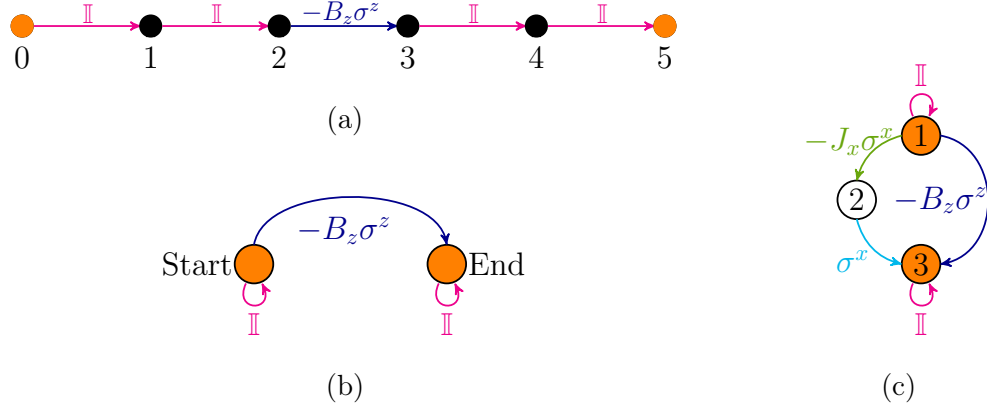


Fig. 3.11 Illustrations of how the MPO formulation can be thought of as a weighted walk. The start and the termination nodes are in orange to highlight them. **(a):** An example of the operator $-B_z \sigma^z$ acting on site three. **(b):** The representation of O_z (in Eq. (3.38)). **(c):** The MPO representation for the whole Hamiltonian in Eq. (3.38).

versatility than this. If we consider the fact that a lot of the actions (operators applied) are the identity, this graph can be written for an on-site density acting on a general site. We form a weighted graph (sometimes called an automaton) which works for an arbitrary number of sites if the lattice is uniform. This is done by having loops of \mathbb{I} as shown in Fig. 3.11b, to represent O_z (from Eq. (3.38)), so that we simply have a path of each possible operator [144]. It should be noted that L steps must be taken from the start node to reach the end node, which is how we recover our L tensors of the operator on each site.

To represent the whole Hamiltonian we also need to add in the nearest-neighbour operators O_{xx} , which will give the full weighted graph shown in Fig. 3.11c. This will require another node as it will in general be $\mathbb{I} \dots \mathbb{I} \otimes (-J_x \sigma^x) \otimes \sigma^x \otimes \mathbb{I} \dots \mathbb{I}$, with one σ_x applied at the site immediately following the previous one. The other subtlety of this method is that the coefficient has to be added into the graph, so for operators acting across sites this can be placed either on the first one to act or on the last. Either formulation can be used, as long as it is used consistently. For example for $-J_x \sum_{j=1}^{L-1} \sigma_j^x \sigma_{j+1}^x$ this can either be written as $\sum_{j=1}^{L-1} (-J_x \sigma_j^x) \sigma_{j+1}^x$ or $\sum_{j=1}^{L-1} \sigma_j^x (-J_x \sigma_{j+1}^x)$. In the graph we have chosen to use the former formulation.

An adjacency matrix can be written from this weighted graph formulation, which makes it much easier to form an MPO. This is simply done by matching

which levels the operator acts between as shown:

$$W = \begin{array}{c} 1 \\ 2 \\ 3 \end{array} \begin{array}{ccc} & 1 & 2 & 3 \\ \left(\begin{array}{ccc} \textcolor{violet}{\mathbb{I}} & 0 & 0 \\ -J_x \sigma^x & 0 & 0 \\ -B_z \sigma^z & \sigma^x & \textcolor{violet}{\mathbb{I}} \end{array} \right) . \end{array} \quad (3.40)$$

Now all that remains is to state the boundary operators which are $Le = [0, 0, 1]$ and $Ri = [1, 0, 0]^T$ to form the complete MPO for the lattice $\mathcal{H}^{MPO} = LeW \dots WRi$ [147].

In order to find the ground state, a variational search to minimise the functional:

$$\epsilon[|\psi\rangle] = \langle \psi | \mathcal{H} | \psi \rangle - \mathcal{L} \langle \psi | \psi \rangle , \quad (3.41)$$

is done, where \mathcal{L} is a Lagrange multiplier which enforces normalisation. The general minimisation is an NP-hard problem so, instead, a local search heuristic is employed, which is either done using a single-site or two-site algorithm [120, 148, 149]. The single-site algorithm has one free site between the two blocks, instead of the two that we have discussed above (see Sec. 3.1.2). It is a convenient representation to avoid getting stuck in a local-minimum and to allow for longer range interactions within the lattice. The procedure is similar to the two-site algorithm except a subspace expansion is also applied. We will focus on the two-site algorithm as this is the one that we will use later on [147, 149]. To be able to perform a local heuristic algorithm we sweep through and calculate an effective Hamiltonian so that we can minimise a pair of states at a time. The procedure is outlined in Alg. 3.3.3 and in Fig. 3.12.

Algorithm 3.3.3 (Two-site Variational minimisation):

- Step 1:** Select the two adjacent sites j and $j + 1$ that the energy is to be minimised on, which occur at the orthogonality center of the chain i.e. have sites $1, \dots, j$ left-normalised and sites $j + 1, \dots, L$ right-normalised.
- Step 2:** Form a tensor of these two sites (contracted) in the MPS called $\Theta_{j,j+1}$.
- Step 3:** Contract the corresponding operators for these two sites to form $W_{j,j+1}$.
- Step 4:** Save the MPS representation of the state and then contract all of the nodes to the left and the right of the ones being updated. This contraction is done by considering the properties in Eq. (3.26) and Eq. (3.33), which when there

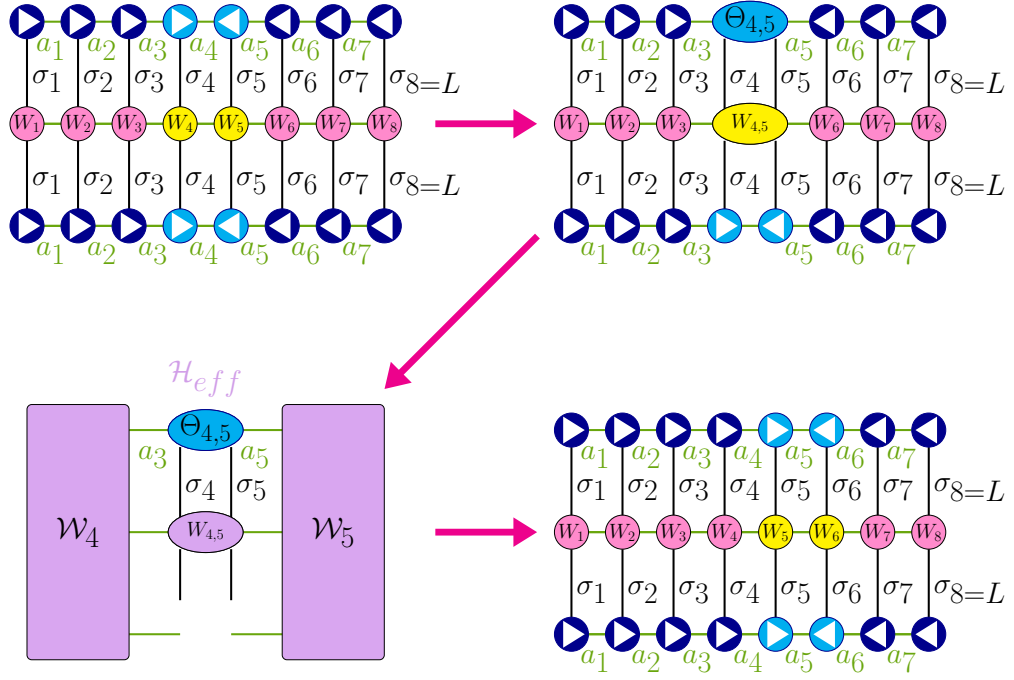


Fig. 3.12 Illustration of the procedure applied within the two-site minimisation procedure for a given pair of sites $j = 4, 5$, where we assume that we are sweeping to the right. The Hamiltonian \mathcal{H} is applied as a tensor of operators, W_j for $j = 1, \dots, L$ (coloured in pink or yellow). In order to highlight the two sites being considered their operators are in yellow and their states in light blue. The triangles show the normalisation as they point to the right for left-normalised (A) matrices and to the left for right-normalised (B) matrices. The effective Hamiltonian, \mathcal{H}_{eff} , is given by the (effective) operators in purple.

is a given operator W_ℓ being applied, can be adapted to:

$$\sum_{\sigma_\ell} A^{\sigma_\ell \dagger} W_\ell A^{\sigma_\ell} = W_\ell, \quad (3.42)$$

$$\sum_{\sigma_\ell} B^{\sigma_\ell} W_\ell B^{\sigma_\ell \dagger} = W_\ell. \quad (3.43)$$

This means that the operators on each side of the two sites being considered can be adjusted to one effective operator, called \mathcal{W}_j and \mathcal{W}_{j+1} after absorbing the Hermitian conjugate of the operators for the state at site j and $j + 1$. The combination of \mathcal{W}_j , \mathcal{W}_{j+1} and $W_{j,j+1}$ form the effective Hamiltonian \mathcal{H}_{eff} to be applied to $\Theta_{j,j+1}$.

Step 5: Solve the eigenvalue problem of:

$$\mathcal{H}_{eff} \Theta_{j,j+1} = E \Theta_{j,j+1}, \quad (3.44)$$

using an appropriate method (see Sec. 3.1.1). Retain the state corresponding to the minimum eigenvalue, which is the new state $\tilde{\Theta}_{j,j+1}$.

- Step 6:** Perform the SVD on $\tilde{\Theta}_{j,j+1}$ to obtain the two left-normalised (right-normalised) MPS matrices if sweeping right (left) and truncate the retained singular values to χ . Load the previous network for all the other sites (sites $1, \dots, j-1, j+1, \dots, L$).
- Step 7:** Continue with the sweep, by repeating steps 1-6 moving forwards (backwards) through the chain for a right (left) sweep until a given sweep is completed and the convergence criterion has been reached.
-

3.3.5 Symmetries and Conserved quantities within MPS

Very often in quantum mechanics, the Hamiltonian is symmetric under a group of transformations. The use of these symmetries can largely improve the performance of numerical algorithms for finding the ground state of strongly correlated systems [120]. If the Hamiltonian commutes with an operator, this implies they both can share the same eigenbasis. This in turn, means that the ground state (eigenstate) of the Hamiltonian will also be an eigenstate of the conserved operator, resulting in a global physical symmetry in the system. This enables us to keep track of the quantum numbers used through the MPS.

Abelian symmetries such as $\mathbb{U}(1)$ symmetries for charge or magnetisation are the ones that have been used the most extensively [120]. To explain how the conservation of an operator can be exploited in an MPS implementation, we will provide an example using the magnetisation operator, M , where the total magnetisation $M = \sum_i \sigma_i^z$ commutes with a given Hamiltonian \mathcal{H} ($[\mathcal{H}, M] = 0$), such that the eigenstates of \mathcal{H} can be chosen as the eigenstates of M . If we use the constraint that all states must have magnetisation as a good quantum number, then this means that we can exclude a large number of coefficients from the calculation, resulting in speed-up. The fact that the states are eigenstates of the magnetisation operator, means that the eigenstates of the reduced density matrix will also be. As a result, the conservation of the relevant quantum numbers requires that some elements of the tensors representing the MPS are always zero. By ordering the tensor indices suitably the elements of the density matrix can, therefore, be decomposed into blocks, where each block possesses a given quantum number.

3.4 Comparison of Methods

In order to summarise the adaptations of the [MPS](#) and [DMRG](#) methods that have been used in this thesis, we will compare the performance of a few different implementations. We assume that we have a [1-D](#) lattice of L sites, which contains bosons. A restriction is placed so that only $n_{\max} = 4$ bosons are allowed at each site, which means that the local dimension of the Hilbert space for each site is $d = 5$. We also assume that we have unit filling, i.e. the number of particles is equal to the length of the lattice, such that $N = L = 10$. The energy of this model is described by the Bose-Hubbard Hamiltonian which is introduced in the previous chapter (see Sec. [2.2.2](#)):

$$\mathcal{H}_{BH} = -J \sum_{j=1}^{L-1} b_j^\dagger b_{j+1} + \frac{U}{2} \sum_{j=1}^L n_j(n_j - 1). \quad (3.45)$$

The aim of this exercise is to compute and compare how well the energy and the measure of on-site density perform depending on the implementation used. We will also examine the computational time taken to obtain these results.

3.4.1 Non-MPS DMRG implementation

The first method in our comparison is done using an implementation of [DMRG](#) without the [MPS](#) ansatz, called Powder with Power ([PwP](#)), realised by De Chiara et al. [127]. This performs the infinite system [DMRG](#) method to build the system up to its size whilst already minimising the energy and then uses the finite DMRG after the required length L is reached. It is advantageous to initially build the length up using the infinite DMRG algorithm because this provides a reasonable approximation, which is close to the minimal energy for a uniform chain. This method needs to be used with caution if there is a deep local minimum in the system because this can lead to the state being trapped within this minimum. In this approach, it is assumed that we only have a short-range Hamiltonian, meaning that the matrix of the Hamiltonian is sparse. A sparse-matrix eigensolver method is then appropriate. The Jacobi-Davidson method is used [129]. The algorithm to perform [DMRG](#) is coded in Fortran 95. The information that needs to be retained is reduced by using symmetries. A global reflection symmetry is used for uniform systems to obtain block \mathcal{B} as a mirror of block \mathcal{A} . A $\mathbb{U}(1)$ symmetry is also used to conserve the particle number throughout the system. In order to calculate the accuracy of results a discarded weight is used. This is calculated by summing the

discarded eigenvalues (square of the singular values) in the system:

$$\epsilon_{trunc} = \left(\sum_{j>\chi} \lambda_j \right). \quad (3.46)$$

3.4.2 MPS DMRG implementations

There are three different implementations of **DMRG** in the **MPS** ansatz that have been considered in this thesis. These are referred to as “OSMPS”, “TNT” and “Independent MPS”. The first, open source matrix product states (**OSMPS**) is a method available from L. Carr, D. Jaschke and M. Wall at Colorado School of Mines [149, 150], which has a user interface in Python but the bulk of the functions are coded in Fortran2003. Another open source code is the tensor network theory (**TNT**) Library which is a collection of code set up by S. Al-Assam, S. R. Clark and D. Jaksch at the University of Oxford [147]. This uses MATLAB/OCTAVE as a user-interface and then C for the main functions. Lastly, the one that we call “Independent **MPS**” is a private code that is an adaptation of the **PwP** described above in **MPS** form [151]. This is based on a flexible Abelian Symmetric Tensor Networks Library, which was developed as a collaboration between M. Rizzi, A. Haller at Johannes Gutenberg Universität and the group of S. Montangero at Universität Ulm (now at University of Padua).

Firstly, I will focus on the build method used in each model. For this I will assume that we are only going to be looking at a lattice which is uniformly filled with one particle per site. The details covered about each method are also summarised in the Table. **3.1. OSMPS** starts with one particle per site and uses an infinite **DMRG** method to obtain a good approximation for a given length L . **TNT** Library and “Independent **MPS**” start with either a randomised or a unit filled initial setup. All of the methods use a two-site variational minimisation for energy minimisation within the **DMRG** algorithm (as described above in Sec. 3.3.4), but **TNT** also has the availability of the single-site minimisation [147, 149]. The eigensolver routine used differs in each case. **TNT** Library and **OSMPS** both use the linear algebra libraries *linear algebra package* (**LAPACK**), basic linear algebra subprograms (**BLAS**) and the *Arnoldi package* (**ARPACK**). **ARPACK** has the availability of using variants on the Arnoldi and the Lanczos methods [129, 152]. **TNT** uses whichever one is appropriate, whereas **OSMPS** uses the Lanczos sparse eigensolver method [129, 153]. For the “Independent **MPS**” the Arnoldi scheme is also used. Another important part in the speedup of each code is to make use of symmetries, “Independent **MPS**”, **TNT** and **OSMPS** all use $U(1)$ symmetry to conserve the number of particles.

Table 3.1 Summary of the methodology used within each of the implementations of **DMRG** within our comparison.

Method	Using MPS	infinite system DMRG used	Symmetries used	Eigensolver Method
PwP	X	✓	$\mathbb{U}(1)$	Jacobi-Davidson
TNT	✓	X	$\mathbb{U}(1)$	ARPACK
OSMPS	✓	✓	$\mathbb{U}(1)$	Lanczos
Independent MPS	✓	X	$\mathbb{U}(1)$	Arnoldi

Each of these methods also has their own way of checking the error of the estimates made. **TNT** Library takes the ℓ^2 norm of the discarded weights:

$$\epsilon_{trunc}^{TNT} = \sqrt{\left(\sum_{j>\chi} \lambda_j^2\right)}. \quad (3.47)$$

“Independent **MPS**” also keeps track of what is discarded but instead of using the discarded weights it uses the sum of the discarded probability p_j :

$$\epsilon_{trunc}^{IndMPS} = 1 - \sum_{j=1}^{\chi} p_j, \quad (3.48)$$

meaning that $0 \leq \epsilon_{trunc}^{IndMPS} \leq 1$. **OSMPS** instead uses a variance-like measure ϵ_{var} between the Hamiltonian represented as an **MPO** and the energy obtained from **DMRG**:

$$\epsilon_{var} = \langle \psi | (\mathcal{H}^2 - \langle \mathcal{H} \rangle^2) | \psi \rangle. \quad (3.49)$$

In order to compare the performance of these methods, we plot a few key values. The first measure that we calculate is the ground state energy of the **BH** Hamiltonian described in Eq. (3.45) with length $L = 10$. We place a few other restrictions on the code to make the comparison as fair as possible. Each method is allowed a maximum of five **DMRG** sweeps and any inbuilt tolerances have been set to the same threshold. As the length chosen is a relatively small one, we use a very small χ so that the inaccuracy that can occur from discarding too much, is evident. In Fig. 3.13a it is clear that the energy is far off in all methods for $\chi < 4$ but once it reaches n_{\max} it becomes a much better estimate, as at least then it has the capability to match the physical dimension in the **MPS**. There is very little to distinguish between the methods once they pass $\chi = 4$, which is not surprising given that the energy is the check for convergence in all cases. It should, however, be noted that the energy has only converged up to $O(10^{-3})$ because of how small χ is.

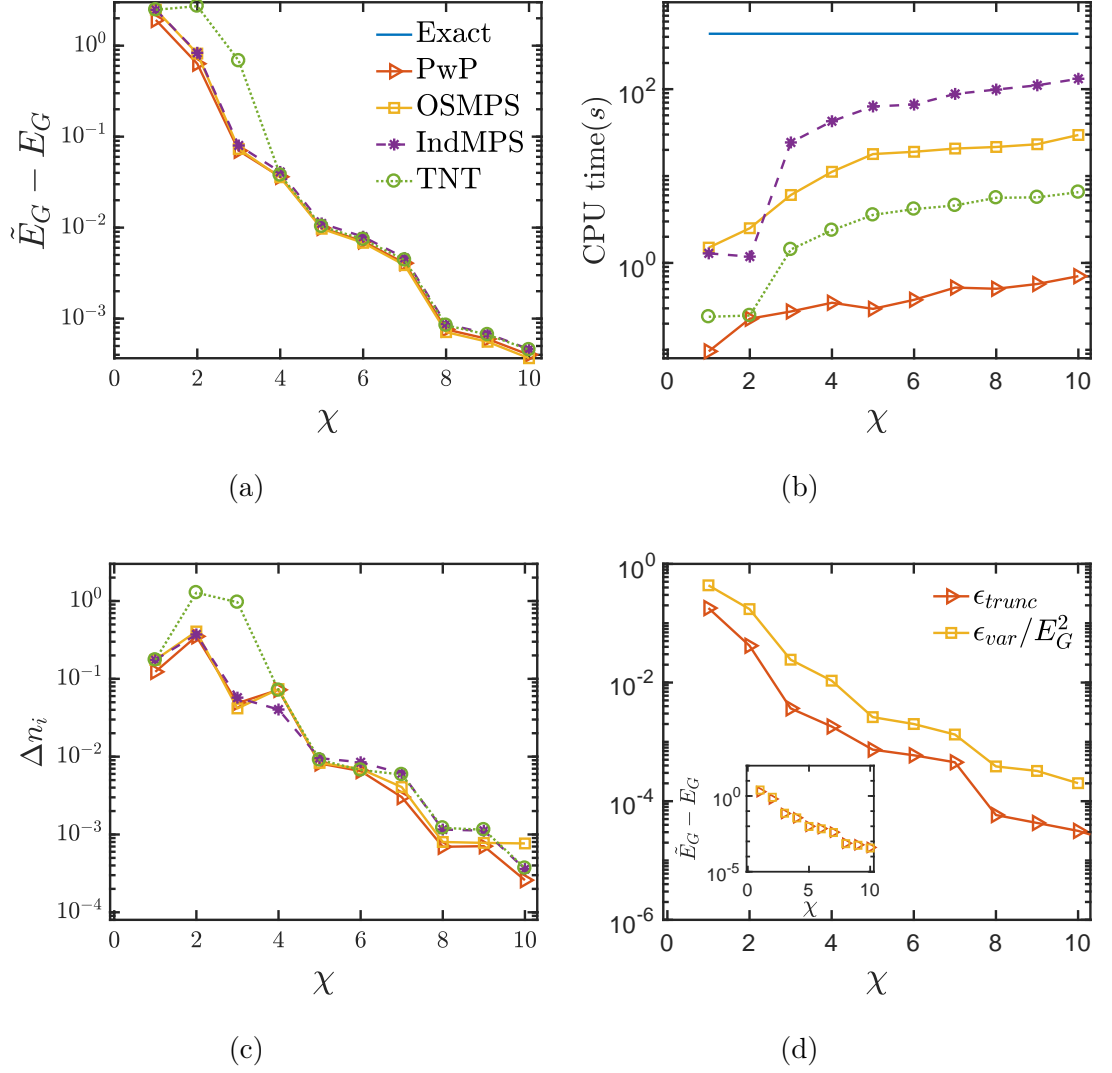


Fig. 3.13 Comparison of how different implementations of **DMRG** perform against the truncation χ when finding the ground state for a chain of length $L = 10$. The methods being compared are **PwP**, which does not explicitly use **MPS** and then **OSMPS**, IndMPS- “Independent **MPS**” and **TNT** Library, which all use **MPS**. A comparison is shown of **(a)** the energy difference of the approximate energy \tilde{E}_G minus the exact E_G and **(b)** the time taken for the different methods. **(c)** shows the ℓ^2 norm of the error of the on-site density $\Delta n_i = ||\langle \tilde{n}_i \rangle - \langle n_i \rangle||$ and finally **(d)** illustrates the measure of error provided by the methods **PwP** and **OSMPS** with the actual error in the energy in the inset.

The optimisation of the time taken to perform each method also has a considerable impact once longer and more complex lattices are considered. In our simple example we have included the time that it takes us to perform the exact diagonalisation (ED) calculation to obtain the measures. This is using an optimisation procedure [154] and is carried out in MATLAB. In fairness this time can be slightly sped up by using parallelisation or by using Fortran. For such a simple calculation it is still clear that despite the initial set-up of the DMRG, in particular DMRG in MPS form it is undoubtedly worth it in speed-up. It should also be noted that ED becomes increasingly more difficult and then impossible as the dimension of the system is increased, whereas the DMRG methods will work for a much larger system size before facing the same difficulty.

It is unsurprising that OSMPS is one of the longest performing methods due to the fact that it has both the initial build with the infinite system DMRG and the MPS notation to implement. It is also unsurprising that PwP takes the least time to complete as it not only uses symmetries to build one block from the other but it also has none of the overhead of the MPS routines. What may seem surprising, however, is that the “Independent MPS” takes longer than the OSMPS method. This might be because setting the tolerance at the same threshold as the others in this method is actually an overkill, because the algorithm adapts the precision as it goes along. It should also be noticed that using these methods for such a small system which can be done exactly, does them a disservice as it does not make their full capability clear. The main advantage of these methods comes for systems when the Hilbert space describing them becomes larger.

We also compare each method’s estimation of an expectation value using the on-site density, $\langle n_i \rangle = \langle \psi | n_i | \psi \rangle$, which is shown in Fig. 3.13c. For this we have chosen to use the ℓ^2 norm of the error $\Delta n_i = ||\langle \tilde{n}_i \rangle - \langle n_i \rangle|| = \sqrt{\sum_i (\langle \tilde{n}_i \rangle - \langle n_i \rangle)^2}$ as an estimate, where $\langle \tilde{n}_i \rangle$ is the estimated on-site density of site i and $\langle n_i \rangle$ is the exact one. We have chosen this measure as the main error occurs at the boundary sites, which typically does not alter the measures in the bulk for a lattice of sufficient length. Instead we have chosen a measure which illustrates the accuracy on the majority of the sites, without giving much weight to a few more extreme values. It is plain to see in Fig. 3.13c that the estimate is reasonable for $\chi > 4$, which is unsurprisingly the same value that the accuracy of the energy improved for.

Lastly, to give an example of how each method measures its error we compare the two models that have an initial build step, PwP and OSMPS. As OSMPS uses ϵ_{var} in Eq. (3.49), which is a measure of the variance and in units of the energy squared, we divide this by the exact square of the energy so that it can be compared to the discarded weight estimate that PwP uses ϵ_{trunc} (Eq. (3.46)). These are plotted against each other in Fig. 3.13d and unsurprisingly the estimated

error decreases as χ increases. It can be seen that both indicators of the error follow the same trend, which also matches the error of the energy in each method shown in the inset.

3.5 Conclusions

The use of the MPS ansatz has greatly improved our numerical capabilities in representing and analysing a 1-D many-body system. There are a number of efficient methods to find the ground state within this ansatz, where arguably the most prominent is the DMRG method. Within each of these methods, there are a number of implementations that can be optimised depending on the model and measures of choice. For simple models, these all perform comparatively well to each other as we have demonstrated by performing BH model simulations with a few implementations.

HAPTER

COMPUTATIONAL METHODS FOR SIMULATIONS OF TIME DYNAMICS

*“A computation is a process that
obeys finitely describable rules.”*

Rudy Rucker

In the previous chapter, we have given a summary of some of the key methods used to obtain the ground state properties of a given lattice system. In this chapter, we will instead examine methods that can be used to perform time dynamics on a given state under a system Hamiltonian. The dynamics of correlated quantum systems provides a rich area of study for non-equilibrium physics. Analysing the non-equilibrium physics can, however, be very challenging both with experimental and theoretical approaches. There have been a number of advancements in tensor network methods equipped to study the dynamics of the system [155]. We will focus on describing a few of these methods within this chapter.

In general, the study of dynamics will involve finding the evolved state under a given Hamiltonian, starting from a given initial state $|\psi(0)\rangle$. For simplicity, we will assume that this Hamiltonian is time-independent and will call it $\tilde{\mathcal{H}}$ to distinguish it from the Hamiltonian employed for the analysis of the ground state properties. It should be noted that despite our assumption some of the methods we will examine are equipped to handle a time-dependent Hamiltonian, as will be pointed out. The evolution of a closed system can be described by Schrödinger’s time-dependent equation [156] for a given time t :

$$i\hbar \frac{\partial |\psi(t)\rangle}{\partial t} = \tilde{\mathcal{H}}|\psi\rangle , \quad (4.1)$$

where $\tilde{\mathcal{H}}$ is the Hamiltonian of the system, \hbar is the reduced Planck's constant, which we assume is set as $\hbar = 1$, and $|\psi\rangle$ is the wave function. This can be adapted to a different form which occurs with the assumption that a time evolution is a unitary system:

$$|\psi(t)\rangle = e^{-i\tilde{\mathcal{H}}t}|\psi(0)\rangle, \quad (4.2)$$

where $\tilde{\mathcal{H}}$ is the time-evolving Hamiltonian, $|\psi(t)\rangle$ is the time-evolved state and $|\psi(0)\rangle$ is the initial state we start with (at $t = 0$). We will denote T as the total time we require.

4.1 Suzuki-Trotter Decomposition

A common decomposition used to assist with the time-evolution of the system is the Suzuki-Trotter decomposition. This provides a useful way to split/estimate the exponential of the Hamiltonian that is used in the time evolution. It is especially useful for lattices that only have next-neighbour interactions and where the Hamiltonian is time-independent.

It is commonplace to discretise the total time into smaller intervals of length δt . Supposing that we require a state after time T , $|\psi(T)\rangle$, then we need to calculate the time evolution operator:

$$\mathcal{U} = e^{-i\tilde{\mathcal{H}}T}. \quad (4.3)$$

Assuming that $T = n\delta t$, then the unitary evolutions operator takes on the form:

$$\mathcal{U} = e^{\sum_{j=1}^n -i\tilde{\mathcal{H}}\delta t} = \prod_{j=1}^n e^{-i\tilde{\mathcal{H}}\delta t}. \quad (4.4)$$

Assuming that the Hamiltonian $\tilde{\mathcal{H}}$ only has nearest-neighbour interactions, the unitary operator can be expressed using the first-order Suzuki-Trotter decomposition [157, 158] as:

$$\begin{aligned} \mathcal{U} &= e^{-i\tilde{\mathcal{H}}T} = \left(e^{-i\tilde{\mathcal{H}}\delta t} \right)^n \\ &\approx \left(\prod_{\ell=1}^{L-1} e^{-i\tilde{\mathcal{H}}(\ell, \ell+1)\delta t} \right)^n, \end{aligned} \quad (4.5)$$

where $\tilde{\mathcal{H}}(\ell, \ell+1)$ contains the interaction terms between the sites ℓ and $\ell+1$ and the local terms on these sites as well. The error within this approximation is due to the non-commutativity of the bond Hamiltonians, i.e. $[\tilde{\mathcal{H}}(\ell, \ell+1), \tilde{\mathcal{H}}(\ell+1, \ell+2)] \neq 0$, in general. The more steps n , and therefore the smaller that δt is, the more accurate this approximation is.

There are also higher order versions of the Suzuki-Trotter decomposition, such as the second-order one, which essentially splits the operators into even and odd components between sites [127, 159]. The even operator is formed of only even (ℓ_e) bonds, $F = \sum_{\ell_e} \tilde{\mathcal{H}}(\ell_e, \ell_e + 1)$ and an odd operator is formed of only odd (ℓ_o) bonds, $G = \sum_{\ell_o} \tilde{\mathcal{H}}(\ell_o, \ell_o + 1)$. The terms F and G commute meaning that an even-odd expansion can be performed giving us the second-order Trotter decomposition:

$$e^{-i\tilde{\mathcal{H}}T} \approx \left(e^{-iF\frac{\delta t}{2}} e^{-iG\delta t} e^{-iF\frac{\delta t}{2}} \right)^n. \quad (4.6)$$

4.2 Time-dependent Density Matrix Renormalisation Group

There is an adaptation of the [DMRG](#) method called time-dependent density matrix renormalisation group ([tDMRG](#)) which is applicable for performing time evolution on a given state. The first implementation of this was introduced by M. A. Cazalilla and J.B. Marston [160], which prompted a number of improvements and adaptations on it [161, 162]. In general, a finite version of [DMRG](#) (see Ch. 3) is performed first in order to obtain an initial state $|\psi(0)\rangle$ of the time evolution. It should be noted that this state does not have to be found using the evolving Hamiltonian $\tilde{\mathcal{H}}$, i.e. it is not necessarily $|\psi_G\rangle$ of $\tilde{\mathcal{H}}$ but may be a ground state of an entirely different Hamiltonian. This algorithm makes use of a Suzuki-Trotter decomposition to express the unitary evolution operator $\mathcal{U} = e^{-i\tilde{\mathcal{H}}T}$ as shown in Eq. (4.5). The procedure works as outlined below in Algorithm 4.2.1.

Algorithm 4.2.1 (tDMRG):

Initial Step

Step 0: Form the initial state $|\psi(0)\rangle$ using the finite [DMRG](#) procedure.

For $\ell = 1, \dots, L - 1$

Step 1: Perform the finite [DMRG](#) procedure but apply the operator $\mathcal{U}_{(\ell, \ell+1)} = e^{-i\tilde{\mathcal{H}}^{(\ell, \ell+1)}\delta t}$ at each step on the free sites ℓ and $\ell + 1$ instead of diagonalising to find the ground state energy as shown in Fig. 4.1.

Step 2: Renormalise, as done in the finite [DMRG](#) method and save to memory the matrices describing the blocks.

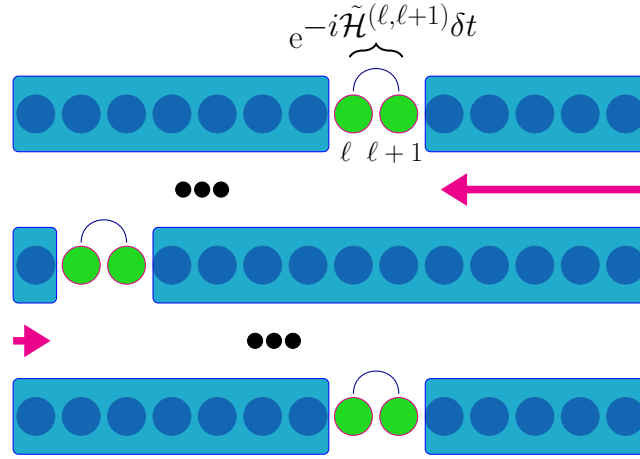


Fig. 4.1 Illustration of the adaptation of the finite [DMRG](#) method to implement the [tDMRG](#) method, where the operator $\mathcal{U}_{(\ell,\ell+1)} = e^{-i\tilde{\mathcal{H}}^{(\ell,\ell+1)}\delta t}$ is applied to the free sites (green circles). The sweeps are carried out in the same manner as the finite procedure, with the blocks (blue rectangles) being expanded and contracted.

Step 3: Update the truncated basis being used to express the instantaneous state, for example, use a state prediction transformation as prescribed by White [163].

Final check

Step 4: Repeat steps 1-4 until this has been carried out n times in order to give the final time $T = n\delta t$.

An important restriction on this is that the initial finite-size [DMRG](#) will have chosen a specific subspace of the Hilbert space which is relevant for the ground state. As we time-evolve, the state will typically leave this initial subspace meaning that in order to improve the accuracy, the algorithm needs to adapt the subspace chosen as it evolves as well. One way to avoid this is to increase the truncation χ [160] but this is not very efficient. A much better approach is to directly choose the subspace based on the current time state i.e. on $|\psi_{t+\delta t}\rangle$ for some time $t < T$ [127] which is what we have pointed to in Step 3.

The features that can cause difficulty in obtaining accurate results with this method, are the amount of truncation and how well the adaptation to the subspace works. There is also the restriction that with the Trotter decomposition this only works for nearest-neighbour lattices. We will now examine a time-evolution method, which is within the [MPS](#) ansatz.

4.3 Time Evolving Block Decimation (TEBD)

The method of time evolution block decimation (TEBD) was developed between 2003-2004 to perform time simulations in both the MPS ansatz and for the original DMRG algorithm. It was first introduced by Vidal [164, 165] as an approach to illustrate the amount of entanglement that needs to be stored for quantum computations. This uses an approach, which in many ways is similar to the DMRG methods, in order to perform an efficient time evolution. A direct incorporation of this within the DMRG procedure is equivalent to the tDMRG algorithm but expressed in the MPS ansatz [161].

4.3.1 MPS in Vidal's Notation

To perform the TEBD procedure, it is more convenient to write the MPS in a different notation which was first introduced by Vidal [164, 165]. Vidal's form is the Lambda-Gamma form, which comes quite naturally from the SVD procedure which we use to form a state in the MPS ansatz. The Λ are diagonal matrices which represent the singular value matrices \mathbf{S} and then Γ corresponds to either the \mathbf{U} or \mathbf{V}^\dagger matrices depending on the normalisation used. For example, if we perform left-normalisation using Alg. 3.3.1, then we have a state of the form:

$$|\psi\rangle = \sum_{a_1, \dots, a_\ell} \sum_{\sigma_1, \dots, \sigma_L} A_{1,a_1}^{\sigma_1} A_{a_1,a_2}^{\sigma_2} \dots A_{a_{L-1},1}^{\sigma_L} |\sigma_1 \dots \sigma_L\rangle, \quad (4.7)$$

where

$$c_{\sigma_1, \dots, \sigma_L} = \sum_{a_1, \dots, a_\ell} A_{1,a_1}^{\sigma_1} A_{a_1,a_2}^{\sigma_2} \dots A_{a_{L-1},1}^{\sigma_L}. \quad (4.8)$$

This can be equivalently written in Vidal's form as:

$$c_{\sigma_1, \dots, \sigma_L} = \sum_{a_1, \dots, a_{L-1}} \Gamma_{a_1}^{[1]\sigma_1} \Lambda_{a_1}^{[1]} \Gamma_{a_1 a_2}^{[2]\sigma_2} \Lambda_{a_2}^{[2]} \dots \Gamma_{a_{L-2} a_{L-1}}^{[L-1]\sigma_{L-1}} \Lambda_{a_{L-1}}^{[L-1]} \Gamma_{a_{L-1} 1}^{[L]\sigma_L}, \quad (4.9)$$

where the site number is included in square brackets and the a_j and σ_j are once again the internal matrix dimensions and physical dimensions, respectively [159, 161].

For TEBD, we will assume that we have a system bipartitioned in a Schmidt decomposition at the site ℓ and $\ell + 1$, i.e. we assume that our system is left-normalised from $j = 1, \dots, \ell - 1$ and that it is right normalised from $j = \ell + 1, \dots, L$. The remaining two sites ℓ and $\ell + 1$ are the free sites of the system. In other words, we assume that our MPS state is the following:

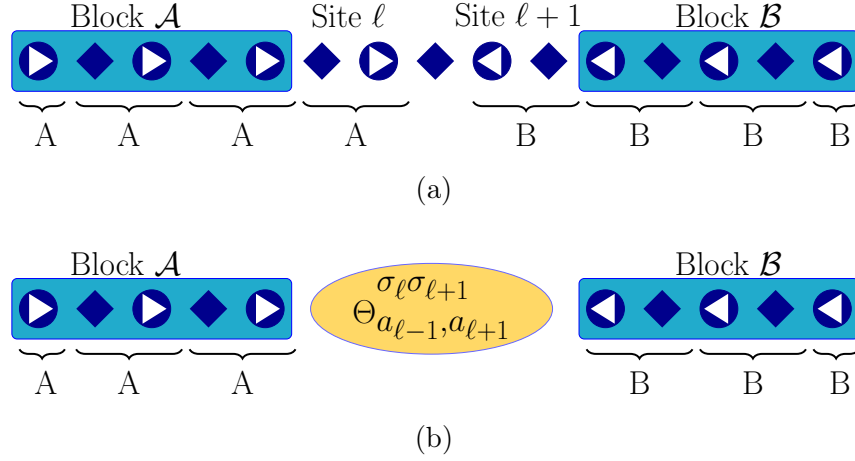


Fig. 4.2 An illustration of Vidal's form of the MPS with two free sites. The diamonds are the singular values (Λ), whereas the circles represent the Γ s. (a) shows the original mixed MPS setup, whereas in (b) the tensor $\Theta_{a_{\ell-1}, a_{\ell+1}}^{\sigma_{\ell} \sigma_{\ell+1}}$ (defined in Eq. (4.12)) has been formed from the free sites.

$$|\psi\rangle = \sum_{\substack{a_{\ell-1}, a_{\ell}, a_{\ell+1} \\ \sigma_{\ell}, \sigma_{\ell+1}}} \Lambda_{a_{\ell-1}}^{[\ell-1]} \Gamma_{a_{\ell-1}, a_{\ell}}^{[\ell] \sigma_{\ell}} \Lambda_{a_{\ell}}^{[\ell]} \Gamma_{a_{\ell}, a_{\ell+1}}^{[\ell+1] \sigma_{\ell+1}} \Lambda_{a_{\ell+1}}^{[\ell+1]} \left| \Theta_{a_{\ell-1}}^{[1, \dots, \ell-1]} \right\rangle \otimes |\sigma_{\ell} \sigma_{\ell+1}\rangle \otimes \left| \Theta_{a_{\ell+1}}^{[\ell+1, \dots, L]} \right\rangle, \quad (4.10)$$

where the kets have been written to make the two subsystems clear. $\left| \Theta_{a_{\ell-1}}^{[1, \dots, \ell-1]} \right\rangle$ corresponds to the **A** matrices up to this site and $\left| \Theta_{a_{\ell+1}}^{[\ell+1, \dots, L]} \right\rangle$ corresponds to the **B** matrices. In fact it can be seen that this equation is exactly the same as the mixed MPS formation (Eq. (3.37)), except we have not summed over the indices $\ell - 1$ and $\ell + 1$ and it is expressed in a different form. In other words, this corresponds to Eq. (3.37) in the following form:

$$c_{\sigma_1 \dots \sigma_L} = \sum_{a_{\ell-1}, a_{\ell}, a_{\ell+1}} (A^{\sigma_1} A^{\sigma_2} \dots A^{\sigma_{\ell-1}})_{a_{\ell-1}} A_{a_{\ell-1}, a_{\ell}}^{\sigma_{\ell}} S_{a_{\ell}, a_{\ell+1}} B_{a_{\ell}, a_{\ell+1}}^{\sigma_{\ell+1}} (B^{\sigma_{\ell+2}} \dots B^{\sigma_L})_{a_{\ell+1}}. \quad (4.11)$$

This formulation is illustrated in Fig. 4.2a. If we call the coefficients of the free sites $\Theta_{a_{\ell-1} a_{\ell+1}}^{\sigma_{\ell} \sigma_{\ell+1}}$, then, as shown in Fig. 4.2b we obtain:

$$\Theta_{a_{\ell-1} a_{\ell+1}}^{\sigma_{\ell} \sigma_{\ell+1}} = \sum_{a_{\ell}} \Lambda_{a_{\ell-1}}^{[\ell-1]} \Gamma_{a_{\ell-1}, a_{\ell}}^{[\ell] \sigma_{\ell}} \Lambda_{a_{\ell}}^{[\ell]} \Gamma_{a_{\ell}, a_{\ell+1}}^{[\ell+1] \sigma_{\ell+1}} \Lambda_{a_{\ell+1}}^{[\ell+1]}, \quad (4.12)$$

meaning that Eq. (4.10) can be rewritten:

$$|\psi\rangle = \sum_{a_{\ell-1}, a_{\ell}, a_{\ell+1} \sigma_{\ell}, \sigma_{\ell+1}} \Theta_{a_{\ell-1} a_{\ell+1}}^{\sigma_{\ell} \sigma_{\ell+1}} \left| \Theta_{a_{\ell-1}}^{[1, \dots, \ell-1]} \right\rangle \otimes |\sigma_{\ell} \sigma_{\ell+1}\rangle \otimes \left| \Theta_{a_{\ell+1}}^{[\ell+1, \dots, L]} \right\rangle. \quad (4.13)$$

4.3.2 TEBD method

As well as expressing the bipartitioned state in Vidal's notation, we also need to express the evolution operator in a form compatible with applying it on the free sites. As we did in the [tDMRG](#) method, we will focus on the two free sites when we perform our evolution. If we use the Suzuki-Trotter decomposition in Eq. (4.5), this lends itself quite naturally to splitting \mathcal{U} into an operator which applies to two sites at a time. Within the [MPS](#) notation, the portion of \mathcal{U} , which only applies on the two free sites, will be labelled using the physical indices as: $\mathcal{U}_{\sigma'_\ell \sigma'_{\ell+1}}^{\sigma_\ell \sigma_{\ell+1}} = e^{(-i\tilde{H}(\ell, \ell+1)\delta t)}$. We will call this operator \mathcal{V} and it will only apply to the physical sites $|\sigma_\ell\rangle$ and $|\sigma_{\ell+1}\rangle$ (and their transpose). It will, therefore, have the effect $\mathcal{V} = \sum_{\sigma_\ell, \sigma_{\ell+1}, \sigma'_\ell, \sigma'_{\ell+1}} \mathcal{U}_{\sigma'_\ell \sigma'_{\ell+1}}^{\sigma_\ell \sigma_{\ell+1}} |\sigma_\ell \sigma_{\ell+1}\rangle \langle \sigma'_\ell \sigma'_{\ell+1}|$ where only the physical indices are included as the others remain unchanged.

Algorithm 4.3.1 (TEBD Procedure):

For $\ell = 2, \dots, L - 1$:

Step 1: Form Θ from Γ s and Λ s using Eq. (4.12) .

Step 2: Update $\Theta_{a_{\ell-1}a_{\ell+1}}^{\sigma_\ell \sigma_{\ell+1}}$ by applying the evolution operator \mathcal{V} :

$$\begin{aligned} \tilde{\Theta}_{a_{\ell-1}a_{\ell+1}}^{\sigma_\ell \sigma_{\ell+1}} &= \sum_{\sigma'_\ell, \sigma'_{\ell+1}} \mathcal{V}_{\sigma'_\ell, \sigma'_{\ell+1}}^{\sigma_\ell, \sigma_{\ell+1}} \Theta_{a_{\ell-1}a_{\ell+1}}^{\sigma_\ell \sigma_{\ell+1}} \\ &= \sum_{\tilde{a}_\ell} \Lambda_{a_{\ell-1}}^{[\ell-1]} \tilde{\Gamma}_{a_{\ell-1}\tilde{a}_\ell}^{[\ell]\sigma_\ell} \Lambda_{\tilde{a}_\ell}^{[\ell]} \tilde{\Gamma}_{\tilde{a}_\ell a_{\ell+1}}^{[\ell+1]\sigma_{\ell+1}} \Lambda_{a_{\ell+1}}^{[\ell+1]} \end{aligned} \quad (4.14)$$

Step 3: Reshape $\tilde{\Theta}_{a_{\ell-1}a_{\ell+1}}^{\sigma_\ell \sigma_{\ell+1}}$ so that it is a $\chi d \times \chi d$ matrix, i.e. form $\tilde{\Theta}_{a_{\ell-1}\sigma_\ell, a_{\ell+1}\sigma_{\ell+1}}$.

Step 4: Perform an [SVD](#) on the $\tilde{\Theta}_{a_{\ell-1}\sigma_\ell, a_{\ell+1}\sigma_{\ell+1}}$, retaining only the largest χ singular values $\tilde{\Lambda}_{a_\ell}^{[\ell]}$.

Step 5: In principal, divide out the previous values of $\Lambda^{[\ell]}$ and $\Lambda^{[\ell+1]}$ in order to compute $\tilde{\Gamma}^\ell$ and $\tilde{\Gamma}^{\ell+1}$ from the matrix elements obtained via [SVD](#) but the division is not numerically stable when $\Lambda^{[\ell]}$ and $\Lambda^{[\ell+1]}$ are small and therefore the division is omitted.

This algorithm makes use of [MPS](#) to focus on a reduced set when finding the wave function $|\psi(t)\rangle$. A key advantage of the method is that it reselects the subspace it is working in as it evolves in time, rather than being rigidly restricted to an initial one, which means that its approximations are more accurate as

the eigenvectors chosen represent the current time. This also makes use of the Suzuki-Trotter decomposition on the evolution operator in order to be able to effectively time evolve a system [120, 161, 166].

TEBD is a very powerful tool and there are still recent advancements working to improve the speedup and other aspects of the algorithm [166, 167]. A major drawback of **TEBD**, however, is that it only works well for a Hamiltonian of nearest-neighbour terms. There are some adaptations that allow for longer interactions but they involve a more complicated procedure to extend this method and attempts to do so can lead to poor scaling [168, 169].

4.4 Time-Dependent Variational Principle (TDVP)

An alternative method using **MPS** which does not restrict us to nearest-neighbour interactions is the time dependent variational principle (**TDVP**) [170, 171]. As previously stated, we are required to redefine the subspace as the time-evolving state leaves the subspace of the initial (typically ground) state. **TDVP** finds a new subspace to time-evolve with, by projecting the right-hand side of the Schrödinger equation, $\tilde{\mathcal{H}}|\psi\rangle$ (from Eq. (4.1)), onto the tangent space of the single-site MPS manifold, which is the space spanned by variations of single MPS tensors, called $T_{|\psi\rangle}$:

$$\frac{d|\psi\rangle}{dt} = -iP_{T_{|\psi\rangle}}\tilde{\mathcal{H}}|\psi\rangle . \quad (4.15)$$

The projector $P_{T_{|\psi\rangle}}$ can be applied to an arbitrary state $|\Upsilon\rangle$ in the Hilbert space and is such that $P_{T_{|\psi\rangle}}|\Upsilon\rangle$ is an **MPS** tangent vector $|\Phi\rangle$, which can be characterised by $\langle\Phi'|\Phi\rangle = \langle\Phi'|\Upsilon\rangle$ for any other tangent vector $|\Phi'\rangle$. In this way, the general formation of **TDVP** differs from **TEBD**, which is aimed at estimating only the time evolution operator. **TDVP** is instead aimed at directly improving the approximation of the action of the evolution operator onto the state $|\psi\rangle$. The motivation behind this is to constrain the time evolution to a specific manifold of **MPS** of a given initial bond dimension. This means that the evolution never leaves the manifold of the Hilbert space that we are focusing on.

Our focus will be on a version of **TDVP**, where the tangent space of a projector is split in order to act procedurally on the sites [172]. In the case of nearest-neighbours, this very closely matches **tDMRG**, where a Suzuki-Trotter splitting of the tangent space can be used. This can be performed using a single-site or a pair of sites update procedure, but only the two-site variant allows for flexibility in the bond dimension. In the single-site case, despite the fact that Eq. (4.15) spans the whole Hilbert space, the differential equation obtained for a single term of the right hand side is exactly integrable. We will focus on the two-site variation,

which enables the dynamical adaptation of the bond dimension and which closely resembles [DMRG](#) and [TEBD](#). In this case, the projection will have a different form as it projects onto the two-site tangent space, which cannot be as easily expressed as a differential equation due to the fact that this necessarily requires finite time steps δt .

A projector is applied to the linear space of the free two-site variations, which is the effective two-site version of $-i\tilde{\mathcal{H}}|\psi\rangle$. One thing to note is that in this formulation, the retained dimensions can vary from site to site, which will be labelled χ_j . In the typical case, the two-site evolution causes the state to leave the manifold of the original [MPS](#), with the fixed bond dimension χ . This can be truncated back to χ , however, in this variation a different bond dimension is instead chosen based on discarding eigenvalues below a certain precision, without substantial computational effort. Once the projection has been carried out, the procedure is explained in [Algorithm 4.4.1](#), where the internal indices are omitted.

Algorithm 4.4.1 (TDVP method):

Step 0: Start with an [MPS](#), which is in a bipartition with two free sites $S^{\sigma_\ell}(\chi_\ell)$ and $S^{\sigma_{\ell+1}}(\chi_{\ell+1})$ as in [Fig. 4.2](#). The coefficients can be written in full as:

$$\Theta = \left[A^{\sigma_1}(\chi_1) A^{\sigma_2}(\chi_2) \dots A^{\sigma_{\ell-1}}(\chi_{\ell-1}) \right] S^{\sigma_\ell}(\chi_\ell) S^{\sigma_{\ell+1}}(\chi_{\ell+1}) \left[B^{\sigma_{\ell+1}}(\chi_{\ell+1}) B^{\sigma_{\ell+2}}(\chi_{\ell+2}) \dots B^{\sigma_L}(\chi_L) \right]. \quad (4.16)$$

Step 1: Form $\Theta(\ell, \ell + 1)$, which consists of the two free sites, $S^{\sigma_\ell}(\chi_\ell)$ and $S^{\sigma_{\ell+1}}(\chi_{\ell+1})$.

Step 2: Evolve Θ according to its effective Hamiltonian $\tilde{\mathcal{H}}(\ell, \ell + 1)$, which is obtained from the [MPO](#) representation (see [Ch. 3](#)).

Step 3: Factor Θ into the separate sites again, i.e. $A^{\sigma_\ell}(\chi_\ell) S^{\sigma_{\ell+1}}(\ell + 1)$.

Step 4: Evolve $S^{\sigma_{\ell+1}}(\chi_{\ell+1})$ backwards in time according to single-site operator $\tilde{\mathcal{H}}(n + 1)$, which is the effective one-site representation, obtained from the [MPO](#) form of $\tilde{\mathcal{H}}$.

Step 5: Absorb this new $S^{\sigma_{\ell+1}}(\chi_{\ell+1})$ into the next two-site block to be acted upon i.e. $\Theta(\ell + 1, \ell + 2) = S^{\sigma_{\ell+1}}(\chi_{\ell+1}) S^{\sigma_{\ell+2}}(\chi_{\ell+2})$.

The splitting of the tangent space of the projector, so that it could act procedurally on sites, was an idea of ingenuity, which greatly advanced the

popularity of [TDVP](#). Before this, the projection within [TDVP](#) was applied instantaneously to all operators, which resulted in the counter-intuitive situation that the method's stability decreased as the approximation of the exact state improved, i.e. as the smallest Schmidt eigenvalue retained was improved [170, 171]. It should be noted that although this algorithm has many advantages such as its possible use for a large variety of Hamiltonians, the algorithm does have a very rigid restriction on the step-size δt that can be used. If this algorithm is applied with no truncation then it was estimated that a finite step error of $\mathcal{O}(\delta t^3)$ exists [172].

4.5 Krylov Based Time Evolution

The most common approach to perform time-evolution with [DMRG](#) or [MPS](#) is to make use of the Suzuki-Trotter expansion as done in the [TEBD](#) and [tDMRG](#) methods. An alternative method is to use the Krylov based time-evolution. This was initially set up only for time-independent Hamiltonians [173, 174]. The initial setups of this method with time-dependence, have a very strict restriction that the time-step must remain very small (compared to the rate of change of the Hamiltonian) in order to avoid errors [175, 176]. The method of focus, however, is the adaptation by Wall and Carr [149] in order to make the error independent of the rate of change of the Hamiltonian, by recasting the [MPO](#) as a finite state automaton. This essentially means that we enumerate the [MPO](#) by all of the physical operators we use to define our local Hilbert space and keep track of Hamiltonian parameters and weights. In this setup, there are separate rules (which consist of a matrix centrally and two vectors at each border) to set up each operator within the Hamiltonian. In this way the special structure of the [MPS/MPO](#) representation is ignored and the procedure is directly implemented as an iterative procedure, as detailed below.

This makes use of the a modification of the Magnus series called the commutator-free Magnus expansion ([CFME](#)) [177, 178]:

$$\mathcal{U}(t, t + \delta t) = \prod_i e^{-i\delta t \Omega_i} , \quad (4.17)$$

where Ω_i is a linear combination of $\tilde{\mathcal{H}}$ at different times in the interval $[t, t + \delta t]$, meaning that \mathcal{U} is still a unitary evolution operator formed from the Hamiltonian $\tilde{\mathcal{H}}$. There are many advantages to using this formulation for a chosen $\tilde{\Omega} = \sum_i \Omega_i$. The ansatz is unitary, meaning that the norm is preserved but it also allows the Hamiltonian to be represented exactly as an [MPO](#), provided only the parameters but not the operators change. Lastly, this means that the time-step is not neces-

sarily fixed by the rate of variation of the Hamiltonian because the CFME ansatz explicitly considers the time-dependence of the Hamiltonian.

The Krylov time method then involves minimising a functional, which equates to making our guess/estimate state $|\Upsilon\rangle$ equal the time-evolution at each time step with a small error (ϵ),

$$||\Upsilon\rangle - e^{-i\tilde{\Omega}\delta t}|\psi\rangle|^2 \leq \epsilon. \quad (4.18)$$

This minimisation is done by performing a Krylov subspace approximation to the exponential [129]. The Lanczos method is chosen to perform the approximation, as it retains the unitary nature of the matrix up to machine precision. The method is explained in Algorithm 4.5.1.

Algorithm 4.5.1 (Krylov Subspace Approximation):

Initialise

Step 0: Form the MPO of the CFME operator $\tilde{\Omega}$, an initial state $|\psi(0)\rangle$ in MPS form and set a tolerance ϵ for truncation. Then set $j = 0$, $\beta_0 = \langle\psi|\psi\rangle$ and $|r\rangle = |\psi(0)\rangle$.

Repeat steps 1-11 until convergence has been reached

Step 1: Set $j = j + 1$.

Step 2: Produce the Krylov vector $|v_j\rangle = \frac{|r\rangle}{\beta_{j-1}}$.

Step 3: $|r\rangle = \tilde{\Omega}|v_j\rangle$

Step 4: $\alpha_j = \langle v_j|r\rangle$

Step 5: Make $|r\rangle$ orthogonal to $|v_{j-1}\rangle$ and $|v_j\rangle$.

Step 6: Re-orthogonalise $|r\rangle$ against all $|v_k\rangle$, where $k \leq j$ if necessary.

Step 7: Form $\beta_j = \langle r|r\rangle$

Step 8: Form the matrix exponential $U^{(j)} = \exp(-i\delta t T^{(j)})$, where $T^{(j)}$ is a symmetric tridiagonal matrix, with α_i ($1 \leq i \leq j$) forming its diagonal and β_j ($1 \leq i \leq j-1$) forming its super diagonal, i.e., $T_{k,l}^{(j)} = \langle v_k|\tilde{\omega}|v_l\rangle$.

Step 9: Obtain the coefficients from the first column of $U^{(j)}$, $c^{(j)} = U_{1:j,1}^{(j)}$

Step 10: Set $|\Upsilon\rangle = \sum_{i=1}^j c_i^{(j)} |v_i\rangle$.

Step 11: Check if convergence is reached, i.e. if Eq. (4.18) is satisfied.

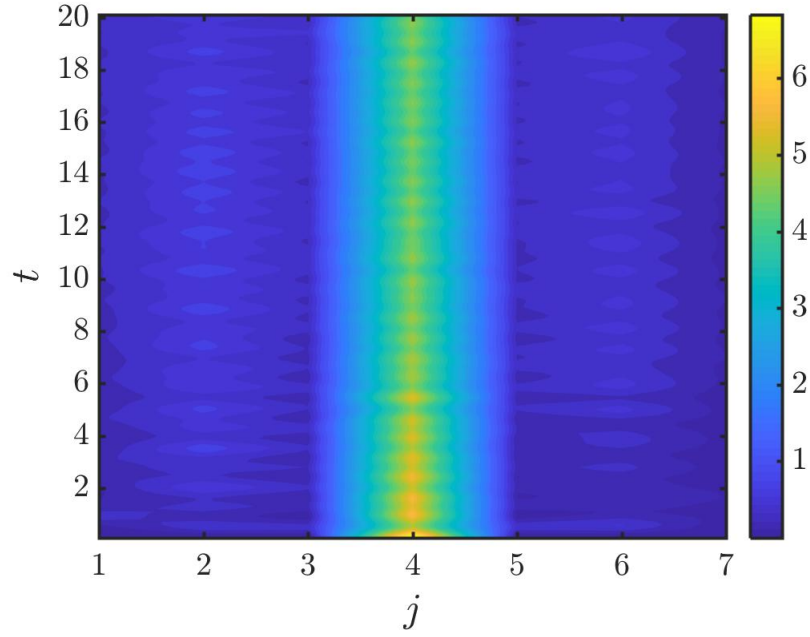


Fig. 4.3 The spreading of the on-site density $\langle n_j \rangle$ with time t , when all of the particles are initially started at the central site $j = 4$ and $J = U = 1$.

If we were to use exact arithmetics with the Hermitian Hamiltonian $\tilde{\mathcal{H}}$, then the Krylov space is constructed in such a way that it reduces to orthogonalising against the previous two vectors $|v_{i-1}\rangle$ and $|v_{i-2}\rangle$, which is equivalent to the Lanczos algorithm. In practice, with round-off errors from the numerical implementation, this orthogonality of the Krylov vectors is usually lost.

4.6 A Case-study of Time Evolution

To provide an illustrative example of time-evolution we will use the BH model with nearest-neighbour and next-nearest neighbour tunnelling, described by the Hamiltonian:

$$\begin{aligned} \mathcal{H}_{BH} = & -J \sum_{j=1}^{L-1} \left(b_j^\dagger b_{j+1} + b_j b_{j+1}^\dagger \right) - J \sum_{j=1}^{L-2} \left(b_j^\dagger b_{j+2} + b_j b_{j+2}^\dagger \right) \\ & + \frac{U}{2} \sum_{j=1}^L n_j (n_j - 1) - \mu \sum_{j=1}^L n_j. \end{aligned} \quad (4.19)$$

We will show a simple example consisting of $L = 7$ sites with $J = U = 1$ set. The initial state has $|n_4\rangle = 7$ and $|n_j\rangle = 0$, when $j \neq 4$. In other words, we begin our evolution from an initial state which has all particles loaded at the central

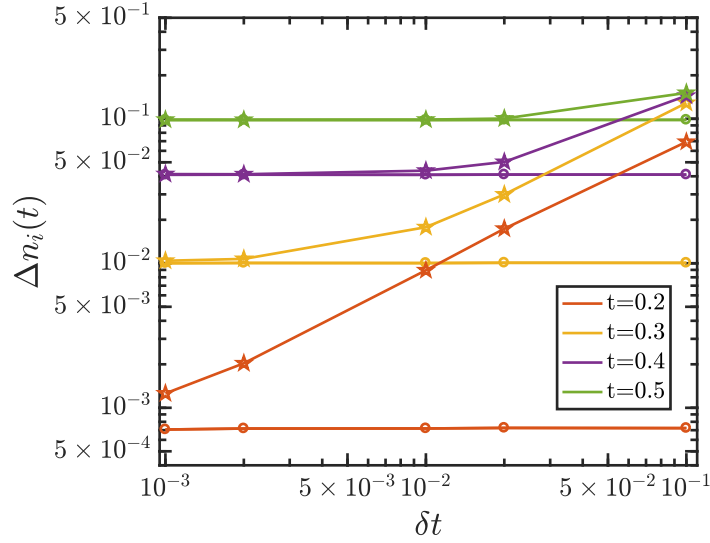


Fig. 4.4 The ℓ^2 norm of the error $\Delta n_i(t) = ||\langle \tilde{n}_i(t) \rangle - \langle n_i(t) \rangle||$ for different times t and $\chi = 200$ against the size of the time steps δt . The results are shown using both the Krylov (circles) and the TDVP method (stars).

site. In Fig. 4.3, the on-site density n_j is shown against the time evolution at the sites $j = 1, \dots, 7$. The results for this figure are obtained from ED. It can be seen that the particle density spreads gradually into the other sites as the system time-evolves, but that the majority of the particles remain at the central site up to time $t = 20$. As this model involves next-nearest neighbour interactions, the TDVP and Krylov method are appropriate choices. These are obtained using the OSMPS library [149, 150]. Numerically, the initial state is obtained by adding an on-site bias to the site $j = 4$, making it more energetically favourable. To accommodate the initial state, the maximum number allowed per site is increased to $n_{\max} = 7$ (see Ch. 3).

To emphasise the effect of step-size in the different methods, we show the error of the on-site density for a few test cases. If we want to use a method of MPS to replicate the results obtained by exact diagonalisation, then we require that the on-site density $\langle n_i(t) \rangle$ retains a good accuracy as the system time-evolves. One of the main issues with these simulations is the progressive nature of the error, i.e. whatever the error is for a given time, when this is used to evolve to a later time, the error will increase. In Fig. 4.4 this effect is illustrated for TDVP and the Krylov method. Before the evolution ($t = 0$), the error between these methods and ED is precision error (a maximum of $O(10^{-13})$) and up until $t = 0.1$ this remains of the order of 10^{-11} . Within Fig. 4.4, the ℓ^2 norm of the error $\Delta n_i(t) = ||\langle \tilde{n}_i(t) \rangle - \langle n_i(t) \rangle|| = \sqrt{\sum_i (\langle \tilde{n}_i(t) \rangle - \langle n_i(t) \rangle)^2}$ is shown as an estimate,

where $\langle \tilde{n}_i(t) \rangle$ is the estimated on-site density of site i and $\langle n_i(t) \rangle$ is the exact one. We have again chosen this measure to observe the overall difference, instead of one biased by a few values, due to the fact that most of the error will arise surrounding the central site where all of the particles begin. The increase of the error as the time-evolves is clear by examining the difference between the times shown. Additionally, we can also see, that within this example, **TDVP** is more sensitive to the time-step δt , as it requires a smaller time-step to obtain even the accuracy that corresponds to the Krylov method at each time.

We hope that this simple example provides an illustration of the care that needs to be taken when performing simulations in time to ensure convergence with not only the bond dimension χ , which was present in the ground state simulations, but also and typically more importantly, of the size of the time steps which are method dependent.

4.7 Conclusion

A number of methods have been formulated in order to approximate a time-evolution, to find the evolved state of a system. These methods are split into two classes: cases where the Hamiltonian only involves nearest-neighbour terms and cases where there is a longer-range interaction. For nearest-neighbour Hamiltonians **TEBD**, which is essentially a form of **tDMRG**, can be used efficiently based on the Trotter expansion. For Hamiltonians with longer interactions, however, **TDVP** or Krylov are amongst the preferred methods. **TEBD**, in analogy to **tDMRG**, approximates the time-evolution operator $\mathcal{U}(\delta t) = e^{-i\delta t \tilde{\mathcal{H}}}$ and then applies it to the state, whereas the **TDVP** method and the Krylov based time evolution method, instead directly approximate the action of the unitary evolution operator \mathcal{U} onto the state $|\psi(t)\rangle$ [155].

Thus, choosing the correct algorithm is very model dependent and there is no universally preferred or superior one. We emphasise that care should be taken with regards to the size of the time steps chosen and that the time is sufficiently small (or the results sufficiently accurate) to ensure that a large error is not accrued over time.

HAPTER

ENTANGLEMENT SCALING OF FIRST ORDER QUANTUM PHASE TRANSITIONS

“Scaling requires both addition and subtraction. The problem of more is also a problem of less.”

Robert I Sutton

Entanglement scaling around a [1OQPT](#) will be the focus of this chapter, based on my work “Entanglement scaling at first order quantum phase transitions” [179]. Entanglement is an invaluable resource in measuring the quantum nature of systems, which justifies its use to identify quantum matter. Understanding how many-body interacting systems order into different quantum phases as well as the transitions between them remains one of the most challenging open problems in modern physics. Additionally, the discovery of topological and new exotic phases [42], which fall outside Landau’s symmetry breaking paradigm, have made a new way of identifying phase transitions necessary [7]. The singular behaviour in [1OQPTs](#) occurs as an abrupt discontinuity of some local observables, while for [2OQPTs](#) the order parameters change continuously with a power law. Finite-size effects can make distinguishing between a [1OQPT](#) and a [2OQPT](#) very difficult despite their clear difference in definition. This becomes even more difficult in the region of multi-critical points, where several [QPTs](#) of different order coexist in a narrow range of Hamiltonian parameters.

For [2OQPTs](#) the thermodynamic limit can be recovered using [FSS](#) [33]. The scaling is characterised by the critical exponents, enabling the classification of apparently different [2OQPTs](#) into the same universality class. A number of seminal papers have examined entanglement in the region of [QPTs](#) and have

shown that this follows a scaling based on conformal symmetry [34, 35]. It has also been shown that entanglement exhibits the same features as other measures, i.e. it has the discontinuity or divergence within the entanglement measure (or a derivative thereof) [12, 13, 66–68]. This has been detailed in more depth in Sec. 2.3.2.

Motivated by the advances in understanding entanglement, we analyse the scaling properties of pairwise entanglement measures for Hamiltonians with only nearest-neighbour interactions near multi-critical points. Although FSS is a tool to obtain the thermodynamical properties of the system for continuous (2OQPT) phase transitions, here we show that such a tool can also be employed with entanglement measures for 1OQPTs. Furthermore, we demonstrate that when finite-size effects are important, it is precisely the scaling of the entanglement measure and not the measure itself, which determines the correct order of the transition. This fact is especially relevant for a 1OQPT crossed in the vicinity of a 2OQPT. It will be shown, that it is in accordance with the recent results reported by Campostrini *et al.* [36], showing that the order parameter of a 1OQPT can be continuous for finite systems and admits an appropriate finite-size scaling.

The work contained within this chapter will focus on bipartite entanglement measures of the spin-1/2 Ising model with a transverse field and the spin-1 XXZ model around a 1OQPT point. The measures used will be concurrence for the spin-1/2 model and negativity for the spin-1 XXZ model. An investigation will also be done of how the density matrix leads to the features that we observe from the entanglement measures.

5.1 Key theorems for Entanglement at a Phase Transition

Before delving into our exploration of the scaling of a bipartite entanglement measure around a 1OQPT, we will state some key theorems that are used in our analysis. The first two theorems are regarding the density matrix of two particles, which is used in the calculation of the bipartite entanglement measures [180]. Then we will describe a theorem for scaling of 1OQPTs [36].

5.1.1 Kohn-Sham Theorem and its Expansion

The first theorem that we focus on was proposed by Wu *et al.* [180] to examine the properties of the reduced density matrix of a subsystem near 1OQPTs and 2OQPTs. This was done by making use of the Kohn-Sham theorem:

Theorem 5.1.1 (Kohn-Sham [181]): Assume that we have an N -partite local Hamiltonian $\mathcal{H}(\lambda)$, which is written as a sum of terms with k -body interactions,

$H_k(\lambda)$ ($k = 1, 2, \dots$), where λ is a parameter in the Hamiltonian phase-space, such as the magnetic field or an interaction strength. Then the Hamiltonian can be rewritten as:

$$\mathcal{H}(\lambda) = \sum_k \mathcal{H}_k(\lambda) . \quad (5.1)$$

and the energy of the ground state $|\psi_G\rangle$ can be written as

$$E_G(\lambda) = \langle \psi_G | \mathcal{H} | \psi_G \rangle = \sum_k \text{Tr} (\mathcal{H}_k(\lambda) \rho^k) , \quad (5.2)$$

where ρ^k is the reduced density matrix acting on the local support of the corresponding local Hamiltonian \mathcal{H}_k .

For the usual case of local Hamiltonians with just two-body interactions, which we will henceforth refer to as two-body local Hamiltonians, $\mathcal{H}_k(\lambda) = \mathcal{H}_{ij}(\lambda)$, where the indexes i and j refer to two spins and it can be shown that $\partial_\lambda E_G \sim (\partial_\lambda \mathcal{H}_{ij}) \rho^{ij}$. If the local Hamiltonians are smooth functions of λ , then a one-to-one correspondence can be made between the singularities of $\partial_\lambda E_G(\lambda)$ arising in a **1OQPT** and the singularities of (the matrix elements) of ρ^{ij} . The above translates into discontinuous pairwise entanglement measures, which depend exclusively on ρ^{ij} . By the same reasoning, a singularity in $\partial_\lambda^2 E_G$, typical of a **2OQPT**, is associated to a singularity in the first derivative of the corresponding pairwise entanglement measure.

Theorem 5.1.2 (Wu-Sarandy-Lidar [180]): Excluding accidental divergences or occurrences of non-analyticity, as outlined in (a)-(b), a discontinuity in (discontinuity in or divergence of the first derivative of) the entanglement measures associated to the corresponding reduced density matrix of the ground state of the local Hamiltonians is both necessary and sufficient to signal a **1OQPT** (**2OQPT**).

- a) The **1OQPT** (**2OQPT**) is associated to a discontinuity in (discontinuity in or divergence of) the first (second) derivative of the ground state energy, apparent in the bipartite entanglement measure which originates exclusively from the elements of the reduced density matrix ρ^{ij} . This means the non-analyticity seen in the entanglement measure is not as the result of any other operation such as the sum, maximum and minimum.
- b) The discontinuous matrix elements of ρ^{ij} (discontinuous or diverging elements of $\frac{\partial \rho^{ij}}{\partial \lambda}$) for a **1OQPT** (**2OQPT**) do not either all accidentally vanish or cancel with other terms in the expression for (the first derivative of) the bipartite entanglement measure.

This theorem confirms that a discontinuity in a pairwise measure of entanglement, in a two-body local Hamiltonian, indicates a **1OQPT** while a discontinuity/divergence in its derivative signals a **2OQPT**, unless some accidental

divergences occur. There are some known cases where the results do not correspond to the order of QPT that you would initially expect. For instance, in the spin-1/2 XXZ chain, at the 1OQPT transition between the ferromagnetic and critical phase, the concurrence is a function of the energy at the critical point and it remains continuous in the thermodynamic limit while its first derivative is discontinuous [69, 182]. For the same transition, it has been shown that a symmetry breaking in the ferromagnetic phase also modifies the origin of the non-analytic behaviour of the concurrence [183]. In Ref. [184], a three-body local Hamiltonian model was presented in which the pairwise concurrence is non-analytical in the absence of any QPT [184]. For 2-D models even less is known.

5.1.2 Scaling Theorem for First-Order Transitions

The main theorem that we will focus on within this chapter is the scaling procedure proposed by Campostrini *et al.* [36, 54] for a 1OQPT in proximity to a 2OQPT. The reasoning which led to this theorem is the general mapping of D -dimensional quantum systems onto classical anisotropic $(D + 1)$ -dimensional systems and the fact that classical first-order phase transitions display some scaling [185, 186]. This led to the proposal that on dimensional grounds the scaling of the 1OQPT would be of a certain form as detailed in Th. 5.1.3.

Theorem 5.1.3 (First-order transition scaling): For a chain of length L in a 1-D lattice, which has a magnetic field h driving a 1OQPT (at $h_c = 0$), there exists a scaling variable κ , which is the ratio between the energy contribution of h and the gap at the critical point $\Delta_L = \Delta_L(L, h = 0) = E_1(L, h = 0) - E_G(L, h = 0)$:

$$\kappa \sim \frac{hL}{\Delta_L} . \quad (5.3)$$

As a result of this scaling, heuristically when $hL \sim \Delta_L$, the ground state energy becomes effectively continuous along the transition and so does the order parameter. There is a caveat with this theorem that arises from the fact that this scaling is only apparent very close to the critical point, which is consequently where numerical results can start to fail. Identifying this scaling, therefore becomes more achievable if the 1OQPT occurs close to a 2OQPT as the correlation length of the system (ξ) diverges, enhancing the nearby finite-size effects.

The energy gap and the magnetisation should then obey the following scaling ansatzes:

$$\Delta(L, h) \approx \Delta_L f_\Delta(\kappa) , \quad (5.4)$$

$$M_x(L, h) \approx m_0 f_M(\kappa) , \quad (5.5)$$

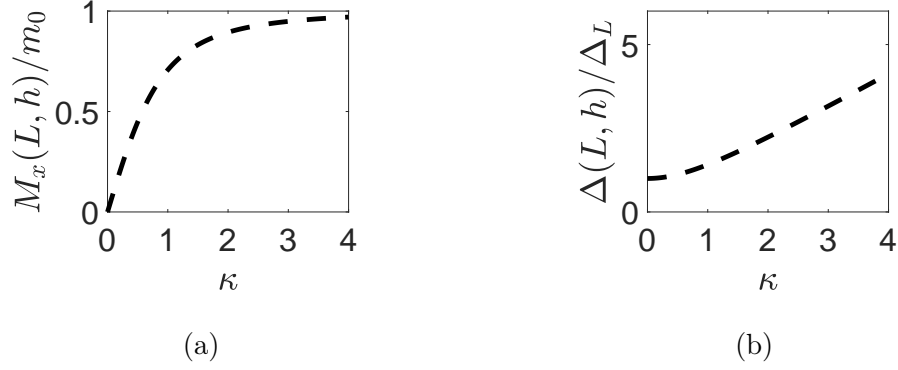


Fig. 5.1 Illustration of **(a)** the analytic magnetisation M_x and **(b)** the energy gap Δ , which measurements taken around the **1OQPT**, with various parameters, should collapse to.

where $f_\Delta(\kappa)$ and $f_M(\kappa)$ are continuous universal functions for all L . The function $f_\Delta(0) = 1$ by definition and $f_\Delta(\kappa) \approx \kappa$ for $\kappa \rightarrow \pm\infty$ so that the expected linear behaviour of $\Delta(L, h) \approx |h|L$ is reproduced for sufficiently large $|h|$. The quantity m_0 is the magnetisation obtained as the critical point is approached, i.e. as $h \rightarrow 0$. $f_M(\kappa) = \pm 1$ as $\kappa \rightarrow \infty$ and $f_M(0) = 0$ as a result of the parity symmetry around h .

Camprostrini *et al.* first tested this proposal by examining the spin-1/2 Ising model (seen in Ch. 2) with an additional longitudinal field, which is described by the Hamiltonian:

$$\mathcal{H}_{Ising} = -J_x \sum_{i=1}^{L-1} \sigma_i^x \sigma_{i+1}^x - B_z \sum_{i=1}^L \sigma_i^z - B_x \sum_{i=1}^L \sigma_i^x, \quad (5.6)$$

where L is the number of spins, σ_i^α are the Pauli matrices for spin i and where a **1OQPT** occurs at $B_x = 0$. In this model the magnetic field driving the **1OQPT** is B_x and the critical point occurs at $B_{xc} = 0$. This model is described by the scaling ansatzes in Eq. (5.4) and Eq. (5.5), where the h is replaced by B_x . Now $f_\Delta(\kappa)$ and $f_M(\kappa)$ are continuous universal functions for all L and B_z . Since the model is integrable when $B_x = 0$, the scaling variable can be defined as [36]:

$$\kappa_1 = \frac{2m_0 B_x L}{\Delta_L}, \quad (5.7)$$

where $\Delta_L = \Delta_{L, B_x=0} \approx 2(1 - B_z^2)B_z^L$, is the first gap at the critical point, $B_x = 0$ for **OBC** and

$$m_0 = \lim_{B_x \rightarrow 0^+} \lim_{L \rightarrow \infty} \langle \sigma_x \rangle = (1 - B_z^2)^{1/8}. \quad (5.8)$$

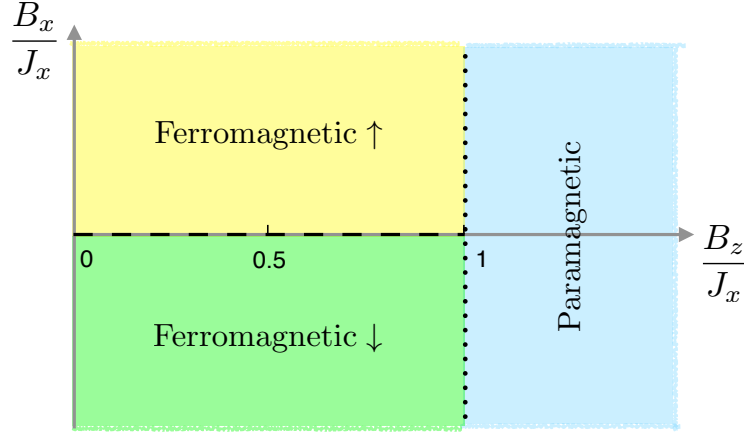


Fig. 5.2 Phase diagram for the spin-1/2 Ising chain with a longitudinal field. The dashed line (- -) depicts the 1OQPT while the dotted line (...) the 2OQPT.

As the critical point at $B_x = 0$ is approached, near the region of the 2OQPT ($B_z = 1$), the gap closes and even at very small values of the driving parameter B_x around the critical point, the 1OQPT transition looks continuous. An illustration of the collapse that should occur is shown in Fig. 5.1 by plotting the analytical functions that were calculated in Ref. [36].

5.2 Scaling applied to Bipartite Entanglement Measures

The main focus of our work is to investigate whether identification of a 1OQPT could be done using the scaling of entanglement measures in a similar fashion. To explore this we focus on the spin-1/2 chain with a uniaxial field and the spin-1 XXZ chain and the bipartite entanglement therein. The scaling procedure proposed by Campostrini *et al.*, stated above (Th. 5.1.3), is adopted, to check if it holds for entanglement as well. The bipartite entanglement measures that are focused on are introduced in Ch. 2 for a pair of particles. Here these measures will be calculated by using the reduced density matrix of the two central spins within the lattice ρ^{ij} .

5.2.1 Spin-1/2 Ising chain with longitudinal field

We focus on the spin-1/2 Ising chain with longitudinal field (Eq. (5.6)) and report how a measure of bipartite entanglement, the concurrence, scales in the vicinity of the 1OQPT when it is crossed near the multi-critical point. We choose the Ising model because this is an integrable model when the longitudinal field vanishes and serves as a good benchmark to analyse our numerical results.

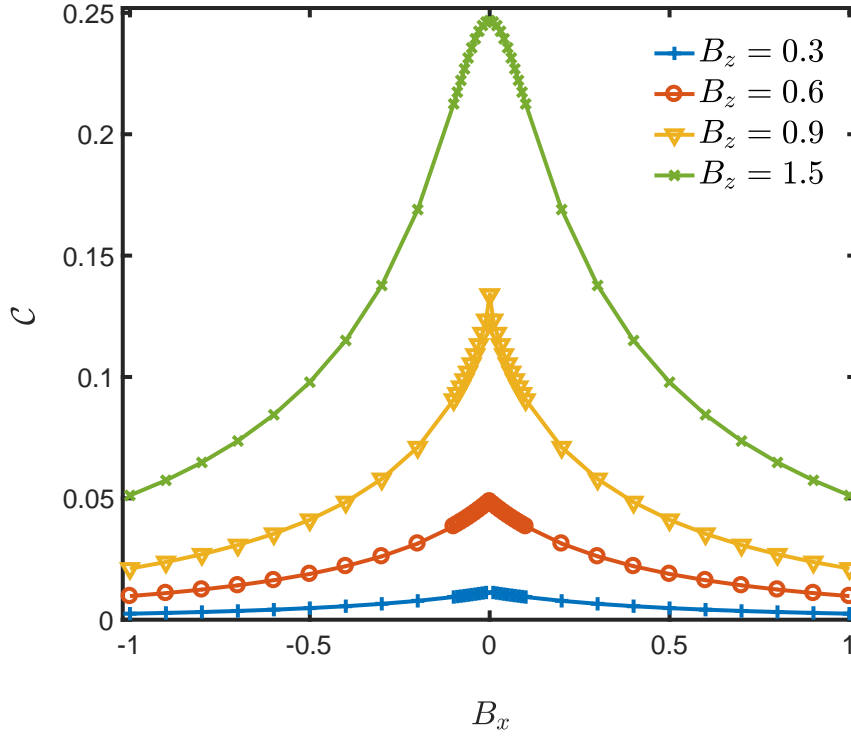


Fig. 5.3 Concurrence of the longitudinal Ising model with length $L = 40$, Eq. (5.6), as a function of B_x near the 1OQPT, for different values of the transverse magnetic field B_z . We observe a spike at the 1OQPT critical point, $B_x = 0$, for $B_z < 1$.

We set $J_x = 1$ and $B_z \geq 0$ in Eq. (5.6). In Fig. 5.2, we provide the phase diagram of the model. For $B_x = 0$, where the system reduces to the integrable Ising model, there is a 2OQPT at $B_z = 1$ between the ferromagnetic ($B_z < 1$) and paramagnetic phases ($B_z > 1$). This 2OQPT was the first one studied by means of bipartite entanglement [12]. When $B_x \neq 0$, the system is no longer integrable and we obtain the ground state of the system using both the density matrix renormalisation group (DMRG) with OBCs (using the PwP implementation described in Ch. 3) and ED calculations. When the system is in the ferromagnetic phase, a 1OQPT takes place at $B_x = 0$ between the two ferromagnetic ground states, ferromagnetic \uparrow and ferromagnetic \downarrow . This transition can be detected by a discontinuity in the magnetisation, $M_x = \sum_i \langle \sigma_i^x \rangle$, which passes from positive to negative values. For finite systems, however, numerical calculations in a region sufficiently close to $B_x = 0$ show a smooth slope in M_x instead of a discontinuity (see Sec. 2.2.1).

We want to examine if a bipartite measure of entanglement, which has similar features, follows the same scaling procedure around a 1OQPT outlined by Campostrini *et al.* Since the Hamiltonian is two-body local, discontinuities in entanglement measures have to be related to two-body (pairwise) entanglement

of two nearest-neighbour spins (i, j) described by the reduced density matrix, ρ^{ij} . For pure states, all measures of bipartite entanglement are in one-to-one correspondence and are all a function of the eigenvalues of the reduced density matrix arising from the chosen partition. For mixed states, this is not the case anymore and the entanglement measure has to be calculated as the convex roof of the corresponding pure state measure. Here we use concurrence as a measure of entanglement for the mixed states of the reduced density matrix ρ^{ij} (see Def. 2.3.7). Since \mathcal{C} is supposed to be discontinuous at the critical point for QPTs, naively we might expect that it will follow a similar scaling behaviour as M_x , Eq. (5.5).

In Fig. 5.3, we show \mathcal{C} for the two central spins which, if boundary effects are neglected, will also hold for the rest of neighbouring spin pairs. We observe that \mathcal{C} is a continuous function with a spike at the critical point which signals a singularity in the first derivative, $\partial_{B_x}\mathcal{C}$. The spike becomes more pronounced as the transition gets closer to the 2OQPT at $B_{zc} = 1$. The reason why the discontinuity cannot occur directly in this measure, as we would expect with a measure of the ground state, is because the concurrence is invariant under the parity transformation of $-B_x \rightarrow B_x$ and as such the concurrence is a symmetric function around $B_x = 0$. It is worth pointing out that the behaviour of the concurrence bears strong similarities with the geometric entanglement, a collective measure of entanglement indicating how much the ground state differs from a separable state [71]. Notice that for $B_z > 1$, when the system is in the paramagnetic phase independently of the sign of the longitudinal field B_x , (as indicated in Fig. 5.3 for $B_z = 1.5$) the concurrence becomes a smooth function of B_x as no 1OQPT occurs.

Now we need to consider how to scale the concurrence in the same manner as Campostrini and co-workers did for the magnetisation and the energy gap. As we are considering the same model (spin-1/2 Ising) the scaling parameter κ_1 (Eq. (5.7)) should be the same. For the magnetisation, Campostrini *et al.* showed the collapse using the scaling variable by plotting M_z/m_0 against κ_1 as shown in Fig 5.1. m_0 is the magnetisation at the critical point which is a known quantity in this model. It should be noted that due to the symmetric nature of the Ising model, the value m_0 is also consequently the maximum value of the magnetisation. In Fig. 5.4a, we plot the scaling of the concurrence normalised by its maximum value, $\tilde{\mathcal{C}} = \mathcal{C}/\mathcal{C}_{max}$, as a function of the scaling variable κ_1 to determine whether \mathcal{C} fulfils a similar scaling relation as in Eq. (5.5). It is enough to investigate what happens for $\kappa_1 > 0$ because $\mathcal{C}(\kappa_1)$ has even parity, i.e., $\mathcal{C}(\kappa_1) = \mathcal{C}(-\kappa_1)$. This is a consequence of the Hamiltonian, and, therefore, the ground state, being invariant under the change $B_x \rightarrow -B_x$ and a local π -rotation of the spins around the z -axis. It can

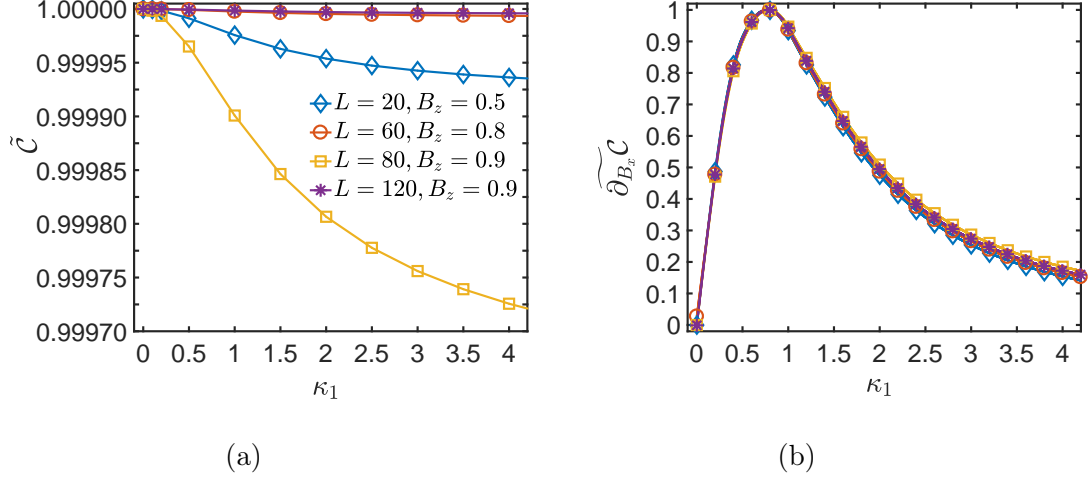


Fig. 5.4 Concurrence of the longitudinal Ising model, Eq. (5.6), as a function of κ_1 , defined in Eq. (5.7), near the 1OQPT for different values of the transverse magnetic field B_z . **(a)**: Concurrence normalised by its maximum, $\tilde{\mathcal{C}}$, as a function of the scaling variable κ_1 ; there is no data collapse. **(b)**: Derivative of the concurrence normalised by its minimum, $\widetilde{\partial_{B_x}\mathcal{C}}$, plotted as a function of κ_1 showing a universal behaviour for the same set of values in **(a)**. The results are obtained with DMRG and bond dimension $\chi = 80$ for which they are converged.

be seen that the scaling of the renormalised concurrence $\tilde{\mathcal{C}}$ for different B_z and L values do not collapse in a universal function, implying that this scaling is not valid.

Finally, in Fig. 5.4b we display the scaling of the derivative of the concurrence normalised by its minimum value $\widetilde{\partial_{B_x}\mathcal{C}} = \partial_{B_x}\mathcal{C}/[\partial_{B_x}\mathcal{C}]_{\min}$. From this we obtain the interesting observation that while the concurrence does not scale with the fitting parameter κ_1 , its derivative does. In Fig 5.4b there is a good data collapse for different values of B_z and L . Thus, $\partial_{B_x}\mathcal{C}$ fulfils the scaling ansatz,

$$\partial_{B_x}\mathcal{C}(L, B_z) = [\partial_{B_x}\mathcal{C}]_{\min} g(\kappa_1), \quad (5.9)$$

where $g(\kappa_1)$ is a universal function for any L and B_z . We discuss the reasoning that the derivative of entanglement scales in Sec. 5.3 by considering how the density matrix elements cause this in accordance with the exclusions contained in Th. 5.1.2.

5.2.2 Spin-1 XXZ chain with uniaxial single-ion anisotropy

In this section, we extend the study of entanglement along 1OQPTs to a spin-1 system by moving to a much more complex model, the spin-1 XXZ chain with uniaxial single-ion anisotropy. This model has been chosen because it has a rich phase diagram with several QPTs whose boundaries are only known approximately.

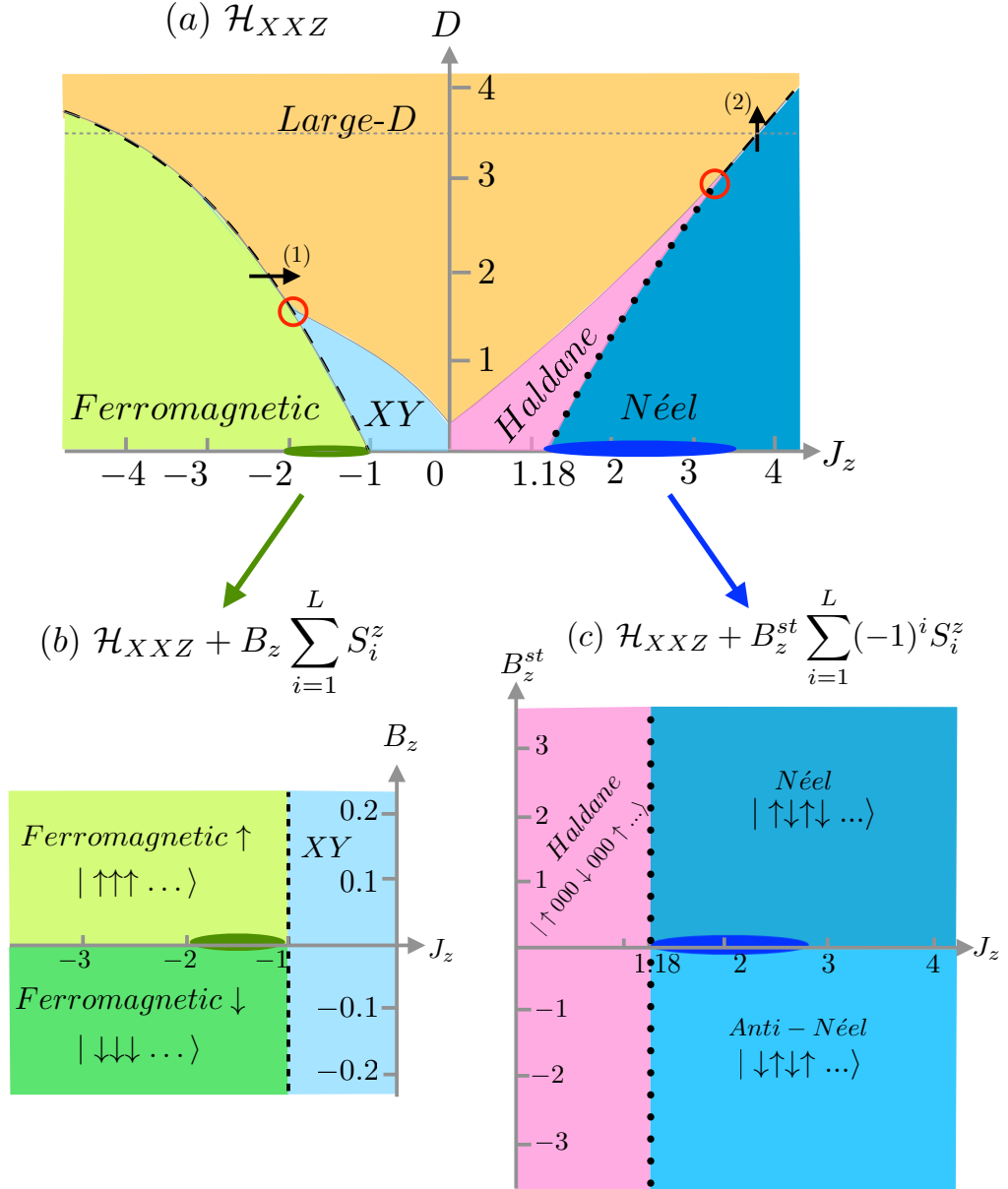


Fig. 5.5 (a): Phase diagram for the spin-1 model in Eq. (5.10) with $D > 0$. The dashed lines depict 1OQPTs and the arrows the points where we cross them. The black dotted line depicts the 2OQPT between Haldane and Néel phases. The red circles signal the tri-critical points present in the phase diagram. The ovals show the areas where we add an external field to induce a 1OQPT between the two-fold degenerate ground states in the ferromagnetic and Néel phases, which are shown fully in (b) and (c) respectively.

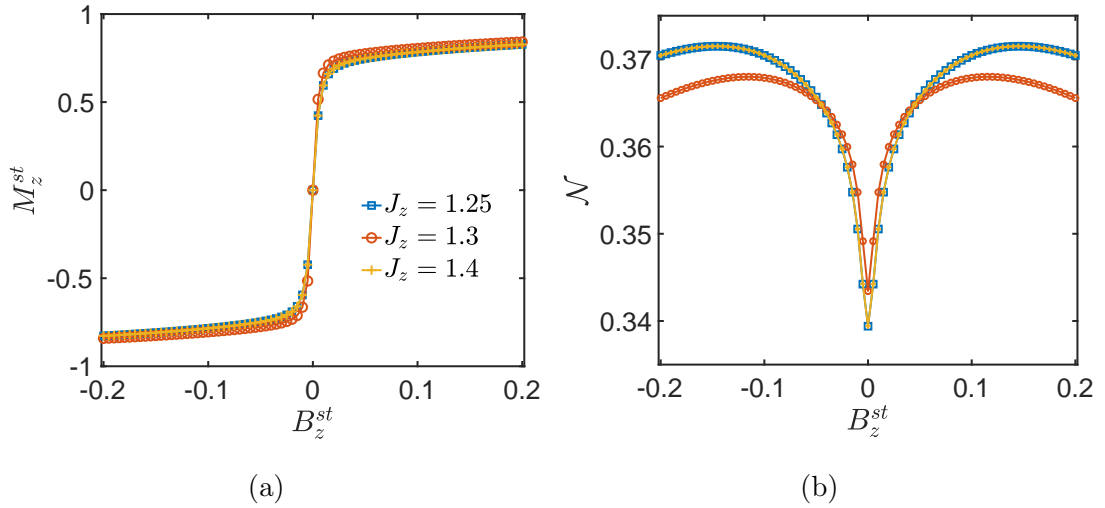


Fig. 5.6 Measures around the 1OQPT between the Néel and the Anti-Néel phases. **(a)** and **(b)**: The staggered magnetisation M_z^{st} and the negativity \mathcal{N} as a function of B_z^{st} for different J_z and $L = 8$, $D = 0$. This is calculated using ED.

We will focus on the 1OQPTs of the model and analyse, by means of numerical techniques, the behaviour of bipartite entanglement in the vicinity of multi-critical points. Since the concurrence, \mathcal{C} , can only be easily computed for the mixed states of two qubits, in order to compute the entanglement between two spin-1 particles we use the negativity (defined in Sec. 2.3.8) [64, 65]. The Hamiltonian for this model is:

$$\mathcal{H}_{XZX} = \sum_{l=1}^{L-1} \left[\tilde{J} S_l^x S_{l+1}^x + \tilde{J} S_l^y S_{l+1}^y + J_z S_l^z S_{l+1}^z \right] + D \sum_{l=1}^L (S_l^z)^2, \quad (5.10)$$

where S_l^α are the spin-1 matrices for spin l and D is the uniaxial single-ion anisotropy which we take as positive. The spin-1 operators are given by:

$$S^x = \frac{1}{\sqrt{2}} \begin{pmatrix} 0 & 1 & 0 \\ 1 & 0 & 1 \\ 0 & 1 & 0 \end{pmatrix}, \quad S^y = \frac{1}{\sqrt{2}i} \begin{pmatrix} 0 & 1 & 0 \\ -1 & 0 & 1 \\ 0 & -1 & 0 \end{pmatrix}, \quad S^z = \begin{pmatrix} 1 & 0 & 0 \\ 0 & 0 & 0 \\ 0 & 0 & -1 \end{pmatrix}. \quad (5.11)$$

We set $\tilde{J} = 1$, and use it as the unit of energy. The rich phase diagram [187] is schematically shown in Fig. 5.5, where the several 1OQPTs have been depicted with dashed lines.

Ising-type Transitions

The first transitions that we examine in this model are the ones of Ising-type so we expect that the same procedures outlined in Ref. [36] and in the section

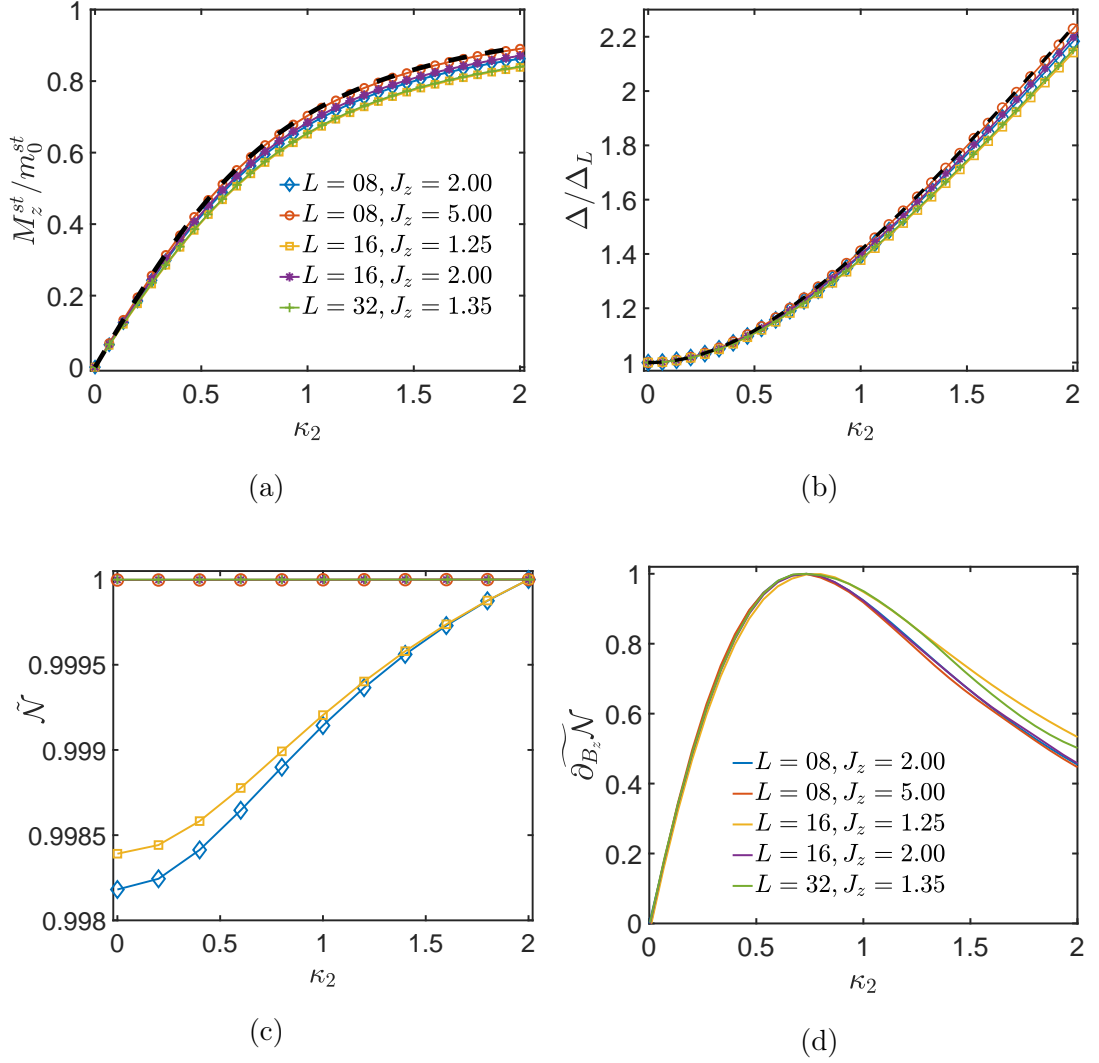


Fig. 5.7 **(a)** and **(b)**: The renormalised magnetisation M_z^{st}/m_0^{st} and energy gap $\Delta(\kappa_2)/\Delta_L$ plotted against the scaling variable κ_2 , Eq. (5.12). M_z^{st} fulfils the universal scaling, Eq. (5.5) and $\Delta(\kappa_2)/\Delta_L$ follows Eq. (5.4). The dashed lines are those Campostrini *et al.* analytically obtained. **(c)**: The renormalised negativity $\tilde{\mathcal{N}} = \mathcal{N}/\mathcal{N}(B_z^{st} = 0)$ plotted against κ_2 (no collapse occurs). **(d)**: The renormalised derivative of the negativity $\widetilde{\partial_{B_z^{st}} \mathcal{N}}(\kappa_2)$ (derivative normalised by its maximum) where a good data collapse is observed. DMRG was used to obtain these results.

before (Sec. 5.2.1) will still apply. We want to analyse the behaviour of the negativity, \mathcal{N} , when the 1OQPT is due to a \mathbb{Z}_2 symmetry breaking of a two fold-degenerated ground state. To this aim we add an extra magnetic field, $B_z \sum_{i=1}^L S_i^z$ (extra magnetic staggered field $B_z^{st} \sum_{i=1}^L (-1)^i S_i^z$) in the ferromagnetic (Néel) phase of the XXZ spin-1 model in Eq. (5.10). These new terms lead to two new 1OQPT between ferromagnetic \uparrow / ferromagnetic \downarrow (Néel / Anti Néel) phases, depicted graphically by ovals along the $D = 0$ line in the phase diagram of the model, with arrows pointing to the relevant phase diagrams (see Fig. 5.5).

The corresponding order parameter for both transitions, the magnetisation (M_z), and the staggered magnetisation (M_z^{st}) respectively, are discontinuous in the thermodynamic limit. For the first induced QPT between the ferromagnetic phases, the entanglement remains always constant and zero. More interesting features appear in the Néel/Anti-Néel transition so we choose to focus on it. In Fig 5.6 we show the staggered magnetisation M_z^{st} and the negativity \mathcal{N} around the 1OQPT as a function of the added staggered magnetic field B_z^{st} . These results have been obtained using ED. We again observe the expected behaviour in M_z^{st} and the pairwise entanglement, \mathcal{N} , appears very similar in nature to the concurrence at the Ising transition. One observation is that in Fig. 5.6b the minimum occurs at the transition point $B_{zc}^{st} = 0$ rather than the maximum as we observed with the spin-1/2 Ising model. In order to apply the proper FSS ansatz for the negativity, we start by defining first the relevant scaling variable. As the transition is of Ising type this will be very similar to Eq. (5.7), but here B_z^{st} drives the transition so we obtain:

$$\kappa_2 = \frac{2m_0^{st}B_z^{st}L}{\Delta_L}. \quad (5.12)$$

In full analogy with the results presented in section 5.2.1, and due to the fact that the 2OQPT between Haldane/Néel phases belongs to the same universality class as the spin-1/2 Ising, we use the expression of m_0^{st} from Eq. (5.8) by substituting $B_z \rightarrow J_{zc}/J_z$, where $J_{zc} \approx 1.186$ corresponds the 2OQPT critical point for $D = 0$ [188].

Our scaling results are summarised in Fig. 5.7, where the results have been obtained using DMRG. The bond dimension in DMRG was chosen in such a way that the results converged, which meant using a bond dimension of $\chi = 100$ or $\chi = 150$. In Fig. 5.7a and Fig. 5.7b we plot the renormalised staggered magnetisation, M_z^{st}/m_0^{st} and the renormalised energy gap Δ/Δ_L against the scaling parameter κ_2 . It can be seen that a collapse of all variables occurs, which is very similar to the collapse Campostrini *et al.* found in the spin-1/2 Ising model [36]. To further ensure the correctness of our results, we also display the comparison between our numerical data, $M^{st}(\kappa_2)$ and $\Delta_L(\kappa_2)$, with the analytic expressions using an effective two level theory as derived in Ref. [36]. It can be seen in Fig. 5.7c that in accordance with the concurrence, \mathcal{C} , in the spin-1/2 Ising chain, the scaling also fails for the negativity \mathcal{N} in this phase transition. Once again it is the derivative of the negativity:

$$\widetilde{\partial_{B_z^{st}}\mathcal{N}}(\kappa_2) = \frac{\partial_{B_z^{st}}\mathcal{N}}{\max(\mathcal{N})}, \quad (5.13)$$

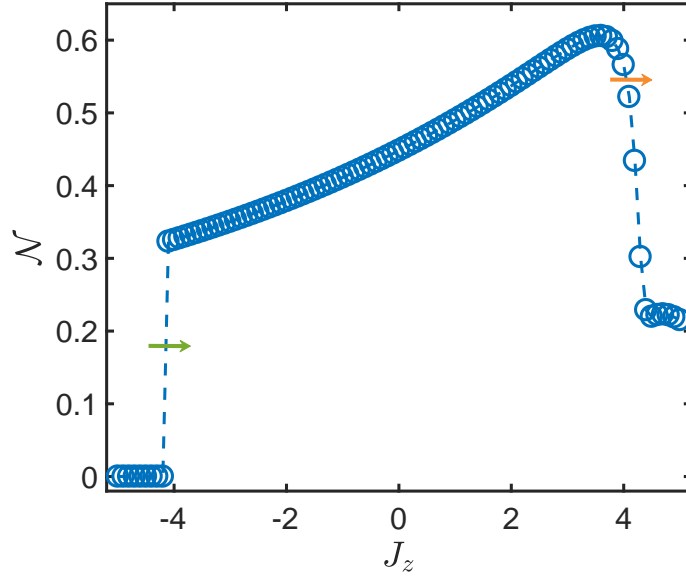


Fig. 5.8 Negativity \mathcal{N} as a function of J_z for $D = 3.5$ and $L = 8$. We observe a discontinuity in the **1OQPT** from ferromagnetic to large- D phases (shown by the green arrow) and a smooth slope for the **1OQPT** between the large- D and Néel phases (shown by the orange arrow). The results are obtained with ED.

(Fig 5.7d), which verifies the scaling ansatz, Eq. (5.9). This last behaviour strongly resembles the behaviour of the derivative on the concurrence for the spin 1/2 Ising chain with the longitudinal field.

The behaviour of \mathcal{N} along the different **1OQPTs** present in the model is very different depending on their proximity to a multi-critical point which also involves **2OQPTs**. We start by examining the negativity as a function of the J_z for a constant uniaxial field $D = 3.5$ and $L = 8$. Two **1OQPTs** are crossed at such a value of D , as indicated in the phase diagram by a grey horizontal line (see Fig. 5.5). The first one corresponds to the transition from ferromagnetic order to the large- D phase, which is crossed approximately at $J_z = -4.2$. Another **1OQPT** appears between large- D /Néel at approximately $J_z = 3.8$. As clearly shown in Fig. 5.8, the former phase transition is clearly signalled by a discontinuity in \mathcal{N} , whereas the latter shows a smooth slope along the transition.

Ferromagnetic/Large- D

In Fig. 5.9, we show in detail the generic behaviour of \mathcal{N} , together with the corresponding level crossing along the ferromagnetic/large- D phase transition. We cross the transitions at a fixed value $D = 2$, as depicted by (1) in Fig. 5.5, in the nearby region of a critical point (depicted by a red circle). We observe that even

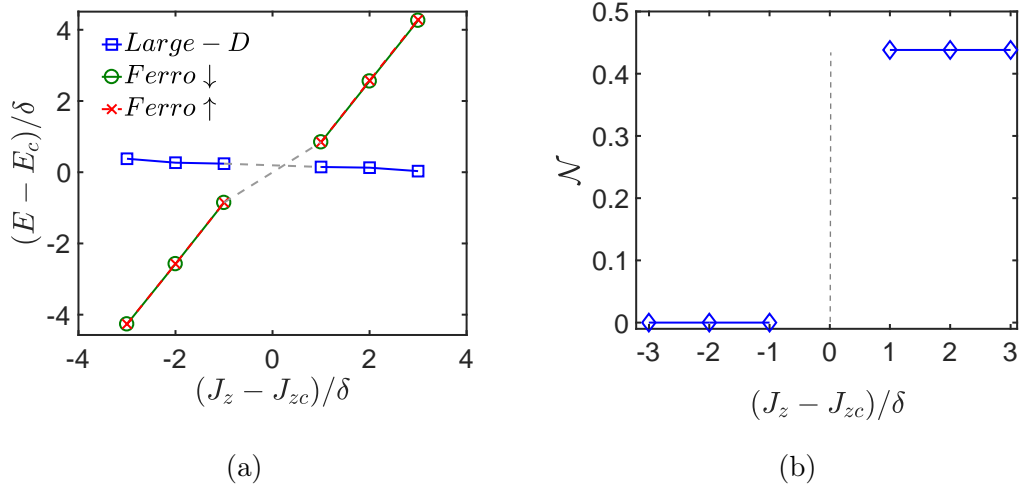


Fig. 5.9 Phase transition between ferromagnetic and large- D for $D = 2$ and $L = 8$. **(a)** The energy crossing between the two-fold degenerate ferromagnetic ground state at $J_z < J_{zc}$ (circles and crosses) and the large- D ground state at $J_z > J_{zc}$ (squares), where the critical energy is $E_c \approx -0.2660$ and $J_{zc} \approx -2.5897$. **(b):** We observe a jump in the negativity (dotted line) for J_{zc} even when using a step $\delta = 10^{-13}$. The results are obtained with ED.

for small steps of the parameter J_z driving the 10QPT, \mathcal{N} is always discontinuous and a neat level crossing is shown between the two-fold degenerated ferromagnetic ground state, for $J_z < J_{zc} \approx -2.5897$, and the large- D ground state, for $J_z > J_{zc}$. This means that, at J_{zc} , there is a sudden change in the ground state which is detected by a discontinuity in \mathcal{N} . In Fig. 5.9b, therefore, we observe the expected discontinuous behaviour for \mathcal{N} along a 10QPT, even for a system of just $L = 8$ spins without any finite-size effects.

Néel/Large- D Transition

Lastly, we focus on to the large- D /Néel 10QPT. In Fig. 5.10 we display the negativity and the staggered magnetisation for a fixed value $J_z = 3.8$ as a function of the anisotropy, D , around the critical point $D_{c,L}$ for a fixed length L , denoted by (2) in Fig. 5.5. We add the subindex L to indicate that this quantity now depends on the system size. In order to show the behaviour for larger systems, we use DMRG calculations for $L = 32, 64, 128$ and 150 . In Fig. 5.10a and Fig. 5.10c, we observe that both, \mathcal{N} and the staggered magnetisation, $M_z^{st} = \sum_{i=1}^L (-1)^i \langle S_i^z \rangle$, change smoothly around the transition point. As L increases, the slope becomes more pronounced getting closer to a discontinuity and we need values of D closer to the critical point to observe the continuous slope. For instance, the necessary step in D to observe a continuous behaviour is $\delta \sim 10^{-4}$ and $\delta \sim 10^{-6}$ for $L = 64$ and $L = 150$, respectively. Note that in this case, as in section 5.2.1, we are very close to a 20QPT. As we get further from the tricritical point, i.e., as we increase

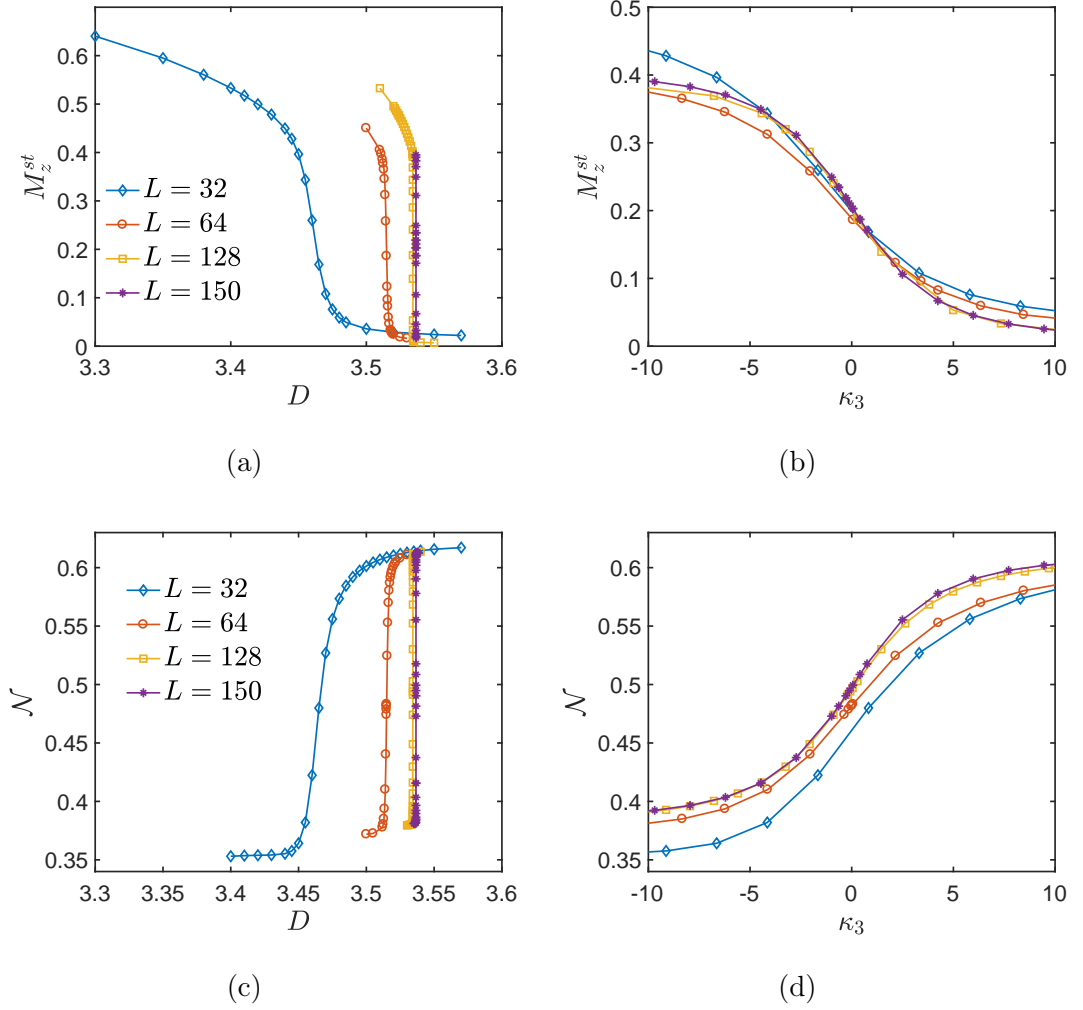


Fig. 5.10 The staggered magnetisation and the negativity around the large- D /Néel transition, where $J_z = 3.8$. The staggered magnetisation M_z^{st} is shown in (a) against the parameter D and in (b) against the scaling variable κ_3 , Eq. (5.14). The negativity is shown against D in (c) and against κ_3 in (d). We observe a smooth slope of both the negativity and the staggered magnetisation where the 1OQPT is expected. Both measurements, as a function of κ_3 , show a tendency to converge towards a universal function. The results are obtained with DMRG and bond dimension $\chi = 150$ for which they are converged.

the value to $J_z \gg J_{zc} = 3.8$, this effect progressively becomes less important and both \mathcal{N} and M_z^{st} are effectively discontinuous. Since the transition is known to be of first-order, we propose a similar FSS as in the previous section, defining a relevant scaling variable, κ_3 , as the ratio between the energy contribution of D along the transition and the gap at the critical point,

$$\kappa_3 \sim \frac{(D - D_{c,L})L}{\Delta_L}. \quad (5.14)$$

Now, Δ_L is obtained numerically and $(D - D_{c,L})L$ is a bare estimation for the energy contribution of the parameter D . In Fig. 5.10b and Fig. 5.10d, we plot M_z^{st} and \mathcal{N} as a function of this scaling variable κ_3 . As we can observe, both quantities seem to converge, though not perfectly, towards a universal scaling, as described by Eq. (5.5). It is worth mentioning that Eq. (5.14) is an approximation whereas, in the previous section we had analytic expressions for Δ_L and m_0 in Eq. (5.7). Actually, in Ref. [189], a similar FSS, with non-analytic expressions, is proposed for the Potts chain with a similar convergence. It seems reasonable, thus, to state that for this 1OQPT, when we are close to the 2OQPT, \mathcal{N} is continuous due to finite-size effects and that it obeys the scaling ansatz for 1OQPT.

5.3 Analysis of Entanglement Features through Density Matrices

Let us discuss here the origin of the concurrence's continuity together with its discontinuous first derivative across the the 1OQPT in the spin-1/2 Ising model described in Eq. (5.6). A similar response is shown by the negativity in the spin-1 XXZ chain across the 1OQPT between the N  el/Anti-N  el phases. These transitions must fall under one of the exclusions to the expected behaviour stated in Ref. [180] (see Th. 5.1.2) that links a singularity in the first derivative of the pairwise entanglement to a 2OQPT, given that this singularity originates exclusively from the elements of ρ^{ij} , in Eq. (5.2).

To determine the origin of this unusual behaviour, we focus on the Ising longitudinal model and analyse the elements of the reduced density matrix of the two central spins (ij) that we denote by $\rho(A, B) \equiv \langle A | \rho^{ij} | B \rangle$ as a function of the longitudinal field, B_x , for different values of the transverse magnetic field B_z . For simplicity of notation we remove from now on the spin indices i, j . Given the symmetries of the Hamiltonian, it suffices to consider just two different matrix elements, $\rho(1, 1) = \langle \uparrow\uparrow | \rho^{ij} | \uparrow\uparrow \rangle$ and $\rho(1, 2) = \langle \uparrow\uparrow | \rho^{ij} | \downarrow\uparrow \rangle$, for analysing the behaviour of the concurrence. As plotted in the Fig. 5.11, $\rho(1, 2)$ is discontinuous along the 1OQPT transition, while $\rho(1, 1)$ presents a spike signalling a singularity in its first derivative. In the bottom panels, we display our results regarding their scaling behaviour as a function of the relevant scaling parameter κ_1 (see Eq. (5.7)). Interestingly enough, as shown in Fig. 5.11d, the matrix element $\rho(1, 2)$ follows exactly the same scaling proposed for 1OQPT [36], when it is renormalised by dividing out its maximum $\rho(1, 2)$, while in Fig. 5.11c it is the renormalised derivative of the matrix element $\rho(1, 1)$ ($\partial_{B_x}\rho(1, 1)$) and not the matrix element itself which scales properly for different values of L and B_z . Furthermore, it can be shown that all the discontinuities present in elements such as $\rho(1, 2)$ cancel out when computing the concurrence. As a result, the concurrence \mathcal{C} shows a

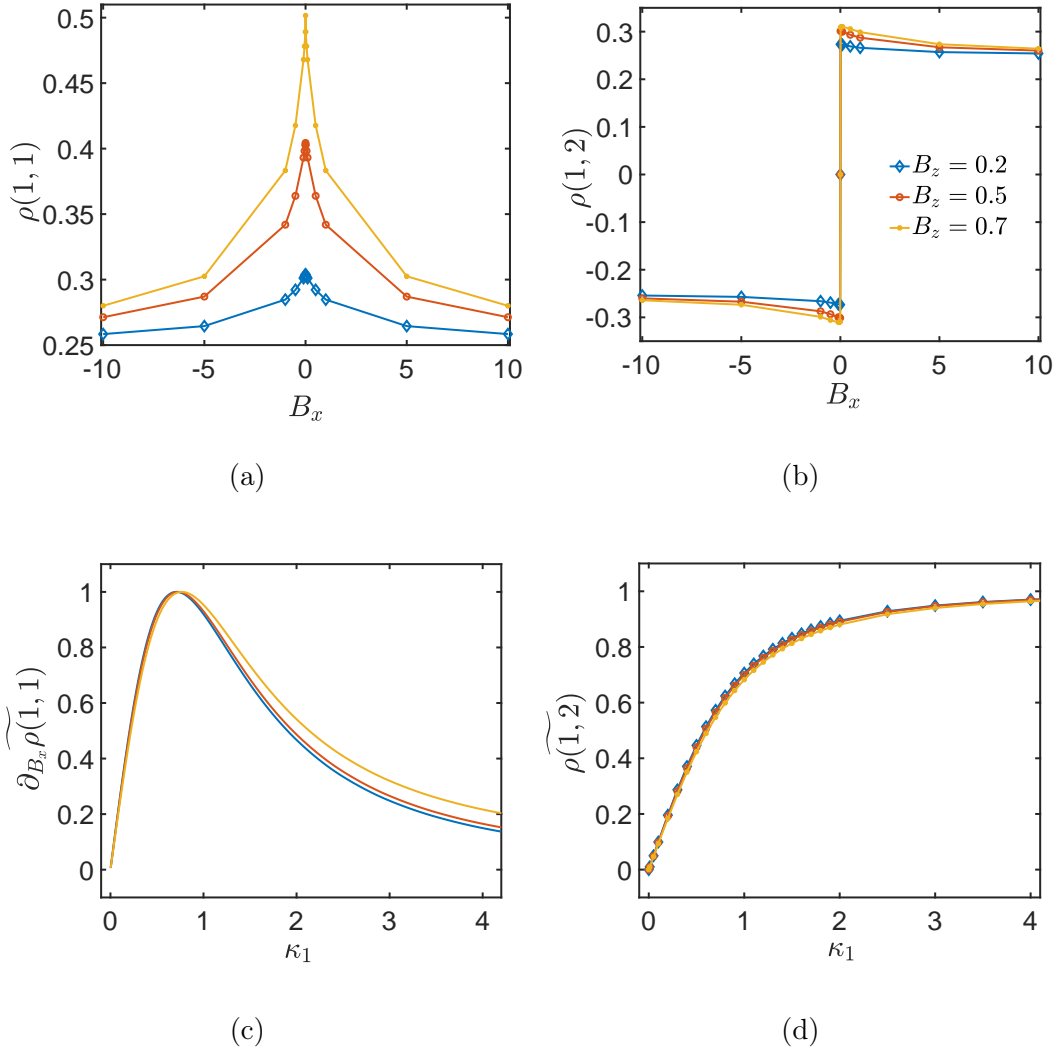


Fig. 5.11 Matrix component behaviour for the reduced density matrix $\rho^{ij}(A, B) = \langle A | \rho^{ij} | B \rangle$ of the two central spins (i, j) for a chain of length $L = 12$ along the 1OQPT for Ising model in the longitudinal field (Eq. (5.6)). For simplicity of notation we remove the indices (i, j) , see text. **(a)**: Example of a spike at the critical point in $\rho(1, 1)$ for different values of B_z . **(b)**: Example of a discontinuity in $\rho(1, 2)$ at the critical point. **(c)**: Scaling behaviour of $\partial_{B_x} \rho(1, 2)$ as a function of κ_1 . **(d)**: Scaling behaviour of renormalised $\rho(1, 2)$ as a function of the scaling parameter κ_1 ; d) Results obtained with ED.

singularity in the first derivative as it would happen in a 2OQPT and $\partial_{B_x} \mathcal{C}$ is precisely the quantity which fulfils the FSS and not \mathcal{C} itself.

The same analysis applies to the spin-1 XXZ chain with on-site anisotropy, where a dip in the negativity, \mathcal{N} , appears at the critical point as shown in Fig. 5.6. This behaviour has the same origin as the previously reported spin-1/2 case, as it also comes from a symmetric Ising type transition and, therefore, it is the

derivative of \mathcal{N} (see Fig. 5.7) and not the negativity itself which fulfils the FSS for 1OQPTs. Hence, in these cases, a singularity in the first derivative of the concurrence/negativity (given that the concurrence/negativity are continuous functions), does not signal a 2OQPT due to accidental cancellations of the density elements as it was conjectured in Ref. [180].

5.4 Conclusions

In conclusion, in this chapter we have analysed pairwise entanglement behaviour in diverse 1OQPT transitions driven by two-body local Hamiltonians. We have shown the dramatic importance of finite-size effects when a 1OQPT occurs in the nearby region of multi-critical point containing also a 2OQPT. To illustrate this fact, we have shown examples of 1OQPTs in two-body local Hamiltonians in which pairwise entanglement measures are continuous across the phase transition while their first derivatives are not. We have extended our results by using non-integrable models in which the same behaviour can be observed. A deeper analysis shows that the behaviour is inherited from the two-body reduced density matrix elements, which for two-body local Hamiltonians, are linked to the non-analyticities of the ground state energy. Our main result has been to demonstrate that for finite systems, the order of the quantum phase transition in symmetry broken phases is given by the scaling behaviour of their bipartite entanglement and not by its non-analytical character. Our results should allow to better determine the order and boundaries of quantum phase transitions near multi-critical points.

CHAPTER VI

THE FRUSTRATED RHOMBI (DIAMOND) MODEL

“When we long for life without difficulties, remind us that oaks grow strong in contrary winds and diamonds are made under pressure.”

Peter Marshall

This chapter will focus on the a frustrated version of the Bose-Hubbard (BH) model in a structured 1-D lattice. The geometry that we have chosen consists of a chain of rhombi (also referred to as diamond, square or AB_2 lattice), based on my work “The Rhombi-Chain Bose-Hubbard Model: geometric frustration and interaction” [190]. This model and others with frustration, have increased in interest in recent years [151, 191–195] both as a result of experimental advancements and due to the promising applications of their features including energy flat-bands, localisation effects and enforced pairing (outlined in Sec. 2.4).

We will focus on a commensurately filled system and explore the phase diagram of the model, particularly to check that we obtain a phase which is an LL of pairs, called pair Luttinger liquid (PLL), when the system is frustrated (with a magnetic flux of π). We analyse the stability of this region and provide a comparison with the unfrustrated case. Lastly, we investigate the entanglement within the system by examining the entanglement entropy and its spectrum.

6.1 Formulation of the Rhombi Model

We will initially describe what the rhombi model is and then we will discuss some of the previous studies exploring it in Sec. 6.2. In this lattice, each rhombus is

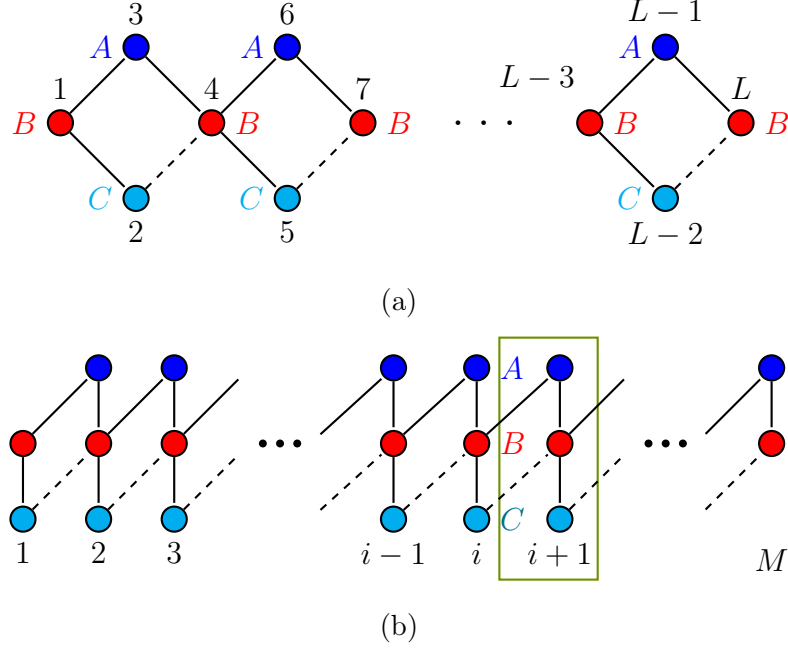


Fig. 6.1 1-D lattice of rhombi with M cells and L sites. Each cell contains three sites labelled A, B, C . Solid (dashed) line connections indicate a tunnelling amplitude $-J$ ($-Je^{i\phi}$). (a) is the representation of the model in real space showing the number of sites whereas (b) is a schematic diagram to illustrate the cells more clearly.

pierced by a tuneable magnetic flux ϕ (which is shown by the dashed lines in Fig. 6.1). When ϕ is an odd multiple of π , the model is fully-frustrated, with a number of interesting properties to investigate.

The Bose-Hubbard model (Sec. 2.2.2) is used to describe the quasi-1-D chain of rhombi. The geometric lattice is depicted in Fig. 6.1. The unit cell of such a lattice is made of three sites that we label A, B and C . The coordination number of the sites A and C is two, whilst it is four for the B sites¹. We consider only nearest-neighbour hopping and on-site interactions, which is common in cold-atomic setups. The Hamiltonian is:

$\mathcal{H}_{BH} = \mathcal{H}_0 + \mathcal{H}_U$ where:

$$\begin{aligned} \mathcal{H}_0 &= -J \sum_j \sum_\ell \sum_{\alpha, \beta} T_{\alpha, \beta}^{(\ell)} b_{j+\ell, \alpha}^\dagger b_{j, \beta}, \\ \mathcal{H}_U &= \frac{U}{2} \sum_j \sum_\alpha n_{j, \alpha} (n_{j, \alpha} - 1). \end{aligned} \quad (6.1)$$

¹The reader is asked to note that this notation differs from that of Vidal and Douçot [84] and of Mukherjee et al. [194]

The index j denotes the lattice cell, the Greek letters label the basis inside a cell, i.e., $\alpha, \beta \in \{A, B, C\}$, and $\ell \in \{0, \pm 1\}$ represents the (relative coordinate of the) cell where the particle is hopping to. The operator $b_{j,\alpha}^{(\dagger)}$ denotes the annihilation (creation) operators, and $n_{j,\alpha} = b_{j,\alpha}^\dagger b_{j,\alpha}$ is the corresponding number operator (defined in Sec. 2.2.2). We will once again consider a chain with OBC, as shown in Fig. 6.1. This chain contains M cells, but to avoid spurious effects at the edges we often only consider the $M - 2$ complete cells. The overall chain consists of $L = 3M - 2$ sites in total, which corresponds to $M - 1$ full rhombi.

To accommodate a piercing (synthetic) magnetic flux ϕ through each rhombus, we choose the hopping matrices to be:

$$T^{(0)} = \begin{pmatrix} 0 & 1 & 0 \\ 1 & 0 & 1 \\ 0 & 1 & 0 \end{pmatrix}, \quad T^{(+1)} = \begin{pmatrix} 0 & 1 & 0 \\ 0 & 0 & e^{i\phi} \\ 0 & 0 & 0 \end{pmatrix}, \quad T^{(-1)} = (T^{(+1)})^\dagger. \quad (6.2)$$

The dashed connections in Fig. 6.1 denote a tunnelling coefficient of $-Je^{i\phi}$, whereas the solid lines have tunnelling coefficient $-J$. We emphasise that this is one of the many possible gauge choices that exist. Provided the full flux of ϕ propagates around each rhombi it can be split in any way and on any from one to four of the legs e.g., distributing homogeneously the flux as $e^{\pm i\phi/4}$ on each of the four links is an alternative form, which might be even more convenient for experimental purposes [196–198].

As we proceed, A and C sites will sometimes be referred to as the rim sites and B sites as the hub sites. This is because if the flux is small enough, the effects due to the geometry are very small and instead the presence of A and C can be thought of as border effects to the strictly 1-D lattice of B sites only.

6.2 Previous studies of the model

In order to make quantum computers attainable, it is required to have a large number of approximately degenerate quantum states without external perturbations, which are insensitive to any random fluctuations that exist. The geometry of a chain of rhombi within the BH model was proposed using JJAs as a method to create topologically protected quantum memory [199–201]. As a result of the geometry, the existence of quantum fluctuations will enforce a condensate of bound Cooper pairs with charge $4e$ (i.e. essentially equivalent to a superfluid of pairs). A system of this type has a locally conserved \mathbb{Z}_2 symmetry, which occurs due to the parity of the number of Cooper pairs on a given superconducting island. The protected state can be stored within this parity to make it secure. This satisfies the criteria stated above for quantum computers. It has a degenerate ground

state described by a topological order parameter and the manifold of the states is considered to be protected because the local perturbations have an exponentially weak effect on the relative phase and transition amplitude.

Vidal and Douçot examined this model in the quantum rotor (large occupation) limit and were able to draw a number of conclusions analytically, with their predictions largely based on symmetry arguments [83, 84]. They discovered that flat-bands occur as the Bloch bands of the model due to a collection of **AB** cages. The presence of these **AB** cages can be emphasised in the occurrence of a $\mathbb{U}(1)$ symmetry within any interaction operator $b_{j,\alpha}^\dagger b_{j,\alpha}$, which physically causes the total number of bosons in each cage to be separately conserved, meaning the system remains in an insulating phase (for us the **MI**). This symmetry can, however, be broken with two-body interactions such as $\sum_j b_{j,\alpha}^{\dagger 2} b_{j,\alpha}^2$ but these still preserve a local \mathbb{Z}_2 symmetry. This local \mathbb{Z}_2 symmetry means that the parity of the total number of bosons in each cage is conserved. They conjectured that if two-particle interactions lead to coherent transport through the chain then **QLRO** may occur for composite objects built for an even number of original bosons, which for them led to bound Cooper pairs of charge $4e$. From this they could predict the occurrence of an **LL** of pairs, which was called the nematic **LL** (but can also be referred to as the pair Tomonaga **LL** or **PLL**). They also motivate that the phase transition between **PLL** and **LL** should be dictated by a \mathbb{Z}_2 symmetry, i.e. it should be of Ising type. A final comment is that they expected the border outlining the region where the **PLL** exists to have exponential decay with the parameters J/U , i.e. the border of the **PLL** should be a curve approximately of the form $e^{(-J/U)}$.

This specific lattice structure has also very recently received a revival in attention, due to both its experimental realisation in two distinct photonic waveguide platforms [194, 195] and to a couple of novel theoretical insights which describe the formation of pairs by focusing on a unifying picture for flat-bands loaded with particles (which should be valid for fermions or bosons) [193] and a hidden topological character of the bands [195].

It should be noted that this model has also previously been studied with fermions by Kobayashi *et al.* [192] with similar effects. Other similar geometrically frustrated models such as the Creutz ladder have been studied in detail in Refs. [95, 191, 202] and a number of recent works have examined fractional fillings [92, 93, 95, 96] where **PLLs** have also been reported.

6.3 Single-Particle Representation of the Model

We will focus on the non-interacting (single) particle case of the model in order to illustrate the flat-bands that occur for the Bloch bands of the system and to describe how the AB cages work within this model. We will also show how the model can be rewritten in terms of the AB cage eigenbasis.

6.3.1 The Energy Eigenspectrum

If the interactions between the model are neglected so that it is described by the Hamiltonian \mathcal{H}_0 , then a single particle considered in the infinite-size, perfectly translational invariant regime (i.e. with no edges) will have the following energy spectrum:

$$E_\tau(k) = 2J\tau \sqrt{1 + \cos\left(k - \frac{\phi}{2}\right) \cos\left(\frac{\phi}{2}\right)}, \quad (6.3)$$

where $\tau = 0, \pm 1$ denotes the three bands and k is the quasi-momentum. This is obtained similarly to how the single particle representation was written for the standard model in Ch. 2. The assumption of infinite-size means that we can again apply the Fourier transform to the Hamiltonian \mathcal{H}_0 in Eq. (6.1) and then obtain the eigenvalues in the new eigenbasis. This results in three eigenvalues as we have a 3×3 matrix to represent the different sites in each cell. An example of this spectrum with $\phi = 0$, $\phi = \frac{\pi}{6}$ and $\phi = \pi$ is shown in Fig. 6.2, where we have considered the range $\phi \in [-\pi, \pi]$ as the band structure is invariant under the insertion of integer flux-quanta (i.e. under $\phi \rightarrow \phi + 2\pi$). When ϕ is an odd multiple of π , full frustration occurs and all three bands of the single particle dispersion relation become flat (Fig. 6.2). This feature of the flat-bands is of importance to mimic physical phenomena as motivated in Sec. 2.4. Interestingly, the flat middle band $\tau = 0$ is insensitive to ϕ and occurs purely due to geometrical reasons [203, 204]. As visible in Fig. 6.2, the curvature of the other two bands decreases with growing flux until they become perfectly flat at *full frustration*, i.e., $\phi = \pi$: $E_\tau^{(\phi=\pi)}(k) = 2J\tau$ [84]. In this formalism there is a chiral (sub-lattice) symmetry operator $\Gamma = \text{diag}\{-1, +1, -1\}$, such that $\Gamma^2 = \mathbb{I}$ and $\Gamma\mathcal{H}_0(k)\Gamma = -\mathcal{H}_0(k)$, is robust with respect to the gauge choice (while other choices could also display lattice-inversion symmetry, for example).

6.3.2 The Aharonov-Bohm Cage Formulation

The simultaneous flatness of *all* bands indicates that this model falls under the property of the AB effect. This means that the model can be split into AB cages, which contain the particle in the absence of interactions [77, 80, 84]. In fact the rhombi model is the geometry that was studied when Vidal *et al.* first coined the

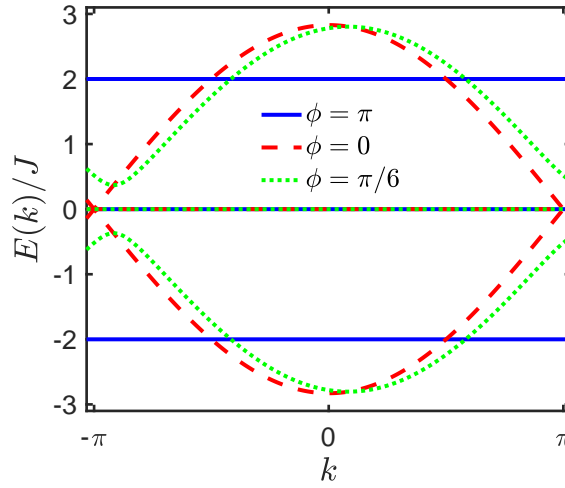


Fig. 6.2 The single particle energy band $E(k)$ as a function of the lattice momentum k . The fully-frustrated $\phi = \pi$ bands are the solid lines, whereas the non-frustrated $\phi = 0$ are shown by dashed lines. An intermediate frustration (at $\phi = \pi/6$) is shown by the dotted lines.

term **AB** cages in 1998 [77]. The sites within a given **AB** cage is shown by opaque circles within the square border in Fig. 6.3. Destructive interference stops a given particle from leaving the cage in either direction (as shown by the lighter circles outside the square and the 0 arising from the probability tunnelling amplitude). This means that a complete basis of fully localised **AB** cages (see Fig. 6.3) can be constructed. Naturally, it is possible to express our model in the basis of these **AB** eigenstates [193].

The perfectly localised eigenmodes $w_{j,\pm}^{(\dagger)}$ for annihilation (creation) occur due to destructive interference preventing the movement of *single* particles from one B site (in cell j) to another (as illustrated in Fig. 6.3). As previously stated, the (middle) zero flat-band is invariant under the ϕ chosen. This means the corresponding eigenmodes $w_{j,0}^{(\dagger)}$ have zero amplitude on the B site of cell j around which they are centred (see Fig. 6.3). In our gauge, these localised modes are:

$$w_{j,\tau} = \frac{(-1)^\tau b_{j-1,C} - (-1)^\tau b_{j,A} - 2\tau b_{j,B} + b_{j,C} + b_{j+1,A}}{(2^{1+|\tau|/2})}. \quad (6.4)$$

As we have chosen an **OBC** setup the cell index j in Eq. (6.4) must be restricted to the full cells, i.e., $j = 2, \dots, M-1$. To describe the edges of the model we require two extra modes $e_{s,\sigma}$ per side ($s = \text{L, R}$ and $\sigma = \pm 1$) which have energies

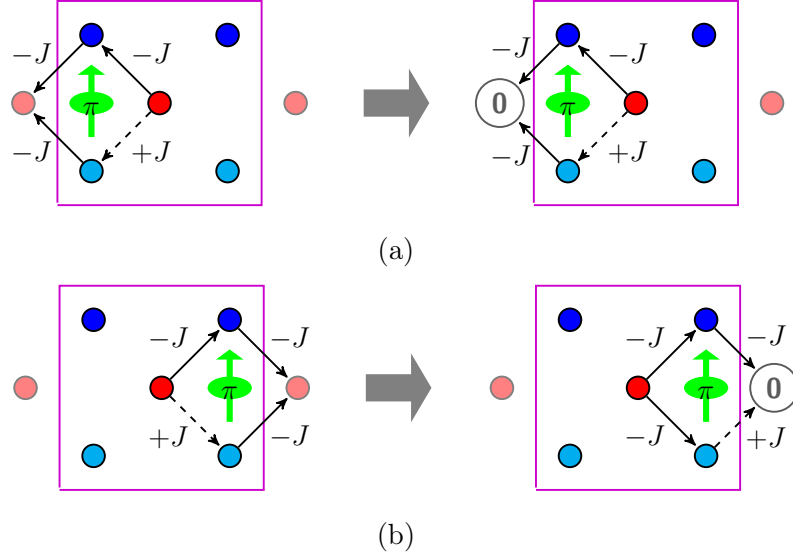


Fig. 6.3 An illustration of a restricted single particle tunnelling for the fully-frustrated system. The sites outside the box are those that leave the AB cage and therefore cannot be accessed. It is shown in (a) and (b) how there is zero probability amplitude of the single particle exiting the cage on the left or the right, respectively.

$\sigma\sqrt{2}J$:

$$\begin{aligned} e_{L,\sigma} &= \frac{-\sigma\sqrt{2}b_{1,B} + b_{1,C} + b_{2,A}}{2} \\ e_{R,\sigma} &= \frac{-\sigma\sqrt{2}b_{M,B} - b_{M-1,C} + b_{M,A}}{2}. \end{aligned} \quad (6.5)$$

The non-interacting Hamiltonian at π flux can be expressed in terms of these eigenmodes as:

$$\mathcal{H}_0^{(\phi=\pi)} = \sum_{j=2}^{M-1} \sum_{\tau \in \{0, \pm\}} 2J\tau w_{j,\tau}^\dagger w_{j,\tau} + \sum_{s \in \{L,R\}} \sum_{\sigma \in \{\pm\}} \sigma\sqrt{2}J e_{s,\sigma}^\dagger e_{s,\sigma}. \quad (6.6)$$

This tunnelling part will be neglected as it simply gives the components $0, \pm 2J$ to the energy bands. The interaction term \mathcal{H}_U in Eq. (6.1) is however, more interesting to analyse. The eigenmodes in Eqs. (6.4)-(6.5) [205] are overlapping, meaning that \mathcal{H}_U , considered only in the bulk of the chain (i.e. avoiding the

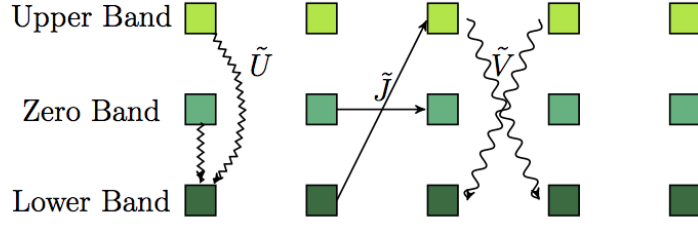


Fig. 6.4 Illustration of the type of cage terms that control the movement and the interaction of the pairs of particles. \tilde{U} is the on-cell interaction of pairs, \tilde{J} is the hopping of pairs between cells and \tilde{V} can be interpreted as nearest-neighbour interaction or correlated swapping of 2 particles across neighbouring sites.

borders), can be rewritten as [84, 202, 206, 207]:

$$\mathcal{H}_U^{(\text{bulk})} = \sum_{\tau_1, \tau_2, \tau_3, \tau_4} \sum_{j=2}^{M-1} \left(\tilde{U}_{\tau_1, \tau_2, \tau_3, \tau_4} w_{j, \tau_1}^\dagger w_{j, \tau_2}^\dagger w_{j, \tau_3} w_{j, \tau_4} \right. \quad (6.7)$$

$$+ \sum_{\ell \in \{\pm 1\}} \tilde{V}_{\tau_1, \tau_2, \tau_3, \tau_4}^{(\ell)} w_{j+\ell, \tau_1}^\dagger w_{j, \tau_2}^\dagger w_{j, \tau_3} w_{j+\ell, \tau_4} \quad (6.8)$$

$$\left. + \sum_{\ell \in \{\pm 1\}} \tilde{J}_{\tau_1, \tau_2, \tau_3, \tau_4}^{(\ell)} w_{j+\ell, \tau_1}^\dagger w_{j+\ell, \tau_2}^\dagger w_{j, \tau_3} w_{j, \tau_4} \right) \quad (6.9)$$

where $\tau_1, \tau_2, \tau_3, \tau_4 \in \{0, \pm\}$ and all of the amplitudes are linear in U . If the full chain is considered there are similar terms for the edges as well. The full form of the different terms in $\mathcal{H}^{(\text{bulk})}$ can be found in the Mathematica script in Appendix. A. As an example of the nature of these terms, we show the Hamiltonian with terms restricted to the lowest band:

$$\begin{aligned} \mathcal{H}_{U, -1}^{(\text{bulk})} = & \frac{5}{32} \sum_{j=2}^{M-2} n_{j, -1} (n_{j, -1} - 1) \\ & + \frac{1}{16} \sum_{j=3}^{M-2} n_{j-1, -1} n_{j, -1} \\ & + \frac{1}{64} \sum_{j=3}^{M-2} (w_{j-1, -1}^\dagger w_{j, -1}^\dagger + w_{j, -1}^\dagger w_{j-1, -1}^\dagger) \end{aligned} \quad (6.10)$$

where $n_{j, -1} = w_{j, -1}^\dagger w_{j, -1}$. The appearance of a pair-tunnelling term, with the minimum of the dispersion relation at momentum $k = \pi$ can be seen in Eq. (6.10).

There are a number of other studies [80, 81, 96] which have performed projection onto lowest-band states, instead of retaining the full description of the model. This

is in analogy to the lowest Landau level projection in quantum Hall systems and is applicable provided interactions are smaller than the gap between the bands. If the interactions are formulated in this way, it is more evident that a local \mathbb{Z}_2 symmetry is preserved by the Hamiltonian, namely the parity of the population of all three kinds of cages localised around each hub B , i.e.,

$$[\mathcal{H}_{\text{BH}}, P_j] = 0 \quad \forall j \quad \text{with} \quad P_j \equiv \exp \left[i\pi \sum_{\tau} w_{j,\tau}^{\dagger} w_{j,\tau} \right]. \quad (6.11)$$

In particular, the interaction effects (Eq. (6.7)-(6.9)) can be sorted out in three different kinds:

- (i) \tilde{U} : interactions and cage flavour-flips around a given hub;
- (ii) \tilde{V} : interactions and correlated flips between nearest-neighbouring hubs;
- (iii) \tilde{J} : pair-tunnelling (possibly with flips) between nearest-neighbouring hubs.

An example of each of these terms is pictorially shown in Fig 6.4. The \tilde{J} terms explicitly show that a delocalisation of particle (bound) pairs is possible, in spite of the single particle perfect localisation. When this takes place and how robust this pair coherent phase actually is, forms the core subject of our work, which aims to extend the seminal results by Douçot and Vidal [84].

6.4 Identifying the Phases

Motivated by the previous studies we expect to observe a PLL for the fully-frustrated case (i.e. when $\phi = \pi$) in the limit of large tunnelling rate and the MI phase when the interactions dominate. At zero interactions and full frustration, we also expect an insulating state, though of a different kind, since all single-particle wavefunctions are localised. This is, however, not the case as soon as a tiny interaction is present. As shown above (Sec. 6.1), the on-site Hubbard interaction induces pair-hopping terms between neighbouring sites (Eq. (6.9)), which in turn can be shown to lead to a pair quasi-condensation (a PLL) [84, 193]. These occur without violating the extensive collection of local \mathbb{Z}_2 invariants of Eq. (6.11).

If the flux is small enough, we have commented that the geometric effects are small and that the rim sites A and C are border effects to the strictly 1-D lattice of B sites only. These rim sites simply change the single-particle band curvature and, therefore, renormalise the critical coupling between the MI and the “standard” LL [46]. For the non-frustrated case, therefore, the model should be more similar to that of the standard BH model, i.e. we should have a renormalised MI phase and an LL phase after a certain critical J/U . If we have zero flux i.e. $\phi = 0$, then we expect the standard MI and LL phases which are only modified due to

geometrical effects.

We will describe how we obtained the transition point and how we confirmed the existence of the [MI](#), [LL](#) and [PLL](#) phases. Examples will be given typically for the fully-frustrated ($\phi = \pi$) and the unfrustrated case ($\phi = 0$) but the same analysis holds for the identification of the phases with intermediate ϕ .

6.4.1 The Mott-Insulator Lobe

We will consider the commensurate filling of one particle per physical site, i.e., three particles per lattice cell ($N = L = 3M - 2$). As motivated by the standard [BH](#) model along a single [1-D](#) chain (Sec. 2.2.2), we expect to observe an [MI](#) phase when the interactions are infinite, i.e. as $J/U \rightarrow 0$. As the kinetic energy has no role in this scenario, the [MI](#) should appear regardless of the flux chosen.

When the flux is zero, we expect to observe the well-known [MI](#) to [LL](#) phase at a critical coupling slightly renormalised due to the microscopic geometry of the lattice. At magnetic flux π , however, single particle transport is absent and the [LL](#) cannot occur but the Mott lobe still closes (Sec. 6.4.1) and transport occurs by the flow of boson-pairs, which forms the more exotic [PLL](#) phase [83, 84].

In the case of unit filling, the dominance of the on-site repulsion U over the tunnelling coefficient J leads to the gapped [MI](#) phase. This [MI](#) phase has the noticeable difference that the particle distribution is uniform across different cells, but not within them.

The position of the [BKT](#) transition from [MI](#) to the compressible gapless phase, in either the [LL](#) or the [PLL](#) case, can be reasonably estimated by the vanishing of the compressibility gap. We can denote the energy cost for adding or removing n particles by:

$$\mu_{+n} = \lim_{L \rightarrow \infty} \frac{E_{L+n} - E_L}{n}; \quad \mu_{-n} = \lim_{L \rightarrow \infty} \frac{E_L - E_{L-n}}{n}, \quad (6.12)$$

where E_N represents the ground-state energy of N particles. The [MI-LL](#) transition happens as soon as $\mu_{+1} = \mu_{-1}$ [46]. The Mott lobe, i.e., the stability region of the [MI](#) in terms of the chemical potential, $\mu_{-1} < \mu < \mu_{+1}$, is illustrated in Fig. 6.5. We notice that since we do not explicitly impose the local \mathbb{Z}_2 constraint, this same criterion works also for the [MI-PLL](#) transition, coinciding exactly with the apparently more appropriate definition of $\mu_{+2} = \mu_{-2}$.

The ground state energies at fixed number of particles have been obtained via numerical [MPS/DMRG](#) simulations (see Ch. 3) on finite-size systems with [OBCs](#), explicitly preserving the Abelian $U(1)$ symmetry. The local Hilbert space has been truncated to $n_{\max} = 4$ bosons per site and the bond dimension χ was increased until convergence. Typically $\chi = 200$ was sufficient to obtain a maximal discarded weight of $\mathcal{O}(10^{-7})$ or better.

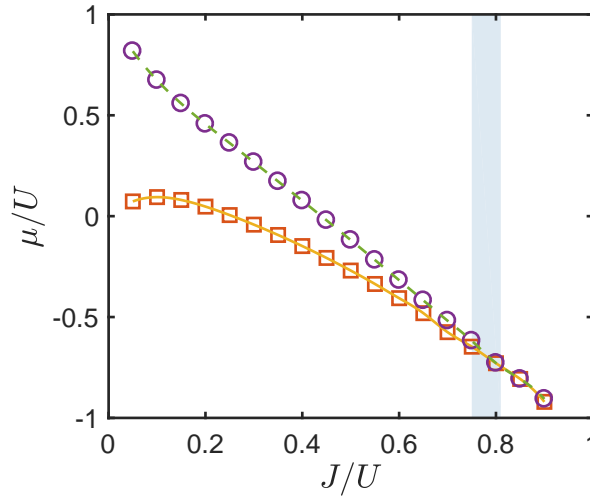


Fig. 6.5 Ground state phase diagram at unit filling $N = L$ and full frustration $\phi = \pi$ in the $\mu/U - J/U$ plane. Circles and squares represent the numerical data for μ_+ and μ_- , respectively. The region $\mu_- < \mu < \mu_+$ is the Mott-insulator lobe. The two lines are cubic splines approximations. Their crossing occurs at the **BKT** point $J_c \approx (0.78 \pm 0.03)U$ indicated by the shaded region.

An **FSS** of the μ 's, has been performed, according to the prediction $\pm(E_{L\pm n} - E_L)/n - \mu_{\pm n} \simeq \mathcal{O}(1/L)$ for chains up to 75 rhombi (i.e., $L = 226$ sites). Finally, the **BKT** tip of the lobe is estimated by cubic splines interpolation of the functions $\mu_{\pm}(J/U)$, as depicted in Fig. 6.5 for the fully frustrated case, $\phi = \pi$: the result is $(J/U)_c^{[\phi=\pi]} = 0.78 \pm 0.03$ as indicated by the shaded region. This frustrated value is considerably larger than the completely unfrustrated one, $(J/U)_c^{[\phi=0]} = 0.14 \pm 0.01$, which was obtained in the same way. This in turn is roughly one half of the purely **1-D-chain** value $(J/U)_c^{[1D]} = 0.30 \pm 0.01$ [46], due to the presence of the rhombi (which enlarge the bandwidth by a factor $\sqrt{2}$).

As we have commented, the on-site density of the **MI** is different between the three sites in each cell but it should be uniform across different cells. To highlight this we plot a sample of the density in Fig. 6.6 for all of the possible phases **MI**, **LL** and **PLL**. The on-site density distribution is reasonably uniform across the cells within the chain, with boundary effects only slightly affecting the two more external cells on either side. In all cases (except for when J/U is very small as shown in Fig. 6.6a) the density on the B sites is always larger than uniform filling (one per site) and has the same approximate magnitude away from the borders. A summary of the on-site density for different tunnellings is shown by plotting the average $\langle n_{\alpha} \rangle$ of a chain of 226 sites (75 rhombi) for $\phi = 0$, $\phi = 0.9\pi$ and $\phi = \pi$ in Fig. 6.7. From this we notice some main features:

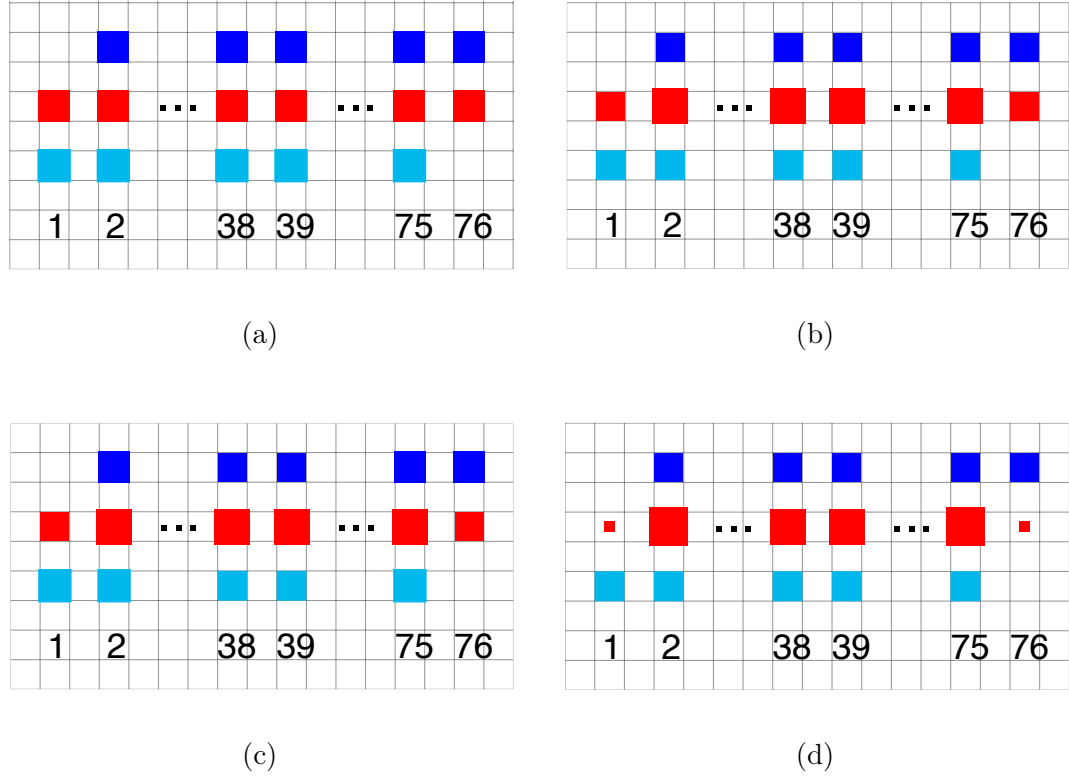


Fig. 6.6 Sample density sites for (a): $J = 0.1$ (MI) and (b): $J = 0.5U$ (LL) in the unfrustrated ($\phi = 0$) case and for (c): $J = 0.5$ (MI) and (d): $J = 0.9$ (PLL) in the frustrated ($\phi = \pi$) case for $L=226$. The sample densities are shown for the A (blue), B (red) and C (cyan) sites in vertical order from top to bottom. The area of each cell on the grid is one, to correspond to uniform filling. The area of the coloured squares are the on-site density at the labelled sites.

- (i) The different connectivity of the sub-lattices leads to an enhanced density $\langle n_\alpha \rangle$ on the hubs $\alpha = B$ with respect to the rims $\alpha = A, C$ (see Fig. 6.6 and Fig. 6.7).
- (ii) The effect of the magnetic flux ϕ is most evident at intermediate J/U but this is where one system is in a different phase to the other (gapped MI or gapless LL/PLL). Deep in the MI phase there is very little discrepancy between the unfrustrated ($\phi = 0$), intermediate frustrated ($\phi = 0.9\pi$) and the fully frustrated ($\phi = \pi$) in Fig. 6.7. Before the first transition out of MI at $J_c^{[\phi=0]} = 0.14$, the discrepancy is as small as 0.2% between the fluxes examined, though here U dominates so strongly that any effects due to the flux are negligible.
- (iii) Finally, the growth of the hub/rim imbalance appears to depend mostly on the competition between J over U , with the hub density experiencing an increase as J/U increases. The function has a less pronounced curve (closer to a linear dependence) in the MI phases, due to the restrictiveness of the

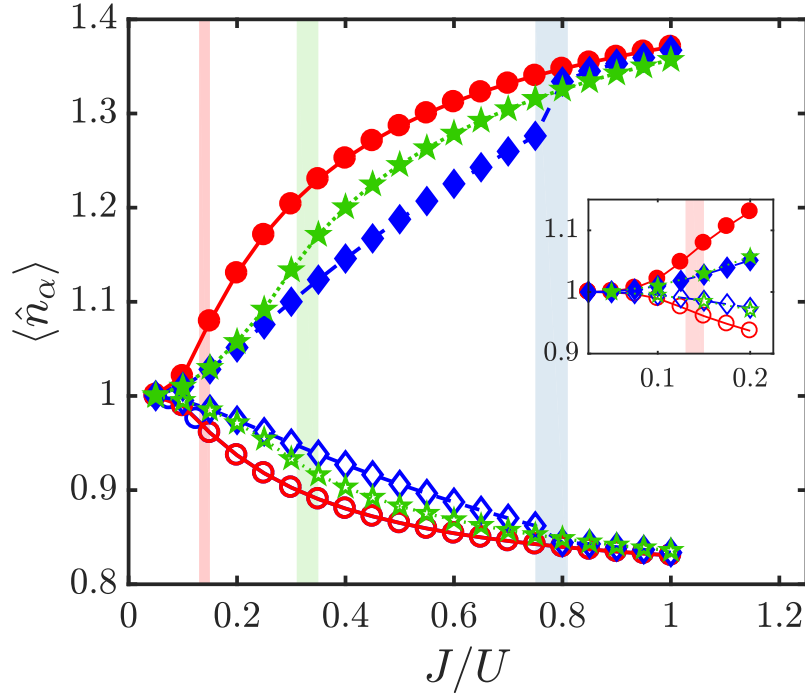


Fig. 6.7 Illustration of the spread of the on-site density $\langle n_\alpha \rangle$ averaged over the lattice of 226 sites for $\chi = 300$ as the tunnelling and frustration is varied. Here the non-frustrated ($\phi = 0$) is shown by the red circles (\circ), the intermediate frustration ($\phi = 0.9\pi$) is shown by the green dotted pentagrams (\star) and the fully frustrated ($\phi = \pi$) are the blue dashed diamonds (\diamond). The density of the B sites is shown by filled markers and sites A and C (which have equal on-site density) are shown by the empty markers. Again the approximate critical points are highlighted by the shaded regions at $J_c^{[\phi=0]} = 0.14$ (red), $J_c^{[\phi=0.9\pi]} = 0.33$ (green) and $J_c^{[\phi=\pi]} = 0.78$ (blue). The inset is a zoomed in version close to the $\phi = 0$ MI-LL transition.

phases (see Fig. 6.7). In the fully frustrated case (blue diamonds) there is a more pronounced jump around the transition point, which does not occur in either of the other cases at $\phi = 0$ and $\phi = 0.9\pi$ (red circles and green pentagrams).

6.4.2 Gapless Phases

The transition point where the system enters into a gapless phase was identified by the closure of the Mott lobe for $\phi \in [0, \pi]$ in increments of 0.1π . In order to characterise these gapless phases outside the Mott insulator lobe, we resort here to spatial correlations of single $[s]$ and pair $[p]$ operators, and their Fourier transform. We formed 3×3 matrices of the different combinations across the i and $i + r$ cells:

$$D_{\alpha,\beta}^{(i,i+r)[s]} = \langle b_{i,\alpha}^\dagger b_{i+r,\beta} \rangle, \quad D_{\alpha,\beta}^{(i,i+r)[p]} = \langle (b_{i,\alpha}^\dagger)^2 (b_{i+r,\beta})^2 \rangle, \quad (6.13)$$

and the corresponding structure factors [57]:

$$S_{\alpha,\beta}^{[\gamma]}(k) = \sum_{i \neq j} \frac{e^{ik(i-j)}}{M-2} D_{\alpha,\beta}^{(i,j)[\gamma]}, \quad (6.14)$$

where $k \in [-\pi, \pi]$, $\gamma = s, p$ and $M-2$ is the number of full cells. Then we evaluated their eigenvalues (and eigenvectors):

$$D^{(i,i+r)[\gamma]} \mathbf{v}_{\varepsilon}^{(i,i+r)[\gamma]} = \eta_{\varepsilon}^{(i,i+r)[\gamma]} \mathbf{v}_{\varepsilon}^{(i,i+r)[\gamma]}, \quad (6.15)$$

$$S^{[\gamma]}(k) \mathbf{w}_{\varepsilon}^{[\gamma]}(k) = \zeta_{\varepsilon}^{[\gamma]}(k) \mathbf{w}_{\varepsilon}^{[\gamma]}(k), \quad (6.16)$$

where $\varepsilon = 1, 2, 3$ in decreasing order and $\gamma = s, p$. We chose this strategy to better illustrate the behaviour of the correlations as a whole, as opposed to focussing individually on all the different matrix elements.

LL Phase

If the gapless phase is the **LL** phase we expect to see **QLRO** in both the single and pair eigenvalues $\eta^{[s]}$ and $\eta^{[p]}$ [96]. We have fixed $i \approx L/4$ in Eq. (6.15) to suppress boundary effects and looked for power-law versus exponential decay of the different correlation eigenvalues.

Phases occurring reasonably far from full-frustration revealed **QLRO** in both the single and pair particle correlations confirming that they enter into the **LL** upon leaving the MI phase. An example is provided in Fig. 6.8 for $\phi = 0.5\pi$, $J = 0.9$ and $L = 226$, where the **QLRO** is evident in the double logarithmic scale. Here values below the discarded weight of $O(10^{-7})$ are neglected as they are considered to be numerical error. It is evident that the largest eigenvalue η_1 is substantially larger (at least an order of two) than the other two. Due to its dominance, the largest eigenvalue describes the main effects within the system, which will be discussed later.

PLL Phase

The **PLL** phase can be identified as the one exhibiting **QLRO** in the pair correlations (given by the $\eta^{[p]}$ eigenvalues), whilst at the same time the single correlations ($\eta^{[s]}$) are disordered and therefore reveal exponential decay [95]. In the fully-frustrated case ($\phi = \pi$) this is what we expect to happen due to the frustration preventing the movement of the single particles [84]. For $\phi = \pi$, we find that the single particle correlations are always short-ranged and the system cannot

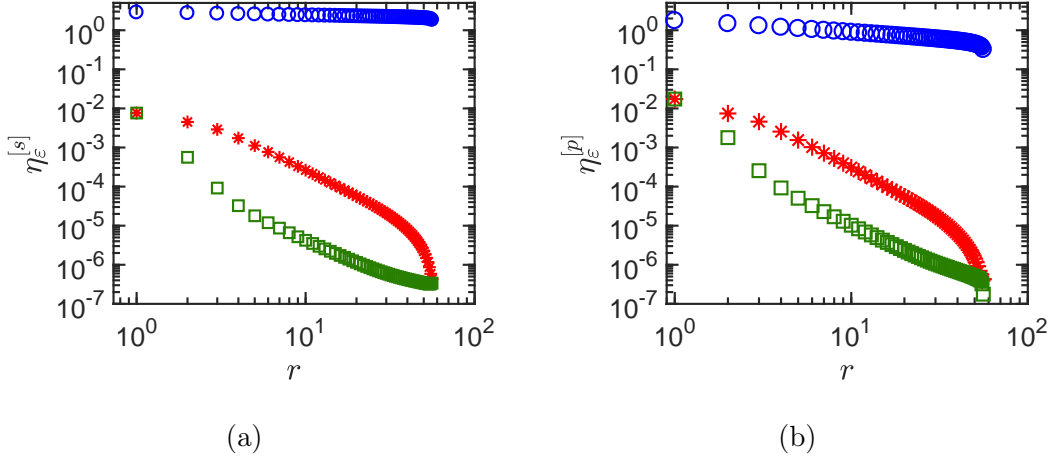


Fig. 6.8 The spatial correlation functions $\eta_\varepsilon^{[\gamma]}$ (where $\gamma = s, p$ and $\varepsilon = 1, 2, 3$) against the intersite distance for an intermediate frustrated case $\phi = 0.5\pi$, $J = 0.9U$, $L = 226$ and $\chi = 300$. The decay is shown of the eigenvalues of the **(a)** single correlations $\langle b_i^\dagger b_{i+r} \rangle$ and **(b)** pair correlations $\langle b_i^{\dagger 2} b_{i+r}^2 \rangle$. Values below a threshold of 10^{-7} , which are below our numerical error, have been excluded. In the diagrams, η_1 (dark blue \bigcirc) is the largest eigenvalue, η_2 (red $*$) is the second largest and η_3 (green \square) is the smallest eigenvalue.

possibly enter the LL phase. In fact all eigenvalues $\eta_\varepsilon^{[s]}$ vanish completely at a distance $r = 2$, thus displaying perfect AB caging (see Eq. (6.4)). This is visible in the insets of panels 6.9a-6.9b.

Concerning the pair correlations, we find that the second and third eigenvalues are always substantially smaller than the dominant one. The second and third eigenvalue are less than 1.5% and 1% of the first respectively at their maximal point, which occurs at the start and then they decay exponentially fast. We therefore focus on $\eta_1^{[p]}$ (blue circles): the semi-logarithmic plot of Fig. 6.9a shows the exponential decay well within the MI ($J = 0.4U < J_c$), while the log-log plot of Fig. 6.9b highlights the algebraic decay a bit beyond the transition to PLL ($J = 0.9U > J_c$).

Fitting the Decay

The decay within the LL and PLL phases can be fitted using the following power-law:

$$\eta_1^{(i,i+r)[\gamma]} \simeq A r^{-\kappa[\gamma]}, \quad (6.17)$$

where $\gamma = [s]$ and $\gamma = [p]$ for the single and pair power law fit, respectively. The exponent $\kappa[\gamma]$ is then plotted in Fig. 6.10 with $\gamma = p$ for $\phi = \pi$ and $\gamma = s$ for $\phi = 0$. In Fig. 6.10a a drastic change in the fitted exponent for $\phi = \pi$ is evident around the critical value $J/U = 0.78 \pm 0.03$, obtained above in Sec. 6.4.1 via the

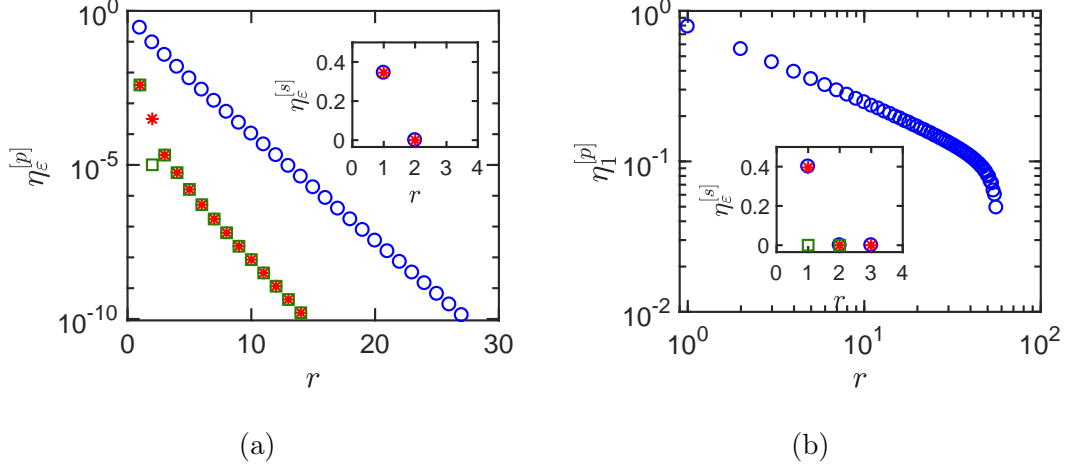


Fig. 6.9 The spatial correlation functions against the intersite distance for the fully frustrated case ($\phi = \pi$) with $L = 226$ and $\chi = 300$. Values below a threshold of 10^{-10} , which constitutes numerical error, have been excluded. η_1 (dark blue \bigcirc) is the largest eigenvalue, η_2 (red $*$) is the second largest and η_3 (green \square) is the smallest eigenvalue. The decay of the eigenvalues of the pair correlations $\langle b_i^{\dagger 2} b_{i+r}^2 \rangle$ for (a) $J = 0.4U$ in semi-logarithmic scale and for (b) $J = 0.9U$ in a double logarithmic scale. The inset is the decay of the eigenvalues of the correlation matrices for the corresponding single correlations $\langle b_i^{\dagger} b_{i+r} \rangle$ at $J = 0.4$ (MI phase) and $J = 0.9U$ (PLL phase).

closure of the compressibility gap. A similar property is seen within the single fitted exponent at $\phi = 0$ (see Fig. 6.10b) which mirrors what is expected within LL theory. LL theory, which we have previously mentioned is the 1-D version of Fermi-liquid theory, has well-defined parameters for the correlations through which all asymptotic properties of these correlations can be obtained exactly [56]. Under this theory,

$$\langle b_i^{\dagger} b_{i+r} \rangle \simeq A r^{-\frac{K}{2}}, \quad (6.18)$$

where $K < \frac{1}{2}$ is the criterion for the MI-LL transition. Here our $\kappa[s] = K/2$ meaning that this system's ground state can be seen to satisfy this criterion for the single correlation functions with $\kappa[s]$ passing through $1/4$ around the transition in Fig. 6.10b at $\phi = 0$. Moreover, the value $\kappa = 0.577 \pm 0.007$ seems to describe very well the PLL, at least in the examined interval $J \in [0.82, 1]U$.

Additionally, we can look at the eigenvector $\mathbf{v}_1^{(i,i+r)[p]}$, which we find to weakly depend on r and on J inside the PLL. For $J = 0.9U$ it reads approximately:

$$v_1^{[p]} = \begin{pmatrix} 0.01 \\ 0.98 \\ 0.01 \end{pmatrix}, \quad (6.19)$$

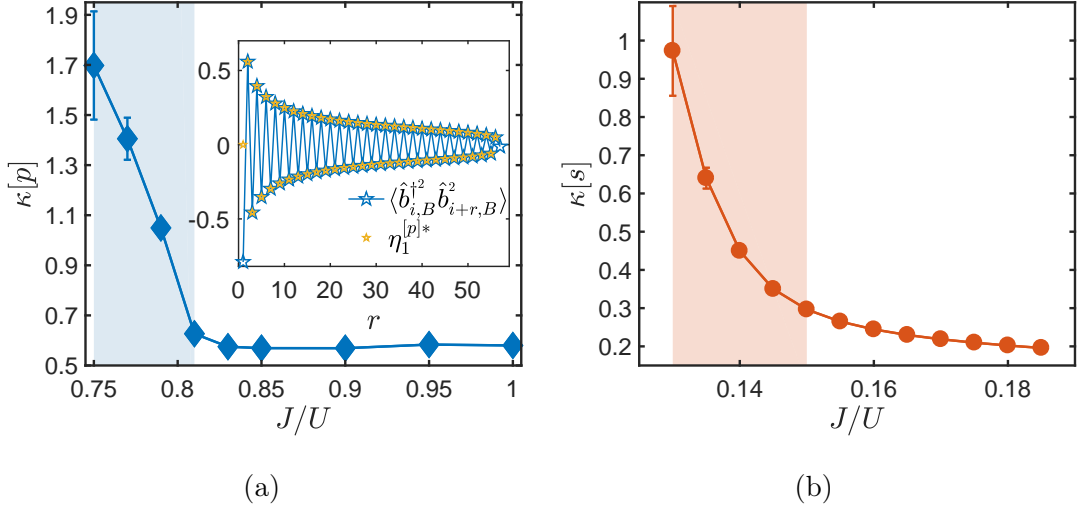


Fig. 6.10 **(a-b)**: Parameter $\kappa[p]$ ($\kappa[s]$) obtained from fitting the pair (single)-correlation function for $\phi = \pi$ ($\phi = 0$) with a power law (see Eq.(6.17)) as a function of J/U for $L=226$. The shaded region indicates the Mott-PLL (Mott-LL) transition region of uncertainty obtained in Sec. 6.5. The inset in **(a)** shows the pair correlations for the B sites $\langle b_i^{\dagger 2} b_{i+r}^2 \rangle$ from $i \approx L/4$ for $J/U = 0.9$ and the corresponding $\eta_1^{[p]*}$ values, which are the maximum eigenvalues retaining their sign.

which highlights the largely predominant role of the hubs B for the QLRO. This is evident by comparing the $\eta_1^{[p]*}$ values (the previously defined $\eta_1^{[p]}$ with their associated sign) with the $B - B$ correlations in the inset of Fig. 6.10a. For $\eta_1^{[p]*}$ we notice the alternating sign for even-odd distances and that the magnitude of this oscillation is practically equal to that of the $B - B$ correlations, except for a case at each end.

Structure Factor

The structure factor of Eq. (6.14) was computed by including all complete cells, excluding only the two incomplete ones at the edges (see Fig. 6.1). The alternating character of the pair correlations gets reflected in a macroscopic peak at $k = \pi$ of the largest structure factor eigenvalue ζ_1 , as shown in Fig. 6.11 for $J = 0.9U$ and $L = 226$ sites. The corresponding eigenvector for the largest eigenvalue reads $\mathbf{w}_\varepsilon^{[\gamma]}(\pi) \simeq (0.1, 0.8, 0.1)^T$, displaying again the dominance of B sites in the pairing mechanism, while the A and C sites have an equal but very small effect. It should be noted that this only differs from the pair correlations eigenvector due to the fact that the structure factor is calculated for all full cells; if it is considered only

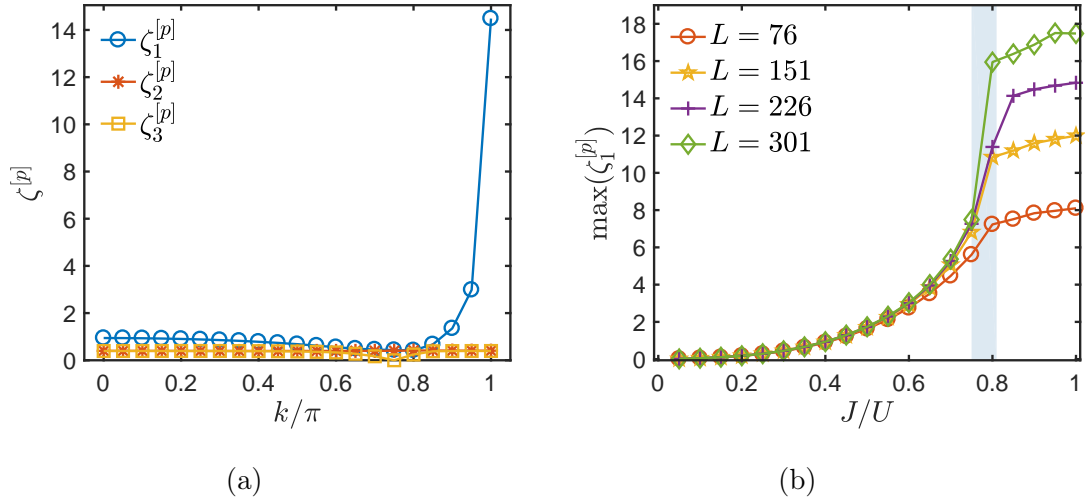


Fig. 6.11 Eigenvalues $\zeta_\epsilon^{[p]}$ of the structure factor matrix for the pair correlations for $J = 0.9U$, $\chi = 300$ for **(a)** $L = 226$ and as a function of the crystal momentum k and **(b)** the peak at $k = \pi$ for different system lengths L .

from the quarter cell then we once again obtain the average:

$$\mathbf{w}_\epsilon^{[\gamma]}(\pi) \simeq \begin{pmatrix} 0.01 \\ 0.98 \\ 0.01 \end{pmatrix}. \quad (6.20)$$

The scaling of the peak at $k = \pi$ of the structure factor with the system size L can also be taken as an indicator of the phase transition. This peak is plotted for different J/U and system sizes as shown in Fig. 6.11b. It can be seen that it starts to become macroscopic (i.e., to diverge with the increasing length L) in the PLL phase ($J \geq 0.75U$), while it stays finite in the Mott region (as indicated by data collapse).

6.5 The Complete Phase Diagram

As we have previously motivated, the full phase diagram with ϕ and J/U varied will consist of regions of MI, LL and PLL phases. In Fig. 6.12 we show the complete phase diagram of the model as J/U and ϕ vary. The transitions from MI to the corresponding gapless phase were obtained by evaluating the compressibility gap, as shown in Sec. 6.4.1, while the LL-PLL transition was determined by examining the correlation decay as done in Sec. 6.4.2. Single-particle Green's functions decay (at least) exponentially fast in the PLL, while pair-correlations display QLRO via an algebraic behaviour (just as the single-particle ones do in the usual LL).

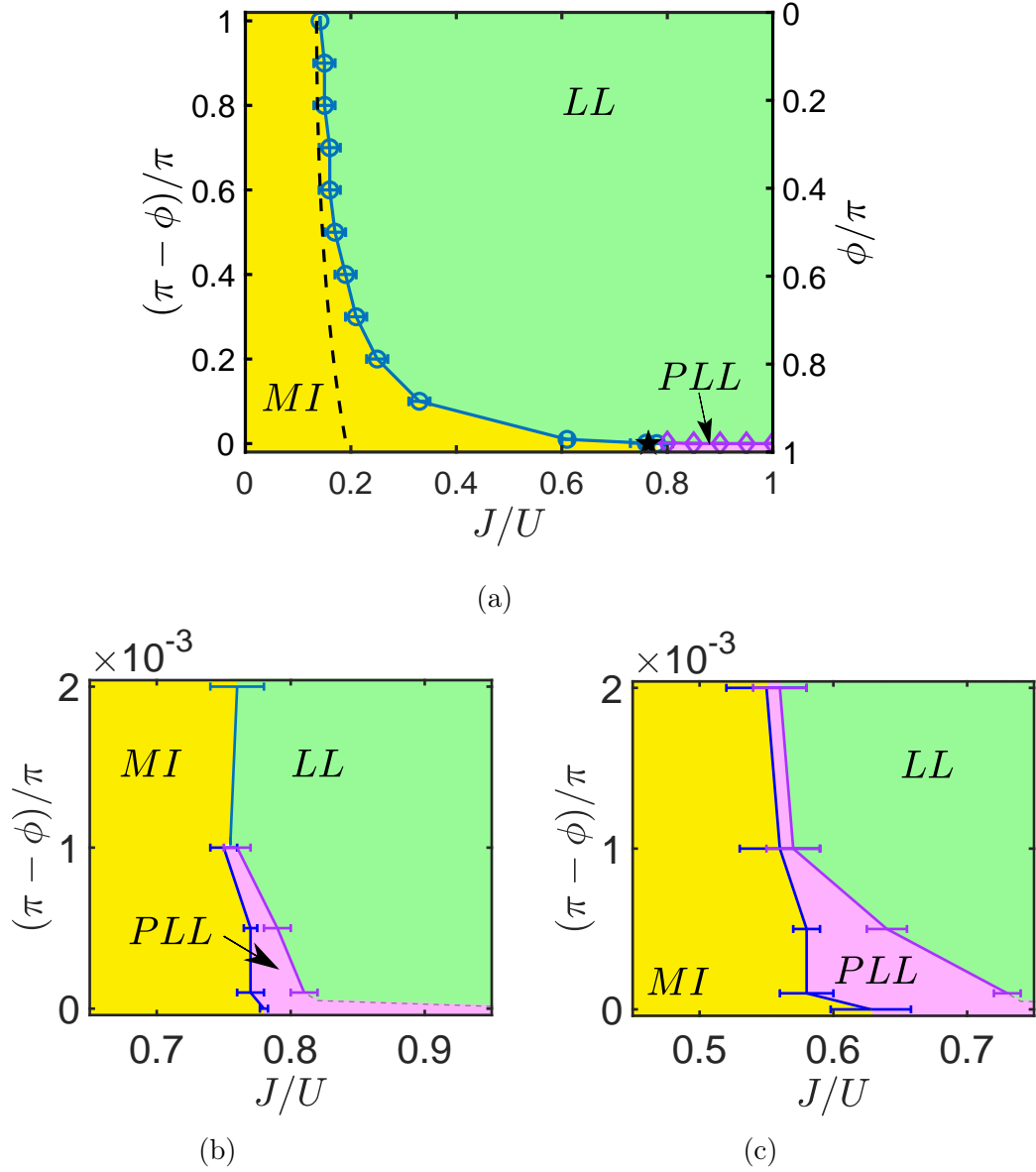


Fig. 6.12 The phase-diagram with different phase shifts ϕ against the tunnelling coefficient J/U . The *LL*, *PLL* and the *MI* regions are labelled. The critical points delimiting the *MI* region are obtained from the energy gap as in Sec. 6.4.1. The critical points separating the *LL* and *PLL* phases are obtained by looking at the decay of the single and pair correlation functions. The error bars have been omitted when they are smaller than the marker size. (a) is the full variation of ϕ using a filling=1, whilst (b) and (c) are regions close to full frustration for filling=1 and filling=2 respectively. The \star in (a) denotes $\tilde{G}(\pi)$, where Vidal and Douçot predicted the *LL*-*PLL* transition to be at $\phi = \pi$. The dashed line represents their *MI*-*LL* transition prediction, $G^*(\phi)$ in Eq. (6.22), which is only valid for small ϕ values.

In our simulations, we observe a small intermediate region between the *LL* and *PLL* phases in which it is indistinguishable whether the single correlations

better fit an exponential or power law scenario. To display this behaviour we have added error bars in the numerical data for the [LL-PLL](#) transition. This could be related to finite-size effects and the nature of the transition between these two gapless phases remains an open problem.

We have performed a comparison of our estimates with those given by Vidal and Douçot [84]. According to Vidal and Douçot, for small ϕ , the following equation should provide an infinite length estimate of where the transition takes place:

$$\begin{aligned} g^*(\phi) &= \sqrt{\cos \frac{\phi}{4}} g^*(0) \\ &= \frac{\pi \sqrt{3 \cos \frac{\phi}{4}}}{2} \end{aligned} \quad (6.21)$$

where $g = \sqrt{E_c/E_j} \iff \sqrt{U\langle n \rangle/J}$. This means that in our notation:

$$G^*(\phi) = \frac{1}{g^*(\phi)^2} = \frac{G^*(0)}{\cos(\frac{\phi}{4})}, \quad (6.22)$$

where $G^*(0) = 4/(3\pi^2) \simeq 0.135$, in good agreement with our numerically found $(J/U)_c^{[\phi=0]} = 0.14 \pm 0.01$ (see Sec. [6.4.1](#)). This curve (6.22) is shown by the dashed line in Fig. [6.12a](#), which is within our error bars up to $\phi = 0.3\pi$ and displays only slight discrepancies (< 0.005) up to $\phi = 0.5\pi$. For large fluxes further corrections are expected and the prediction at perfect frustration given by Vidal and Douçot is $\tilde{g}(\pi) = g^*(\pi)/4$ which is equivalently $\tilde{G}(\pi) = 4G^*(\pi) \simeq 0.764$. This is shown by the \star symbol in Fig. [6.12a](#) and is again in good agreement with our numerical estimate $(J/U)_c^{[\pi]} = 0.78 \pm 0.03$.

From our analysis, it can be seen that the [PLL](#) only exists in a very narrow region at imperfect frustration, consistent with the qualitative prediction of this region exponentially decaying $|\pi - \phi_c| \simeq e^{-J/U}$ by Douçot and Vidal [84]. The presence of a large [MI](#) region at unit filling prevents such an exponential from growing large enough to be evident. A possible strategy to increase the stability of [PLL](#), therefore, is to reduce the [MI](#) by resorting to higher filling factors, (which, incidentally, should also allow for better signal-to-noise ratio in the experimental detection). Using a higher filling pushes the Mott fluctuations further back to a smaller J/U as shown by the lobes in Sec. [2.2.2](#). We tested this by using filling $N/L = 2$, as shown in Fig [6.12c](#). Despite the sizeable shrinking of the [MI](#) region (by almost 25%), it seems that the prefactor of the exponential also changes, resulting in quite a marginal overall increase of the [PLL](#) region.

Determining an optimal filling for [PLL](#) detection under common experimental constraints could constitute an interesting extension for future works. It is possible

that the best filling is the original large N/L , quantum rotor, limit of [JJAs](#) (which Vidal and Douçot [84] studied).

Vidal and Douçot [84] predicted that the transition between the [PLL](#) and the [LL](#) phase should be of Ising \mathbb{Z}_2 type. The [PLL](#) region is so narrow that we cannot accumulate a reasonable region of points to perform a precise enough [FSS](#) to identify the universality class of the transition. We will show that neither the entanglement entropy scaling of Sec. 6.7 will be able to discriminate the predicted $c = 3/2$ conformal central charge of the critical line. Thus, the final answer about the critical behaviour of this $U(1) \times \mathbb{Z}_2$ system still remains as elusive as for the square ladder incarnations [208–213].

Another feature to note is that there is a similarity between this phase diagram and the one found for a fermionic (imbalanced) Creutz-Hubbard ladder [202], although there all phases are of reasonable size and insulating (see also Ref. [193]). It would be interesting to see whether the robustness of the [PLL](#) towards band curvature might be different against different deformations of the model, and whether this has any relation to the (emergent) topological character [195]. We will now consider the experimental setup of this model and some alternative formulations of the model, which make it more experimentally appealing.

6.6 Experimental Realisation of the Model

We perform a thorough theoretical analysis of this model, which in itself is useful to explore the features that arise. It is also beneficial to understand how this model would be realised in an experimental setup. We will briefly describe possible experimental implementations for this model and possible adaptations to our model that could make the experimental setup more resilient to errors.

6.6.1 Appropriate Experimental Implementations

In Ch. 2 we described some experimental setups (adapted optical lattices, [DMDs](#) and single-atom microscopes) which we expect to be possible platforms for implementing the rhombi model. As mentioned, the phase imprinting on the tunnelling matrix elements can be achieved by laser-assisted hopping [100, 101, 103, 214] and/or shaking of the lattice barrier amplitude [102–104, 215]. The gauge choice within this chapter is on a single leg, i.e. this requires imprinting the phase on a single link, which we envision could be achieved by shaking only the corresponding lattice barriers.

Two recent experiments have been conducted on photonic waveguides, the tunnelling coefficients were engineered in a similar spirit, either by insertion of extra elements with different refractive index [195] or by Floquet schemes [194]. In

these, however, interactions between the photons are a bit more difficult to obtain and tune with current technologies. There is effort being put into this and we might expect some progress in the near future.

6.6.2 Alternative Formulations of the Rhombi Model

The gauge choice of applying the flux to a single leg is one of the many possible gauge choices: e.g., distributing homogeneously the flux as $e^{\pm i\phi/4}$ on each link, giving a symmetric gauge choice, might be even more convenient for experimental purposes [22, 100, 196–198]. We notice that the already mentioned recent photonic implementations make use of the single-link [195] and the four-link gauge [194], respectively.

Another alternative formulation of this model is an adaptation to increase the robustness of the **PLL** phase. This is done by formulating the Hamiltonian using a tunnelling modulation instead of the magnetic flux used previously (see Sec. 6.1). This requires the following Hamiltonian:

$$\begin{aligned}\mathcal{H}_{BH} &= \mathcal{H}_0 + \mathcal{H}_U \\ &\equiv -J \sum_j \sum_\ell \sum_{\alpha,\beta} T_{\alpha,\beta}^{(\ell)} b_{j+\ell,\alpha}^\dagger b_{j,\beta} + \frac{U}{2} \sum_j \sum_\alpha n_{j,\alpha} (n_{j,\alpha} - 1) ,\end{aligned}\quad (6.23)$$

where the labels are as previously defined (Sec. 6.1). In order to modulate the amplitude, a $\cos(\phi)$ factor is included in the $C - B$ leg of each rhombi (as shown by the dashed lines in Fig. 6.1). This means the hopping matrices are now instead:

$$T^{(0)} = \begin{pmatrix} 0 & 1 & 0 \\ 1 & 0 & 1 \\ 0 & 1 & 0 \end{pmatrix}, \quad T^{(+1)} = \begin{pmatrix} 0 & 1 & 0 \\ 0 & 0 & \cos(\phi) \\ 0 & 0 & 0 \end{pmatrix}, \quad T^{(-1)} = (T^{(+1)})^\dagger . \quad (6.24)$$

It should be noted that this modulation will be exactly the same Hamiltonian in either extreme case, i.e. fully unfrustrated ($\phi = 0$) and fully-frustrated ($\phi = \pi$). The differences and advantages to an experimental replication only occur when exploring imperfect frustration. This advantage is evident in the increased size and therefore robustness of the **PLL** region (see Fig. 6.13). In practice, this setup requires the ability to imprint a different local tunnelling on one connection within each rhombus. This formulation can be achieved using a single atom microscope, **DMDs**, or an adaptation of other methods.

The reason for the increased region of **PLL** can be connected to the curvature of the single particle momentum bands. When a magnetic flux is applied a slight shift from full frustration i.e. ($\phi = \pi - \epsilon$), results in a an almost immediate loss

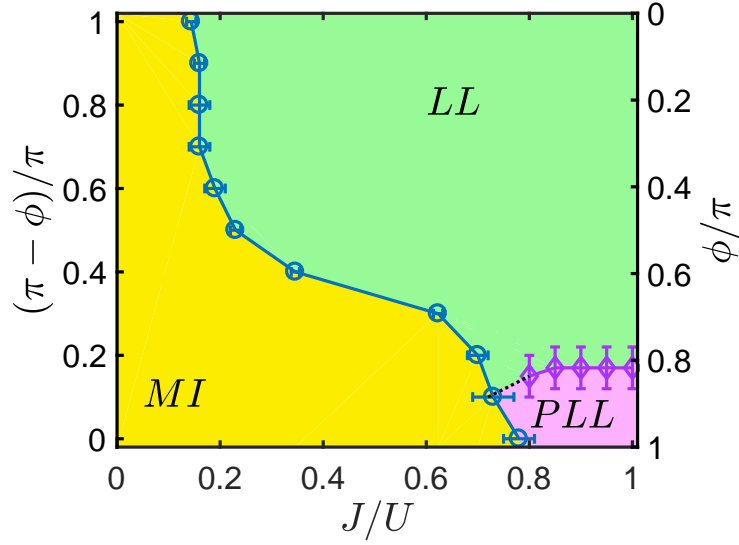


Fig. 6.13 The phase diagram for an infinite estimated length of the Hamiltonian Eq. (6.23) for amplitude modulation of $\cos(\phi)$ against parameters J/U . The MI, LL and PLL regions are as labelled. The MI-LL and the MI-PLL transitions are again obtained from the compressibility of the energy gap (see Sec. 6.4.1). The LL and PLL phases are characterised by the decay of the correlation functions as illustrated in Sec. 6.4.2).

of the flat-band property of the bands. Using the $\cos(\phi)$ adaptation, the bands retain their flat property (i.e. almost full frustration) for small shifts away from $\phi = \pi$, so the PLL remains intact. An illustration of this is shown in Fig. 6.14, where for $\phi = 0.9\pi$ the bands almost remain flat using this modulation procedure. In this case the single-particle band is given by:

$$\tilde{E}_\tau(k) = J\tau\sqrt{3 + \cos(k)(1 + \cos(\phi)) + \cos^2(\phi)}, \quad (6.25)$$

where $\tau = 0, \pm$ again.

6.7 Entropy and Entanglement Measures

Here we employ bipartite entanglement as a supplementary detection tool for the different gapless phases [112, 216, 217]. We consider the von Neumann entropy as defined in Def. 2.3.6, where we change our notation slightly to emphasise how many sites are in each block. Here, we consider the reduced density matrix ρ_ℓ of a bipartition of the rhombi chain into two segments of lengths ℓ and $L - \ell$, and we examine its entanglement entropy $\mathcal{S}_L(\ell)$ and spectrum λ_i (sorted in decreasing

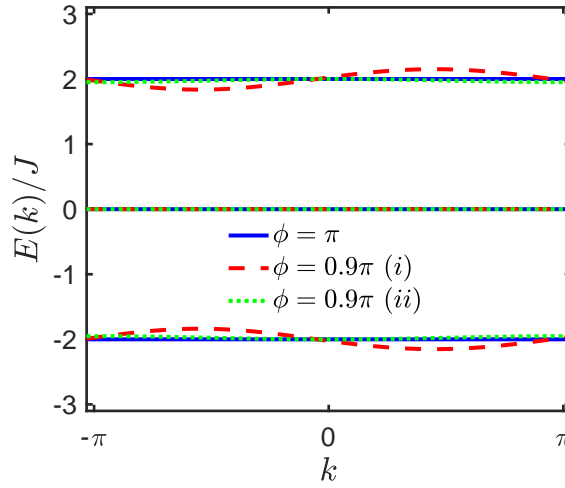


Fig. 6.14 The single particle energy band $E(k)$ as a function of the lattice momentum k . The fully-frustrated $\phi = \pi$ bands are the solid lines, whereas the intermediate frustrated $\phi = 0.9\pi$ are shown for method (i) which is the original model using the magnetic field and for method (ii) which is using the $\cos(\phi)$ amplitude modulation.

order):

$$\mathcal{S}_L(\ell) = -\text{Tr}(\rho_\ell \ln \rho_\ell) = -\sum_i \lambda_i \ln \lambda_i, \quad (6.26)$$

where we drop the dependence of the eigenvalues on ℓ and L for the sake of simplicity.

6.7.1 Entanglement Entropy

For a critical system with [OBC](#), conformal field theory ([CFT](#)) predicts that the von Neumann entanglement entropy scales as:

$$\mathcal{S}_L(\ell) = \frac{c}{6} \ln \left[\frac{L}{\pi} \sin \left(\frac{\pi \ell}{L} \right) \right] + F + \mathcal{O} \left(\frac{1}{\ell} \right), \quad (6.27)$$

where c is the central charge, which can be used as an indicator of the universality class of the corresponding field theory, and F is a model dependent (i.e., non-universal) constant [34, 133].

In Fig. 6.15 we distinguish three different cuts of the chain, according to the sub-lattice after which they take place (see 6.15a). An illustration of the whole von Neumann entropy against all sites is shown in Fig. 6.15b. Here we can see that the maximum entropy occurs when the cut is at the center of the chain, which is the typical case for the von Neumann entropy. It can also be seen that there is a difference in the amount of entropy between the different types of sites. The C -cut splits a rhombus in half and therefore gives rise to a higher entropy with respect

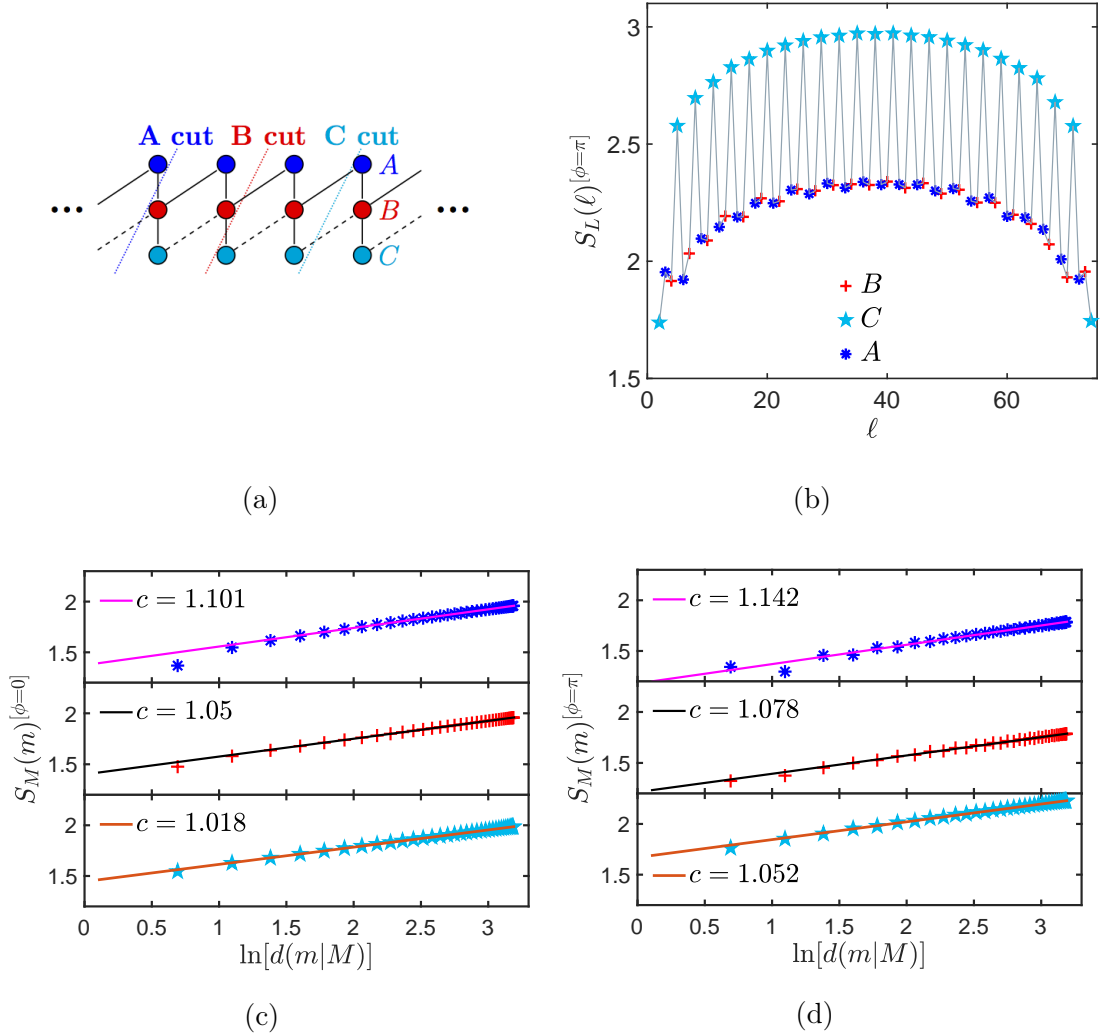


Fig. 6.15 **(a)**: An illustration of the different cuts that can be made on the model. The cuts after A, B and C are distinguished using the symbols $*$, $+$, \star respectively. **(b)**: Block entanglement entropy of the whole system (Eq. (6.26)) for $L = 76$. **(c)-(d)**: Block entanglement entropy for $J = 0.9U$ and $L = 226$ as a function of the chord length $\ln(d(m|M)) = \ln\left(\left[\frac{M}{\pi} \sin\left(\frac{m\pi}{M}\right)\right]\right)$ and compared to the conformal field theory (CFT) prediction, Eq. (6.27) for **(c)** the non-frustrated case ($\phi = 0$) and **(d)** the fully frustrated case ($\phi = \pi$).

to the A, B -cuts. Alternatively, we can understand this by considering that the C -cut separates two cells and that correlations have a strong oscillatory character between neighbouring cells, causing a supplementary amount of entanglement. As an aside this is more noticeable in the case of full-frustration ($\phi = \pi$), whereas for non-frustrated systems the entropies for the different types of sites are more similar in value.

We perform the fit of Eq. (6.27) for each cut separately based on which cell each site occupies, meaning L is replaced by M and m is used to show which

cell we are cutting. Data are shown for $J/U = 0.9$ and we introduced the chord distance $d(m|M) = \left\lceil \frac{M}{\pi} \sin\left(\frac{m\pi}{M}\right) \right\rceil$ for convenience.

For the **LL** of the unfrustrated regime $\phi = 0$, in Fig. 6.15c, we find that the cut after the maximal cut C has the central charge $c_C^{[\phi=0]} = 1.0180 \pm 0.0003$. The cuts after A and B have central charges $c_A^{[\phi=0]} = 1.101 \pm 0.001$ and $c_B^{[\phi=0]} = 1.050 \pm 0.001$ respectively. For the **PLL** of the frustrated regime $\phi = \pi$, in Fig. 6.15d, we find that the maximal cut fits such that the central charge $c_C^{[\phi=\pi]} = 1.052 \pm 0.002$, which is comparable to the unfrustrated case. For the cuts after A and B the central charges are $c_A^{[\phi=\pi]} = 1.142 \pm 0.006$ and $c_B^{[\phi=\pi]} = 1.078 \pm 0.005$ respectively.

Values for both the frustrated and the unfrustrated models are thus fully compatible with the well-known result for the **LL** phase of the Bose-Hubbard model on a purely 1-D chain [34, 57, 133], i.e., $c = 1$. This confirms that only one bosonic component (out of three possible ones) becomes gapless, in either case, as we have already seen via the correlations in the previous section. This holds regardless of which cut in the system is fitted, i.e. even if we fit every cut after A or B which is a cut across cells we get $c \simeq 1$, once we have considered that finite-size effects are taking place. We, therefore conclude that the central charge c is not a good indicator to distinguish **PLL** from **LL**. The low-lying levels of the entanglement spectrum, however, may allow this as shown in the next section.

Before turning to the entanglement spectrum analysis, let us mention that the entropy scaling across the **PLL-LL** transition at finite deviations from $\phi = \pi$ is not displaying any clear signature of a $c = 3/2$ **CFT** line, as one would expect from its predicted Ising character [84, 200]. The difficulties in analysing transitions between gapless phases has already been noticed in spin models [218].

6.7.2 Entanglement Spectrum

Despite having the same central charge, we expect qualitative differences between the wavefunction structure inside the **LL** and **PLL** phase. We, therefore, resort to the entanglement spectrum, which is capable of revealing key properties about the system, such as symmetries and excitations, which the von Neumann entropy, being a single number, is unable to provide [140, 219–222].

Here we choose to focus on the C -cut which leaves $(M - 1)/2$ rhombi on each side, so that the bipartition is perfectly symmetric, at least concerning the number of sites. Due to the conservation of the total number of particles in the system, each Schmidt eigenvalue λ_i can be associated to an eigenvector of the reduced density matrix with a fixed number of particles. In Fig. 6.16a we plot the λ_i 's for a chain of 75 rhombi, according to the excess number of particles δN with respect to a homogeneously distributed unit filling (i.e., $L/2$ particles on both sides of the bipartition), similarly to Ref. [223]. This is obtained from the **DMRG**

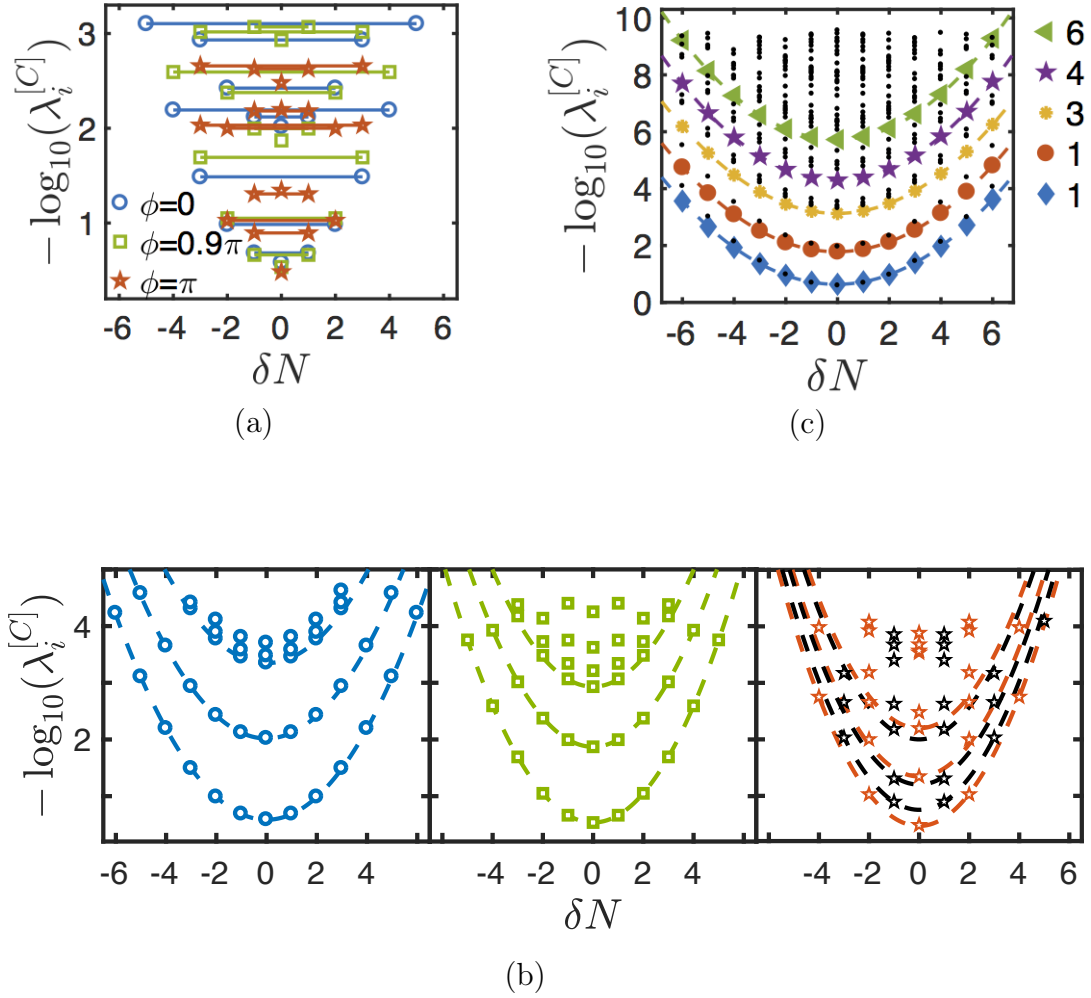


Fig. 6.16 **(a)**: The entanglement spectrum as a function of the dispersion from uniform filling δN of the number of bosons for the cut after C . $\phi = 0$ denotes the unfrustrated case (\circ), $\phi = 0.9\pi$ the intermediate frustration (\square) and $\phi = \pi$ denotes the fully frustrated case (\star), simulated at $J = 0.9U$. In **(a)** a solid line is used to join the degenerate eigenvalues in all cases. **(b)**: Approximate parabolas for $\phi = 0$, $\phi = 0.9\pi$ and $\phi = \pi$ (left to right) based on the length $L = 226$. In the third panel different colours denote the possible curve fitting to even and odd δN . **(c)**: The unfrustrated ES for a cut after C at $L = 226$ with the thermodynamic limit approximation shown by the parabolas. The legend shows the degeneracy of each parabola.

calculations through the enforcement of $\mathbb{U}(1)$ symmetry and the subsequent block formation in the density matrix, as motivated in Sec. 3.3.5. The tunnelling value we consider is $J/U = 0.9$, inside both the LL and PLL phases (see Fig. 6.12a).

Läuchli *et al.* studied the entanglement spectrum on the BH model in depth [223]. It has been found that for a standard BH model on a single line, the entanglement spectrum taken at the central site of the system (i.e. in a symmetric bipartition) will consist of symmetric parabolas (with their minimum at $\delta N = 0$), if referenced against the particle imbalance δN . Läuchli *et al.* showed that there

are a collection of stacked parabolas, which are commonly referred to as a **CFT** tower, all of which have the exact same curvature and spacing between them. Each of these parabolas occurs by joining the entanglement spectrum points at each level, where, for example the first level consists simply of the lowest values at each δN .

In Fig. 6.16, the eigenvalues are clearly symmetric with respect to $\delta N = 0$ regardless of the amount of frustration. For the unfrustrated **LL** at $\phi = 0$ (blue \circ) and the intermediate frustrated **LL** at $\phi = 0.9\pi$ (green \square), it is easy to recognise both the $-\log \lambda_i \propto \delta N^2$ dependence and also the starting of the equally spaced **CFT** tower within each distinct δN , as predicted for the standard **1-D** Bose-Hubbard chain [223]. Both features apparently disappear for the **PLL** at full frustration $\phi = \pi$ (red \star), thus signalling a dramatic change in the underlying wavefunction, undetected by the entropy scaling analysis. In order to examine this more clearly we plot fitted curves at length $L = 226$ of the same curvature for a given ϕ in Fig. 6.16b, for $\phi = 0$, $\phi = 0.9\pi$ and $\phi = \pi$ from left to right. It is evident from this that the unfrustrated cases can be extrapolated to the typical curves. For $\phi = \pi$, however, it is impossible to fit the eigenvalues with functions of the same curvature. For example, if the first five points are examined closely it can be seen that a parabola would not be able to fit adequately both 1 to 2 and 3 and 1 to 4 and 5. Instead it seems that two distinct parabola sets are appearing at the even and odd δN 's as shown by the red and black curves.

In Fig. 6.16c we present the results of an **FSS** towards the thermodynamic limit for the unfrustrated case ($\phi = 0$) shown by the parabolas. A modified degeneracy counting and the appearance of a secondary tower, both possibly related to the internal structure of the lattice, are evident. Examining these at $\delta N = 0$, the spacing of the parabolas between every second one is approximately equal i.e., $1 - 3 \approx 2 - 4 \approx 3 - 5$, whereas the spacing between neighbouring parabolas differs. Higher parabolas are excluded as they fall below the accuracy of our results. For the fully frustrated case, instead, where it seems that two distinct parabola sets are appearing, a reasonable **FSS** procedure is not possible without conserving explicitly the local \mathbb{Z}_2 quantities. Both these aspects go beyond the scope of the present work and deserve future investigation.

We do, however, notice that the resulting pattern of (quasi-) degenerate multiplets in the entanglement spectrum changes quite radically in the fully frustrated case from the unfrustrated and intermediate frustrated cases. So we are confident that the entanglement spectrum can be used to distinguish between the two cases, where the entropy cannot.

6.8 Conclusions

In this chapter we have analysed the ground state phase diagram of a system of interacting bosons on a geometrically frustrated lattice; namely, we have considered a quasi-1-D chain of rhombi pierced by magnetic flux. For unit filling and a sufficiently low tunnelling amplitude the system is in the MI phase as expected. For larger tunnelling values, we have numerically confirmed that when full geometric frustration prevents the movement of single particles (i.e., the energy bands become flat), the system still enters into a gapless phase where the elementary moving objects are pairs of particles. We have explored the regime where the frustration is not perfect, highlighting that the pair superfluid can only be obtained for a very small region. If the imperfect frustration is $\phi = \pi(1 - \epsilon)$, then this is consistent with the qualitative exponential prediction by Douçot and Vidal [84], i.e., $\epsilon \simeq \exp(-J/U)$. This makes an experimental realisation quite challenging, especially at low particle filling. It is, however, possible to extend this region by a small amount using higher filling and even more by using amplitude modulation within the system, instead of the phase shifts we applied, which is also possible experimentally. From a different perspective, we have highlighted that, whilst the central charge obtained from the entropy cannot be used to distinguish between the PLL and LL phase, the features and quantum numbers of the entanglement spectrum do have noticeable differences between the two.

There are still a number of directions to expand upon this work, such as:

- (i) comparing the robustness of the PLL phase with respect to other deformations of the flat bands (such as different types of amplitude modulation), and compare it to other flat band models (e.g., the Creutz ladder [193, 202]), to see whether the (here hidden [195]) topological character plays any role;
- (ii) working out an explicit mapping to the effective Ising model predicted by Douçot and Vidal [84], in terms of measurable quantities (as done for Creutz ladder fermions [202]), in order to shed new light on the nature of the PLL-LL transition (possibly once the PLL region is also extended to simplify things);
- (iii) deepen the understanding of the striking change in the entanglement spectrum, possibly by also explicitly enforcing the extensive number of \mathbb{Z}_2 symmetries [84, 193] in the numerics.

Lastly, it would also be interesting to examine the dynamics of our interacting chain, which would allow the formulation of experimental detection strategies. In the next chapter we describe some initial analysis of the dynamics within this model.

CHAPTER VII

TIME DYNAMICS OF THE FRUSTRATED RHOMBI MODEL

“Time is the longest distance between two places.”

Tennessee Williams, The Glass Menagerie

In this chapter we will examine the time dynamics of the previously studied quasi 1-D rhombi model (see Ch. 6). Exploring its dynamics allows us to investigate the model in more depth to confirm some of our previous conclusions such as the strong localisation effect caused under full-frustration. The dynamics can also be used as a tool to discover what experimental detection strategies are required. The dynamics of geometrically frustrated systems is an area which has had very little exploration, with only a few works delving into it [107, 224–227]. This means that there is still a large amount that requires investigation. The ability to replicate such models in experiments is also becoming more possible, as we have previously motivated, meaning that a thorough theoretical analysis of frustrated models is required.

The geometrical frustration within this model causes localisation due to the AB effect, meaning that under full-frustration the system comprises of AB cages. This localisation also leads to the perfectly flat Bloch bands within a single particle representation. We expect these cages to break down when interactions occur between the particles as, in the limit $J/U \rightarrow \infty$, pairs form which are delocalised within the PLL phase. If J/U is small, so interactions dominate, the presence of the AB cage is no longer valid, however, we expect the system to be localised as

it enters into the **MI** phase. The work reported within this chapter will focus on the presence and the absence of the **AB** cages, i.e. on when the localisation is enforced by the cages. Our main analysis will be conducted using a single particle loaded into the **OBC** chain, where we will illustrate that under full-frustration the movement of the particle within the cage can be explained by the concept of Rabi oscillations. We then briefly examine the effects of loading a pair of particles, which we expect to break out of the **AB** cages and lastly briefly show some initial analysis with unit filling.

7.1 Recent Studies of Non-Equilibrium Geometric Models

A very recent work has been carried out by Di Liberto *et al.* [224], who were focusing on the dynamics of the Rhombi model, to explore when the **AB** cages are valid in a non-equilibrium scenario. The experimental realisation that they recommend is using a photonic system, i.e. based on an optical-waveguides platform [194]. To analyse whether the **AB** cage survives in the presence of strong mean-field interactions, they use a semi-classical approach in the large occupation/density limit, where a mean-field description in terms of a condensate wavefunction is valid. Contrary to the prediction that interactions destroy the **AB** cage states, they discover that with specific initial conditions, namely if the initial condition has the same phase pattern as the eigenstate of the ground state $|w_- \rangle$ (introduced in Ch. 6), then the localisation of an **AB** cage state still remains in effect even in the non-equilibrium scenario with mean-field interactions.¹ Another discovery they made is that within each **AB** cage the density fluctuates (or undergoes a breathing motion), which they show can be modelled by a simple two-mode theory (using the Gross-Pitaevskii equation).

An exploration of the dynamics of models with non-trivial geometries was also carried out for the two-leg ladder by Kasztelan *et al.* [226]. They evaluate the transfer efficiency of the particles loaded into one leg and travelling to the other, when there is a time-dependent energy bias between the two chains forming the legs. Within their work they also investigate the effect of using a linear or a sudden quench.

Another recent work has investigated the dynamics within the Creutz ladder, which as we have previously stated, shares a number of similarities with the diamond model even in the fermionic case [225]. There have also been recent

¹We ask the reader to note that our notation differs to the notation given by Di Liberto *et al.* [224] and also the flux is applied on a different leg, but both models are still physically equivalent.

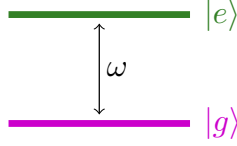


Fig. 7.1 Illustration of the two-level atom that can be described by a Rabi model, where the two possible states are $|e\rangle$, $|g\rangle$ and ω is the transition frequency, which measures the separation between the energies.

works performing a comparative study of few-particle fermionic and bosonic quasi 1-D systems [107] and scattering processes [228] within a flat-band system.

Lastly, there have been a number of illuminating works exploring the dynamics of an exactly 1-D (i.e. not quasi 1-D) BH model, such as a detailed study of density matrices after quenches [229, 230] and an analysis of the correlations under a quench from the LL to the MI, revealing a memory of the initial state [231], amongst some other quench analyses [232–236].

7.2 The Rabi Model

It will be shown that the movement of a single particle loaded at a specific site within a fully-frustrated system can be described by the Rabi oscillation. We will briefly explain this phenomenon here. In 1936, Rabi examined the semi-classical version of a model (now called the Rabi model) which describes the simplest interaction between a two-level atom and a classical light field [237]. The Rabi cycle (sometimes called the Rabi-flop) is the cyclic behaviour of a two-level quantum system in the presence of an oscillatory driving field.

If a two-level system is considered then the basis of the atomic Hilbert space consists of only two states, which we will label $|g\rangle$ and $|e\rangle$ as shown in Fig. 7.1 [238]. If the driving field is excluded from the model, then the Hamiltonian to describe a two-level system simply consists of the Pauli matrix σ_x :

$$\mathcal{H}_{Rab} = \frac{\omega}{2} \sigma_x , \quad (7.1)$$

where ω is the transition frequency (assuming $\hbar = 1$) and we assume there is an initial state $|\psi_0\rangle$ which evolves under \mathcal{H}_{Rab} . The states $|g\rangle$ and $|e\rangle$ are not eigenstates of this simplified model Hamiltonian in Eq. 7.1. Then this evolution is

described by an evolution operator:

$$\begin{aligned}\mathcal{U}_{Rab}(t) &= e^{-i\mathcal{H}_{Rab}t} = e^{-i\frac{\omega\sigma_x}{2}t} \\ &\equiv \begin{pmatrix} \cos\left(\frac{\omega t}{2}\right) & -i\sin\left(\frac{\omega t}{2}\right) \\ -i\sin\left(\frac{\omega t}{2}\right) & \cos\left(\frac{\omega t}{2}\right) \end{pmatrix}\end{aligned}\quad (7.2)$$

The initial state can be rewritten as the combination of the two states:

$$|\psi(0)\rangle = a|e\rangle + b|g\rangle, \quad (7.3)$$

where $|a|^2 + |b|^2 = 1$, $\sigma_z|e\rangle = |e\rangle$ and $\sigma_z|g\rangle = -|g\rangle$. The state after the time evolution is then:

$$|\psi(t)\rangle = \mathcal{U}_{Rab}|\psi_0\rangle = \begin{pmatrix} a\cos(\omega t/2) - ib\sin(\omega t/2) \\ b\cos(\omega t/2) - ia\sin(\omega t/2) \end{pmatrix}. \quad (7.4)$$

If the initial state is in $|e\rangle$, i.e. if $a = 1$, $b = 0$, then we have:

$$|\psi(t)\rangle = \begin{pmatrix} \cos(\omega t/2) \\ -i\sin(\omega t/2) \end{pmatrix} = \cos(\omega t/2)|e\rangle - i\sin(\omega t/2)|g\rangle. \quad (7.5)$$

From this we can obtain that the probability of finding $|e\rangle$ or $|g\rangle$ after a time t is given by:

$$P_s(t) = |\langle\psi(t)|s\rangle|^2, \quad (7.6)$$

where $s = e$ or $s = g$. This means that we have the probabilities:

$$P_e(t) = \frac{1}{2}\left(1 + \cos(\omega t)\right), \quad (7.7)$$

$$P_g(t) = \frac{1}{2}\left(1 - \cos(\omega t)\right). \quad (7.8)$$

From these probabilities it can be seen that when the initial state begins in the state $|e\rangle$, it will oscillate between remaining in $|e\rangle$ or entering into $|g\rangle$, where the probability follows a sinusoidal pattern. As the evolution depends solely on $|\sigma_x\rangle$, there is perfect resonance, meaning that the probabilities reach one and that there is an exact flip-flop motion from one state $|e\rangle$ to the other $|g\rangle$.

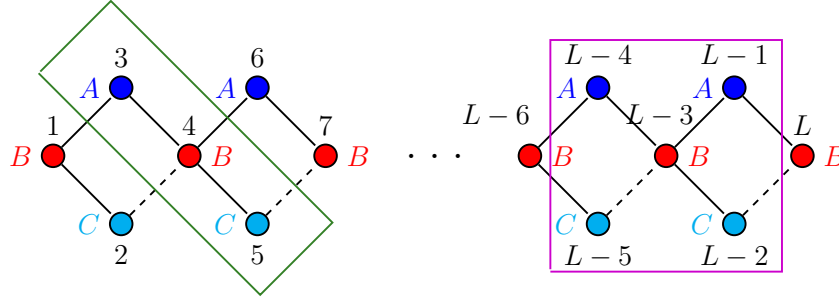


Fig. 7.2 The representation of the one-dimensional lattice of rhombi in real space showing the number of sites. The (green) rectangle encloses a given cell to show that each cell contains three sites labelled A, B, C . Solid (dashed) line connections indicate a tunnelling amplitude $-J$ ($-Je^{i\phi}$). The square highlights the sites that are contained in a full AB cage, when $\phi = \pi$.

7.3 Dynamics of the Single Particle

Time-dynamics will be examined on the BH chain of rhombi (diamonds) as studied in Ch. 6. The Hamiltonian is therefore once again described by Eq. (6.1), where we again assume that the flux is added on a single leg. It should, however, be noted that within this model we vary the interaction parameter U instead of the tunnelling parameter J , which we fix $J = 1$. This means that we will often refer to the parameter ratio U/J (or simply U) which is the inverse of parameters shown in the phase diagrams of Ch. 6.

Before we begin our analysis, let us fix the notation. A site can be referenced either by a single running index ℓ or by two indices consisting of the cell it occupies combined with its sublattice index, j_α , where $\alpha = A, B, C$, as previously shown in Fig. 6.1 and refreshed in Fig. 7.2. It is possible to change between these two references, using the following:

$$\ell = \begin{cases} 3(j-1) & \text{if } \alpha = A \\ 3(j-1) + 1 & \text{if } \alpha = B \\ 3(j-1) + 2 & \text{if } \alpha = C \end{cases} . \quad (7.9)$$

Within Fig. 7.2, the sites within the rectangle, labelled 3, 4 and 5, corresponding to the ℓ index, can be written as $j_\alpha = 2_A, 2_B, 2_C$. To account for both referencing systems, our operators will have three possible indices (though within context, the irrelevant ones will be omitted). For example, the annihilation operator will be represented by $b_{j,C}^{[\ell]}$, where ℓ is the site numbering, j is the cell and $\alpha = A, B, C$.

All of the following calculations for a single and a pair of particles will be performed using exact diagonalisation. We will examine the single particle when $\phi = \pi$ and when $\phi = \pi - \delta\phi$ for some small $\delta\phi > 0$.

7.3.1 Single Particle with Perfect Frustration

We have previously stated (see Ch. 6) that if a single particle is considered within the BH model of rhombi (ignoring the boundaries) then we obtain the energy eigenvalues:

$$E(k) = \pm 2J \sqrt{1 + \cos\left(k - \frac{\phi}{2}\right) \cos\left(\frac{\phi}{2}\right)} \quad (7.10)$$

$$E(k) = 0 ,$$

where k is the quasimomentum.

In the fully-frustrated case, $\phi = \pi$, these then form flat-bands, which effectively means that a single particle (or more than one with no interactions) should be localised within its given AB cage. As an initial test of the dynamics we will ensure that this holds true. We have stated that the AB cages can be described by the eigenstates of these flat-bands as:

$$w_{j,\tau} = \frac{(-1)^\tau b_{j-1,C} - (-1)^\tau b_{j,A} - 2\tau b_{j,B} + b_{j,C} + b_{j+1,A}}{(2^{1+|\tau|/2})} , \quad (7.11)$$

where $\tau = 0, \pm 1$ within the bulk of the system (i.e. away from border effects) and j is the index of the cell. We will explicitly state the inverse transformation here as this will be illuminative later on:

$$b_{j,B} = \frac{1}{\sqrt{2}} \left(w_{j,-} - w_{j,+} \right) , \quad (7.12)$$

$$b_{j,A} = \frac{1}{\sqrt{8}} \left(3w_{j-1,+} - w_{j-1,-} + 3w_{j,-} - w_{j,+} \right) - \frac{1}{2}w_{j-1,0} - \frac{1}{2}w_{j,0} , \quad (7.13)$$

$$b_{j,C} = \frac{1}{\sqrt{8}} \left(-w_{j,+} + 3w_{j,-} - 3w_{j+1,-} + w_{j+1,+} \right) + \frac{3}{2}w_{j,0} + \frac{1}{2}w_{j+1,0} . \quad (7.14)$$

From these equations it can be seen that $b_{j,B}$ consists of only two cage eigenmodes whereas the operators for sites j_A and j_C , $b_{j,A}$ and $b_{j,C}$, instead consist of six. The additional complexity in the j_A and j_C eigenmodes is clearly a result of the fact that they occupy the overlap between two cages as shown in Fig. 7.3. In the case of $\phi = \pi$, the single particle will remain localised within the cage(s) it initially occupies forever, unless some other factor is changed to break the cage localisation.

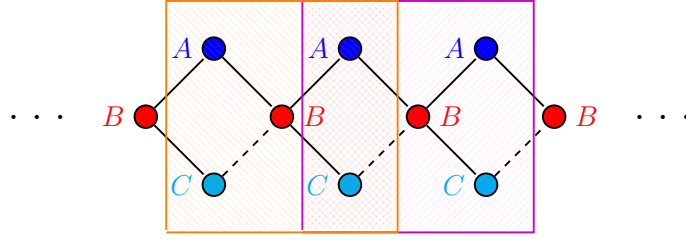


Fig. 7.3 One-dimensional lattice of rhombi, where each cell contains three sites labelled A, B, C . Solid (dashed) line connections indicate a tunnelling amplitude $-J$ ($-Je^{i\phi}$). This is the representation of the model in real space showing the number of sites. The squares highlight the sites that are contained in a full AB cage, when $\phi = \pi$. The overlap between two different cages is shown occurring at the A and C sites. Each square has parallel lines in a given direction to represent which sites are obtained within a cage and which intersect two cages.

Due to the nature of the A and C sites, if any of these are the initial site then the particle can move freely between two cages rather than one. This is because they connect two cages at all times (see Fig. 7.3), meaning that this will still result in a perfectly localised case, but across more sites (8 instead of 5). We expect the same behaviour for a generic j_A and j_C within the bulk of the chain (i.e. avoiding border effects). For this reason, we restrict our analysis to the sites within the central cell, which for a chain of length $L = 19$, corresponds to investigating the sites in cell $j = 4$. An example is shown of the localisation of the on-site density for the single particle in a chain of length $L = 19$ where the initial state is started at j_A , specifically at $\ell = 9$ in Fig. 7.4a and an example is shown where the single particle is initially at the j_C ($\ell = 11$) in Fig. 7.4b. It is also clear that the dynamics starting from a j_A site and j_C site is symmetric to each other. The movement of the single particle from the site j_A (starting left of center) mirrors the movement from the site j_C (starting right of the center in terms of numbering).

The time evolution of a single particle started at the site j_B can, however, be expressed exactly due to the fact that any initial state only consists of two eigenmodes as shown in Eq. 7.12. This means it is only formed of the positive $w_{j,+}$ and the negative $w_{j,-}$ cage eigenstates (see Eq. (7.11) and Eq. (7.12)), which have eigenvalues $2J$ and $-2J$ respectively. As there are only two possible states, the movement of the particle can be described by a Rabi frequency, where $\omega = E_+ - E_- = 2J + 2J = 4J$.

For $\phi = \pi$, the fully frustrated case, the particle can only circulate around the five sites within the cage. The possible states considered will be within the site j_B or across the other four sites in the cage, $(j-1)_C, j_A, j_C, (j+1)_A$. The probability

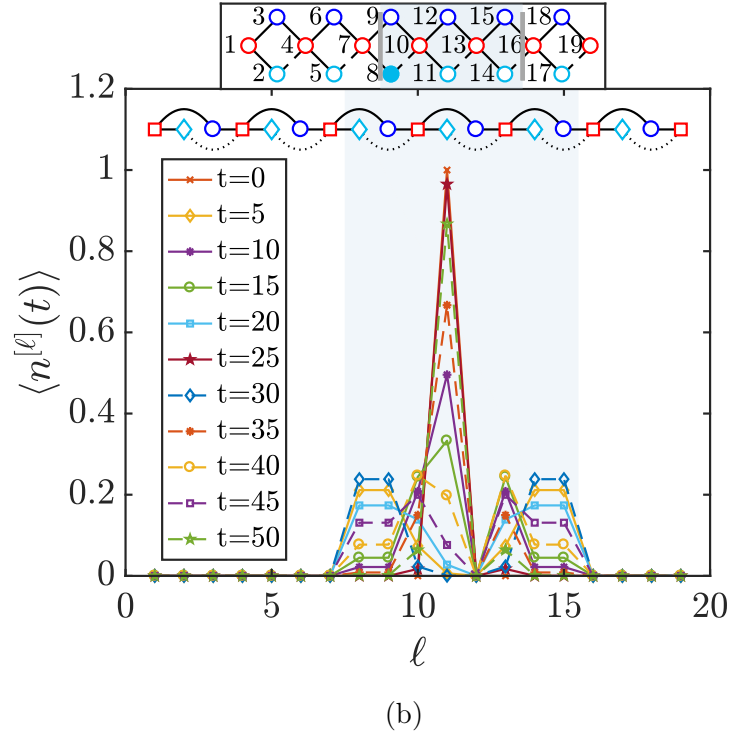
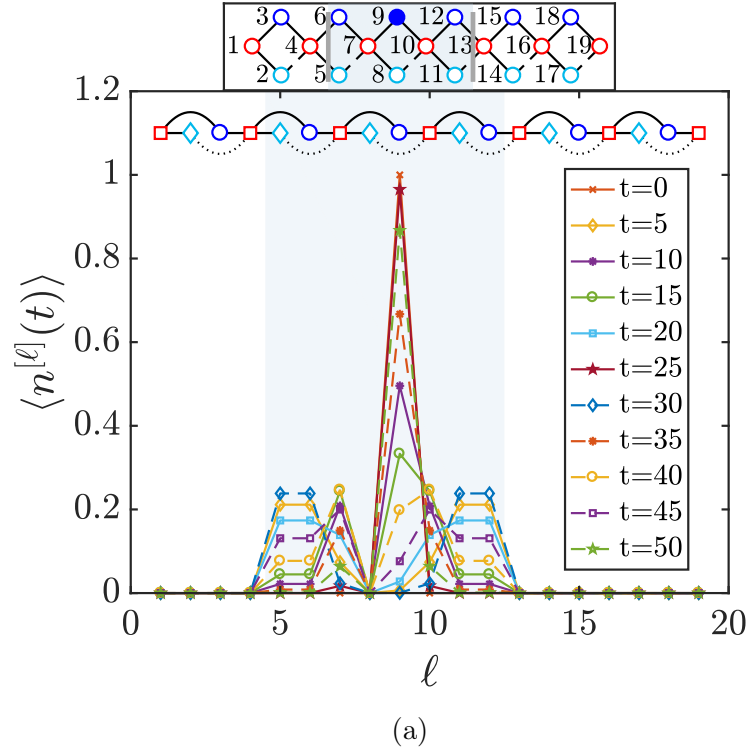


Fig. 7.4 The movement of the single particle throughout the system over time t described by the on-site density $\langle n^{[\ell]}(t) \rangle$. A single particle is loaded at site **(a)**: $\ell = 9$ (a central A site) and at **(b)**: $\ell = 11$ (a central C site). The insets above each figure show the initial site the particle is in by the filled circle and the corresponding cage borders to this site by the lines. We have also included a small diagram of the connections of each site inside the top of each figure, where B sites are squares, C sites are diamonds and A sites are circles.

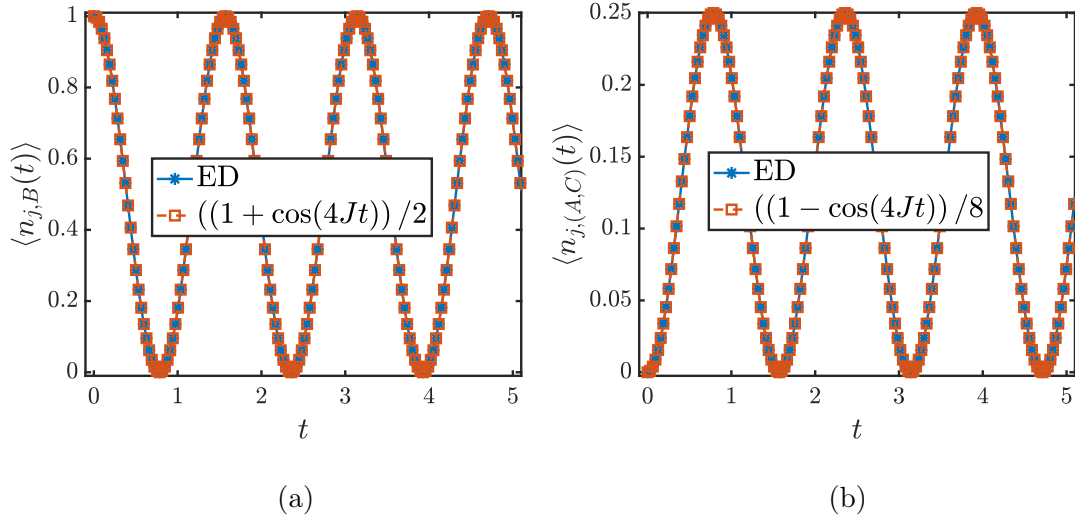


Fig. 7.5 The Rabi oscillation from Eq. (7.15) and Eq. (7.16) of the single particle within its cage and the on-site density $\langle n_{j,\alpha}(t) \rangle$ from ED. **(a)**: The oscillation on the j_B site that the particle was originally placed in (which in this case is $\ell = 10$ and $j = 4$). **(b)**: The oscillation on the j_A and j_C sites (which are equal to the oscillation on $(j-1)_C$ and $(j+1)_A$ in the corresponding cage (i.e. for any of $\ell = 8, 9, 11, 12$).

of remaining in the initial j_B site is the same as in Eq. (7.7) and is given by:

$$P_{j,B} = \frac{1 + \cos\left((E_+ - E_-)t\right)}{2} = \frac{1 + \cos(4Jt)}{2} \quad (7.15)$$

$$= \cos^2(2Jt) ,$$

This leaves the probability of **not** being in the B site as the probability equivalent to Eq. (7.8) in the two-level atom. This is split across the rim (A and C) sites with equal probability meaning that the probability of instead being in one of the other sites in the cage is given by:

$$P_{j-1,C} = P_{j,A} = P_{j,C} = P_{j+1,A}$$

$$= \frac{1 - \cos\left((E_+ - E_-)t\right)}{8} = \frac{1 - \cos(4Jt)}{8} \quad (7.16)$$

$$= \frac{\sin^2(2Jt)}{4} .$$

To confirm this feature, we examine a chain of length $L = 19$ and focus on the central cage, which has the expected Rabi frequencies shown above. From this, it can be seen that when the particle leaves the site j_B at $\ell = 10$ it divides equally between the surrounding A and C sites (at $\ell = 8, 9$ and $\ell = 11, 12$) as one would expect. In Fig. 7.5 we have shown the on-site density $\langle n_{j,B}(t) \rangle = \langle n_{4,B}^{[10]}(t) \rangle$,

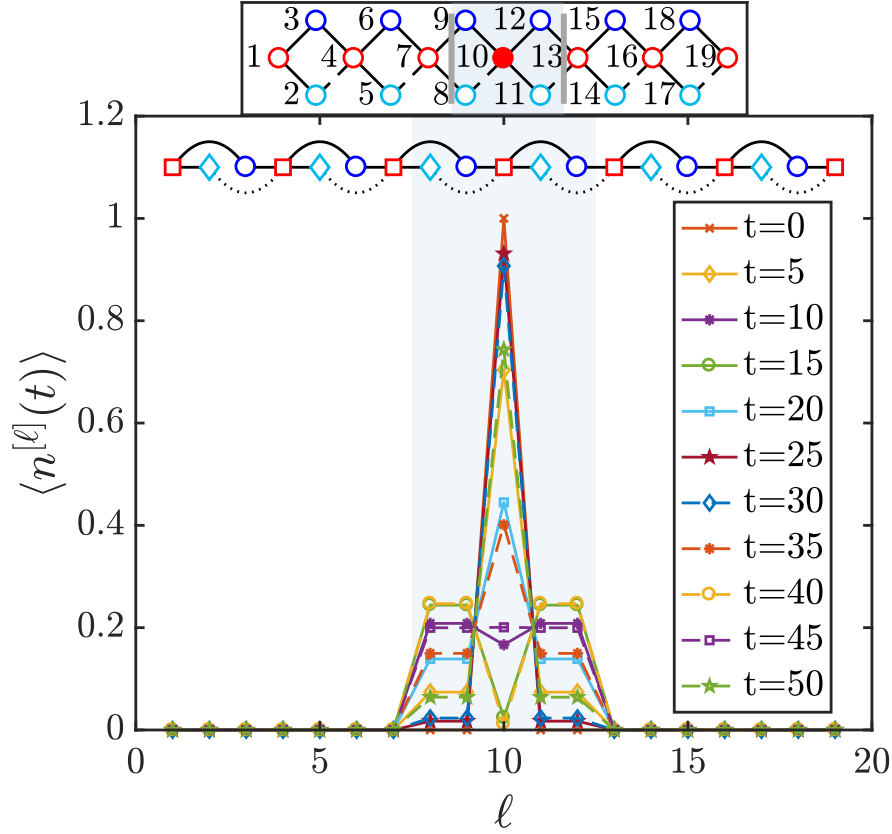


Fig. 7.6 The on-site density $\langle n^{[\ell]}(t) \rangle$ of a single particle where the initial setup is $n_{4,B}^{[10]}(t) = 1$ for a chain of length $L = 19$ and where $\phi = \pi$. The inset shows this initial condition, where the grey lines mark the borders of the corresponding AB cage. We have also included a small diagram of the connections of each site inside the top of the figure, where B sites are squares, C sites are diamonds and A sites are circles.

which agrees with the Rabi probability of remaining at the site j_B . We have also shown the on-site density of the sites $\ell = 8, 9, 11, 12$ ($\langle n_{j,(A,C)}(t) \rangle$) which are described by Eq. (7.16). Unsurprisingly if the number of bosons, N , is increased and the interaction is set $U = 0$ then the amplitude of the Rabi frequency is just multiplied by the number of particles initially injected at site j_B .

In Fig. 7.6 we show the on-site density across all sites to illustrate the boundary of the cage and the oscillation from a different perspective. A single particle started at the site j_B , specifically at $j = 4$, $\ell = 10$, only oscillates between the sites $\ell = 8, \dots, 13$, with sites $\ell = 1, \dots, 9$ and sites $\ell = 14, \dots, 19$ having on-site density strictly $\langle n^{[\ell]}(t) \rangle = 0$. It can be seen that the particle oscillates within the cage in such a manner that the symmetry around the j_B site (which is the central cage site in our example) remains intact and such that we observe apparent uniform on-site density across all j_A and j_C sites within the cage, in agreement

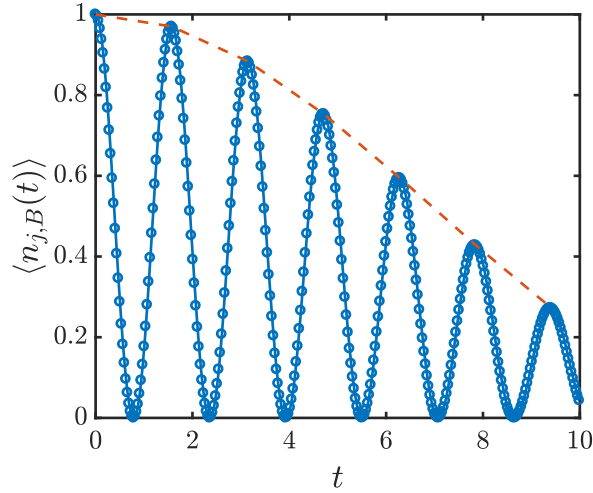


Fig. 7.7 The oscillation of the single particle density at the central B site, $\langle n_{j,B}(t) \rangle$, where $j = 4$ (which corresponds to $\ell = 10$) when it can escape its cage due to imperfect frustration $\phi = 0.9\pi$. The dashed line joins the maximal values at the top of the peaks to emphasise the effect of the damping more clearly.

with the Rabi oscillation.

The feature of the oscillation within the cages is attributed to a breathing motion of the condensate studied by Di Liberto *et al.* [194], who state that this motion within the cage can be explained through a simple two-mode theory. In our case where we are examining a single particle, we have shown that the movement can be described exactly by two-level theory, namely Rabi oscillations.

7.3.2 Single Particle with Imperfect Flux

In the single particle case, when $\phi \neq \pi$ the highest and lowest band cease to be flat, meaning that the boson is able to escape from the cage that it started in. This means that, although the frequency retains a Rabi oscillation, the amplitude is damped as shown in Fig. 7.7 for $\phi = 0.9\pi$. We have also joined the maximum points with a dashed line to illustrate the nature of the damping more clearly.

The rate at which this is damped can be approximated using time-dependent perturbation theory for small $\delta\phi$ away from π and for small times t [156, 239]. Since this is for the single particle, we will use the notation $|j_\alpha\rangle = b_{j,\alpha}^\dagger |0, \dots, 0\rangle$ (similarly to the notation used for the single particle in Ch. 2), where $\alpha = A, B, C$. Under general time-dependent perturbation theory, the Hamiltonian evolving in time consists of the following:

$$\mathcal{H}(t) = \mathcal{H}_0 + V(t) , \quad (7.17)$$

where \mathcal{H}_0 is the non-perturbed time-independent Hamiltonian and $V(t)$ is, in principle, a time-dependent perturbation. For our case, the Hamiltonian and the perturbation are only changed instantaneously at $t = 0$ and have no further dependence on time, meaning that the time-dependence is omitted. If considering a flux $\phi = \pi - \delta\phi$, our time-evolving Hamiltonian is:

$$\mathcal{H}_{BH} = -J \sum_j \sum_{\iota \in \{0, \pm 1\}} \sum_{\substack{\alpha, \beta \\ \in \{A, B, C\}}} T_{\alpha, \beta}^{(\iota)} |(j + \iota)_\alpha\rangle \langle j_\beta| + |j_\beta\rangle \langle (j + \iota)_\alpha| , \quad (7.18)$$

where $T_{\alpha, \beta}^{(\ell)}$ are as described in Eq. (6.2). Within this Hamiltonian only one element of T depends on the flux ϕ , $T_{B, C}^{(+1)} = e^{i\phi}$. The coefficient of the tunnelling between $(j + 1)_B$ and j_C is $-Je^{i\phi} = -Je^{i(\pi - \delta\phi)}$. Assuming a small $\delta\phi$ from $\phi = \pi$, this can be written as $-Je^{i(\pi - \delta\phi)} = -Je^{i\pi}e^{-i\delta\phi} \approx J(1 - i\delta\phi)$, which enables us to split the Hamiltonian into two parts. The Hamiltonian describing the unperturbed model is then the Hamiltonian for $\phi = \pi$:

$$\mathcal{H}_0 = -J \sum_j \sum_{\iota \in \{0, \pm 1\}} \sum_{\substack{\alpha, \beta \\ \in \{A, B, C\}}} T_{\alpha, \beta}^{(\iota)} |(j + \iota)_\alpha\rangle \langle j_\beta| + |j_\beta\rangle \langle (j + \iota)_\alpha| , \quad (7.19)$$

where $T_{B, C}^{(+1)} = -1$. The perturbation is:

$$V = -Ji\delta\phi \sum_j |(j + 1)_B\rangle \langle j_C| - |j_C\rangle \langle (j + 1)_B| , \quad (7.20)$$

where $J = 1$ is still set. We have previously shown that the eigenstates of \mathcal{H}_0 are $|w_{j, -}\rangle$, $|w_{j, 0}\rangle$ and $|w_{j, +}\rangle$ in Eq. (7.11), with corresponding energies $-2J$, 0 and $2J$.

Using time-dependent perturbation theory [156, 239], it can be shown that a generic state evolved in time has the form:

$$|\psi(t)\rangle = \sum_n c_n(t) e^{-iE_n t/\hbar} |n\rangle , \quad (7.21)$$

where $c_n(t)$ are the coefficients expanded from the time $t = 0$, when $V = 0$, case. E_n are the eigenvalues of \mathcal{H}_0 and $|n\rangle$ are the corresponding eigenstates. The expansion of the coefficients can be analysed using the time-dependent Schrödinger equation to obtain:

$$\tilde{V}_{mn}(t) = e^{i(E_m - E_n)t/\hbar} \langle m| V |n\rangle , \quad (7.22)$$

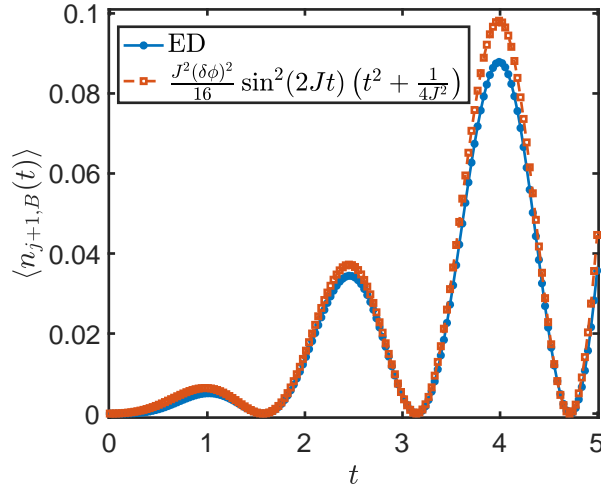


Fig. 7.8 The density on the next B site $\langle n_{j+1,B}(t) \rangle$, which is at $\ell = 13$ here, given that this is for a single particle initially loaded at $\ell = 10$ for $\delta\phi = 0.1\pi$. The on-site density is obtained both using ED and a perturbation theory fitting (see Eq. (7.24)).

and expanding the coefficients in powers of V , so that we have $c_m(t) = c_m^{(0)} + c_m^{(1)} + c_m^{(2)} \dots$. We state the zeroth and first order of the coefficients:

$$\begin{aligned} c_m^{(0)}(t) &= c_m^{(0)}(0) \\ c_m^{(1)}(t) &= -i \sum_n \int_0^t \tilde{V}_{mn}(t') c_n^{(0)}(t') dt' . \end{aligned} \quad (7.23)$$

Within our model, we calculate the first order coefficients from Eq. (7.23) to obtain the time-evolved state $|\psi(t)\rangle$ from Eq. (7.21). We then obtain the probability of the particle being in a given site. This prediction is only accurate for small time-steps and small J and $\delta\phi$ values, meaning that if we examine a smaller $\delta\phi$ this is even more accurate.

The damping occurs as some of the particle leaks out of the AB cage due to the imperfect cage basis. To observe the leakage from the initial cage, we focus on one of the B sites outside of the cage, $\langle n_{j+1,B}(t) \rangle$. The approximation of the on-site density at the next B site is given by:

$$\langle n_{j+1,B}(t) \rangle = \frac{J^2(\delta\phi)^2}{16} \sin^2(2Jt) \left(t^2 + \frac{1}{4J^2} \right) . \quad (7.24)$$

The ED result and this approximation from Eq. (7.24) are shown in Fig. 7.8 when $\delta\phi = 0.1\pi$ and the $(j+1)_B$ site used is then $\ell = 13$. It can be seen that for small time steps this perturbation fits very well, however, as t is increased the accuracy diminishes. In this case (when $\delta\phi = 0.1\pi$ and $T < 1$), we have a maximum error

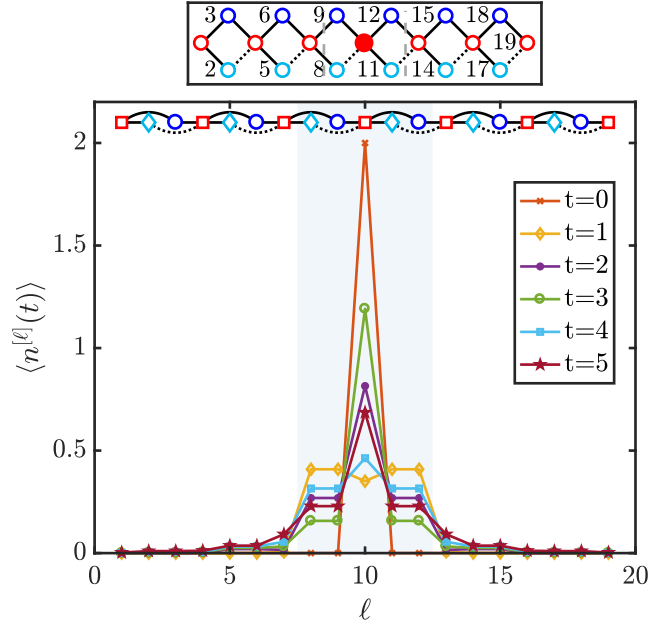


Fig. 7.9 The on-site density of a pair of particles which are initially started at the central $\ell = 10$ site within an $L = 19$ chain, where $\phi = \pi$. A snapshot is shown of the on-site density $\langle n^{[\ell]}(t) \rangle$ for $t = 0, 1, 2, 3, 4, 5$. The inset shows the initial setup with the dashed lines where the cage borders would appear.

of ≈ 0.001 which is less than 1%, whereas if we examine $\delta\phi = 0.01\pi$ the maximum error is instead 7.29×10^{-8} where the damping is of the order of 10^{-3} . We observe that the occurrence of on-site density at $\langle n_{j+1,B}(t) \rangle$ follows a sinusoidal function, which has an increasing amplitude as more of the particle leaks out of the AB cage environment. When the on-site density $\langle n_{j+1,B}(t) \rangle$ experiences a minimum, some of its density spreads to the $(j+2)_A$ ($\ell = 15$) and the $(j+1)_C$ ($\ell = 14$) sites, promoting further propagation away from the original cage.

7.4 Dynamics of a Pair of Particles

We now extend our discussion of the AB effect by examining a pair of particles within the chain. A pair of particles is able to escape the cage as long as there is an interaction between them, as motivated in Ch. 6. This is illustrated in Fig. 7.9, where $U/J = 1$ and a pair of particles is initially loaded at the central B site, $\ell = 10$. This analysis was carried out using ED [154]. From Fig. 7.9 it is clear that although the cage basis is no longer intact, the leakage out of the sites that are within the cage is still very gradual. To make this more evident, Fig. 7.10 is of the on-site density $\langle n_{j,B}^{[\ell]} \rangle$ at $\ell = 10$, where $\phi = \pi$. Initially, the damping appears to be similar to the damping caused by imperfect frustration in the single particle

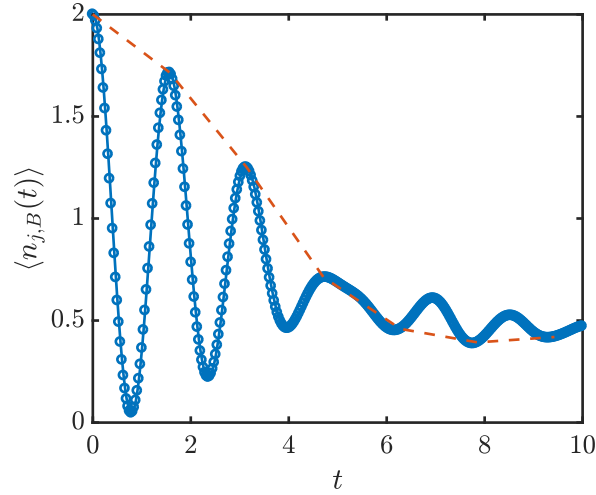


Fig. 7.10 The on-site density $\langle n_{j,B}(t) \rangle$ for $j = 4$ which is at $\ell = 10$ with $U = 1$ for a pair of particles which are loaded at the same center site. The dashed line is a guide for the eye to observe the type of damping.

case (see Fig. 7.7) but a closer inspection reveals that the initial periodicity breaks down in the pair case at $t \approx 4.7$, whereas in the single case this remained for the same examined times. As the breakdown of the AB cage states is a result of the interaction between the particles, it is unsurprising that the pair of particles would evolve differently to a single particle with imperfect frustration, even if there is a similar initial leakage out of the AB cage.

The typical pattern that leads to the oscillation within the on-site density at the j_B site is that some of the density from the B site spreads to the other A and C sites within the cage, then some of this returns to the central B site from the A and C sites (less each time when the density is leaking out). The initial periodicity of the on-site density is broken just after the peak at $t \approx 4.7$, where there is a peak at the central B site (j_B), which should spread to the A and C sites within the cage ($(j-1)_C, j_A, j_C, (j+1)_A$). Instead, only a fractional amount leaves the site j_B to spread to the A and C sites within the cage and a substantial amount of the density leaks out from the A and C sites into the B sites outside the cage ($(j-1)_B$ and $(j+1)_B$). This results in a second peak in $\langle n_{j,B}(t) \rangle$, instead of a trough which would have continued the cycle.

To investigate the leakage out of the AB cage further, an examination will be performed of how the parameter U effects the time at which the particles can escape the cage.

7.4.1 The Effect of Interaction on Escaping the Cage

Once a pair of particles is loaded, it can escape the cage provided that $U \neq 0$. When $U \ll J$, the particles interact less meaning that it is harder for them to overcome the AB cage effect, however, when U becomes too large the effective mass of the bosons is very large which will make tunnelling less energetically favourable. There should be some optimal, or approximately optimal, U at some point between these two extreme cases, that leads to the largest leakage for short times. In order to investigate this, $J = 1$ is set and the amount escaping the initial cage $\langle n_{out} \rangle$:

$$\langle n_{out} \rangle = \sum_{\ell=1}^L \langle n^{[\ell]}(t) \rangle - \langle n_{in} \rangle , \quad (7.25)$$

is considered over time for different U parameters. Here the initial condition is the central B site labelled Ξ , meaning that the on-site density within the cage is given by:

$$\langle n_{in} \rangle = \sum_{\ell \in [\Xi-2, \Xi+2]} \langle n^{[\ell]}(t) \rangle . \quad (7.26)$$

It is impossible to find an optimal U for longer time lengths due to the fact that there is interference between particles leaking back into the cage and additional leakage to cages further away. In order to avoid this we focus on times $t \leq 1$. Within this region, there is still some competition as to which U provides the maximal amount of escape from the cage over time. In Fig. 7.11 we plot $\langle n_{in} \rangle$ for specified values of U against the time t , to illustrate the fact that there appear to be optimal U values at given times (see the peaks in $U = 7.5$ and $U = 9$ for example). From the inset, it is also clear that there is a definite region enclosed by the full range of U parameters where $1 \leq U \leq 30$ in steps of 0.5.

To better illustrate that an optimal U exists for each specific time t (when this is small enough so that multiple interference is not occurring), we fix the time and examine the amount that escapes against the parameter U in Fig. 7.12. An example of $\langle n_{out} \rangle$ is shown for $t = 0.7$ in Fig. 7.12a. It is apparent that the amount that has escaped the cage is still very small at this time-step and it should be noted that this is even smaller for smaller times. It is, however, clear that there is a specific interaction strength U , which provides the maximal escape probability. The normalised amount that has escaped the cage:

$$\widetilde{\langle n_{out} \rangle} = \frac{\langle n_{out} \rangle}{\max(\langle n_{out} \rangle)} , \quad (7.27)$$

is used for convenience to examine the peak positions rather than their amplitudes which are dependent on the fact that the system has evolved for longer. It is

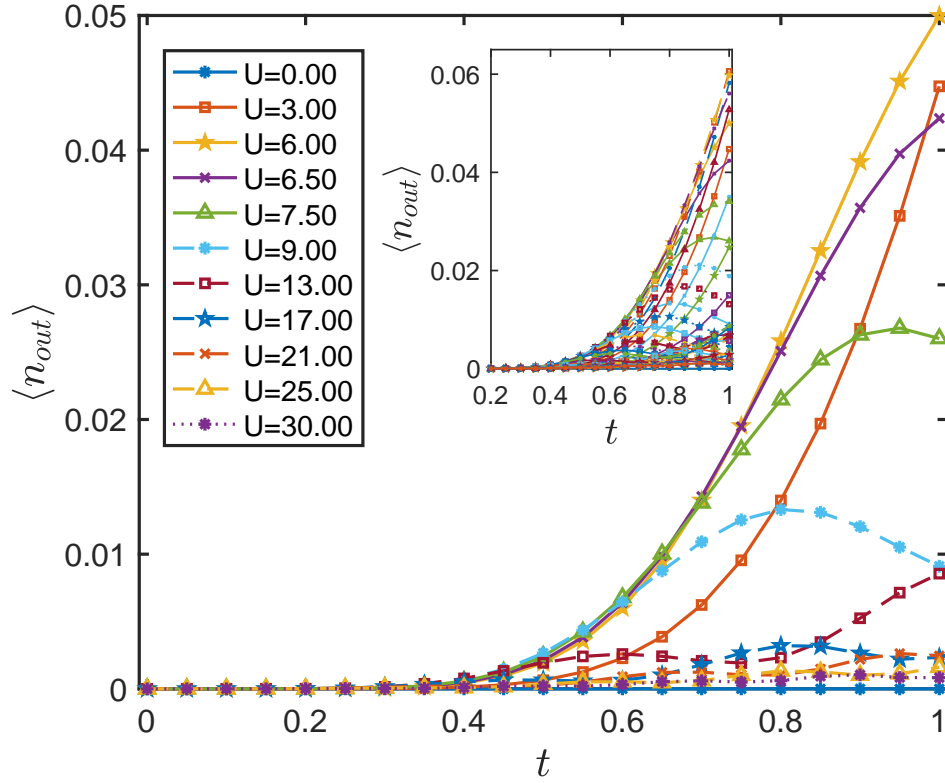


Fig. 7.11 The evolution of the particles when the parameter U is changed. The amount that has escaped the cage $\langle n_{out} \rangle$ is shown for different U values against time t . The inset is a plot of the range from $U \in [1, 30]$ in steps of 0.5 in order to illustrate that there is a clear boundary of the U parameters which will be optimal at a given time t .

clear from Fig. 7.12 that there is a well-defined maximum point occurring at different U parameters corresponding to a given time, except for when t is very small, specifically for $t = 0.1$ as its optimal U occurs past the range that we have examined. In fact, not only is there a specific maximum, but it can be seen that the oscillation with U parameters above and below the optimal one at a fixed time all follow the same pattern. It can also be observed that as the time is increased within this range, the U parameter which corresponds to the maximum amount escaping from the cage decreases.

7.5 Dynamics of a System with Unit Filling

Lastly, it is informative to examine the system dynamics in a many-body case, so we will examine the dynamics under unit filling. In this section, we will provide some initial analysis that can be expanded upon. There are a number of extensions that would be useful, such as analysing the entropy or entanglement spectrum

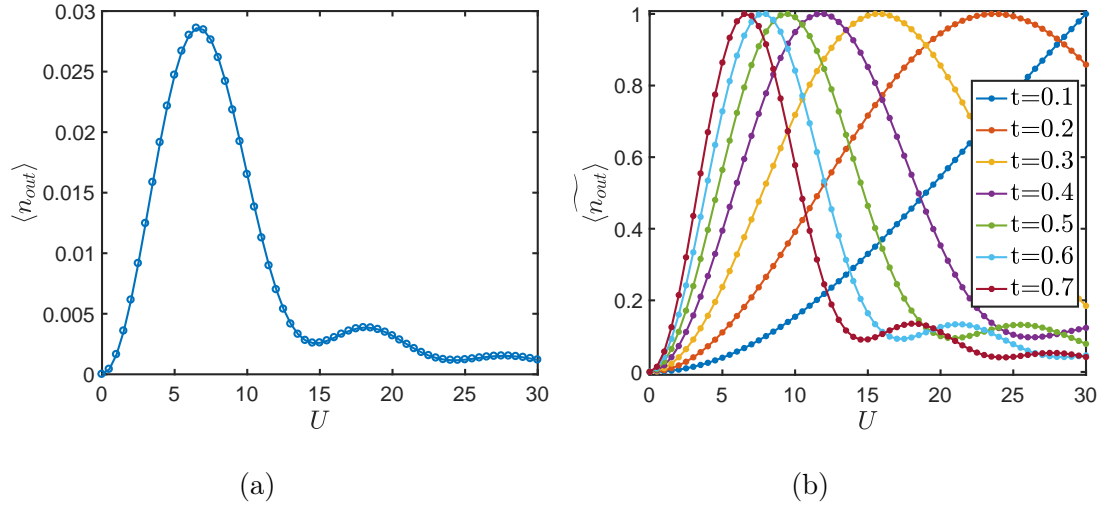


Fig. 7.12 The dependence of $\langle n_{out} \rangle$ on U . **(a):** An example is given for $t = 0.7$ against different interaction strengths U . **(b):** The dependence of $\langle n_{out} \rangle$ on U is considered for a range of t , where at each time step the value $\langle n_{out} \rangle$ is normalised by its maximum, giving $\widetilde{\langle n_{out} \rangle}$, so that it is more clear which U dominates excluding the effect that as more time has occurred more particles will have escaped.

over time. Also if we apply a quench within the dynamics there are a number of interesting aspects that can be explored, such as the occurrence of Mott domains and their subsequent melting to superfluid, examined by Bernier *et al.* close to unit filling, by varying the interaction strength [236]. Another interesting analysis is the work conducted by Kasztelan *et al.* who performed an analysis of the transfer efficiency by biasing the particles within one section (in their case one leg of a two-leg ladder) and seeing how it spreads to the rest of the system [226]. In order to perform our initial analysis, we will now rely completely on MPS methods so we will briefly give a description of which method was considered the most appropriate for our model.

7.5.1 Finding the Optimal MPS Implementation

As mentioned in Ch. 4, finding the best method to use for time-evolution can be very model-specific. For our model using TEBD (or indeed tDMRG) is not ideal because numerically our model contains next-nearest neighbour tunnelling terms. Although adaptations to these methods exist which can handle longer-range interactions they require more complicated procedures and attempts to do so can lead to poor scaling [168, 169]. It is, therefore, preferable to use a different method which is better equipped for longer interactions, instead. For these calculations we use the OSMPs set of codes [149, 150] (see Ch. 3 and 4), meaning the two methods that are left in our arsenal (though not the only methods available if using other implementations) are TDVP and the Krylov based time evolution.

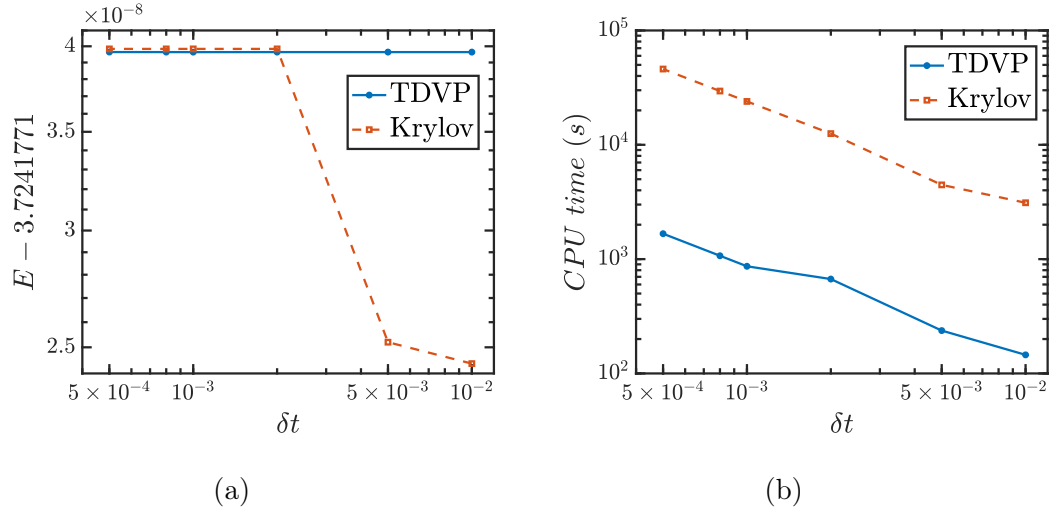


Fig. 7.13 Comparison between the Krylov and the **TDVP** method for an example case $T = 1$, $U = 1.2$, $\chi = 200$ and $L = 10$ as the time-step size δt is varied. **(a)**: The evolution energy for the two methods as the step-size is changed. **(b)**: The CPU time required to perform the method and obtain the measures of observables for each method.

We carried out a comparison of both the Krylov and the **TDVP** method in order to decide which one is the most appropriate for the rhombi model. A comparison was done of the number of sweeps, the truncation χ , the number of steps and varying the internal tolerances such as the Lanczos tolerance, which controls the accuracy of the estimate of the evolution at each time step (see Ch. 4).

In order to perform a comparison, we chose a parameter close to the critical point, $U = 1.2J$, as this is one of the places where the algorithm should perform worst. In Fig. 7.13, an example of the time evolution up to the total time $T = 1.0$ is shown with varying step-size using both the Krylov and the **TDVP** method. From our comparisons we were able to draw the conclusion that both methods converge under the correct scenarios. For example, in Fig. 7.13a once the step size is reasonably small ($\delta t \leq 2 \times 10^{-3}$ in this case) the two methods agree on the value of the evolution energy E with reasonable accuracy. There is, however, a substantial difference in the computation time between the two methods as shown in Fig. 7.13b. **TDVP** is, therefore, the preferential method as it requires less computation time.

7.5.2 Propagation from Half of the Chain

Inspired by Kasztelan *et al.* [226], we have loaded two particles onto all sites in the first half of the chain, leaving the rest of the chain empty, to see how they transfer to the rest of the chain. This is evolved under the $\phi = \pi$ Hamiltonian

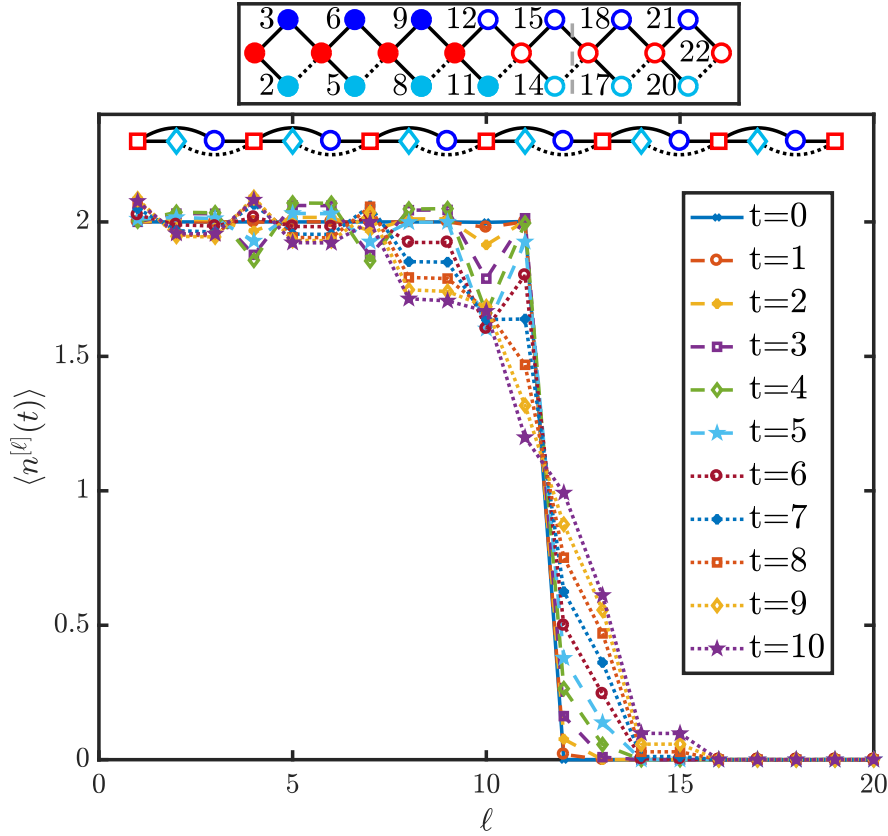


Fig. 7.14 The evolution $\langle n^{[\ell]} \rangle$ of the bosons for different times t , $\phi = \pi$, $L = 22$ and $U = 1$ obtained using TDVP with time steps $\delta t = 2 \times 10^{-4}$. The initial state is double occupation in the first half of the chain as shown in the inset. The border of the occupied cages is shown by the grey dashed line. These results have converged to a suitable tolerance. The connections between sites is shown at the top of the figure, where squares correspond to the B sites, diamonds to the C sites and circles to the A sites.

to observe the cage restriction once again. In Fig 7.14 we have chosen to show a chain of length $L = 22$, which is large enough so that the border effects should not restrict/affect the movement of the particles into the first unoccupied cage. For the initial times $t \leq 1$ shown, the only oscillations are within the cage bases that were already occupied. First, we will focus on the movement from the first half into the second unoccupied half of the chain. The initial propagation is from site $\ell = 11$ (a C site) to site $\ell = 12$ (an A site). It then slowly spreads from $\ell = 12$ to $\ell = 13, 14, 15$ but does not spread into the B site in the next cage, $\ell = 16$ for $t \leq 1$. We do, however, expect that with longer times the propagation through the system will result in a leakage into sites $\ell = 16$ and beyond.

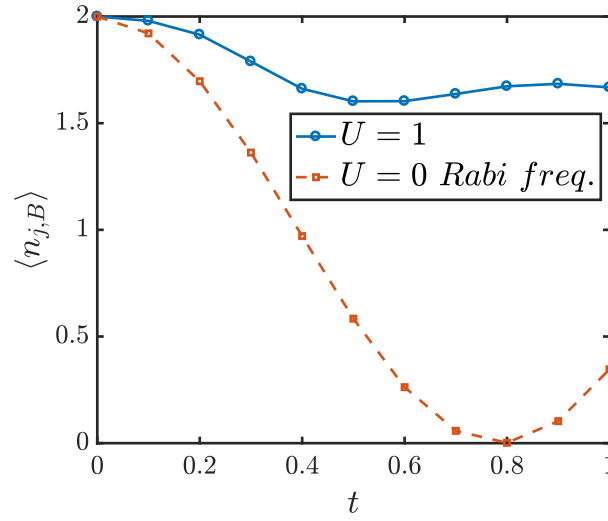


Fig. 7.15 A comparison of the damped interference that occurs at $\langle n_{4,B}(t) \rangle$ which corresponds to $\ell = 10$ and the Rabi frequency that corresponds to a pair of particles with no interaction, i.e. $U = 0$.

As well as this spreading into the rest of the chain, there is an oscillation between the A and the C sites within the loaded half of the chain. For sites $\ell = 1, \dots, 7$ there is some semblance of the oscillations that were observed for both the single and the pair particles. The B sites lose/gain density as the A and C sites surrounding them gain/lose their on-site density, implying that the oscillation back and forth still exists to some extent. This oscillation, however, has many factors which makes fitting it difficult. The oscillations within a given cage are affected by particles leaking out (due to interaction) and the interference of other particles leaking into it from other cages. On top of this, more interactions can take place within each cage as there are approximately two particles at each site. In Fig. 7.15, we have plotted the oscillation at $\langle n_{4,B}(t) \rangle$ to illustrate its difference from what the Rabi oscillation is for a pair of non-interacting particles. It can be seen that there is no distinct period and that the amplitude has dramatically changed due to all of the different interference effects.

It should also be noted that aside from $j = 11$ and $j = 12$, the A and C sites beside each other (i.e. the ones that appear on the same side of the border of the cage) have the same on-site density. As the evolution proceeds, it is likely that the on-site density will continue to adjust so that all of the A and C sites have approximately equal density (aside from at the borders). This is, however, beyond the times that we have reached with calculations.

7.6 Conclusions and Further Analyses

In this chapter we have expanded our analysis of the 1-D BH rhombic chain by considering how a particle (or a collection of particles) move through this system depending on the amount of geometrical frustration implemented through the flux ϕ . In the fully-frustrated case we observe, as expected, full-frustration and perfect AB cages meaning that regardless of the length of time that the system is evolved for, a single particle cannot escape the cage. For this case, the movement of the single particle can be described by a Rabi oscillation where the on-site density probability oscillates between the particle being in the B site or spread across the A and C sites which form the cage. If, however, we have imperfect or no frustration, a single particle can escape the cage over time. Additionally, if we have full frustration and a pair of interacting particles, as motivated by the occurrence of the PLL in the static case, the particles are able to leak out of the cage restriction. We finally performed a full many-body calculation that could be realised experimentally. In the case where half of the chain is initially doubly filled, a similar oscillation takes place within the cages. We also expect the particles to leak into the unoccupied cage basis sites with longer times of evolution.

As this is an initial analysis, there are still a number of aspects that can be investigated further. More perturbation analysis could be carried out of the single particle under imperfect frustration to observe the damping of sites within the initial cage. A closer comparison could also be performed of the leakage from the cage resulting from imperfect flux with a single particle or from a pair of particles, to identify more precisely the differences in the leakage as a result of having interactions between the pair of particles.

In the case of unit average filling, it would be informative to measure the entanglement and the von Neumann entropy to see how these vary with time evolution. Further analysis can be done on this model under time dynamics to discover the effect of both linear and instantaneous quenches with time. A quench can be done of the ϕ value to observe the changes from LL to PLL or by varying the interaction to observe the MI to gapless transitions. The bias of particles within certain sites of the system can also be examined under quenches to obtain an estimate of the transfer efficiency throughout the chain.

CHAPTER VIII

CONCLUSION

*“So long and thanks for all the fish.”
Douglas Adams, The Hitchhiker’s
Guide to the Galaxy*

The work within this thesis has been orientated around quantum lattice systems. In particular, an analysis has been done of quantum critical phenomena, as this provides a number of very interesting features to explore. Explorations of more complex critical phenomena (or measures of it) are becoming more in-depth and attainable. This is as a result of improved theoretical methods to provide approximations [120, 155] and due to advancements within experimental setups [14, 29]. There are a number of advancing experimental implementations but we have limited ourselves to focusing on experiments involving ultracold atoms, some of which were motivated in Ch. 2. These have advanced greatly, allowing the control and probing of a single atom at a time through the single atom microscope, which was first realised with bosonic rubidium atoms in 2009 [29, 110, 111].

Within Ch. 3 and Ch. 4 we have provided a detailed description of some theoretical methods that can be used for approximating the ground state and the dynamics of a 1-D quantum lattice system. The methods that we mostly focused on are those that require the use of a renowned ansatz, called the matrix product states (MPS) [120]. This provides a very efficient way of representing states as a tensor product of a representation on each site. The main method to perform simulations to obtain the ground state is the DMRG method, which was first set up by White [121, 125] in 1992. We have also explored briefly a number of implementations of these methods and have provided a comparison in one simple case.

We have described a number of methods within the MPS ansatz to obtain the time evolution of a given state. Two of these methods, TEBD and the almost equivalent tDMRG only perform well for systems with nearest-neighbour interactions, which makes them unsuitable for the time analysis we perform later in Ch. 7. The Krylov and the TDVP methods are equipped for longer interactions and tunnellings. We have also commented on the fact that the time simulation methods can be very model dependent meaning that they should be chosen with care.

We use the DMRG method to explore the critical phenomena within 1-D 1OQPTs in Ch. 5. We analysed pairwise entanglement behaviour in diverse 1OQPTs driven by Hamiltonians with only nearest-neighbour terms. Our analysis expanded upon the work of Campostrini *et al.* [36, 54], who provided a FSS for 1OQPTs. Entanglement is an invaluable resource when dealing with quantum correlations, which motivated us to examine if it followed the same FSS that other physical observables, such as the magnetisation, were shown to. We studied the concurrence in the spin-1/2 Ising model with a transverse and longitudinal field and the entanglement negativity within the spin-1 XXZ model of the two central spins.

This work motivates the dramatic importance of finite-size effects when a 1OQPT occurs in the nearby region of a multi-critical point containing also a 2OQPT. Without caution, the finite results can lead to incorrect interpretation of the QPTs, as the pairwise entanglement measures are continuous across the phase transition, while their first derivatives are not. We investigated this feature further and found that the behaviour of the entanglement measure arises from the two-body reduced density matrix elements, which for two-body local Hamiltonians, are linked to the non-analyticities of the ground state energy.

We have demonstrated that for finite systems, the order of the QPT in symmetry broken phases is given by the scaling behaviour of their bipartite entanglement and not by its non-analytical character. This can be used for determining the order and boundaries of quantum phase transitions near multi-critical points. A further analysis could be done of non-symmetric cases (i.e. of transitions of non-Ising type) in addition to the Néel/ Large- D transition to see if a more precise scaling behaviour can be observed.

To explore more aspects of critical phenomena, we examined frustrated systems, specifically the geometrically frustrated quasi-1-D chain of rhombi. In Ch. 2 we motivated that exploring critical phenomena lends itself to a number of interesting features, such as the occurrence of energy flat-bands, a localisation effect as a result of AB caging [77] and the possibility of particles forming pairs.

The chain of rhombi is a very relevant model which has received increasing attention for a number of reasons. One motivation for using a rhombi chain that has been shown, is that it forms bound Cooper pairs (of charge $4e$) within [JJAs](#), which has possible applications towards quantum computing. We have also mentioned that this model should be realisable experimentally with ultracold atoms using a single atom microscope and shaking of the lattice barrier amplitudes [102–104, 215] to imprint the phase on the tunnelling matrix elements. A recent work by Mukherjee *et al.* [194] has also motivated the realisation of such a model in a photonic lattice. If an experimental realisation is being done of many-body particles to obtain the [PLL](#), then it is more appropriate to use an experimental setup which has a larger region of [PLL](#) away from perfect flux $\phi = \pi$, to make the experiment more resilient against errors. The robustness is increased by introducing the frustration through modulation of the tunnelling amplitude instead of through an applied magnetic flux.

The chain of rhombi was used by Vidal *et al.* [77] to coin the term [AB](#) cages, where each rhombi was shown to localise the movement of the particle due to the [AB](#) effect. We performed a detailed analysis of the model under full-frustration (which is implemented by applying a magnetic flux of π to each rhombus) to confirm that a localisation occurs due to the [AB](#) effect. Through consideration of the single-particle case we obtained the eigenstates of the [AB](#) cage, which correspond to flat energy bands when $\phi = \pi$ and provide some motivation of the terms that arise. A further analysis that could be done within this model is a direct projection of the Hamiltonian onto the flat-band as performed in Refs. [80, 81, 96, 191].

We then examined this model under unit filling and found that when the interactions dominate we obtain the [MI](#). When the tunnelling dominates, the particles form pairs and are able to escape the cage effect, causing the system to enter into a [PLL](#) phase. A different analysis could be carried out of the mean-field theory describing the pair of particles to see more clearly how the pair moves within the system [81, 240]. This could also be used to confirm our intuition that for large tunnelling, the [PLL](#) phase has the exact same features as the [LL](#) but travelling as bound pairs.

As we have motivated in the [Ch. 2](#) and [Ch. 5](#), entanglement is an invaluable resource for obtaining more information about the nature of quantum systems, which led to our exploration of both the entanglement spectrum and the scaling of the von Neumann entropy of the reduced density matrix of a block against its length. The von Neumann entropy is unable to distinguish between the two phases [LL](#) and [PLL](#) arising from the non-frustrated and fully-frustrated case. Exploring

the entanglement spectrum, though requiring a more in-depth analysis shows a fundamental difference within the two phases. This analysis could be expanded on by enforcing the \mathbb{Z}_2 symmetry within the model to allow for a sensible FSS.

In Ch. 7 we expanded our analysis of the AB cage effect by examining how particles evolve throughout the system with time. We found, as motivated in the previous chapter, that a single particle under full frustration is unable to break out of the AB cage it begins in. This effect also held for multiple particles with the interaction strictly set to zero. The movement of a single particle (or non-interacting particles) which are strictly localised within a cage is described by a Rabi oscillation, where the particles move between the central (B) hub site and the four rim (A and C) sites surrounding it. The AB cage is no longer able to strictly enforce localisation when imperfect flux is loaded, meaning that there is some probability of leaking out of the cage. We have used perturbation theory in order to calculate what the probability is of a particle leaking out onto the next B site, which is still relatively small for $\delta\phi = 0.1\pi$. As expected by the occurrence of the PLL phase, the AB cage also breaks down when there are multiple interacting particles that can form pairs. We have shown that a single pair within a cage, has a probability of leakage, which also damps the Rabi oscillations and then destroys them, within the cage over time t . Further analysis could be done using perturbation theory, perhaps even for a pair of particles, to observe more precisely how the particle moves throughout the system.

Lastly, we performed a brief analysis with unit average filling of the particles loaded into half of the chain and observed that the particles move very gradually for initial times as they interact with particles in the first half of the chain, within each cage. Longer times could be explored to confirm that we observe the particles leaking out of the cages that they initially occupied. With unit filling there are a number of further analyses that would prove illuminating. This includes examining the time-evolution of the von Neumann entropy and the entanglement spectrum to observe how their structures vary with time. Additionally, performing a quantum quench either with the parameter J or ϕ so that we cross into the different phases from gapped to gapless or between the two gapless LL and PLL could provide further insightful information.

To summarise, this thesis has explored quantum critical phenomena within quantum lattice systems by focusing on measures of entanglement and its scaling features surrounding a IOQPT. We have also provided an analysis of a model with geometric frustration through the chain of rhombi. This provided a platform to explore a number of interesting effects, including how the localisation is enforced

through the [AB](#) cage effect and how the particles form pairs to overcome this when it is more energetically favourable to tunnel. There are still a number of extensions that can be performed on these works in order to further understand the properties and features that we have illustrated, some of which we have motivated above.

Further exploration of measures of quantum lattices and the identification of phases through theoretical techniques is crucial to understanding how the phenomenon behaves surrounding critical points of different types and also to motivate how to perform the experimental realisation of these systems. Despite all of the advancements within experimental techniques, performing experiments with many body lattices is still very challenging. Any optical experiment can suffer from losses, which decrease the total power during propagation and these must be carefully optimised within the experimental realisation. It also remains a constant open experimental challenge to be able to explore experimental systems with larger system sizes and with longer coherent evolution times [23, 29]. The efforts being put in to achieve these experiments, makes a corresponding theoretical study of the phenomena on larger scales or in deeper depth even more crucial.

REFERENCES

- [1] Clerk-Maxwell, J. (1875). On the dynamical evidence of the molecular constitution of bodies. *Nature*, 11(279):357. [online].
- [2] Jaeger, G. (1998). The Ehrenfest classification of phase transitions: introduction and evolution. *Archive for history of exact sciences*, 53(1):51. [online].
- [3] Sauer, T. (2017). A look back at the Ehrenfest classification. *The European Physical Journal Special Topics*, 226(4):539. [online].
- [4] Landau, L., Lifshitz, E. and Pitaevskii, L. (1981). *Statistical Physics, Part I*. Butterworth Heinemann, Oxford, U.K.
- [5] Sachdev, S. (2011). *Quantum phase transitions*. Cambridge University Press, Cambridge, U.K.
- [6] Nishimori, H. and Ortiz, G. (2010). *Elements of phase transitions and critical phenomena*. Oxford University Press, Oxford, U.K.
- [7] Amico, L., Fazio, R., Osterloh, A. and Vedral, V. (2008). Entanglement in many-body systems. *Rev. Mod. Phys.*, 80:517. [online].
- [8] Nielsen, M. A. and Chuang, I. L. (2010). *Quantum Computation and Quantum Information*. Cambridge University Press, Cambridge, U.K.
- [9] Stasińska, J., Rogers, B., Paternostro, M., De Chiara, G. and Sanpera, A. (2014). Long-range multipartite entanglement close to a first-order quantum phase transition. *Phys. Rev. A*, 89:32,330. [online].
- [10] Hofmann, M., Osterloh, A. and Gühne, O. (2014). Scaling of genuine multiparticle entanglement close to a quantum phase transition. *Phys. Rev. B*, 89:134,101. [online].
- [11] Barnum, H., Knill, E., Ortiz, G., Somma, R. and Viola, L. (2004). A Subsystem-Independent Generalization of Entanglement. *Phys. Rev. Lett.*, 92:107,902. [online].
- [12] Osterloh, A., Amico, L., Falci, G. and Fazio, R. (2002). Scaling of entanglement close to a quantum phase transition. *Nature*, 416(6881):608. [online].
- [13] Osborne, T. J. and Nielsen, M. A. (2002). Entanglement in a simple quantum phase transition. *Phys. Rev. A*, 66:32,110. [online].
- [14] Leykam, D., Andreanov, A. and Flach, S. (2018). Artificial flat band systems: from lattice models to experiments. *Advances in Physics: X*, 3(1):1473,052. [online].

- [15] Reimann, S. M. and Manninen, M. (2002). Electronic structure of quantum dots. *Rev. Mod. Phys.*, 74:1283. [online].
- [16] Fazio, R. and Van Der Zant, H. (2001). Quantum phase transitions and vortex dynamics in superconducting networks. *Physics Reports*, 355(4):235. [online].
- [17] Haldane, F. D. M. and Raghu, S. (2008). Possible Realization of Directional Optical Waveguides in Photonic Crystals with Broken Time-Reversal Symmetry. *Phys. Rev. Lett.*, 100:13,904. [online].
- [18] Hafezi, M., Mittal, S., Fan, J., Migdall, A. and Taylor, J. (2013). Imaging topological edge states in silicon photonics. *Nature Photonics*, 7(12):1001. [online].
- [19] Ningyuan, J., Owens, C., Sommer, A., Schuster, D. and Simon, J. (2015). Time- and Site-Resolved Dynamics in a Topological Circuit. *Phys. Rev. X*, 5:21,031. [online].
- [20] Deng, X.-H., Lai, C.-Y. and Chien, C.-C. (2016). Superconducting circuit simulator of Bose-Hubbard model with a flat band. *Phys. Rev. B*, 93:54,116. [online].
- [21] Ozawa, T., Price, H. M., Amo, A., Goldman, N., Hafezi, M., Lu, L., Rechtsman, M., Schuster, D., Simon, J., Zilberberg, O. and Carusotto, L. (2018). Topological photonics. *ArXiv e-prints*. [arXiv:1802.04173].
- [22] Bloch, I., Dalibard, J. and Zwerger, W. (2008). Many-body physics with ultracold gases. *Rev. Mod. Phys.*, 80:885. [online].
- [23] Lewenstein, M., Sanpera, A. and Ahufinger, V. (2012). *Ultracold Atoms in Optical Lattices: Simulating quantum many-body systems*. Oxford University Press, Oxford, U.K.
- [24] Bloch, I., Dalibard, J. and Nascimbene, S. (2012). Quantum simulations with ultracold quantum gases. *Nature Physics*, 8(4):267. [online].
- [25] Anderson, M. H., Ensher, J. R., Matthews, M. R., Wieman, C. E. and Cornell, E. A. (1995). Observation of Bose-Einstein condensation in a dilute atomic vapor. *Science*, 269(5221):198. [online].
- [26] Bradley, C. C., Sackett, C., Tollett, J. and Hulet, R. G. (1995). Evidence of Bose-Einstein condensation in an atomic gas with attractive interactions. *Phys. Rev. Lett.*, 75(9):1687. [online].
- [27] Davis, K. B., Mewes, M.-O., Andrews, M. R., Van Druten, N., Durfee, D., Kurn, D. and Ketterle, W. (1995). Bose-Einstein condensation in a gas of sodium atoms. *Phys. Rev. Lett.*, 75(22):3969. [online].
- [28] DeMarco, B. and Jin, D. S. (1999). Onset of Fermi degeneracy in a trapped atomic gas. *Science*, 285(5434):1703. [online].
- [29] Gross, C. and Bloch, I. (2017). Quantum simulations with ultracold atoms in optical lattices. *Science*, 357(6355):995. [online].
- [30] Moore, G. E. (1965). Cramming more components onto integrated circuits, Reprinted from Electronics. *IEEE Solid-State Circuits Society Newsletter*, 38(8):114. [online].

- [31] Bourzac, K. (2016). Intel: Chips will have to sacrifice speed gains for energy savings. *MIT Technology Review*, 5:2016.
- [32] Simonite, T. (2016). Moore's Law is dead. Now what. *MIT Technology Review*.
- [33] Fisher, M. E. and Barber, M. N. (1972). Scaling Theory for Finite-Size Effects in the Critical Region. *Phys. Rev. Lett.*, 28:1516. [online].
- [34] Vidal, G., Latorre, J. I., Rico, E. and Kitaev, A. (2003). Entanglement in Quantum Critical Phenomena. *Phys. Rev. Lett.*, 90:227,902. [online].
- [35] Latorre, J. I., Rico, E. and Vidal, G. (2004). Ground State Entanglement in Quantum Spin Chains. *Quant. Info. Comput.*, 4(1):48.
- [36] Campostrini, M., Nespolo, J., Pelissetto, A. and Vicari, E. (2014). Finite-Size Scaling at First-Order Quantum Transitions. *Phys. Rev. Lett.*, 113:70,402. [online].
- [37] Moessner, R. and Ramirez, A. P. (2006). Geometrical frustration. *Phys. Today*, 59(2):24. [online].
- [38] Balents, L. (2010). Spin liquids in frustrated magnets. *Nature*, 464(7286):199. [online].
- [39] Goldenfeld, N. (1992). *Lectures on Phase Transitions and the Renormalization Group*. Westview Press, U.S.A.
- [40] Dutta, A., Aeppli, G., Chakrabarti, B. K., Divakaran, U., Rosenbaum, T. F. and Sen, D. (2015). *Quantum phase transitions in transverse field spin models: from statistical physics to quantum information*. Cambridge University Press.
- [41] Berezinskii, V. (1971). Destruction of long-range order in one-dimensional and two-dimensional systems having a continuous symmetry group I. Classical systems. *Sov. Phys. JETP*, 32(3):493.
- [42] Kosterlitz, J. M. and Thouless, D. J. (1973). Ordering, metastability and phase transitions in two-dimensional systems. *Journal of Physics C: Solid State Physics*, 6(7):1181. [online].
- [43] Hadzibabic, Z., Krüger, P., Cheneau, M., Battelier, B. and Dalibard, J. (2006). Berezinskii–Kosterlitz–Thouless crossover in a trapped atomic gas. *Nature*, 441(7097):1118. [online].
- [44] Nelson, D. R. and Kosterlitz, J. (1977). Universal jump in the superfluid density of two-dimensional superfluids. *Phys. Rev. Lett.*, 39(19):1201. [online].
- [45] Greiner, M., Mandel, O., Esslinger, T., Hänsch, T. W. and Bloch, I. (2002). Quantum phase transition from a superfluid to a Mott insulator in a gas of ultracold atoms. *Nature*, 415(6867):39. [online].
- [46] Kühner, T. D., White, S. R. and Monien, H. (2000). One-dimensional Bose-Hubbard model with nearest-neighbor interaction. *Phys. Rev. B*, 61:12,474. [online].

- [47] Ising, E. (1925). Beitrag zur theorie des ferromagnetismus. *Zeitschrift für Physik*, 31(1):253. [online].
- [48] Kramers, H. A. and Wannier, G. H. (1941). Statistics of the Two-Dimensional Ferromagnet. Part I. *Phys. Rev.*, 60:252. [online].
- [49] Haligua, Y. L. B. (2010). *The Ising Model and Its Dualities*. Ph.D. thesis, Imperial College London.
- [50] Hubbard, J. (1963). Electron correlations in narrow energy bands. *Proc. R. Soc. Lond. A*, 276(1365):238. [online].
- [51] Hubbard, J. (1964). Electron correlations in narrow energy bands. II. The degenerate band case. *Proc. R. Soc. Lond. A*, 277(1369):237. [online].
- [52] Hubbard, J. (1964). Electron correlations in narrow energy bands III. An improved solution. *Proc. R. Soc. Lond. A*, 281(1386):401. [online].
- [53] Schulz, H. J., Cuniberti, G. and Pieri, P., Fermi liquids and Luttinger liquids. In *Field theories for low-dimensional condensed matter systems*, page 9. Springer.
- [54] Campostrini, M., Pelissetto, A. and Vicari, E. (2014). Finite-size scaling at quantum transitions. *Phys. Rev. B*, 89:94,516. [online].
- [55] Landau, D. P. and Binder, K. (2014). *A guide to Monte Carlo simulations in statistical physics*. Cambridge University Press, Cambridge, U.K.
- [56] Giamarchi, T. (2004). *Quantum Physics in One Dimension*, volume 121. Oxford university press, Oxford.
- [57] Ejima, S., Fehske, H., Gebhard, F., zu Münster, K., Knap, M., Arrigoni, E. and von der Linden, W. (2012). Characterization of Mott-insulating and superfluid phases in the one-dimensional Bose-Hubbard model. *Phys. Rev. A*, 85:53,644. [online].
- [58] Elstner, N. and Monien, H. (1999). Dynamics and thermodynamics of the Bose-Hubbard model. *Phys. Rev. B*, 59:12,184–12,187. [online].
- [59] Peres, A. (1996). Separability criterion for density matrices. *Phys. Rev. Lett.*, 77(8):1413. [online].
- [60] Horodecki, M., Horodecki, P. and Horodecki, R. (1997). Inseparable Two Spin- $\frac{1}{2}$ Density Matrices Can Be Distilled to a Singlet Form. *Phys. Rev. Lett.*, 78:574. [online].
- [61] Hill, S. and Wootters, W. K. (1997). Entanglement of a Pair of Quantum Bits. *Phys. Rev. Lett.*, 78:5022. [online].
- [62] Coffman, V., Kundu, J. and Wootters, W. K. (2000). Distributed entanglement. *Phys. Rev. A*, 61:52,306. [online].
- [63] Osborne, T. J. and Verstraete, F. (2006). General Monogamy Inequality for Bipartite Qubit Entanglement. *Phys. Rev. Lett.*, 96:220,503. [online].
- [64] Vidal, G. and Werner, R. F. (2002). Computable measure of entanglement. *Phys. Rev. A*, 65:32,314. [online].

- [65] Życzkowski, K., Horodecki, P., Sanpera, A. and Lewenstein, M. (1998). Volume of the set of separable states. *Phys. Rev. A*, 58:883. [online].
- [66] Vidal, J., Mosseri, R. and Dukelsky, J. (2004). Entanglement in a first-order quantum phase transition. *Phys. Rev. A*, 69:54,101. [online].
- [67] Alcaraz, F. C., Saguia, A. and Sarandy, M. S. (2004). Entanglement and quantum phases in the anisotropic ferromagnetic Heisenberg chain in the presence of domain walls. *Phys. Rev. A*, 70:32,333. [online].
- [68] Vidal, J., Palacios, G. and Mosseri, R. (2004). Entanglement in a second-order quantum phase transition. *Phys. Rev. A*, 69:22,107. [online].
- [69] Gu, S.-J., Lin, H.-Q. and Li, Y.-Q. (2003). Entanglement, quantum phase transition, and scaling in the XXZ chain. *Phys. Rev. A*, 68:42,330. [online].
- [70] Bose, I. and Chattopadhyay, E. (2002). Macroscopic entanglement jumps in model spin systems. *Phys. Rev. A*, 66:62,320. [online].
- [71] Orús, R. and Wei, T.-C. (2010). Visualizing elusive phase transitions with geometric entanglement. *Phys. Rev. B*, 82:155,120. [online].
- [72] Lacroix, C., Mendels, P. and Mila, F. (2013). *Introduction to Frustrated Magnetism: Materials, Experiments, Theory*. Springer, Berlin, Germany.
- [73] Wannier, G. H. (1950). Antiferromagnetism. The Triangular Ising Net. *Phys. Rev.*, 79:357. [online].
- [74] Lagendijk, A., Van Tiggelen, B. and Wiersma, D. S. (2009). Fifty years of Anderson localization. *Phys. Today*, 62(8):24. [online].
- [75] Anderson, P. W. (1958). Absence of Diffusion in Certain Random Lattices. *Phys. Rev.*, 109:1492. [online].
- [76] Sutherland, B. (1986). Localization of electronic wave functions due to local topology. *Phys. Rev. B*, 34:5208. [online].
- [77] Vidal, J., Mosseri, R. and Douçot, B. (1998). Aharonov-Bohm cages in two-dimensional structures. *Phys. Rev. Lett.*, 81(26):5888. [online].
- [78] Aharonov, Y. and Bohm, D. (1959). Significance of electromagnetic potentials in the quantum theory. *Phys. Rev.*, 115(3):485. [online].
- [79] Wigner, E. (1934). On the Interaction of Electrons in Metals. *Phys. Rev.*, 46:1002. [online].
- [80] Huber, S. D. and Altman, E. (2010). Bose condensation in flat bands. *Phys. Rev. B*, 82:184,502. [online].
- [81] Möller, G. and Cooper, N. R. (2012). Correlated Phases of Bosons in the Flat Lowest Band of the Dice Lattice. *Phys. Rev. Lett.*, 108:45,306. [online].
- [82] Mielke, A. (2018). Pair Formation of Hard Core Bosons in Flat Band Systems. *Journal of Statistical Physics*, 171(4):679. [online].
- [83] Vidal, J., Douçot, B., Mosseri, R. and Butaud, P. (2000). Interaction Induced Delocalization for Two Particles in a Periodic Potential. *Phys. Rev. Lett.*, 85:3906. [online].

- [84] Douçot, B. and Vidal, J. (2002). Pairing of Cooper Pairs in a Fully Frustrated Josephson-Junction Chain. *Phys. Rev. Lett.*, 88:227,005. [online].
- [85] Rizzi, M., Cataudella, V. and Fazio, R. (2006). $4e$ -condensation in a fully frustrated Josephson junction diamond chain. *Phys. Rev. B*, 73:100,502. [online].
- [86] Daley, A. J., Taylor, J. M., Diehl, S., Baranov, M. and Zoller, P. (2009). Atomic Three-Body Loss as a Dynamical Three-Body Interaction. *Phys. Rev. Lett.*, 102:40,402. [online].
- [87] Diehl, S., Baranov, M., Daley, A. J. and Zoller, P. (2010). Observability of Quantum Criticality and a Continuous Supersolid in Atomic Gases. *Phys. Rev. Lett.*, 104:165,301. [online].
- [88] Diehl, S., Baranov, M., Daley, A. J. and Zoller, P. (2010). Quantum field theory for the three-body constrained lattice Bose gas. I. Formal developments. *Phys. Rev. B*, 82:64,509. [online].
- [89] Mazza, L., Rizzi, M., Lewenstein, M. and Cirac, J. I. (2010). Emerging bosons with three-body interactions from spin-1 atoms in optical lattices. *Phys. Rev. A*, 82:43,629. [online].
- [90] Daley, A. J. and Simon, J. (2014). Effective three-body interactions via photon-assisted tunneling in an optical lattice. *Phys. Rev. A*, 89:53,619. [online].
- [91] Sowiński, T., Chhajlany, R. W., Dutta, O., Tagliacozzo, L. and Lewenstein, M. (2015). Criticality in the Bose-Hubbard model with three-body repulsion. *Phys. Rev. A*, 92:43,615. [online].
- [92] Phillips, L. G., De Chiara, G., Öhberg, P. and Valiente, M. (2015). Low-energy behavior of strongly interacting bosons on a flat-band lattice above the critical filling factor. *Phys. Rev. B*, 91(5):54,103. [online].
- [93] Anisimovas, E., Račiūnas, M., Sträter, C., Eckardt, A., Spielman, I. B. and Juzeliūnas, G. (2016). Semisynthetic zigzag optical lattice for ultracold bosons. *Phys. Rev. A*, 94:63,632. [online].
- [94] Noack, R., White, S. and Scalapino, D. (1996). The ground state of the two-leg hubbard ladder a density-matrix renormalization group study. *Physica C: Superconductivity*, 270(3-4):281. [online].
- [95] Takayoshi, S., Katsura, H., Watanabe, N. and Aoki, H. (2013). Phase diagram and pair Tomonaga-Luttinger liquid in a Bose-Hubbard model with flat bands. *Phys. Rev. A*, 88:63,613. [online].
- [96] Tovmasyan, M., van Nieuwenburg, E. P. L. and Huber, S. D. (2013). Geometry-induced pair condensation. *Phys. Rev. B*, 88:220,510. [online].
- [97] Cornell, E. A. and Wieman, C. E. (2002). Nobel Lecture: Bose-Einstein condensation in a dilute gas, the first 70 years and some recent experiments. *Rev. Mod. Phys.*, 74(3):875. [online].
- [98] Bloch, I. (2005). Ultracold quantum gases in optical lattices. *Nature Physics*, 1(1):23. [online].

- [99] Jaksch, D., Bruder, C., Cirac, J. I., Gardiner, C. W. and Zoller, P. (1998). Cold Bosonic Atoms in Optical Lattices. *Phys. Rev. Lett.*, 81:3108–3111. [online].
- [100] Goldman, N., Juzeliūnas, G., Öhberg, P. and Spielman, I. B. (2014). Light-induced gauge fields for ultracold atoms. *Reports on Progress in Physics*, 77(12):126,401. [online].
- [101] Dalibard, J., Gerbier, F., Juzeliūnas, G. and Öhberg, P. (2011). Colloquium: Artificial gauge potentials for neutral atoms. *Rev. Mod. Phys.*, 83:1523. [online].
- [102] Drese, K. and Holthaus, M. (1997). Ultracold atoms in modulated standing light waves. *Chemical Physics*, 217(2):201. [online].
- [103] Sias, C., Lignier, H., Singh, Y. P., Zenesini, A., Ciampini, D., Morsch, O. and Arimondo, E. (2008). Observation of Photon-Assisted Tunneling in Optical Lattices. *Phys. Rev. Lett.*, 100:40,404. [online].
- [104] Struck, J., Ölschläger, C., Le Targat, R., Soltan-Panahi, P., Eckardt, A., Lewenstein, M., Windpassinger, P. and Sengstock, K. (2011). Quantum Simulation of Frustrated Classical Magnetism in Triangular Optical Lattices. *Science*, 333(6045):996. [online].
- [105] Eckardt, A. (2017). Colloquium: Atomic quantum gases in periodically driven optical lattices. *Rev. Mod. Phys.*, 89:11,004. [online].
- [106] Tarruell, L., Greif, D., Uehlinger, T., Jotzu, G. and Esslinger, T. (2012). Creating, moving and merging Dirac points with a Fermi gas in a tunable honeycomb lattice. *Nature*, 483:302. [online].
- [107] Hyrkäs, M., Apaja, V. and Manninen, M. (2013). Many-particle dynamics of bosons and fermions in quasi-one-dimensional flat-band lattices. *Phys. Rev. A*, 87:23,614. [online].
- [108] Perego, E. (2015). *Generation of arbitrary optical potentials for atomic physics experiments using a Digital Micromirror Device*. Ph.D. thesis, School of Mathematical, Physical and Natural Sciences, University of Florence.
- [109] Gauthier, G., Lenton, I., Parry, N. M., Baker, M., Davis, M. J., Rubinsztein-Dunlop, H. and Neely, T. W. (2016). Direct imaging of a digital-micromirror device for configurable microscopic optical potentials. *Optica*, 3(10):1136. [online].
- [110] Bakr, W. S., Gillen, J. I., Peng, A., Fölling, S. and Greiner, M. (2009). A quantum gas microscope for detecting single atoms in a Hubbard-regime optical lattice. *Nature*, 462(7269):74. [online].
- [111] Sherson, J. F., Weitenberg, C., Endres, M., Cheneau, M., Bloch, I. and Kuhr, S. (2010). Single-atom-resolved fluorescence imaging of an atomic mott insulator. *Nature*, 467(7311):68. [online].
- [112] De Chiara, G. and Sanpera, A. (2018). Genuine quantum correlations in quantum many-body systems: a review of recent progress. *Reports on Progress in Physics*, 81(7):74,002. [online].

- [113] Carmelo, J. M., Lopes Dos Santos, J. and Rocha, V. V. J. (2007). *Strongly correlated systems, coherence and entanglement*. World Scientific, London.
- [114] Ceperley, D. and Alder, B. (1986). Quantum Monte Carlo. *Science*, 231(4738):555. [online].
- [115] Santos, M. and De Oliveira, M. (1999). The Transverse Ising Model Under a Time Oscillating Field. *International Journal of Modern Physics B*, 13(02):207. [online].
- [116] Kolorenč, J. and Mitas, L. (2011). Applications of quantum Monte Carlo methods in condensed systems. *Reports on Progress in Physics*, 74(2):26,502. [online].
- [117] Neirotti, J. P. and de Oliveira, M. J. (1996). Monte Carlo method for obtaining the ground-state properties of quantum spin systems. *Phys. Rev. B*, 53:668. [online].
- [118] Carleo, G. and Troyer, M. (2017). Solving the quantum many-body problem with artificial neural networks. *Science*, 355(6325):602. [online].
- [119] Saito, H. and Kato, M. (2018). Machine Learning Technique to Find Quantum Many-Body Ground States of Bosons on a Lattice. *Journal of the Physical Society of Japan*, 87(1):14,001. [online].
- [120] Schollwöck, U. (2011). The density-matrix renormalization group in the age of matrix product states. *Annals of Physics*, 326(1):96. [online].
- [121] White, S. R. (1992). Density matrix formulation for quantum renormalization groups. *Phys. Rev. Lett.*, 69:2863. [online].
- [122] Verstraete, F., Murg, V. and Cirac, J. I. (2008). Matrix product states, projected entangled pair states, and variational renormalization group methods for quantum spin systems. *Advances in Physics*, 57(2):143. [online].
- [123] Vidal, G. (2008). Class of Quantum Many-Body States That Can Be Efficiently Simulated. *Phys. Rev. Lett.*, 101:110,501. [online].
- [124] Orús, R. (2014). A practical introduction to tensor networks: Matrix product states and projected entangled pair states. *Annals of Physics*, 349:117. [online].
- [125] White, S. R. (1993). Density-matrix algorithms for quantum renormalization groups. *Phys. Rev. B*, 48:10,345. [online].
- [126] Wilson, K. G. (1975). The renormalization group: Critical phenomena and the Kondo problem. *Rev. Mod. Phys.*, 47:773. [online].
- [127] De Chiara, G., Rizzi, M., Rossini, D. and Montangero, S. (2008). Density Matrix Renormalization Group for Dummies. *Journal of Computational and Theoretical Nanoscience*, 5(7):1277. [online].
- [128] van der Vorst, H. A., Computational methods for large eigenvalue problems. In *Solution of Equations in \mathbb{R}^n (Part 4)*, *Techniques of Scientific Computing (Part 4)*, *Numerical Methods for Fluids (Part 2)*, volume 8 of *Handbook of Numerical Analysis*, page 3. Elsevier, Amsterdam.

- [129] Saad, Y. (2011). *Numerical Methods for Large Eigenvalue Problems: Revised Edition*, volume 66. Society for Industrial and Applied Mathematics, Philadelphia, U.S.A.
- [130] Hastings, M. B. (2007). An area law for one-dimensional quantum systems. *Journal of Statistical Mechanics: Theory and Experiment*, 2007(08):P08,024. [online].
- [131] Eisert, J., Cramer, M. and Plenio, M. B. (2010). Colloquium: Area laws for the entanglement entropy. *Rev. Mod. Phys.*, 82:277. [online].
- [132] Holzhey, C., Larsen, F. and Wilczek, F. (1994). Geometric and renormalized entropy in conformal field theory. *Nuclear Physics B*, 424(3):443. [online].
- [133] Calabrese, P. and Cardy, J. (2004). Entanglement entropy and quantum field theory. *Journal of Statistical Mechanics: Theory and Experiment*, 2004(06):P06,002. [online].
- [134] Verstraete, F. and Cirac, J. I. (2004). Renormalization algorithms for Quantum-Many Body Systems in two and higher dimensions. *ArXiv e-prints*. [arXiv:cond-mat/0407066].
- [135] Fannes, M., Nachtergaele, B. and Werner, R. F. (1992). Finitely correlated states on quantum spin chains. *Communications in Mathematical Physics*, 144(3):443. [online].
- [136] Schollwöck, U. (2005). The density-matrix renormalization group. *Rev. Mod. Phys.*, 77(1):259. [online].
- [137] Östlund, S. and Rommer, S. (1995). Thermodynamic limit of density matrix renormalization. *Phys. Rev. Lett.*, 75(19):3537. [online].
- [138] Dukelsky, J., Martín-Delgado, M. A., Nishino, T. and Sierra, G. (1998). Equivalence of the variational matrix product method and the density matrix renormalization group applied to spin chains. *Europhysics Letters*, 43(4):457. [online].
- [139] Burden, R. L. and Faires, J. D. (2010). *Numerical Analysis*. Brooks/Cole, Cengage Learning, Boston, U.S.A.
- [140] Li, H. and Haldane, F. D. M. (2008). Entanglement Spectrum as a Generalization of Entanglement Entropy: Identification of Topological Order in Non-Abelian Fractional Quantum Hall Effect States. *Phys. Rev. Lett.*, 101:10,504. [online].
- [141] Zaletel, M. P., Mong, R. S. K., Karrasch, C., Moore, J. E. and Pollmann, F. (2015). Time-evolving a matrix product state with long-ranged interactions. *Phys. Rev. B*, 91:165,112. [online].
- [142] McCulloch, I. P. (2007). From density-matrix renormalization group to matrix product states. *Journal of Statistical Mechanics: Theory and Experiment*, 2007(10):P10,014. [online].
- [143] Pirvu, B., Murg, V., Cirac, J. I. and Verstraete, F. (2010). Matrix product operator representations. *New Journal of Physics*, 12(2):25,012. [online].

- [144] Crosswhite, G. M., Doherty, A. C. and Vidal, G. (2008). Applying matrix product operators to model systems with long-range interactions. *Phys. Rev. B*, 78:35,116. [online].
- [145] Pavlopoulos, G. A., Secrier, M., Moschopoulos, C. N., Soldatos, T. G., Kossida, S., Aerts, J., Schneider, R. and Bagos, P. G. (2011). Using graph theory to analyze biological networks. *BioData mining*, 4(1):10. [online].
- [146] Paeckel, S., Köhler, T. and Manmana, S. R. (2017). Automated construction of $U(1)$ -invariant matrix-product operators from graph representations. *SciPost Physics*, 3(5):35. [online].
- [147] Al-Assam, S., Clark, S. R. and Jaksch, D. (2017). The tensor network theory library. *Journal of Statistical Mechanics: Theory and Experiment*, 2017(9):93,102. [online].
- [148] Hubig, C., McCulloch, I. P., Schollwöck, U. and Wolf, F. A. (2015). Strictly single-site DMRG algorithm with subspace expansion. *Phys. Rev. B*, 91:155,115. [online].
- [149] Wall, M. L. and Carr, L. D. (2012). Out-of-equilibrium dynamics with matrix product states. *New Journal of Physics*, 14(12):125,015. [online].
- [150] Jaschke, D., Wall, M. L. and Carr, L. D. (2018). Open source Matrix Product States: Opening ways to simulate entangled many-body quantum systems in one dimension. *Computer Physics Communications*, 225:59. [online].
- [151] Silvi, P., Tschirsich, F., Gerster, M., Jünemann, J., Jaschke, D., Rizzi, M. and Montangero, S. (2018). The Tensor Networks Anthology: Simulation techniques for many-body quantum lattice systems. *ArXiv e-prints*. [arXiv:1710.03733].
- [152] Lehoucq, R. B., Sorensen, D. C. and Yang, C. (1998). *ARPACK users' guide: solution of large-scale eigenvalue problems with implicitly restarted Arnoldi methods*. Siam, Philadelphia, U.S.A.
- [153] Golub, G. H. and Van Loan, C. F. (1996). *Matrix computations*. The Johns Hopkins University Press, Baltimore, U.S.A.
- [154] Zhang, J. and Dong, R. (2010). Exact diagonalization: the Bose–Hubbard model as an example. *European Journal of Physics*, 31(3):591. [online].
- [155] Paeckel, S., Köhler, T., Swoboda, A., Manmana, S. R., Schollwöck, U. and Hubig, C. (2019). Time-evolution methods for matrix-product states. *ArXiv e-prints*. [arXiv:arXiv:1901.05824].
- [156] Griffiths, D. J. and Schroeter, D. F. (2018). *Introduction to quantum mechanics*. Cambridge University Press, Cambridge, U.K.
- [157] Suzuki, M. (1976). Relationship between d-dimensional quantal spin systems and (d+ 1)-dimensional Ising systems: Equivalence, critical exponents and systematic approximants of the partition function and spin correlations. *Progress of Theoretical Physics*, 56(5):1454. [online].
- [158] Trotter, H. F. (1959). On the product of semi-groups of operators. *Proceedings of the American Mathematical Society*, 10(4):545. [online].

- [159] Mishmash, R. V. (2008). *Quantum Many-Body Dynamics of Ultracold Bosons in One-Dimensional Optical Lattices: Theoretical Aspects, Simulation Methods, and Soliton Formation and Stability*. Ph.D. thesis, Colorado School of Mines.
- [160] Cazalilla, M. and Marston, J. (2002). Time-dependent density-matrix renormalization group: A systematic method for the study of quantum many-body out-of-equilibrium systems. *Phys. Rev. Lett.*, 88(25):256,403. [online].
- [161] Daley, A. J., Kollath, C., Schollwöck, U. and Vidal, G. (2004). Time-dependent density-matrix renormalization-group using adaptive effective Hilbert spaces. *Journal of Statistical Mechanics: Theory and Experiment*, 2004(04):P04,005. [online].
- [162] White, S. R. and Feiguin, A. E. (2004). Real-time evolution using the density matrix renormalization group. *Phys. Rev. Lett.*, 93(7):76,401. [online].
- [163] White, S. R. (1996). Spin gaps in a frustrated Heisenberg model for CaV₄O₉. *Phys. Rev. Lett.*, 77(17):3633. [online].
- [164] Vidal, G. (2003). Efficient classical simulation of slightly entangled quantum computations. *Phys. Rev. Lett.*, 91(14):147,902. [online].
- [165] Vidal, G. (2004). Efficient simulation of one-dimensional quantum many-body systems. *Phys. Rev. Lett.*, 93(4):40,502. [online].
- [166] Tamascelli, D., Rosenbach, R. and Plenio, M. B. (2015). Improved scaling of time-evolving block-decimation algorithm through reduced-rank randomized singular value decomposition. *Phys. Rev. E*, 91(6):63,306. [online].
- [167] White, C. D., Zaletel, M., Mong, R. S. and Refael, G. (2018). Quantum dynamics of thermalizing systems. *Phys. Rev. B*, 97(3):35,127. [online].
- [168] Schachenmayer, J., Lesanovsky, I., Micheli, A. and Daley, A. J. (2010). Dynamical crystal creation with polar molecules or Rydberg atoms in optical lattices. *New Journal of Physics*, 12(10):103,044. [online].
- [169] Stoudenmire, E. M. and White, S. R. (2010). Minimally entangled typical thermal state algorithms. *New Journal of Physics*, 12(5):55,026. [online].
- [170] Haegeman, J., Cirac, J. I., Osborne, T. J., Pižorn, I., Verschelde, H. and Verstraete, F. (2011). Time-dependent variational principle for quantum lattices. *Phys. Rev. Lett.*, 107(7):70,601. [online].
- [171] Lubich, C., Rohwedder, T., Schneider, R. and Vandereycken, B. (2013). Dynamical approximation by hierarchical Tucker and tensor-train tensors. *SIAM Journal on Matrix Analysis and Applications*, 34(2):470. [online].
- [172] Haegeman, J., Lubich, C., Oseledets, I., Vandereycken, B. and Verstraete, F. (2016). Unifying time evolution and optimization with matrix product states. *Phys. Rev. B*, 94(16):165,116. [online].
- [173] Schmitteckert, P. (2004). Nonequilibrium electron transport using the density matrix renormalization group method. *Phys. Rev. B*, 70(12):121,302. [online].

- [174] Kleine, A., Kollath, C., McCulloch, I., Giamarchi, T. and Schollwöck, U. (2008). Spin-charge separation in two-component Bose gases. *Phys. Rev. A*, 77(1):13,607. [online].
- [175] García-Ripoll, J. J. (2006). Time evolution of matrix product states. *New Journal of Physics*, 8(12):305. [online].
- [176] Keilmann, T. and García-Ripoll, J. J. (2008). Dynamical creation of bosonic Cooper-like pairs. *Phys. Rev. Lett.*, 100(11):110,406. [online].
- [177] Blanes, S. and Moan, P. (2006). Fourth-and sixth-order commutator-free Magnus integrators for linear and non-linear dynamical systems. *Applied Numerical Mathematics*, 56(12):1519. [online].
- [178] Blanes, S., Casas, F., Oteo, J. and Ros, J. (2009). The Magnus expansion and some of its applications. *Physics reports*, 470(5-6):151. [online].
- [179] Yuste, A., Cartwright, C., Chiara, G. D. and Sanpera, A. (2018). Entanglement scaling at first order quantum phase transitions. *New Journal of Physics*, 20(4):43,006. [online].
- [180] Wu, L.-A., Sarandy, M. S. and Lidar, D. A. (2004). Quantum Phase Transitions and Bipartite Entanglement. *Phys. Rev. Lett.*, 93:250,404. [online].
- [181] Kohn, W. (1965). W. Kohn and LJ Sham, *Phys. Rev.* 140, A1133 (1965). *Phys. Rev.*, 140:A1133. [online].
- [182] Syljuåsen, O. F. (2003). Entanglement and spontaneous symmetry breaking in quantum spin models. *Phys. Rev. A*, 68:60,301. [online].
- [183] Pereira, L. J. and de Oliveira, T. R. (2016). Effects of Spontaneous Symmetry Break in the Origin of Non-analytic Behavior of Entanglement at Quantum Phase Transitions. *Frontiers in Physics*, 4:51. [online].
- [184] Yang, M.-F. (2005). Reexamination of entanglement and the quantum phase transition. *Phys. Rev. A*, 71:30,302. [online].
- [185] Privman, V. (1990). *Finite-size Scaling Theory*. World Scientific, London, U.K.
- [186] Vollmayr, K., Reger, J. D., Scheucher, M. and Binder, K. (1993). Finite size effects at thermally-driven first order phase transitions: A phenomenological theory of the order parameter distribution. *Zeitschrift für Physik B Condensed Matter*, 91(1):113. [online].
- [187] Chen, W., Hida, K. and Sanctuary, B. C. (2003). Ground-state phase diagram of $S = 1$ XXZ chains with uniaxial single-ion-type anisotropy. *Phys. Rev. B*, 67:104,401. [online].
- [188] Ejima, S. and Fehske, H. (2015). Comparative density-matrix renormalization group study of symmetry-protected topological phases in spin-1 chain and Bose-Hubbard models. *Phys. Rev. B*, 91:45,121. [online].
- [189] Campostrini, M., Nespolo, J., Pelissetto, A. and Vicari, E. (2015). Finite-size scaling at the first-order quantum transitions of quantum Potts chains. *Phys. Rev. E*, 91:52,103. [online].

- [190] Cartwright, C., De Chiara, G. and Rizzi, M. (2018). Rhombi-chain Bose-Hubbard model: Geometric frustration and interactions. *Phys. Rev. B*, 98:184,508. [online].
- [191] Tovmasyan, M., Peotta, S., Törmä, P. and Huber, S. D. (2016). Effective theory and emergent SU(2) symmetry in the flat bands of attractive Hubbard models. *Phys. Rev. B*, 94:245,149. [online].
- [192] Kobayashi, K., Okumura, M., Yamada, S., Machida, M. and Aoki, H. (2016). Superconductivity in repulsively interacting fermions on a diamond chain: Flat-band-induced pairing. *Phys. Rev. B*, 94:214,501. [online].
- [193] Tovmasyan, M., Peotta, S., Liang, L., Törmä, P. and Huber, S. D. (2018). Preformed pairs in flat Bloch bands. *Phys. Rev. B*, 98:134,513. [online].
- [194] Mukherjee, S., Di Liberto, M., Öhberg, P., Thomson, R. R. and Goldman, N. (2018). Experimental Observation of Aharonov-Bohm Cages in Photonic Lattices. *Phys. Rev. Lett.*, 121:75,502. [online].
- [195] Kremer, M., Petrides, I., Meyer, E., Heinrich, M., Zilberberg, O. and Szameit, A. (2018). Non-quantized square-root topological insulators: a realization in photonic Aharonov-Bohm cages. *ArXiv e-prints*. [arXiv:1805.05209].
- [196] Pannetier, B., Chaussy, J., Rammal, R. and Villegier, J. C. (1984). Experimental Fine Tuning of Frustration: Two-Dimensional Superconducting Network in a Magnetic Field. *Phys. Rev. Lett.*, 53:1845. [online].
- [197] Lee, S. and Lee, K.-C. (1998). Phase transitions in the fully frustrated triangular XY model. *Phys. Rev. B*, 57:8472. [online].
- [198] Polini, M., Fazio, R., MacDonald, A. H. and Tosi, M. P. (2005). Realization of Fully Frustrated Josephson-Junction Arrays with Cold Atoms. *Phys. Rev. Lett.*, 95:10,401. [online].
- [199] Gladchenko, S., Olaya, D., Dupont-Ferrier, E., Douçot, B., Ioffe, L. B. and Gershenson, M. E. (2009). Superconducting nanocircuits for topologically protected qubits. *Nature Physics*, 5:48. [online].
- [200] Ioffe, L. B. and Feigel'man, M. V. (2002). Possible realization of an ideal quantum computer in Josephson junction array. *Phys. Rev. B*, 66:224,503. [online].
- [201] Douçot, B. and Ioffe, L. B. (2012). Physical implementation of protected qubits. *Reports on Progress in Physics*, 75(7):72,001. [online].
- [202] Jünemann, J., Piga, A., Ran, S.-J., Lewenstein, M., Rizzi, M. and Bermudez, A. (2017). Exploring Interacting Topological Insulators with Ultracold Atoms: The Synthetic Creutz-Hubbard Model. *Phys. Rev. X*, 7:31,057. [online].
- [203] Travkin, E., Diebel, F. and Denz, C. (2017). Compact flat band states in optically induced flatland photonic lattices. *Applied Physics Letters*, 111(1):011,104. [online].
- [204] Mukherjee, S. and Thomson, R. R. (2015). Observation of localized flat-band modes in a quasi-one-dimensional photonic rhombic lattice. *Opt. Lett.*, 40(23):5443. [online].

- [205] Aoki, H., Ando, M. and Matsumura, H. (1996). Hofstadter butterflies for flat bands. *Phys. Rev. B*, 54:R17,296. [online].
- [206] Kazymyrenko, K., Dusuel, S. and Douçot, B. (2005). Quantum wire networks with local \mathbb{Z}_2 symmetry. *Phys. Rev. B*, 72:235,114. [online].
- [207] Lopes, A. A. and Dias, R. G. (2011). Interacting spinless fermions in a diamond chain. *Phys. Rev. B*, 84:85,124. [online].
- [208] Granato, E. and Kosterlitz, J. M. (1986). Critical behavior of coupled XY models. *Phys. Rev. B*, 33:4767. [online].
- [209] Granato, E., Kosterlitz, J. M., Lee, J. and Nightingale, M. P. (1991). Phase transitions in coupled XY-Ising systems. *Phys. Rev. Lett.*, 66:1090. [online].
- [210] Teitel, S. and Jayaprakash, C. (1983). Phase transtions in frustrated two-dimensional XY models. *Phys. Rev. B*, 27:598. [online].
- [211] Halsey, T. C. (1985). Topological defects in the fully frustrated XY model and in 3 He-A films. *Journal of Physics C: Solid State Physics*, 18(12):2437. [online].
- [212] Korshunov, S. E. (1986). Phase transitions in two-dimensional uniformly frustratedXY models. II. General scheme. *Journal of Statistical Physics*, 43(1):17. [online].
- [213] Li, M. S. and Cieplak, M. (1994). Renormalization-group study of the coupled XY-Ising models. *Phys. Rev. B*, 50:955. [online].
- [214] Ma, R., Tai, M. E., Preiss, P. M., Bakr, W. S., Simon, J. and Greiner, M. (2011). Photon-Assisted Tunneling in a Biased Strongly Correlated Bose Gas. *Phys. Rev. Lett.*, 107:95,301. [online].
- [215] Eckardt, A., Hauke, P., Soltan-Panahi, P., Becker, C., Sengstock, K. and Lewenstein, M. (2010). Frustrated quantum antiferromagnetism with ultracold bosons in a triangular lattice. *Europhysics Letters*, 89(1):10,010. [online].
- [216] Calabrese, P. and Cardy, J. (2009). Entanglement entropy and conformal field theory. *Journal of Physics A: Mathematical and Theoretical*, 42(50):504,005. [online].
- [217] Lafflorencie, N. (2016). Quantum entanglement in condensed matter systems. *Physics Reports*, 646:1 – 59. [online].
- [218] De Chiara, G., Lewenstein, M. and Sanpera, A. (2011). Bilinear-biquadratic spin-1 chain undergoing quadratic Zeeman effect. *Phys. Rev. B*, 84:54,451. [online].
- [219] Pollmann, F., Turner, A. M., Berg, E. and Oshikawa, M. (2010). Entanglement spectrum of a topological phase in one dimension. *Phys. Rev. B*, 81:64,439. [online].
- [220] Deng, X. and Santos, L. (2011). Entanglement spectrum of one-dimensional extended Bose-Hubbard models. *Phys. Rev. B*, 84:85,138. [online].

- [221] De Chiara, G., Lepori, L., Lewenstein, M. and Sanpera, A. (2012). Entanglement Spectrum, Critical Exponents, and Order Parameters in Quantum Spin Chains. *Phys. Rev. Lett.*, 109:237,208. [online].
- [222] Lepori, L., De Chiara, G. and Sanpera, A. (2013). Scaling of the entanglement spectrum near quantum phase transitions. *Phys. Rev. B*, 87:235,107. [online].
- [223] Läuchli, A. M. (2013). Operator content of real-space entanglement spectra at conformal critical points. *ArXiv e-prints*. [arXiv:1303.0741].
- [224] Di Liberto, M., Mukherjee, S. and Goldman, N. (2018). Nonlinear dynamics of Aharonov-Bohm cages. *ArXiv e-prints*. [arXiv:1810.07641].
- [225] Jafari, R., Johannesson, H., Langari, A. and Martin-Delgado, M. A. (2019). Quench dynamics and zero-energy modes: The case of the Creutz model. *Phys. Rev. B*, 99:54,302. [online].
- [226] Kasztelan, C., Trotzky, S., Chen, Y.-A., Bloch, I., McCulloch, I. P., Schollwöck, U. and Orso, G. (2011). Landau-Zener Sweeps and Sudden Quenches in Coupled Bose-Hubbard Chains. *Phys. Rev. Lett.*, 106:155,302. [online].
- [227] Menu, R. and Roscilde, T. (2018). Quench dynamics of quantum spin models with flat bands of excitations. *Phys. Rev. B*, 98:205,145. [online].
- [228] Bercioux, D., Dutta, O. and Rico, E. (2017). Solitons in one-dimensional lattices with a flat band. *Annalen der Physik*, 529:1600,262. [online].
- [229] Roux, G. (2009). Quenches in quantum many-body systems: One-dimensional Bose-Hubbard model reexamined. *Phys. Rev. A*, 79:21,608. [online].
- [230] Roux, G. (2010). Finite-size effects in global quantum quenches: Examples from free bosons in an harmonic trap and the one-dimensional Bose-Hubbard model. *Phys. Rev. A*, 81:53,604. [online].
- [231] Kollath, C., Läuchli, A. M. and Altman, E. (2007). Quench Dynamics and Nonequilibrium Phase Diagram of the Bose-Hubbard Model. *Phys. Rev. Lett.*, 98:180,601. [online].
- [232] Clark, S. R. and Jaksch, D. (2004). Dynamics of the superfluid to Mott-insulator transition in one dimension. *Phys. Rev. A*, 70:043,612. [online].
- [233] Biroli, G., Kollath, C. and Läuchli, A. M. (2010). Effect of Rare Fluctuations on the Thermalization of Isolated Quantum Systems. *Phys. Rev. Lett.*, 105:250,401. [online].
- [234] Trefzger, C. and Sengupta, K. (2011). Nonequilibrium Dynamics of the Bose-Hubbard Model: A Projection-Operator Approach. *Phys. Rev. Lett.*, 106:95,702. [online].
- [235] Venumadhav, T., Haque, M. and Moessner, R. (2010). Finite-rate quenches of site bias in the Bose-Hubbard dimer. *Phys. Rev. B*, 81:54,305. [online].
- [236] Bernier, J.-S., Poletti, D., Barmettler, P., Roux, G. and Kollath, C. (2012). Slow quench dynamics of Mott-insulating regions in a trapped Bose gas. *Phys. Rev. A*, 85:33,641. [online].

-
- [237] Rabi, I. I. (1936). On the Process of Space Quantization. *Phys. Rev.*, 49:324. [online].
 - [238] Allen, L. and Eberly, J. H. (1987). *Optical resonance and two-level atoms*, volume 28. Courier Corporation, New York.
 - [239] Landau, L. and Lifshitz, E. (1977). *Quantum Mechanics: Non-relativistic Theory, Volume 3*. Elsevier Science Ltd., Oxford.
 - [240] Amico, L. and Penna, V. (1998). Dynamical Mean Field Theory of the Bose-Hubbard Model. *Phys. Rev. Lett.*, 80:2189. [online].

APPENDIX

CAGE BASIS FOR THE RHOMBI MODEL AT FULL-FRUSTRATION

This appendix contains the Mathematica of the AB cage eigenbasis formulation of the single particle within the the quasi-1-D rhombi chain at full frustration $\phi = \pi$. This corresponds to the work done in Ch. 6. Specifically the work done within this script is in order to replicate Eq. (6.7), (6.9) and (6.8), which are the different components of the Hamiltonian in the AB cage eigenbasis. This is split into two main sections: the initial setup to change the cage basis and then simplification of the interaction terms to the form shown in the aforementioned equations. The tunnelling is neglected as this merely forms the bands at $-2J$, 0 and $2J$.

Throughout this script, expressions should be read as normal ordered ($w^\dagger w$), which is not automatically evident, because in the notebook we denoted $w\text{dag}=w^\dagger$ and this follows w in the alphabetical order employed by Mathematica, instead of preceding it as we would wish.

```
In[1]:= SetOptions[SelectedNotebook[],
  PrintingStyleEnvironment -> "Printout", ShowSyntaxStyles -> True]
```

Initial setup of the cages

Defining the boundary conditions and the free Hamiltonian

Here we define which boundary condition is being used. For the purposes of the thesis, only the full rhombi case was used (see Fig. 6.1). The alternative case is where only the full cells are retained so an additional A site is added at the start and an additional C site at the end.

```
In[2]:=
R = 6; (*number of full rhombi in the chain*)
L = R + 1; (*number of cells in the chain, with our boundary conditions*)

(*in case of full rhombi, we should run the index from 1 to 3L-2 == 3R+1 *)
(*in case of full cells,
we should instead run the extremes of the index from 0 to 3L-1 ...*)

bc = "fullrhombi"; (*"fullrhombi" or "fullcells"*)
{Smin, Smax} = Switch[bc,
  "fullrhombi", {1, 3 L - 2},
  "fullcells", {0, 3 L - 1}
];
S = Smax - Smin + 1; (*number of sites in the chain*)

(*encode/decode the site position from the coordinate/basis index
into the running index of the 1D mapping, same as in MPS/DMRG
j = cell index // s = site index (A,B,C) corresponding to (1,2,3) *)
enc[{j_, s_}] = 3 * (j - 1) + (s - 1);
dec[ind_] = {Quotient[ind, 3] + 1, Mod[ind, 3] + 1};

(*Array[dec, S]^T // MatrixForm*)
Clear[Htmp, Hfree]
Htmp = -SparseArray[{
  {ind1_, ind2_} /;
    ((dec[ind1 + (Smin - 1)][[2]] == 3) && (dec[ind2 + (Smin - 1)][[2]] == 2) &&
    (dec[ind1 + (Smin - 1)][[1]] == dec[ind2 + (Smin - 1)][[1]])) -> +1,
  {ind1_, ind2_} /; ((dec[ind1 + (Smin - 1)][[2]] == 3) &&
    (dec[ind2 + (Smin - 1)][[2]] == 2) &&
    (dec[ind1 + (Smin - 1)][[1]] + 1 == dec[ind2 + (Smin - 1)][[1]])) -> -1,
  {ind1_, ind2_} /; ((dec[ind1 + (Smin - 1)][[2]] == 1) &&
    (dec[ind2 + (Smin - 1)][[2]] == 2) &&
    (dec[ind1 + (Smin - 1)][[1]] == dec[ind2 + (Smin - 1)][[1]])) -> +1,
  {ind1_, ind2_} /; ((dec[ind1 + (Smin - 1)][[2]] == 1) &&
```

Defining Aharanov-Bohm cages

In this subsection we define the Aharonov-Bohm cages i.e. the localised eigenvectors corresponding to each (flat) energy band and perform some checks on them.

```
In[15]:= (*Define and check the definition of cages in the bulk*)
Clear[ww]
Do[
  Do[
    ww[{j, a}] = Normalize[SparseArray[{
      {ind1_} /; ((dec[ind1 + (Smin - 1)][[2]] == 3) &&
        (dec[ind1 + (Smin - 1)][[1]] == j - 1) → If[a ≠ 0, -1, +1],
      {ind1_} /; ((dec[ind1 + (Smin - 1)][[2]] == 1) &&
        (dec[ind1 + (Smin - 1)][[1]] == j) → If[a ≠ 0, +1, -1],
```

```

      {ind1_} /; ((dec[ind1 + (Smin - 1)][[2]] == 2) &&
        (dec[ind1 + (Smin - 1)][[1]] == j)) → -2 a,
      {ind1_} /; ((dec[ind1 + (Smin - 1)][[2]] == 3) &&
        (dec[ind1 + (Smin - 1)][[1]] == j)) → +1,
      {ind1_} /; ((dec[ind1 + (Smin - 1)][[2]] == 1) &&
        (dec[ind1 + (Smin - 1)][[1]] == j + 1)) → +1
    }, {S}]];
  , {a, -1, 1}];
, {j, 2, L - 1}];

Tally[Flatten[
  Table[Table[Hfree.ww[{j, a}] == +2 a ww[{j, a}], {a, -1, 1}], {j, 2, L - 1}]]];
% == {{True, 3 * (R - 1)}}; (*gives True *)

(*Define and check the definition of cages on the edges*)
Clear[ee];
Switch[bc,
  (*-----*)
  "fullrhombi",
  Do[
    ee[{1, a}] = Normalize[SparseArray[{
      {ind1_} /; ((dec[ind1 + Smin - 1][[2]] == 2) && (dec[ind1 + Smin - 1][[1]] == 1)) →
        -√2 a,
      {ind1_} /; ((dec[ind1 + Smin - 1][[2]] == 3) &&
        (dec[ind1 + Smin - 1][[1]] == 1)) → +1,
      {ind1_} /; ((dec[ind1 + Smin - 1][[2]] == 1) &&
        (dec[ind1 + Smin - 1][[1]] == 2)) → +1
    }, {S}]];
    , {a, {-1, 1}}];

  Do[
    ee[{L, a}] = Normalize[SparseArray[{
      (*{i_, i_}→-2.,*)
      {ind1_} /; ((dec[ind1 + Smin - 1][[2]] == 3) &&
        (dec[ind1 + Smin - 1][[1]] == L - 1)) → If[a ≠ 0, -1, +1],
      {ind1_} /; ((dec[ind1 + Smin - 1][[2]] == 1) &&
        (dec[ind1 + Smin - 1][[1]] == L)) → If[a ≠ 0, +1, -1],
      {ind1_} /; ((dec[ind1 + Smin - 1][[2]] == 2) &&
        (dec[ind1 + Smin - 1][[1]] == L)) → -√2 a
    }, {S}]];
    , {a, {-1, 1}}];,
  (*-----*)
  "fullcells",
  Do[
    ee[{1, a}] = Normalize[SparseArray[{
      {ind1_} /;

```



```

      ((dec[ind1 + Smin - 1][[2]] == 1) && (dec[ind1 + Smin - 1][[1]] == 1)) → +1,
    {ind1_} /; ((dec[ind1 + Smin - 1][[2]] == 2) &&
      (dec[ind1 + Smin - 1][[1]] == 1)) → -√3 a,
    {ind1_} /; ((dec[ind1 + Smin - 1][[2]] == 3) &&
      (dec[ind1 + Smin - 1][[1]] == 1)) → +1,
    {ind1_} /; ((dec[ind1 + Smin - 1][[2]] == 1) &&
      (dec[ind1 + Smin - 1][[1]] == 2)) → +1
  }, {S}]]];
, {a, {-1, 1}}];
Do[
  ee[{L, a}] = Normalize[SparseArray[{
    {ind1_} /; ((dec[ind1 + Smin - 1][[2]] == 3) &&
      (dec[ind1 + Smin - 1][[1]] == L - 1)) → -1,
    {ind1_} /; ((dec[ind1 + Smin - 1][[2]] == 1) &&
      (dec[ind1 + Smin - 1][[1]] == L)) → +1,
    {ind1_} /; ((dec[ind1 + Smin - 1][[2]] == 2) &&
      (dec[ind1 + Smin - 1][[1]] == L)) → -√3 a,
    {ind1_} /; ((dec[ind1 + Smin - 1][[2]] == 3) &&
      (dec[ind1 + Smin - 1][[1]] == L)) → +1
  }, {S}]]];
, {a, {-1, 1}}];
(*The presence of the extra sites
induces two extra zero modes at the edges*)
ee[{1, 0}] = Normalize[SparseArray[{
  {ind1_} /;
    ((dec[ind1 + Smin - 1][[2]] == 1) && (dec[ind1 + Smin - 1][[1]] == 1)) → -2,
  {ind1_} /; ((dec[ind1 + Smin - 1][[2]] == 3) && (dec[ind1 + Smin - 1][[1]] == 1)) →
    +1,
  {ind1_} /; ((dec[ind1 + Smin - 1][[2]] == 1) && (dec[ind1 + Smin - 1][[1]] == 2)) →
    +1
}, {S}]]];
ee[{L, 0}] = Normalize[SparseArray[{
  {ind1_} /;
    ((dec[ind1 + Smin - 1][[2]] == 3) && (dec[ind1 + Smin - 1][[1]] == L - 1)) → -1,
  {ind1_} /; ((dec[ind1 + Smin - 1][[2]] == 1) && (dec[ind1 + Smin - 1][[1]] == L)) →
    +1,
  {ind1_} /; ((dec[ind1 + Smin - 1][[2]] == 3) && (dec[ind1 + Smin - 1][[1]] == L)) →
    -2
}, {S}]]];
]

Tally[Flatten[Table[Table[Hfree.ee[{j, a}] ==
  +Switch[bc, "fullrhombi", √2, "fullcells", √3] a ee[{j, a}],
  {a, {-1, 1}}, {j, {1, L}}]]]; (*gives {{True,4}}*)

```

```

If[bc == "fullcells",
  Tally[
    Flatten[Table[Table[Hfree.ee[{j, a}] == +a ee[{1, a}], {a, {0}}], {j, {1, L}}]]]
]
(*Define the transformation between the standard and cage basis,
and its inverse/transpose *)
Clear[modes, basis, U]

(*modes = list of cage / edge mode names,
useful later for symbolic calculations*)
modes = Join[
  Switch[bc, "fullrhombi", {}, "fullcells", {e[{1, 0}]}],
  Table[e[{1, a}], {a, {-1, 1}}],
  Flatten[Table[w[{j, a}], {j, 2, L-1}, {a, {-1, 1}}, 1],
  Table[e[{L, a}], {a, {-1, 1}}],
  Switch[bc, "fullrhombi", {}, "fullcells", {e[{L, 0}]}]
];

(*U=cage2standard- N.B. this is no longer the parameter for the on-
site interaction, which is set to 1 in the Chpt. 6 *)
U = Transpose[modes /. {e → ee, w → ww}];
Print["U(1:14,1:14)=" MatrixForm[U[[1 ;; 14, 1 ;; 14]]]
Print["U'.Hfree.U=", U'.Hfree.U // FullSimplify // MatrixForm]

(*standard provides the list of standard
modes as linear combinations of cage/edge modes*)
standard = Factor[U.modes];
Print["standard=" MatrixForm[standard]]

(*modes = list of single site names, useful later for symbolic calculations*)
(*one could also use the notation of indices*)
basis = Table[bos[ind], {ind, Smin, Smax}];

(*cage provides the list of cage modes
as linear combinations of standard modes*)
cage = Factor[U'.basis];
Print["cage=" MatrixForm[cage]]

(*a symbolic simplification of symbols*)
conjdagssimpl = {Conjugate[e[aaa_]] → edag[aaa],
  Conjugate[w[aaa_]] → wdag[aaa], Conjugate[bos[aaa_]] → bosdag[aaa]};
(*FullSimplify[standard*]/.conjdagssimpl;*)

```

[illegible]

[illegible]

$$\begin{aligned}
& \text{standard=} \left(\begin{array}{c} \frac{e[\{1,-1\}]-e[\{1,1\}]}{\sqrt{2}} \\ \frac{1}{4} \left(2 e[\{1, -1\}] + 2 e[\{1, 1\}] - \sqrt{2} w[\{2, -1\}] + 2 w[\{2, 0\}] - \sqrt{2} w[\{2, 1\}] \right) \\ \frac{1}{4} \left(2 e[\{1, -1\}] + 2 e[\{1, 1\}] + \sqrt{2} w[\{2, -1\}] - 2 w[\{2, 0\}] + \sqrt{2} w[\{2, 1\}] \right) \\ \frac{w[\{2,-1\}]-w[\{2,1\}]}{\sqrt{2}} \\ \frac{1}{4} \left(\sqrt{2} w[\{2, -1\}] + 2 w[\{2, 0\}] + \sqrt{2} w[\{2, 1\}] - \sqrt{2} w[\{3, -1\}] + 2 w[\{3, 0\}] - \sqrt{2} w[\{3, 1\}] \right) \\ \frac{1}{4} \left(\sqrt{2} w[\{2, -1\}] + 2 w[\{2, 0\}] + \sqrt{2} w[\{2, 1\}] + \sqrt{2} w[\{3, -1\}] - 2 w[\{3, 0\}] + \sqrt{2} w[\{3, 1\}] \right) \\ \frac{w[\{3,-1\}]-w[\{3,1\}]}{\sqrt{2}} \\ \frac{1}{4} \left(\sqrt{2} w[\{3, -1\}] + 2 w[\{3, 0\}] + \sqrt{2} w[\{3, 1\}] - \sqrt{2} w[\{4, -1\}] + 2 w[\{4, 0\}] - \sqrt{2} w[\{4, 1\}] \right) \\ \frac{1}{4} \left(\sqrt{2} w[\{3, -1\}] + 2 w[\{3, 0\}] + \sqrt{2} w[\{3, 1\}] + \sqrt{2} w[\{4, -1\}] - 2 w[\{4, 0\}] + \sqrt{2} w[\{4, 1\}] \right) \\ \frac{w[\{4,-1\}]-w[\{4,1\}]}{\sqrt{2}} \\ \frac{1}{4} \left(\sqrt{2} w[\{4, -1\}] + 2 w[\{4, 0\}] + \sqrt{2} w[\{4, 1\}] - \sqrt{2} w[\{5, -1\}] + 2 w[\{5, 0\}] - \sqrt{2} w[\{5, 1\}] \right) \\ \frac{1}{4} \left(\sqrt{2} w[\{4, -1\}] + 2 w[\{4, 0\}] + \sqrt{2} w[\{4, 1\}] + \sqrt{2} w[\{5, -1\}] - 2 w[\{5, 0\}] + \sqrt{2} w[\{5, 1\}] \right) \\ \frac{w[\{5,-1\}]-w[\{5,1\}]}{\sqrt{2}} \\ \frac{1}{4} \left(\sqrt{2} w[\{5, -1\}] + 2 w[\{5, 0\}] + \sqrt{2} w[\{5, 1\}] - \sqrt{2} w[\{6, -1\}] + 2 w[\{6, 0\}] - \sqrt{2} w[\{6, 1\}] \right) \\ \frac{1}{4} \left(\sqrt{2} w[\{5, -1\}] + 2 w[\{5, 0\}] + \sqrt{2} w[\{5, 1\}] + \sqrt{2} w[\{6, -1\}] - 2 w[\{6, 0\}] + \sqrt{2} w[\{6, 1\}] \right) \\ \frac{w[\{6,-1\}]-w[\{6,1\}]}{\sqrt{2}} \\ \frac{1}{4} \left(-2 e[\{7, -1\}] - 2 e[\{7, 1\}] + \sqrt{2} w[\{6, -1\}] + 2 w[\{6, 0\}] + \sqrt{2} w[\{6, 1\}] \right) \\ \frac{1}{4} \left(2 e[\{7, -1\}] + 2 e[\{7, 1\}] + \sqrt{2} w[\{6, -1\}] + 2 w[\{6, 0\}] + \sqrt{2} w[\{6, 1\}] \right) \\ \frac{e[\{7,-1\}]-e[\{7,1\}]}{\sqrt{2}} \end{array} \right) \\
& \text{cage=} \left(\begin{array}{c} \frac{1}{2} \left(\sqrt{2} \text{bos}[1] + \text{bos}[2] + \text{bos}[3] \right) \\ \frac{1}{2} \left(-\sqrt{2} \text{bos}[1] + \text{bos}[2] + \text{bos}[3] \right) \\ - \frac{\text{bos}[2]-\text{bos}[3]-2 \text{bos}[4]-\text{bos}[5]-\text{bos}[6]}{2 \sqrt{2}} \\ \frac{1}{2} \left(\text{bos}[2] - \text{bos}[3] + \text{bos}[5] + \text{bos}[6] \right) \\ - \frac{\text{bos}[2]-\text{bos}[3]+2 \text{bos}[4]-\text{bos}[5]-\text{bos}[6]}{2 \sqrt{2}} \\ - \frac{\text{bos}[5]-\text{bos}[6]-2 \text{bos}[7]-\text{bos}[8]-\text{bos}[9]}{2 \sqrt{2}} \\ \frac{1}{2} \left(\text{bos}[5] - \text{bos}[6] + \text{bos}[8] + \text{bos}[9] \right) \\ - \frac{\text{bos}[5]-\text{bos}[6]+2 \text{bos}[7]-\text{bos}[8]-\text{bos}[9]}{2 \sqrt{2}} \\ - \frac{\text{bos}[8]-\text{bos}[9]-2 \text{bos}[10]-\text{bos}[11]-\text{bos}[12]}{2 \sqrt{2}} \\ \frac{1}{2} \left(\text{bos}[8] - \text{bos}[9] + \text{bos}[11] + \text{bos}[12] \right) \\ - \frac{\text{bos}[8]-\text{bos}[9]+2 \text{bos}[10]-\text{bos}[11]-\text{bos}[12]}{2 \sqrt{2}} \\ - \frac{\text{bos}[11]-\text{bos}[12]-2 \text{bos}[13]-\text{bos}[14]-\text{bos}[15]}{2 \sqrt{2}} \\ \frac{1}{2} \left(\text{bos}[11] - \text{bos}[12] + \text{bos}[14] + \text{bos}[15] \right) \\ - \frac{\text{bos}[11]-\text{bos}[12]+2 \text{bos}[13]-\text{bos}[14]-\text{bos}[15]}{2 \sqrt{2}} \\ - \frac{\text{bos}[14]-\text{bos}[15]-2 \text{bos}[16]-\text{bos}[17]-\text{bos}[18]}{2 \sqrt{2}} \\ \frac{1}{2} \left(\text{bos}[14] - \text{bos}[15] + \text{bos}[17] + \text{bos}[18] \right) \\ - \frac{\text{bos}[14]-\text{bos}[15]+2 \text{bos}[16]-\text{bos}[17]-\text{bos}[18]}{2 \sqrt{2}} \\ \frac{1}{2} \left(-\text{bos}[17] + \text{bos}[18] + \sqrt{2} \text{bos}[19] \right) \\ \frac{1}{2} \left(-\text{bos}[17] + \text{bos}[18] - \sqrt{2} \text{bos}[19] \right) \end{array} \right)
\end{aligned}$$

In[34]:=

Computing interaction terms & symmetries in the AB-cages basis, see Vidal-Doucot PRL Eqs. 3-5

Computing interaction terms & symmetries in the AB-cage basis, see Eqs. 3-5 in B. Douçot and J. Vidal, Phys. Rev. Lett. 88, 227005 (2002).

In[35]:=

```
(*We compute here the density and the on-
site interaction operators in the new basis,
normal ordering is assumed, i.e. all dag come before all non-dag...*)
density[ind_] :=
Expand[standard[[ind - Smin + 1]]*standard[[ind - Smin + 1]] /. conjdagsimpl

interaction[ind_] := Expand[ $\frac{1}{2}$  standard[[ind - Smin + 1]]*standard[[ind - Smin + 1]]*
standard[[ind - Smin + 1]] standard[[ind - Smin + 1]] /. conjdagsimpl

(*Let us have a closer look at the Hubbard on-
site interaction: sum it over the three sites around a rhombus*)

Do[
Print["Rhombus index ", jj]; (*cycle on rhombus index*)

ind0 = enc[{jj, 2}]; (*four-fould coordinate site, type B*)
ind1 = enc[{jj, 3}]; (*four-fould coordinate site, type C*)
ind2 = enc[{jj + 1, 1}]; (*four-fould coordinate site, type A*)
expr =
interaction[ind0] + If[jj < R + 1, interaction[ind1] + interaction[ind2], 0];

(*Notice that in sites that participate with the same cages,
a lot of terms appear with opposite signs and cancel out once summed*)
If[jj < R + 1,
Print["Addend lengths ", {Length[interaction[ind0]],
Length[interaction[ind1]], Length[interaction[ind2]], Length[expr]}]];

(*We perform a check to confirm that that the parity of combined
occupation of the three cages centered around each site is preserved*)
Which[2 ≤ jj ≤ R,
Print["total cage  $w_{jj,\alpha}^{(+)} w_{jj,\beta}^{(+)}$  ",
Sort[Tally[(Sum[bb Count[#, w[{jj, aa}]bb], {bb, 1, 4}, {aa, -1, 1}] +
Sum[bb Count[#, wdag[{jj, aa}]bb], {bb, 1, 4}, {aa, -1, 1}]) & /@
Table[expr[[ii]], {ii, Length[expr]}]]] // MatrixForm];

(*The single cage states alone do not, however, preserve the parity*)
Print["single cages ",
Table[Sort[Tally[(Sum[bb Count[#, w[{jj, aa}]bb], {bb, 1, 4}] +
Sum[bb Count[#, wdag[{jj, aa}]bb], {bb, 1, 4}]) & /@
```

```

Table[expr[[i]], {i, Length[expr]}], {aa, -1, 1}] // MatrixForm];

jj = 1,
Print["total cage  $e_{1,\alpha}^{(+)} e_{1,\beta}^{(+)}$  ",
Sort[Tally[(Sum[bb Count[#, e[{jj, aa}]bb], {bb, 1, 4}, {aa, {-1, 1}}] +
Sum[bb Count[#, edag[{jj, aa}]bb], {bb, 1, 4}, {aa, {-1, 1}}]) & /@
Table[expr[[i]], {i, Length[expr]}]]] // MatrixForm];

(*Nor do they preserve the parity for the edge states*)
Print["single cages ",
Table[Sort[Tally[(Sum[bb Count[#, e[{jj, aa}]bb], {bb, 1, 4}] +
Sum[bb Count[#, edag[{jj, aa}]bb], {bb, 1, 4}]) & /@
Table[expr[[i]], {i, Length[expr]}]], {aa, {-1, 1}}] // MatrixForm];

jj = R + 1,
Print["total cage  $e_{R+1,\alpha}^{(+)} e_{R+1,\beta}^{(+)}$  ",
Sort[Tally[(Sum[bb Count[#, e[{jj, aa}]bb], {bb, 1, 4}, {aa, {-1, 1}}] +
Sum[bb Count[#, edag[{jj, aa}]bb], {bb, 1, 4}, {aa, {-1, 1}}]) & /@
Table[expr[[i]], {i, Length[expr]}]]] // MatrixForm];

];
Print["-----"];
, {jj, 1, R + 1}]

Rhombus index 1
Addend lengths {9, 225, 225, 117}
total cage  $e_{1,\alpha}^{(+)} e_{1,\beta}^{(+)}$   $\begin{pmatrix} 0 & 36 \\ 2 & 72 \\ 4 & 9 \end{pmatrix}$ 
single cages  $\begin{pmatrix} \begin{pmatrix} 0 \\ 58 \end{pmatrix} & \begin{pmatrix} 1 \\ 32 \end{pmatrix} & \begin{pmatrix} 2 \\ 24 \end{pmatrix} & \begin{pmatrix} 3 \\ 2 \end{pmatrix} & \begin{pmatrix} 4 \\ 1 \end{pmatrix} \\ \begin{pmatrix} 0 \\ 58 \end{pmatrix} & \begin{pmatrix} 1 \\ 32 \end{pmatrix} & \begin{pmatrix} 2 \\ 24 \end{pmatrix} & \begin{pmatrix} 3 \\ 2 \end{pmatrix} & \begin{pmatrix} 4 \\ 1 \end{pmatrix} \end{pmatrix}$ 
-----

Rhombus index 2
Addend lengths {9, 441, 441, 225}
total cage  $w_{jj,\alpha}^{(+)} w_{jj,\beta}^{(+)}$   $\begin{pmatrix} 0 & 36 \\ 2 & 153 \\ 4 & 36 \end{pmatrix}$ 
single cages  $\begin{pmatrix} \begin{pmatrix} 0 \\ 117 \end{pmatrix} & \begin{pmatrix} 1 \\ 72 \end{pmatrix} & \begin{pmatrix} 2 \\ 31 \end{pmatrix} & \begin{pmatrix} 3 \\ 4 \end{pmatrix} & \begin{pmatrix} 4 \\ 1 \end{pmatrix} \\ \begin{pmatrix} 0 \\ 117 \end{pmatrix} & \begin{pmatrix} 1 \\ 72 \end{pmatrix} & \begin{pmatrix} 2 \\ 31 \end{pmatrix} & \begin{pmatrix} 3 \\ 4 \end{pmatrix} & \begin{pmatrix} 4 \\ 1 \end{pmatrix} \\ \begin{pmatrix} 0 \\ 117 \end{pmatrix} & \begin{pmatrix} 1 \\ 72 \end{pmatrix} & \begin{pmatrix} 2 \\ 31 \end{pmatrix} & \begin{pmatrix} 3 \\ 4 \end{pmatrix} & \begin{pmatrix} 4 \\ 1 \end{pmatrix} \end{pmatrix}$ 
-----

Rhombus index 3
Addend lengths {9, 441, 441, 225}

```

$$\text{total cage } w_{jj,\alpha}^{(+)} w_{jj,\beta}^{(+)} \begin{pmatrix} 0 & 36 \\ 2 & 153 \\ 4 & 36 \end{pmatrix}$$

$$\text{single cages } \begin{pmatrix} \begin{pmatrix} 0 \\ 117 \end{pmatrix} & \begin{pmatrix} 1 \\ 72 \end{pmatrix} & \begin{pmatrix} 2 \\ 31 \end{pmatrix} & \begin{pmatrix} 3 \\ 4 \end{pmatrix} & \begin{pmatrix} 4 \\ 1 \end{pmatrix} \\ \begin{pmatrix} 0 \\ 117 \end{pmatrix} & \begin{pmatrix} 1 \\ 72 \end{pmatrix} & \begin{pmatrix} 2 \\ 31 \end{pmatrix} & \begin{pmatrix} 3 \\ 4 \end{pmatrix} & \begin{pmatrix} 4 \\ 1 \end{pmatrix} \\ \begin{pmatrix} 0 \\ 117 \end{pmatrix} & \begin{pmatrix} 1 \\ 72 \end{pmatrix} & \begin{pmatrix} 2 \\ 31 \end{pmatrix} & \begin{pmatrix} 3 \\ 4 \end{pmatrix} & \begin{pmatrix} 4 \\ 1 \end{pmatrix} \end{pmatrix}$$

Rhombus index 4

Addend lengths {9, 441, 441, 225}

$$\text{total cage } w_{jj,\alpha}^{(+)} w_{jj,\beta}^{(+)} \begin{pmatrix} 0 & 36 \\ 2 & 153 \\ 4 & 36 \end{pmatrix}$$

$$\text{single cages } \begin{pmatrix} \begin{pmatrix} 0 \\ 117 \end{pmatrix} & \begin{pmatrix} 1 \\ 72 \end{pmatrix} & \begin{pmatrix} 2 \\ 31 \end{pmatrix} & \begin{pmatrix} 3 \\ 4 \end{pmatrix} & \begin{pmatrix} 4 \\ 1 \end{pmatrix} \\ \begin{pmatrix} 0 \\ 117 \end{pmatrix} & \begin{pmatrix} 1 \\ 72 \end{pmatrix} & \begin{pmatrix} 2 \\ 31 \end{pmatrix} & \begin{pmatrix} 3 \\ 4 \end{pmatrix} & \begin{pmatrix} 4 \\ 1 \end{pmatrix} \\ \begin{pmatrix} 0 \\ 117 \end{pmatrix} & \begin{pmatrix} 1 \\ 72 \end{pmatrix} & \begin{pmatrix} 2 \\ 31 \end{pmatrix} & \begin{pmatrix} 3 \\ 4 \end{pmatrix} & \begin{pmatrix} 4 \\ 1 \end{pmatrix} \end{pmatrix}$$

Rhombus index 5

Addend lengths {9, 441, 441, 225}

$$\text{total cage } w_{jj,\alpha}^{(+)} w_{jj,\beta}^{(+)} \begin{pmatrix} 0 & 36 \\ 2 & 153 \\ 4 & 36 \end{pmatrix}$$

$$\text{single cages } \begin{pmatrix} \begin{pmatrix} 0 \\ 117 \end{pmatrix} & \begin{pmatrix} 1 \\ 72 \end{pmatrix} & \begin{pmatrix} 2 \\ 31 \end{pmatrix} & \begin{pmatrix} 3 \\ 4 \end{pmatrix} & \begin{pmatrix} 4 \\ 1 \end{pmatrix} \\ \begin{pmatrix} 0 \\ 117 \end{pmatrix} & \begin{pmatrix} 1 \\ 72 \end{pmatrix} & \begin{pmatrix} 2 \\ 31 \end{pmatrix} & \begin{pmatrix} 3 \\ 4 \end{pmatrix} & \begin{pmatrix} 4 \\ 1 \end{pmatrix} \\ \begin{pmatrix} 0 \\ 117 \end{pmatrix} & \begin{pmatrix} 1 \\ 72 \end{pmatrix} & \begin{pmatrix} 2 \\ 31 \end{pmatrix} & \begin{pmatrix} 3 \\ 4 \end{pmatrix} & \begin{pmatrix} 4 \\ 1 \end{pmatrix} \end{pmatrix}$$

Rhombus index 6

Addend lengths {9, 225, 225, 117}

$$\text{total cage } w_{jj,\alpha}^{(+)} w_{jj,\beta}^{(+)} \begin{pmatrix} 0 & 9 \\ 2 & 72 \\ 4 & 36 \end{pmatrix}$$

$$\text{single cages } \begin{pmatrix} \begin{pmatrix} 0 \\ 52 \end{pmatrix} & \begin{pmatrix} 1 \\ 40 \end{pmatrix} & \begin{pmatrix} 2 \\ 20 \end{pmatrix} & \begin{pmatrix} 3 \\ 4 \end{pmatrix} & \begin{pmatrix} 4 \\ 1 \end{pmatrix} \\ \begin{pmatrix} 0 \\ 52 \end{pmatrix} & \begin{pmatrix} 1 \\ 40 \end{pmatrix} & \begin{pmatrix} 2 \\ 20 \end{pmatrix} & \begin{pmatrix} 3 \\ 4 \end{pmatrix} & \begin{pmatrix} 4 \\ 1 \end{pmatrix} \\ \begin{pmatrix} 0 \\ 52 \end{pmatrix} & \begin{pmatrix} 1 \\ 40 \end{pmatrix} & \begin{pmatrix} 2 \\ 20 \end{pmatrix} & \begin{pmatrix} 3 \\ 4 \end{pmatrix} & \begin{pmatrix} 4 \\ 1 \end{pmatrix} \end{pmatrix}$$

Rhombus index 7

total cage $e_{R+1,\alpha}^{(+)} e_{R+1,\beta}^{(+)} (4 \ 9)$

Quick checks

Performing some quick checks to make sure the cage basis is correct.

```
In[38]:= eigspace = Orthogonalize[NullSpace[Hfree - 2 IdentityMatrix[S]]];
eigspace // MatrixForm;
eigspace.eigspace^T // MatrixForm

Out[40]//MatrixForm=

$$\begin{pmatrix} 1 & 0 & 0 & 0 & 0 \\ 0 & 1 & 0 & 0 & 0 \\ 0 & 0 & 1 & 0 & 0 \\ 0 & 0 & 0 & 1 & 0 \\ 0 & 0 & 0 & 0 & 1 \end{pmatrix}$$


In[41]:= jj = 2; (*rhombus index*)
ww[{jj, +1}] // Normal
ww[{jj + 1, +1}] // Normal
(*modes are already normalised*)

Out[42]= {0, -\frac{1}{2\sqrt{2}}, \frac{1}{2\sqrt{2}}, -\frac{1}{\sqrt{2}}, \frac{1}{2\sqrt{2}}, \frac{1}{2\sqrt{2}}, 0, 0, 0, 0, 0, 0, 0, 0, 0, 0, 0, 0}

Out[43]= {0, 0, 0, 0, -\frac{1}{2\sqrt{2}}, \frac{1}{2\sqrt{2}}, -\frac{1}{\sqrt{2}}, \frac{1}{2\sqrt{2}}, \frac{1}{2\sqrt{2}}, 0, 0, 0, 0, 0, 0, 0, 0, 0}

In[44]:= eigspace.{ww[{jj, +1}], ww[{jj + 1, +1}]}^T // MatrixForm // Simplify

Out[44]//MatrixForm=

$$\begin{pmatrix} \frac{1}{\sqrt{5}} & -\frac{1}{\sqrt{5}} \\ -\frac{1}{2\sqrt{5}} & \frac{1}{2\sqrt{5}} \\ \frac{1}{2\sqrt{3}} & -\frac{1}{2\sqrt{3}} \\ -\frac{1}{\sqrt{6}} & \frac{1}{\sqrt{6}} \\ \frac{1}{\sqrt{2}} & \frac{1}{\sqrt{2}} \end{pmatrix}$$

```

Simplification of the interaction in the cages

Defining the interaction in the cage basis for A,B,C on a given cell.

The following interaction definitions only make sense within the bulk of the cage, so $3 \leq \text{cell} \leq L - 2$. Here we are extracting the interaction terms in order to be able to simplify them later.


```

In[45]:= cell = 4; (* This means that in the further
    calculations we are focusing on points between cells 3 and 4,
    the other bulk terms follow by translational invariance*)
    (*indb=inda+1, indc=inda-1 or inda+2*)
cageinta[indin_] :=
    Expand[(standard[enc[{indin, 1}]]*standard[enc[{indin, 1}]]])
    (standard[enc[{indin, 1}]]*standard[enc[{indin, 1}]])] /. conjdagsimpl
cageintb[indin_] := Expand[
    (standard[enc[{indin, 2}]]*standard[enc[{indin, 2}]]])
    (standard[enc[{indin, 2}]]*standard[enc[{indin, 2}]])] /. conjdagsimpl
cageintc[indin_] := Expand[
    (standard[enc[{indin, 3}]]*standard[enc[{indin, 3}]]])
    (standard[enc[{indin, 3}]]*standard[enc[{indin, 3}]])] /. conjdagsimpl
Print["Number of A_j, B_j, C_{j-1}, C_j and A_{j+1} terms that make
    up the 5 sites within a given cage: A_", Length[cageinta[cell]],
    "B_", Length[cageintb[cell]], "C_", Length[cageintc[cell-1]],
    "C2_", Length[cageintc[cell]], "A2_", Length[cageinta[cell+1]]]
Print["Total number of terms in a cell=",
    Length[Expand[cageinta[cell] + cageintb[cell] + cageintc[cell-1]]]]

```

Number of A_j, B_j, C_{j-1}, C_j and A_{j+1} terms that
make up the 5 sites within a given cage: A_441B_9C_441C2_441A2_441

Total number of terms in a cell=225

Now we perform an approximation of the lowest band projection. This would correspond to filter out all terms involving higher bands:

at least, this is giving a brute-force approach to obtain the first order expression, useful for $J/U \gg 1$, while higher orders could be obtained by perturbation theory, see e.g., the references by Tovmasyan et al.

```

In[51]:= LBproj = {w[{a_, 0}] → 0, w[{a_, 1}] → 0, wdag[{a_, 0}] → 0, wdag[{a_, 1}] → 0};

```

```

In[52]:= (*Properly summed,
this will give the interaction-induced terms in the lowest band,
which we have simplified in Eq. (6.10) *)
+interaction[enc[{4, 2}]] +
  
$$\frac{1}{2} \left( \text{interaction}[\text{enc}[\{4, 1\}]] + \text{interaction}[\text{enc}[\{4, 3\}]] + \right. \\
\left. \text{interaction}[\text{enc}[\{3, 3\}]] + \text{interaction}[\text{enc}[\{5, 1\}]] \right) /. \text{LBproj} // \text{Expand}$$

```

$$\text{Out[52]} = \frac{1}{128} w[\{3, -1\}]^2 \text{wdag}[\{3, -1\}]^2 + \frac{1}{128} w[\{4, -1\}]^2 \text{wdag}[\{3, -1\}]^2 +$$

$$\frac{1}{32} w[\{3, -1\}] w[\{4, -1\}] \text{wdag}[\{3, -1\}] \text{wdag}[\{4, -1\}] +$$

$$\frac{1}{128} w[\{3, -1\}]^2 \text{wdag}[\{4, -1\}]^2 +$$

$$\frac{9}{64} w[\{4, -1\}]^2 \text{wdag}[\{4, -1\}]^2 + \frac{1}{128} w[\{5, -1\}]^2 \text{wdag}[\{4, -1\}]^2 +$$

$$\frac{1}{32} w[\{4, -1\}] w[\{5, -1\}] \text{wdag}[\{4, -1\}] \text{wdag}[\{5, -1\}] +$$

$$\frac{1}{128} w[\{4, -1\}]^2 \text{wdag}[\{5, -1\}]^2 + \frac{1}{128} w[\{5, -1\}]^2 \text{wdag}[\{5, -1\}]^2$$

Finding the terms with \tilde{U} coefficients (Eq. (6.7))

Finding the terms that have on-site interactions and cage flavour flips around a given hub (i.e the terms in Eq. (6.7)).

It should be noted that A will only include j and j-1 terms, B only includes j terms and C will only include j and j+1 terms where j is the cell that each one occurs on. This means that C from the previous cell and A from the next cell both have an influence on the current cell being looked at. Either all 5 sites within a cage can be considered or to simplify the problem only the $C_{\{j-1\}}$, $B_{\{j\}}$ and the $A_{\{j\}}$ can be considered.

```

In[53]:=
Ub[cell_] := With[{expr = cageintb[cell]},
  expr /. {
    f_[{a_, _}] => 0 /; a != cell
  }
]
Uc[cell_] := With[{expr = cageintc[cell]},
  expr /. {
    f_[{a_, _}] => 0 /; a != cell
  }
] (*This is only the part of C that is actually in cell*)
Ucall[cell_] := With[{expr = cageintc[cell]},
  expr /. {
    f_[{a_, _}] => 0 /; a != cell
  }
] + With[{expr = cageintc[cell]},
  expr /. {
    f_[{a_, _}] => 0 /; a != cell + 1
  }
]
```

```

    }
  ] (*This is the total contribution of U_c terms to the cell of interest*)
Ua[cell_] := With[{expr = cageinta[cell]},
  expr /. {
    f_[{a_, _}] => 0 /; a ≠ cell
  }
] (*This is only the part of A that is actually in cell*)

Uaall[cell_] := With[{expr = cageinta[cell]},
  expr /. {
    f_[{a_, _}] => 0 /; a ≠ cell
  }
] + With[{expr = cageinta[cell]},
  expr /. {
    f_[{a_, _}] => 0 /; a ≠ cell - 1
  }
]

Print["Ua_", Length[Ua[cell]], "Ub_", Length[Ub[cell]], "Ucback_",
  Length[Uc[cell - 1]], "Uafor_", Length[Ua[cell + 1]], "Uc_", Length[Uc[cell]]]
Length[Ua[cell] + Ub[cell] + Uc[cell]];
Length[Ua[cell] + Ub[cell] + Uc[cell] + (Ucall[cell - 1] - Uc[cell - 1]) +
  (Uaall[cell + 1] - Ua[cell + 1])] ; (*we want to inc. j-1,
j and j+1 to find which of the j components cancel out. *)
Print["-----tilde{U} terms-----"]
Utildecell = Ua[cell] + Ub[cell] + Uc[cell] +
  (Ucall[cell - 1] - Uc[cell - 1]) + (Uaall[cell + 1] - Ua[cell + 1])
(*TeXForm[%];*) (*This should be the pattern regardless of if cell is a
different value provided that cell is at least 2 in from the edge...*)
Print["Number of Utilde terms: ", Length[Utildecell]]

Ua_36Ub_9Ucback_36Uafor_36Uc_36
-----tilde{U} terms-----

```

$$\begin{aligned}
\text{Out}[62]= & \frac{5}{16} w[\{4, -1\}]^2 \text{wdag}[\{4, -1\}]^2 + \frac{1}{8} w[\{4, 0\}]^2 \text{wdag}[\{4, -1\}]^2 - \\
& \frac{3}{8} w[\{4, -1\}] w[\{4, 1\}] \text{wdag}[\{4, -1\}]^2 + \frac{5}{16} w[\{4, 1\}]^2 \text{wdag}[\{4, -1\}]^2 + \\
& \frac{1}{2} w[\{4, -1\}] w[\{4, 0\}] \text{wdag}[\{4, -1\}] \text{wdag}[\{4, 0\}] + \\
& \frac{1}{2} w[\{4, 0\}] w[\{4, 1\}] \text{wdag}[\{4, -1\}] \text{wdag}[\{4, 0\}] + \\
& \frac{1}{8} w[\{4, -1\}]^2 \text{wdag}[\{4, 0\}]^2 + \frac{1}{4} w[\{4, 0\}]^2 \text{wdag}[\{4, 0\}]^2 + \\
& \frac{1}{4} w[\{4, -1\}] w[\{4, 1\}] \text{wdag}[\{4, 0\}]^2 + \frac{1}{8} w[\{4, 1\}]^2 \text{wdag}[\{4, 0\}]^2 - \\
& \frac{3}{8} w[\{4, -1\}]^2 \text{wdag}[\{4, -1\}] \text{wdag}[\{4, 1\}] + \frac{1}{4} w[\{4, 0\}]^2 \text{wdag}[\{4, -1\}] \text{wdag}[\{4, 1\}] + \\
& \frac{5}{4} w[\{4, -1\}] w[\{4, 1\}] \text{wdag}[\{4, -1\}] \text{wdag}[\{4, 1\}] - \\
& \frac{3}{8} w[\{4, 1\}]^2 \text{wdag}[\{4, -1\}] \text{wdag}[\{4, 1\}] + \\
& \frac{1}{2} w[\{4, -1\}] w[\{4, 0\}] \text{wdag}[\{4, 0\}] \text{wdag}[\{4, 1\}] + \\
& \frac{1}{2} w[\{4, 0\}] w[\{4, 1\}] \text{wdag}[\{4, 0\}] \text{wdag}[\{4, 1\}] + \\
& \frac{5}{16} w[\{4, -1\}]^2 \text{wdag}[\{4, 1\}]^2 + \frac{1}{8} w[\{4, 0\}]^2 \text{wdag}[\{4, 1\}]^2 - \\
& \frac{3}{8} w[\{4, -1\}] w[\{4, 1\}] \text{wdag}[\{4, 1\}]^2 + \frac{5}{16} w[\{4, 1\}]^2 \text{wdag}[\{4, 1\}]^2
\end{aligned}$$

Number of Utilde terms: 20

In[64]:= **Print["1st order projection on lowest band: ", Utildecell /. LBproj]**

1st order projection on lowest band: $\frac{5}{16} w[\{4, -1\}]^2 \text{wdag}[\{4, -1\}]^2$

Finding the terms with \tilde{V} coefficients (Eq. (6.8))

Here we find the terms corresponding to interactions and correlated flips between nearest neighbour hubs, which are shown in Eq. (6.8) where the coefficient has been labelled \tilde{V} .

Defining the V terms so that they can be selected

Firstly, we extract any of the terms of type \tilde{V} (Eq. (6.8)) that include the cell j in them, i.e. terms between $j-1$ and j or terms between j and $j+1$ of the correct form.

```

In[65]:=
(*A only includes j-1 and j. C only includes j+1 and j. B includes only j*)
Vcplus[cell_] := Module[{a, b, f},
  With[{expr = cageintc[cell]},
    expr /. {
      s : wdag[{a_, _}] wdag[{b_, _}] w[{a_, _}] w[{b_, _}] /;
        (Sort@{a, b} == {cell, cell + 1}) => f[s]
    } // Replace[#,
      {s_Times /; ! MatchQ[s, f[_] * ___] => 0},
      {1}
    ] & // ReplaceAll[#, f[s___] => s] &
  ]
]

Vamin[cell_] := Module[{a, b, f},
  With[{expr = cageinta[cell]},
    expr /. {
      s : wdag[{a_, _}] wdag[{b_, _}] w[{a_, _}] w[{b_, _}] /;
        (Sort@{a, b} == {cell - 1, cell}) => f[s]
    } // Replace[#,
      {s_Times /; ! MatchQ[s, f[_] * ___] => 0},
      {1}
    ] & // ReplaceAll[#, f[s___] => s] &
  ]
]

Length[Vcplus[cell - 1]];
Length[Vamin[cell]];
Length[cageintc[cell - 1]];
(*The majority of the terms do not fall into these special cases*)
Print["Cback_", Length[Vcplus[cell - 1]], "A_", Length[Vamin[cell]],
  "C_", Length[Vcplus[cell]], "Afor_", Length[Vamin[cell + 1]]]
Vpartcage[cellin_] := Vamin[cellin] + Vcplus[cellin - 1];
(*We can only consider these 2 to simplify as will be replicated*)
TeXForm[%];
Vcage = Vcplus[cell - 1] + Vamin[cell] + Vcplus[cell] + Vamin[cell + 1];
(*if we want to consider the cage as a whole*)
Length[Vcage]
Print["Number of terms in Vtilde between C_j-1 and A_j: ",
  Length[Vpartcage[cell]]]

(*But the Vtilde (and the J as we will see later)
  contain an h.c in all of their terms:*)

```

```

Cback_81A_81C_81Afor_81
Out[74]= 162

Number of terms in Vtilde between C_j-1 and A_j: 81

In[76]:= Print["1st order projection on lowest band: ", Vcage /. LBproj]
1st order projection on lowest band:

$$\frac{1}{8} w[\{3, -1\}] w[\{4, -1\}] \text{wdag}[\{3, -1\}] \text{wdag}[\{4, -1\}] +$$


$$\frac{1}{8} w[\{4, -1\}] w[\{5, -1\}] \text{wdag}[\{4, -1\}] \text{wdag}[\{5, -1\}]$$


```

Step 1) Check that all the terms in V have an h.c

We can reduce the complexity of these terms by only retaining one half of the Hermitian conjugate. A few possible terms of V have their h.c self-contained so remove this first, then we perform a check to ensure that all of the other terms have an Hermitian conjugate also contained within the cage basis of the Hamiltonian.

```

In[77]:= Vpartmatch = Module[{a, b, f},
  With[{expr = Vpartcage[cell]},
    expr /. {
      s : wdag[{cell - 1, a_}]
        wdag[{cell, b_}] w[{cell - 1, a_}] w[{cell, b_}]  $\Rightarrow$  f[s]
    } // Replace[#,
      {s_Times /; ! MatchQ[s, f[___] * ___]  $\Rightarrow$  0},
      {1}
    ] & // ReplaceAll[#, f[s___]  $\Rightarrow$  s] &
  ]
];

Module[{a, b, c, d},
  With[{expr = Vpartcage[cell] - Vpartmatch},
    For[a = -1, a  $\leq$  1, a++,
      For[b = -1, b  $\leq$  1, b++,
        For[c = -1, c  $\leq$  1, c++,
          For[d = -1, d  $\leq$  1, d++,
            (*Print[a,b,c,d]*)
            (*Print[
              Coefficient[testcase,{w[{3,a}] w[{4,b}] wdag[{3,c}] wdag[{4,d}]}]]
              Print[Coefficient[testcase,{w[{3,c}] w[{4,d}]
              wdag[{3,a}] wdag[{4,b}]}]]*)
            If[Coefficient[expr, {w[{3, a}] w[{4, b}] wdag[{3, c}] wdag[{4, d}]}]  $\neq$ 
              Coefficient[expr, {w[{3, c}] w[{4, d}] wdag[{3, a}] wdag[{4, b}]}],
              Print["False", a, b, c, d];
            Print[
              Coefficient[expr, {w[{3, c}] w[{4, d}] wdag[{3, a}] wdag[{4, b}]}]]];
            Print[Coefficient[expr, {w[{3, c}] w[{4, d}]
              wdag[{3, a}] wdag[{4, b}]}]]];
          ]
        ]
      ]
    ]
  ]
]

```

Step 2) Retain only one part of the h.c

Now that we have confirmed that each term has a corresponding Hermitian conjugate we only retain one of the possible h.c terms. N.B the terms that had their h.c self-contained are Vpartmatch and these are merely divided by 2.

```

In[79]:= Print["Original length before h.c taken: ", Length[Vpartcage[cell]]]
Print["Hamiltonian terms which have h.c self-contained: ", Length[Vpartmatch]]
exprhcin = Vpartcage[cell] - Vpartmatch;
Module[{a, b, c, d},
  exprhc = exprhcin;
  For[a = -1, a ≤ 1, a++,
    For[b = -1, b ≤ 1, b++,
      For[c = -1, c ≤ 1, c++,
        For[d = -1, d ≤ 1, d++,

          If[Coefficient[exprhc, {w[{3, a}] w[{4, b}] wdag[{3, c}] wdag[{4, d}]}] ==
            Coefficient[exprhc, {w[{3, c}] w[{4, d}] wdag[{3, a}] wdag[{4, b}]}],
            exprhc = exprhc - (Coefficient[exprhc, w[{3, c}] w[{4, d}] wdag[{3, a}]
              wdag[{4, b}]] w[{3, c}] w[{4, d}] wdag[{3, a}] wdag[{4, b}]);

          ]
        ]
      ]
    ]
  ]
]
Clear[exprhcin]
Length[Vpartmatch];
Vherm = exprhc;
Print["Number of Hermitian terms extracted: ", Length[Vherm]];
Length[Vpartmatch];
Vhermnew = Vherm + Expand[Vpartmatch/2];
Print["Total number of terms kept in h.c of Vtilde type terms: ",
  Length[Vhermnew]]

Original length before h.c taken: 81
Hamiltonian terms which have h.c self-contained: 9
Number of Hermitian terms extracted: 36
Total number of terms kept in h.c of Vtilde type terms: 45

```

Step 3) Collect together the V terms

Now we try to sort these terms in a logical sense so that the form they take will be more self-evident.

We have the case which have the self-contained h.c from above (9 terms)

```

In[90]:= Print["Terms of which contain a w and wdag of the same type for each: ",
  Length[Vpartmatch]]
Expand[Vpartmatch/2];

Terms of which contain a w and wdag of the same type for each: 9

```

Now let's consider what other ones make up these 45 terms-> 36 left.


```

In[92]:= Vhermother = Vherm;
Length[Vhermother];
(* Number of terms remaining after Vpartmatch is removed*)
Vhermmatch = Vpartmatch/2; (*removing the h.c part*)
(*Finding the terms that have wdag(cell-1) and w(cell-1) on the same band*)
Vhermmatchfirst = Module[{a, b, f},
  With[{expr = Vhermother},
    expr /. {
      s : wdag[{cell-1, a_}]
        wdag[{cell, b_}] w[{cell-1, a_}] w[{cell, c_}] => f[s]
    } // Replace[#,
      {s_Times /; ! MatchQ[s, f[___] * ___] => 0},
      {1}
    ] & // ReplaceAll[#, f[s___] => s] &
  ]
];
Print["Number of terms which have wdag(cell-1)
  and w(cell-1) on the same energy band (and w(cell) and
  wdag(cell) on different bands): ", Length[Vhermmatchfirst]]
Vhermmatchfirst // Simplify;

(*Finding the terms that have wdag(cell) and w(cell) on the same band*)
Vhermmatchlast = Module[{a, b, f},
  With[{expr = Vhermother - Vhermmatchfirst},
    expr /. {
      s : wdag[{cell-1, a_}]
        wdag[{cell, c_}] w[{cell-1, b_}] w[{cell, c_}] => f[s]
    } // Replace[#,
      {s_Times /; ! MatchQ[s, f[___] * ___] => 0},
      {1}
    ] & // ReplaceAll[#, f[s___] => s] &
  ]
];
Print["Number of terms which have wdag(cell)
  and w(cell) on the same energy band (and w(cell-1) and
  wdag(cell-1) on different bands):", Length[Vhermmatchlast]]
Vhermmatchlast // Simplify;

Number of terms which have wdag(cell-1) and w(cell-1) on the
  same energy band (and w(cell) and wdag(cell) on different bands): 9
Number of terms which have wdag(cell) and w(cell) on the same
  energy band (and w(cell-1) and wdag(cell-1) on different bands): 9

```

Classifying the remaining terms (18 left)

```

In[101]:= Vhermrest = Vhermother - Vhermmatchfirst - Vhermmatchlast;
Print["Number of terms left over: ", Length[Vhermrest]]

```

```

(*Number of terms remaining unclassified*)
Vhermrest;

(*Finding the terms that have both wdags on the same band and both w
terms on the same band but don't match the previous requirements*)
Vhermrestbothsame = Module[{a, b, f},
  With[{expr = Vhermrest},
    expr /. {
      s : wdag[{cell - 1, a_}]
        wdag[{cell, a_}] w[{cell - 1, c_}] w[{cell, c_}] => f[s]
    } // Replace[#,
      {s_Times /; ! MatchQ[s, f[___] * ___] => 0},
      {1}
    ] & // ReplaceAll[#, f[s___] => s] &
  ]
];
Print["Number of terms which have the both wdags
      occupying the same band and both w occupying the same band
      (but not the same as each other): ", Length[Vhermrestbothsame]]
Vhermrestbothsame;

(*Finding the terms that have both w terms on
the same band and the wdag terms on different bands*)
Vhermrestsame = Module[{a, b, f},
  With[{expr = Vhermrest - Vhermrestbothsame},
    expr /. {
      s : wdag[{cell - 1, a_}]
        wdag[{cell, b_}] w[{cell - 1, c_}] w[{cell, c_}] => f[s]
    } // Replace[#,
      {s_Times /; ! MatchQ[s, f[___] * ___] => 0},
      {1}
    ] & // ReplaceAll[#, f[s___] => s] &
  ]
];

Vhermrestsame // Simplify;
Length[Vhermrestsame];

(*Finding the terms that have both wdag terms
on the same band and the w terms on different bands*)
Vhermrestdagsame = Module[{a, b, f},
  With[{expr = Vhermrest - Vhermrestbothsame},
    expr /. {
      s : wdag[{cell - 1, a_}]
        wdag[{cell, a_}] w[{cell - 1, b_}] w[{cell, c_}] => f[s]
    } // Replace[#,

```

```

      {s_Times /; ! MatchQ[s, f[___] * ___] >= 0},
      {1}
    ] & // ReplaceAll[#, f[s___] >= s] &
  ]
];

Length[Vhermrestdagsame];
Vhermrestdagsame;
(* But h.c of Vhermrestdagsame is in the same form as Vhermrestsame so we
   can re-order the terms to make this one simplified section of terms
*)

(* Changing the Vhermrestdagsame to be its h.c*)
Vhermrestdagchanged = Vhermrestdagsame /. wdag -> wnew;
Vhermrestdagchanged = Vhermrestdagchanged /. w -> wdagnew;
Vhermrestdagchanged = Vhermrestdagchanged /. wdagnew -> wdag;
Vhermrestdagchanged = Vhermrestdagchanged /. wnew -> w;
Length[Vhermrestbothsame];
Length[Vhermrestsame];
Length[Vhermrestdagchanged];
(*Defining Vhermrestsameboth to have the h.c of Vhermrestdagsame and
   Vhermrestsame*) Vhermrestsameboth = Vhermrestsame + Vhermrestdagchanged;
Print["The number of terms which have the w terms occupying the same band and
      the wdag terms occupying different ones: ", Length[Vhermrestsameboth]]
Vhermlastsamecomb = Vhermrestbothsame + Vhermrestsameboth;
Length[Vhermlastsamecomb];

(*The remaining 9 terms that have not been classified elsewhere*)
Vabsolutelast =
  Vhermrest - Vhermrestbothsame - Vhermrestsame - Vhermrestdagsame // FullSimplify;
Print["Number of terms of type V remaining: ", Length[Expand[Vabsolutelast]]]

Number of terms left over: 18
Number of terms which have the both wdags occupying the same band and
  both w occupying the same band (but not the same as each other): 3
The number of terms which have the w terms occupying
  the same band and the wdag terms occupying different ones: 6
Number of terms of type V remaining: 9

```

Finding the \tilde{J} coefficients (Eq. (6.9))

Here we define the terms that describe the pair tunnelling possibly with flips between nearest-neighbour hubs that are in Eq. (6.9).

Define the \tilde{J} type terms

Firstly, we collect together all of the terms of type \tilde{J} that include the cell of interest, i.e. all of the tunnellings between cell-1 and cell and cell and cell+1. We decide to actually use only the terms in cell-1 and cell as this will be repeated (in the cell and cell+1 case).

```

in[126]:= Jc[celluse_] := Module[{a, b, f, g, h, i, j, k, l},
  With[{expr = cageintc[celluse]},
    expr /. {
      s: (wdag[{a_, g_}] wdag[{a_, h_}] | wdag[{a_, i_}]^2) (w[{b_, j_}] w[{b_, k_}] |
        w[{b_, l_}]^2) /; Sort@{a, b} == {celluse, celluse + 1} => f[s]
    } // Replace[#,
      {s_Times /; ! MatchQ[s, f[_] * ___] => 0},
      {1}
    ] & // ReplaceAll[#, f[s___] => s] &
  ]
] (*terms coming from the C site that contain the cell of interest*)
Length[cageintc[cell - 1]];
Length[Uc[cell - 1]];
Length[Vcplus[cell - 1]];
Length[Jc[cell - 1]];

Ja[celluse_] := Module[{a, b, f, g, h, i, j, k, l},
  With[{expr = cageinta[celluse]},
    expr /. {
      s: (wdag[{a_, g_}] wdag[{a_, h_}] | wdag[{a_, i_}]^2) (w[{b_, j_}] w[{b_, k_}] |
        w[{b_, l_}]^2) /; Sort@{a, b} == {celluse - 1, celluse} => f[s]
    } // Replace[#,
      {s_Times /; ! MatchQ[s, f[_] * ___] => 0},
      {1}
    ] & // ReplaceAll[#, f[s___] => s] &
  ]
] (*terms coming from the A site that contain the cell of interest*)
Length[Ja[cell]];
Print["Cback", Length[J[cell - 1]], "A", Length[Ja[cell]], "C", Length[Jc[cell]]]
Print["Number of terms for a given cell of type J: ",
  Length[Jc[cell - 1] + Ja[cell]]]
Jpart[cellin_] := Jc[cellin - 1] + Ja[cellin];
Jcage[cellin_] := Jc[cellin - 1] + Jc[cellin] + Ja[cellin] + Ja[cellin + 1];
(*Defining all of them so that we can project with whole cage*)

Cback1A72C72
Number of terms for a given cell of type J: 72

```

```
In[137]:= Print["1st order projection on lowest band: ", Jcage[4] /. LBproj]
```

```
1st order projection on lowest band:
```

$$\frac{1}{32} w[\{4, -1\}]^2 \text{wdag}[\{3, -1\}]^2 + \frac{1}{32} w[\{3, -1\}]^2 \text{wdag}[\{4, -1\}]^2 + \frac{1}{32} w[\{5, -1\}]^2 \text{wdag}[\{4, -1\}]^2 + \frac{1}{32} w[\{4, -1\}]^2 \text{wdag}[\{5, -1\}]^2$$

```
In[138]:=
```

Step 1) Check that all the terms of \tilde{J} type have a h.c

Again we simplify the number of terms we are looking at by removing the h.c of each J term. This is the check that a h.c term does correspond for each term.

```
In[139]:= Module[{a, b, c, d},
  With[{expr = Jpart},
    If [Coefficient[expr, {w[{cell, a}] w[{cell, b}]
      wdag[{cell - 1, c}] wdag[{cell - 1, d}]}] ≠ Coefficient[expr,
      {w[{cell - 1, c}] w[{cell - 1, d}] wdag[{cell, a}] wdag[{cell, b}]}],
      Print["False"] ×
      Print[Coefficient[expr,
        {w[{cell, a}] w[{cell, b}] wdag[{cell - 1, c}] wdag[{cell - 1, d}]}] ×
        Print[Coefficient[expr, {w[{cell - 1, c}] w[{cell - 1, d}]
          wdag[{cell, a}] wdag[{cell, b}]}]]
    ]
  ]
]
```

Step 2) Retain only the h.c of terms of type \tilde{J}

Now we only retain the one of each pair of h.c terms, already restricting the order of the terms so that it will be easier to sort them.

```

In[140]:= Jaherm[celluse_] := Module[{a, b, f, g, h, i, j, k, l},
  With[{expr = cageinta[celluse]},
    expr /. {
      s: (wdag[{a_, g_}] wdag[{a_, h_}] | wdag[{a_, i_}]^2) (w[{b_, j_}] w[{b_, k_}] |
        w[{b_, l_}]^2) /; {a, b} == {celluse - 1, celluse} => f[s]
    } // Replace[#,
      {s_Times /; ! MatchQ[s, f[_] * _] => 0},
      {1}
    ] & // ReplaceAll[#, f[s_] => s] &
  ]
]

Jcherm[celluse_] := Module[{a, b, f, g, h, i, j, k, l},
  With[{expr = cageintc[celluse]},
    expr /. {
      s: (wdag[{a_, g_}] wdag[{a_, h_}] | wdag[{a_, i_}]^2) (w[{b_, j_}] w[{b_, k_}] |
        w[{b_, l_}]^2) /; {a, b} == {celluse, celluse + 1} => f[s]
    } // Replace[#,
      {s_Times /; ! MatchQ[s, f[_] * _] => 0},
      {1}
    ] & // ReplaceAll[#, f[s_] => s] &
  ]
]

Length[Jcherm[cell - 1]];
Print["JCback_", Length[Jcherm[cell - 1]], "Ja_", Length[Jaherm[cell]],
  "JCback+Ja_", Length[Jcherm[cell - 1] + Jaherm[cell]]]
Jhermcage = Jcherm[cell - 1] + Jaherm[cell];
Print["Number of J terms only retaining h.c: ", Length[Jhermcage]]
Jhermcage;
FullSimplify[Jhermcage];
JCback_36Ja_36JCback+Ja_36
Number of J terms only retaining h.c: 36

```

Step 3) Collect together the \tilde{J} terms

Combining the terms of type \tilde{J} into different types.

```

In[148]:= (*The terms such that both wdag terms are on
the same band and both w terms are on the same band*)
Jhermbothsame = Module[{a, b, f, g, h, i, j, k, l},
  With[{expr = Jhermcage},
    expr /. {
      s: wdag[{a_, i_}]^2 w[{b_, l_}]^2 /; Sort@{a, b} == {cell - 1, cell} => f[s]
    } // Replace[#,
      {s_Times /; ! MatchQ[s, f[_] * _] => 0},

```

```

      {1}
    ] & // ReplaceAll[#, f[s___]  $\Rightarrow$  s] &
  ]
];
Simplify[Jhermbothsame];
Print["Terms which have both w on the same band and which
      have both wdags on the same band: ", Length[Jhermbothsame]]

(* Terms that have wdag(cell-1) on the same band and w(cell)
on different bands*) Jhermsame = Module[{a, b, f, g, h, i, j, k, l},
  With[{expr = Jhermcage - Jhermbothsame},
    expr /. {
      s : wdag[{a_, i_}]2 w[{b_, l_}] w[{b_, m_}] /;
        Sort@{a, b} == {cell - 1, cell}  $\Rightarrow$  f[s]
    } // Replace[#,
      {s_Times /; ! MatchQ[s, f[___] * ___]  $\Rightarrow$  0},
      {1}
    ] & // ReplaceAll[#, f[s___]  $\Rightarrow$  s] &
  ]
];
Print["Number of terms which have wdags(cell-1) on the
      same band and w on different bands: ", Length[Jhermsame]]
Jhermsame;
Jhermrest = Jhermcage - Jhermbothsame - Jhermsame;

(* Terms that have w(cell) on the same band and wdag(cell-1) on
different bands*) Jhermdagsame = Module[{a, b, f, g, h, i, j, k, l},
  With[{expr = Jhermrest},
    expr /. {
      s : w[{a_, i_}]2 wdag[{b_, l_}] wdag[{b_, m_}] /;
        Sort@{a, b} == {cell - 1, cell}  $\Rightarrow$  f[s]
    } // Replace[#,
      {s_Times /; ! MatchQ[s, f[___] * ___]  $\Rightarrow$  0},
      {1}
    ] & // ReplaceAll[#, f[s___]  $\Rightarrow$  s] &
  ]
];
Print["Number of terms which have w(cell) on the same
      band and wdag on different bands: ", Length[Jhermdagsame]]
Jhermlast = Jhermrest - Jhermdagsame;
Print["Number of terms remaining unclassified of tilde{J} type: ",
      Length[Jhermlast]]
Simplify[Jhermlast];

```

Terms which have both w on the same band and which have both wdags on the same band:

Number of terms which have $w_{dags}(cell-1)$ on the same band and w on different bands: 9

Number of terms which have $w(cell)$ on the same band and w_{dag} on different bands: 9

Number of terms remaining unclassified of \tilde{J} type: 9

Check if there are any remaining terms

Lastly, we perform a check to make sure that all terms are included in types \tilde{U} , \tilde{V} and \tilde{J} . We are considering the terms that come from A_j , B_j and C_{j-1} only here.

```

In[160]:= cageconsider = cageinta[cell] + cageintb[cell] + cageintc[cell - 1];
Print["Number of terms in considered cage: ", Length[cageconsider]]
(*removing the U part*)
Other = cageconsider - Uaall[cell] - Ucall[cell - 1] - Ub[cell];
Print["U_terms: ", Length[Uaall[cell] + Ucall[cell - 1] + Ub[cell]]];
Print["Removing_U: ", Length[Other]];
Other = Other - Vpartcage[cell];
Print["V_terms: ", Length[Vpartcage[cell]]];
Print["Removing_V: ", Length[Other]];
Print["J_terms: ", Length[Jpart[cell]]];
Other = Other - Jpart[cell];
Print["Removing_J: ", Length[Other]];

Number of terms in considered cage: 225

U_terms: 72
Removing_U: 153
V_terms: 81
Removing_V: 72
J_terms: 72
Removing_J: 0

```